IPPT Reports on Fundamental Technological Research
1/2013

Irena Sielamowicz, Robertas Balevičius

EXPERIMENTAL AND COMPUTATIONAL ANALYSIS OF GRANULAR MATERIAL FLOW IN MODEL SILOS

Institute of Fundamental Technological Research
Polish Academy of Sciences
Warsaw 2013

IPPT Reports on Fundamental Technological Research

ISSN 2299-3657
ISBN 978-83-89687-81-4

Praca wpłynęła do redakcji 23 czerwca 2012 roku

Instytut Podstawowych Problemów Techniki Polskiej Akademii Nauk
Pawińskiego 5b, 02-106 Warszawa

Nakład 100 egz. Ark. wyd. 24,5
Oddano do druku w lipcu 2013 roku

Druk i oprawa: EXPOL, P. Rybiński, J. Dąbek, Sp. J., Włocławek, ul. Brzeska 4

Dedicated to Our Master,
Professor Zenon Mróz

ACKNOWLEDGEMENTS

The authors are indebted to the following persons and institutions:

- Mr Roman Sakowski, BSc, Eng. for his unstinted and selfless assistance in preparing and editing the book;
- Mr Mirosław Sawicki, BSc, Eng from the Soil Mechanics Department of BTU for his help in the research on granular materials;
- and many other persons who helped us by taking part in the experiments and devoting their time in the process of editing the book.

Finally, we wish to thank all our close friends who so willingly helped with all the necessary but tedious and time-consuming activities related to the book.

Irena Sielamowicz, Robertas Balevičius

Composite Silo Systems
Vilnius Gediminas Technical University

Abstract

The study described here was undertaken to explore the phenomena occurring in silo problems. For these problems, no experimental results exist, but simpler tests for validation can be used. This book identifies theses phenomena which are presented in two chapters. The first presents experimental investigations of granular material flows with a detailed description of phenomena occurring during filling and discharge processes in silo models. It also pertains to empirical descriptions of velocities and flow rates considered via statistical analysis. The experiments were conducted using a Digital Particle Image Velocimetry Optical Flow (DPIV OF). Applying this innovative technique allowed the obtaining and identification of a large volume of quantitative data characterizing the granular material flow, such as, velocities patterns within granular material, outflow rate, deformations, strains, dilation and stagnant zones boundaries; especially in the eccentric modes of flows for the plane silo models. The chapter also includes the analysis on verification of a Radial Flow assumption. The new mathematical description of kinematic parameter *b* for radial flow was applied with new formula for defining velocities in radial flows. Furthermore, the DPIV technique was applied to verify mass and volume conservation in the flowing material. The results obtained in this chapter serve as the basis of further verification via numerical simulations made by the Discrete Element Method (DEM).

Hence, the second Chapter discusses implementation of DEM in simulation of the processes observed during the performed experiments. The presented DEM mathematical model was applied to verify the wall stress distributions, this is presented first with a limited number of particles and then with an increased number of particles. This approach made it possible to verify parameters or indicators

derived from the well-known continuum-based methods. The computational analyses presented also provides a micromechanical insight into the filling and discharge of the granular materials in the 3D silo models. In particular, this chapter deals with the results of investigation of such specific phenomena known as “a free-fall arch”, material dilation forming, porosity fields evolution, distribution of stress within the granular material, outflow rates and velocity profiles.

The key finding of the analysis was the comparison of the measured wall pressure distribution in the experiments with those obtained numerically with DEM, Janssen solution and the Standard Eurocod 1. It was particularly demonstrated that the wall pressure calculated by the recommended formula in the design Standard gives lower values than those obtained from the experimental measurements. While a well known Janssen's theory cannot be expected to represent pressures during silo discharge. Also, the analysis of the influence of rolling friction on wall pressure and velocities distributions within the flowing granular material were considered in detail. Such important phenomena like a “pressure switch” were also successfully captured numerically and experimentally during the discharge process.

Finally, the general conclusions arising from the study appear to be very useful for the designers of silo structures one of the most difficult tasks in the field of civil engineering.

Streszczenie

Podstawowym celem pracy jest opisanie zjawisk występujących w procesach technologicznych w silosach. Z uwagi na brak badań eksperymentalnych silosów w skali naturalnej badania tych zjawisk przeprowadza się w skali laboratoryjnej. W książce podjęto próbę zidentyfikowania niniejszych zjawisk a wyniki prac podano w dwóch odrębnych rozdziałach.

Pierwszy z nich przedstawia wyniki badań eksperymentalnych płynięcia materiałów ziarnistych w czasie napełniania i opróżniania modelów silosu. Rozdział ten zawiera również empiryczne opisy prędkości i analizę wydatków wypływu wykonane metodami analizy statystycznej. Obrazy płynięcia materiału ziarnistego w modelach rejestrowano techniką cyfrową Digital Particle Image Velocimetry, Optical Flow, tzw. potokami optycznymi (DPIV OF). Zastosowanie tej innowacyjnej techniki pozwoliło na uzyskanie dużej ilości danych ilościowych charakteryzujących przepływy materiałów ziarnistych, takich jak: profile prędkości płynącego materiału ziarnistego, wartości wydatku wypływu, deformacje, odkształcenia, zakres stref zastoju w przepływach symetrycznych i niecentrycznych w płaskich modelach silosów. Rozdział pierwszy przedstawia również analizę weryfikacji założenia przepływu radialnego, gdzie podano nowy opis matematyczny parametru kinematycznego b dla przepływu radialnego, zastosowano nową formułę określenia prędkości w przepływach radialnych. Dzięki technice DPIV dokonano weryfikacji prawa zachowania masy i objętości w płynącym materiale. Wyniki przedstawione w tym rozdziale stały się podstawą do dalszej weryfikacji poprzez symulacje numeryczne wykonane metodą elementów dyskretnych (DEM).

Rozdział drugi omawia zastosowanie metody DEM do symulacji procesów zarejestrowanych w czasie eksperymentów. Przedstawiony model matematyczny DEM wykorzystano do weryfikacji rozkładu naporów w ścianie, w pierwszej fazie analizy z mniejszą liczbą cząstek, a następnie z większą liczbą cząsteczek. Takie podejście pozwoliło na dokonanie oceny porównawczej różnych parametrów ze

znanymi rozwiązaniami mechaniki continuum oraz na zastosowanie podejścia mikromechaniki na ocenę procesów napełniania i opróżniania w trójwymiarowych modelach silosów. W rozdziale tym dalej omówiono wyniki symulacji konkretnych zjawisk, takich jak tworzące się zawieszenia w materiale, kształtowanie się stref rozluźniania materiału, ewolucję pola porowatości, rozkłady naprężeń w materiale, wartości wydatku wpływu i kształty profili prędkości.

Finalnym ważkim wynikiem analizy było porównanie rozkładu ciśnienia pomierzonego eksperymentalnie w ścianie z wynikami analizy numerycznej metodą elementów dyskretnych DEM, a następnie z rozwiązaniem Janssena oraz zaleceniami normy Eurocod 1. Wykazano, że ciśnienie powstałe w ścianie w wyniku naporu materiału obliczone zgodnie z normą Eurokod 1 przedstawia niższe wartości niż te, które otrzymano w trakcie eksperymentów, a rozwiązanie Janssena nie podaje wartości ciśnień w czasie opróżniania silosu. Nadto, podano analizę wpływu tarcia tocznego na ciśnienia w ścianie i na rozkłady prędkości oraz zjawisko powstania „skoku ciśnień" w ścianie. W końcowej części monografii podano wnioski wypływające z badań, które mogą posłużyć projektantom konstrukcji silosów – jednym z najtrudniejszych zadań w zakresie inżynierii lądowej i wodnej.

Contents

Preface

This book presented here is the result of several years of our scientific cooperation with Professor Zenon Mróz from the Institute of Fundamental Technological Research of the Polish Academy of Sciences in Warsaw (IPPT PAN). Without his immensely valuable professional advice and suggestions, patience and dedication the book would never have been completed.

The first author also wishes to express her gratitude to Professor Tomasz A. Kowalewski, Head of the Department of Mechanics and Physics of Fluids of the Institute of Fundamental Technological Research of the Polish Academy of Sciences (IPPT PAN) and his staff – particularly Andrzej Cybulski and Sławomir Błoński, PhD, who kindly made it possible for us to conduct a large number of model experiments and use their unique equipment and software for the DPIV technique. Also thanks to Sławomir Błoński, PhD for making many figures for this book.

We are also indebted to Professor Andrew Drescher from the University of Minnesota for all his invaluable suggestions and fruitful discussions concerning the experimental research.

Our deep gratitude also goes to Professor Lech Dietrich, Head of the Laboratory of Strength of Materials and also to Professor Jan Holnicki-Szulc, Head of the Intelligent Technology Laboratory of IPPT PAN and his team (particularly Jerzy Motylewski PhD, and Anita Orłowska, PhD), for allowing us to use their diagnostic equipment to measure pressures in the silo model and for their helpful assistance with the experiments.

We also offer our thanks to Professor Zbigniew Ranachowski and Tomasz Dębowski, McS, from the Laboratory of Analysis of Acoustic Emission Signal at the Department of Physical Acoustics, Institute of Fundamental Technological Research of the Polish Academy of Sciences for their deep engagement in our experiments and for performing tests using their laboratory equipment. Additionally, special thanks are extended to Prof. Marek Molenda from the Institute of Agrophysics of

Polish Academy of Sciences in Lublin for investigation of the physical properties of the pea grains determined in the experiments presented.

Our thanks also go to Professor Michał Czech of the Chair of Mechanics and Applied Numerical Methods at Bialystok Technical University for his wide help with empirical descriptions presented in the book and to our colleague Professor Rimantas Kačianauskas of the Numerical Laboratory at Vilnius Gediminas Technical University for their limitless cooperation in numerical modelling in DEM.

Furthermore, the first author wishes to express her gratitude to Mr. Timothy A. Bell, PE, who recommended her research for financial support from the European University Support Program by the DuPont Centre for Collaborative Research & Education (CCRE). The first author also extends her thanks to Mr. Timothy Bell for his helpful debates at the scientific conferences we attended together and especially for his assistance in providing her with financial support for her participation in the 5th World Congress on Particle Technology held in Orlando, Florida, USA in April 2006.

Last but not least, we are very grateful to all our colleagues of "The Silo Research Group" (Working Party) especially to Professor Francisco Ayuga, Dr John Carson of Jenike & Johanson Corporation, Professor Gisle Enstad, Professor Haim Kalman (especially for the financial support for our participation in the 5th International Conference for Conveying and Handling of Particulate Solids in Sorrento, Italy, August 27–31, 2006), Professor Jin Y. Ooi, Professor Jean Rajchenbach, Professor J. Michael Rotter, Professor Ugur Tüzün, for their fruitful discussions during our congresses and conferences and for sharing their professional experience with us.

Introduction

Reasons for completing the book

In our natural environment we are surrounded by a large number of buildings and special structures designed according to recommended standards and technical parameters suited to climatic conditions and static load requirements. Among these special structures we find silos and tanks for bulk storage of granular materials, powders or liquids commonly used in industry. The most important issues in the flow analysis of materials in silos are:

- knowledge of wall pressures caused by stored or flowing materials,
- and identification of flow modes in silos.

The silo walls are expected to withstand pressures exerted by the materials stored inside. Silos are filled from above and the material is stored and discharged at proper time. During storing, filling and discharging the wall pressures of the stored material must be precisely determined. The wall pressure is a basic parameter in the designing of the silo wall thickness. The values of wall pressures vary at different stages of the load coming from the stored material. In addition, the design of silos and hoppers need to include a structural consideration to accommodate any vacuum pressures arising during the discharge process of various materials. A wall buckling in steel silos and hoppers caused by the vacuum pressure is extremely dangerous and the silo wall stability modes and the load under which a structure will buckle should be carefully checked considering the compressive load case induced by a vaccum pressure value, provided by the silo monitoring specialists. On the other hand, the buckling does not necessarily equal catastrophic failure and the silo structure may still be able to support the load after buckling has taken place. Namely, the nonlinear analysis can explain postbuckling bahavior. A combined pressure and vacuum relief valves are always designed to protect the silos from the effects of over-pressures during either a fill or empty conditions. Any steel silo or hopper cannot retain its load-bearing capabilities, if the complete emptying occurs without installation of vaccum relief valves. When calculating wall stresses, one must also consider flow

patterns. The phenomena associated with filling, storage and discharge in silos are still not fully understood despite the many experimental and theoretical attempts that have been made to explain them.

The issue of wall pressures is very important for designers of silos and is regulated by various codes and standards. Not only Polish and European but also world standard committees recommend standards that relate to silos, e.g., Part 4 of Eurocode 1 – EN 1991-4, [166]. In the United States the codes are ACI-313, [168], in Australia AS 3774, [169], ENV 1991 – Part 4, [174].

In the standards mentioned above, some essential principles concerning the phenomena occurring in silos including silo failures or disasters are lacking. Expertises following silo accidents or disasters often indicate that the obligatory standards are not reliable.

As regards the issue of investigating the flow modes in silos the first author has made an attempt to verify the classical flow modes described by Jenike in 1961. However, in the case of radial velocity fields, some inconsistencies have been discovered concerning the constant flow parameter. The assumptions made by [1] concerning the radial flow were not clearly defined. In [2], the author also adopted a constant value for the relation describing the flow velocity. In our experiments supported by the DPIV technique, it was possible to prove that the radial flow velocity depends on the exponential function and thus verify the radial flow field.

In the book, the DEM-based computational model is developed. The model has been experimentally verified and found to be in good agreement with experimental measurements during filling, storage and discharge. It is also important to know the values of the velocities and the range of stagnant zones formed during the flow and how long and how much of the material rests in the stagnant zone.

The investigation also showed that in the lower part of the hopper, an active stress state occurs $\sigma_x^e < \sigma_z^e$, but in the upper part a passive state, $\sigma_z^e < \sigma_x^e$, develops, where σ_x^e is the normal stress to the vertical wall and σ_z^e denotes vertical stress in the silo. This pattern of stress distribution changes during the discharge process where the passive state develops at the bottom hopper position. This observation does not support the view, of [3, 4] that the active stress state develops within the hopper after the filling process.

In the book some experimental measurements of velocities and stagnant zone range in a model of different wall roughness are also presented. This issue plays a signifi-

cant role in natural scale silos when, after many cycles of discharging, organic materials stored in the stagnant zones may begin to putrefy and decay. Such a putrefied part of the material in the silo is undesirable. Also materials that age quickly (e.g. grains and powders) and remain in the stagnant zones for a long time form arches which may fall down in hard blocks of material and damage the bottom of the hopper.

It is hoped that the present research will clarify in greater detail some aspects of the bahavior of granular material and its impact on silo walls.

To give a better idea of the nature of silo failures and disasters, some recent accidents are shown in the following Figures A.1–A.6. In [5], the author mentioned four major causes of silo failures that are due to shortcomings in one or more of four categories: design, constructions, usage and maintenance. Damage and failures are far much frequent in silos than in any other constructions. Many complicated phenomena occur during the flow in silos (e.g. arches, explosions, implosions, cluster forms or rat holes). In the USA alone, a total of 13 grain explosions were reported in 2005, as compared with 6 in 2004 in Poland. A serious silo disaster – wall implosion – occurred in Brzeg, near Opole in 2005, (cf. Figure A.4).

Figure A.1. Failure of grain silo, (dust explosion).

http://www.bulk-solidshandling.com/webcasts

Figure A.2. Failure of grain silo.

http://www.bulk-solidshandling.com/webcasts

Figure A.3. Collapse of a granular (corn) silo due to a poor design.

http://www.bulk-solidshandling.com/webcasts

Figure A.4. Failure of grain silo, 2005, Brzeg, Poland, (implosion).

http://www.inzynierbudownictwa.pl/biznes,bhp,artykul, przyczyny_techniczne_wystepowania_zagrozen _awarii_i_katastrof_budowlanych

Figure A.5. A hole in a 12.7 mm thick stainless steel plate and a movement of a 2000 ton silo by shearing its foundation bolts, the USA.

http://www.bulk-solidshandling.com/webcasts

Figure A.6. Failure of steel silo, implosion.

http://www.bulk-solidshandling.com/webcasts

An example of a case when rat holes collapsed in a silo with loads large enough to tear a hole in a 12.7 mm thick stainless steel plate and enough to move a 2000 ton silo by shearing its foundation bolts is presented in Figure A.5. Unfortunately silo disasters usually involve not only material losses (structural and content damage) but also heavy human casualties.

In view of all the problems of silo structure and operation, it was quite a challenge to re-examine the impact of the bahavior of granular material in silos and to suggest some innovative technical and statistical solutions concerning granular flow in silos during the filling, storing and discharging processes.

The results presented in the work will be useful in gaining a greater knowledge of flow phenomena in natural scale silos. A better understanding of properties of stored materials and their interactions with the structure is of importance for improvement of the design of silos.

The book discusses the following problems:

- using the Digital Particle Image Velocimetry Technique that has made it possible to obtain a large number of quantitative data characterizing granular flow,
- identification the flow in models in detail, velocities, flow rate, stagnant zone boundaries,
- identification the eccentric flows in the plane model, empirical description of velocities and the flow rate in the model,
- verification of Radial Flow Assumption in hoppers,
- verification of mass and volume conservation in the flowing material,
- verification of the kinematic model, the new distribution of the kinematic parameter was presented,
- a mathematical model using DEM applied to verify the nature of wall stresses with limited number of particles,
- improvement of the methods and computational analyses in order to gain a better knowledge of the phenomena occurring during the filling and discharge of the granular materials in the models and to distinguish and quantitatively investigate them,
- the application of the method – the Discrete Element Method (DEM), ("the grain method") with 20,400 particles in the mathematical model to simulate the flow in silo models of different shapes,
- verification of the DEM model by comparison with the results obtained during the experiments.

1. Investigations of flow processes – Experiments in silos

1.1. Experimental analysis of flow in the plane model by the DPIV (Digital Particle Image Velocimetry) technique

1.1.1. Introduction

Investigation of flow patterns and wall stresses in silos and other hoppers is usually carried out on laboratory models. Many different measurement techniques have been used in such studies: visual measurements through transparent walls, coloured layers and photography, coloured layers and dissection after freezing the flow with paraffin wax, photographic or video techniques, tracer techniques using X-rays and radio pills and insertion of markers to measure residence times, [6]. In laboratory tests very significant scale effects in silo flow and pressures were reported by [7, 8, 9, 10, 11]. However, almost all of these techniques are not viable at full scale. Many tests on full scale silos were made to measure wall pressures in Denmark, France, Great Britain, Holland, Poland – [12, 13, 14, 15, 16, 17, 18, 19, 20, 21, 22], (both in models and in full scale silos), in Sweden, Australia and South Africa, [23]. But there are a few examples given in literature where the measurements of flow patterns were performed on line, [6, 23, 24]. Such investigations are very expensive, not only due to enormous size of the silo but also to difficulties in accessing the structure. Because of the difficulties of access at natural scale such as opaque walls, opaque solids, surface covered with dust and intrusive investigation techniques, such as the penetration of the wall, rarely acceptable by silo owners, model silo studies seem to be very useful in the recognizing flow patterns. Though the challenge of observing flow processes at full scale remains still considerable. The flow inside the silo has been poorly identified till today and the investigation of flow modes inside the silo is almost impossible.

Silos are structures having round horizontal cross sections. Usually all laboratory models are flat and only flat flow are investigated. There are also round laboratory models but in this case, it is much more difficult to measure stagnant zone boundaries. In such models usually the problem of flow modes and determining wall pressures are made.

In this Chapter, the use of the latest diagnostic tool – the DPIV (Digital Particle Image Velocimetry) technique is presented in order to identify the flow in some cases of both central and eccentric flow in the models made of Plexiglas, one with vertical walls and another one in a converging model. The technique introduced in the 90's as PIV (Particle Image Velocimetry) was developed into DPIV as an alternative approach of the PIV. In general, this technique was applied in fluid mechanics and its first applications to granular material flow were presented in [25, 26] or in [27]. One of the first successful attempts to apply the PIV technique to granular matter was described in [27, 28, 29, 30, 31, 32, 33, 34, 35, 36, 37]. In [38], the authors reported the use the PIV technique in their experiments to obtain information on local velocities of particles at several elevations in densely packed materials. In [29], the authors combined PIV measurements with wall normal stress measurements at different points of time in a large scale silo. The 2D flow close to the transparent walls of the model silo was observed.

Using PIV to measure particle displacement or velocity in granular flows we should consider that it is impossible to illuminate an arbitrary plane within the flow held and record the particle motion in that plane due to the opacity of the particles. The application of PIV to granular flows is limited to quasi-two dimensional flows, where the flow can be viewed at a free surface or through a clear bounding wall. Two dimensional models of hopper flows have been studied in an effort to shed light on the three dimensional cases, [39, 40, 41, 42, 43]. Applying PIV to granular flows is also limited by the number of particles. Too many particles may be present in the image resulting in a speckle pattern rather than an image of individual particles, [44]. In [27], the authors found that by using a mixture of light and dark particles, this problem can be avoided.

Observations of the discharge process allow us to understand the behaviour of the material. As mentioned above, different measurement techniques have been used in investigations of flow in silo models. The first works [45], where two different colours of material were used, allowed detection of zones of flow and stagnant zones. The flow was observed through transparent walls of the model to register

flow profiles. A number of experimental works have been focused to measure flow patterns. Optical techniques are commonly used in the analysis of velocity profiles near the transparent silo walls. The X-ray technique was frequently applied (e.g. in [46, 47]) to obtain information from deeper flow layers. Also, other non-invasive measurement techniques were applied to register granular flow, density and velocity fields in flowing zones, among others tomography, spy-holes, radio transmitters, positron emission [48], magnetic resonance imaging [49, 50], radioactive tracers [51] and ultrasonic speckle velocimetry [52]. More details on different techniques used in investigations of granular flow in small models can be found in references given in [27] and in [48].

Particle Image Velocimetry (PIV) is a method used for two-dimensional flow structure evaluation. It enables the measurement of the instantaneous in-plane velocity field within a planar section of the flow field, the spatial gradients, dissipation of turbulent energy or spatial correlations. In the early days of the PIV technique multiple-exposure images and optical auto-spectrum or autocorrelation analysis were applied, [53]. Images taken for PIV analysis were recorded on a film and the flow field was obtained via the computation of the spatial correlation in a small search region. It was a very laborious task to process large numbers of images. Therefore, an alternative approach – Digital Particle Image Velocimetry (DPIV) was introduced the by authors in [54, 55]. Here digital images are recorded directly with a CCD camera and frame-grabber, and can be studied without the unnecessary delay and associated with the digitisation of photographs. The DPIV allows for a simple realization of the cross-correlation technique for pairs of two separate images. The typical DPIV evaluation procedure is based on the analysis of two successive images of the flow. Despite recent progress in the DPIV development, further improvement of the accuracy and minimization of the computational time still remains a current research goal, [56, 57]. One of the main drawbacks of classical DPIV is its inability to accurately resolve flow regions characterized by large velocity gradients. This is due to the strong deformation of the particle image pattern within a DPIV search window. A group of researchers [58, 59, 60] – proposed several alternative evaluation methods to remove the above limitations. It appeared that the optical flow method may be an interesting alternative, offering high evaluation accuracy without most of the typical DPIV limitations. This technique which was developed for detecting the motion of large objects in real world, was adopted to measure fluid flow [61], yielding a significant increase in the accuracy and spatial resolution of the velocity field. More details on

the technique, its accuracy and principles one can find in works [44, 62, 63, 64, 65, 66, 67, 68, 69].

1.1.2. Basic assumptions in granular material flow

In granular material flow the main assumptions were introduced by Jenike in his reports published in 1961 and 1964, [1, 95]. He was the first to call the processes as RVF & RSF – (Radial Velocity Field) and (Radial Stress Field). Jenike presented two types of flow during the discharge of granular material from hoppers: mass flow and funnel flow. In [70], the authors classified funnel flow into semi-mass flow and internal or pipe flow. The flow channel boundary is also defined as the interface between flowing and stationary solid. The methods based on the concepts of plasticity can predict the existence of stagnant zones but there are no reliable methods of predicting the shape of the stagnant zone boundaries, [71]. Plasticity theory is well established for the prediction of small displacements in granular material and can be extended to effectively infinite strains in flowing materials. It was later found that the flowing zone predicted by Jenike's radial velocity field was far narrower than that observed in practice, [72]. Many experiments are aimed at investigating types of flow and shapes of the flowing regions. Some factors such as: hopper geometry, height of packed materials, size of particles, material density, material-wall interface friction influence the shape of flow patterns, [28, 70, 73, 74, 75, 76].

Many theoretical works classify steady state flow [77, 78, 79] into two cases: loosely packed material in either tall bins or shorter bins but the bin should be filled in a continuous way. To predict velocities and stagnant boundaries in the flowing material, several theoretical models were introduced into the analyses. The applied mathematical models assume a rigid-perfectly plastic model [80, 81, 82] or purely kinematic material model, proposed in [83,84], further developed in [85, 86] and applied in [28, 87, 88], or in the revised form by [89, 90, 91] and [92] presented gravitational movement of granular materials based on the method proposed by [83, 84].

It was usually assumed that material density is constant in the hopper. In this thesis, we verify this assumption and we present variation of the density at all analyzed elevations. In [89], the authors modelled the evolution of flow zones in cohesionless granular materials introducing a revised kinematic model. They considered stresses developing during the flow and the funnel-type of flow. In [93], the author

developed a new "softening" variable-density plastic flow model and applied it to the steady radial flow of a cohesionless granular material from steep-walled wedge and conical hopper. The flow conditions given by [93] include the time derivative of density in order to satisfy mass conservation. The author in [93] also assumed a variation of density with pressure and the variation of density was shown to decrease the mass discharge rate. There are also analytical approximate methods applied in the analysis of hopper loads and hopper geometry design like the limit state methods, the methods of differential slices, the method of plastic limit analysis, [2] or computational studies by FEM, [94].

The process of discharge is unsteady if the size of the flow region increases with time. The theoretical model for this type of flow assumes an incompressible radial velocity field and bases on kinematic theory, [71]. Provided a discharge from a densely packed hopper, a plug flow zone, formed in the material is observed and extends upward to the upper surface and then this zone widens and quickly reaches hopper walls. The boundaries of the flowing zones are shown in Figures 1.3, 1.30, 1.31, 1.64, 1.66, 1.68, 1.70, 1.72, 1.79, 1.90 obtained by the DPIV analysis in this Chapter.

1.1.3. Theory and experiments in plane flow

Jenike in his models distinguished radial stress fields (RSF) and radial velocity fields (RVF) and presented the results in a graphical form [1, 95]. The radial velocity field (RVF) presents a particular solution to the full stress equation for an ideal Coulomb material. The radial velocity field (RVF) is derived from the radial stress field on the assumption that a material obeys the principle of coaxiality, sometimes known as the principle of isotropy, [96]. The methods built by Jenike can predict the existence of stagnant zones in a flowing material. The observations of batch discharge also showed that the position of the stagnant zone boundary changes slowly in time. Since the kinematic model cannot predict the existence of the stagnant zone boundary, hence, the stagnant zone boundary was defined to be the position at which the velocity was equal to 1% of the centreline velocity at the same height, [70]. It was also found as a satisfactory approximation for the steady state. In [77], the authors showed that the stagnant zone boundary should be taken to be the stream surface within which 99% of the total flow takes place. In [97], the authors presented simulations of flow patterns in silos with a cellular automaton. Theoretical predictions of velocities and the flow boundary were also based on the

use of a purely kinematic model or a rigid perfectly plastic model. Both models assumed the constancy of the material density throughout the bin, i.e., incompressible flow was considered. The kinematic models mentioned above differ slightly in their qualitative aspects but all three describe the velocity distribution by the following differential equation:

$$\frac{\partial \upsilon}{\partial y} = B\frac{\partial^2 \upsilon}{\partial x^2}, \tag{1.1}$$

where v is the vertical velocity and x and y are horizontal and vertical distances, respectively. In [71], the author presents that Eq. (1.1) is not invariant with respect to the rotation of coordinates because the models are concerned with the gravity flow and y-coordinate must be directed vertically. Parameter B has the dimension of length and is often taken in the order of particle diameter. Eq. (1.1) is parabolic and cannot have discontinuous solutions and is used only for two dimensional systems. For cylindrical symmetry, the kinematic model has the form:

$$\frac{\partial \upsilon}{\partial z} = \frac{B}{r}\frac{\partial}{\partial r}\left(r\frac{\partial \upsilon}{\partial r}\right). \tag{1.2}$$

In [70], the authors showed that the streamlines in a discharging cylindrical bunker are indeed similar to those predicted from the kinematic model. Using the Finite Element Method, the solution of Eq. (1.2) for cylindrical bunkers for many different values of kinematic constant B was presented and considerable agreement between the predictions and the streamlines in steady flow was shown. In [70], the authors recognized three regions in the solution. Plug flow was found in the upper part of the bunker, where the velocity is presented as the ratio of the volumetric flow rate divided by the cross-sectional area. In the region close to the orifice, velocities of passing particles are high. It was also found that the only region where the velocity of the flowing material cannot be predicted is the intermediate region, located far from the orifice and far from the walls. In [28], the authors in their paper indicated that the predicted velocities are higher along the centre line and decrease gradually towards the boundary. The shape of the boundary was called as “a growing candlelight”. In some discussion, it was shown that the kinematic model gives no information about the stagnant zones, [71]. That is why a new model was proposed assuming that on filling, the material is compacted to its initial density and when the process of discharge starts the material density assumes another value. More details of the above discussion can be found in the literature, [71]. In [28], the authors modelled plug flow in bins and proposed a theoretical model (purely kinematic) for

describing the evolution of the plug flow zone. They did not consider the evolution of the velocity field and the stress field and only a simplified velocity field. The model relates to symmetric flow as well.

1.1.4. Experimental setup

In this section a series of experiments registered by the DPIV, conducted in a plane model made of Plexiglas is presented. The optical flow DPIV technique is used to register the evolution of the flow, velocity fields and velocity distributions in the granular material.

Figure 1.1 shows experimental setup used for the flow analysis, described in detail in [35]. It consists of a Plexiglas box, a set of illumination lamps, and a high resolution CCD camera (PCO SensiCam). Two Plexiglas models were used in the experiments. Both models have a height of 80 cm, and a width of 26 cm. One has a depth of 10 cm and the other 5 cm. The model of 5 cm in depth was used in the eccentric flow discussed in section 1.3.

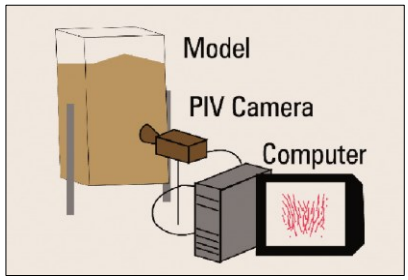

Figure 1.1. Experimental setup.

Recording the flow in the model of the depth 10 cm, the 12-bit flow images with resolution of 1280 pixels x 1024 pixels and maximum frequency of 3.75 Hz were acquired by Pentium 4 personal computer. Long sequences of 100–400 images were taken at variable time intervals for subsequent evaluation of the velocity fields. The velocity field was evaluated for triplets of images using optical flow PIV technique. Dense velocity fields with vectors for each pixel of the image were obtained and used for further evaluation of the velocity profiles, velocity contours and streamlines. The term “streamline” is defined as a direction of the flow of different particles at the same time. Intrinsic resolution of the PIV technique is limited by the size of the area of interest that is used in the application of the cross correlation algorithm between subsequent images and this is generally one order of magnitude larger than a single pixel.

Three kinds of granular material were used in the experiments: amaranth, flax-seeds and buckwheat. These materials show certain static electricity when flowing and sliding over Plexiglas. The properties of the materials used in the experiments are presented in Table 1.1, [35].

Table 1.1. Properties of the granular materials used in the experiments

Granular material	Angle of wall friction against Plexiglas φ_w [°]	Angle of internal friction φ_e [°]	Young modulus [MPa]	Granular material density deposited through a pipe with zero free-fall ρ_b [kg/m^3]
Amaranth	25	28	12.96	832 at 1 kPa 833 at 8 kPa
Flax-seed	26	25	6.11	746 at 1 kPa 747 at 8 kPa
Buckwheat	28	25	–	669 at 1 kPa 671 at 8 kPa

A single amaranth grain has a shape of regular round balls of 1 mm diameter, straw--coloured. The surface of the grain is plain, a flax-seed has a shape of flattened rotational ellipse 4 mm × 2 mm, brown in colour and plain, brilliant surface. A buckwheat seed is like a pyramid of total height 2 mm. Its surface is not as brilliant as flax-seed, being a little darker brown colour than flax-seed. The values of the angle of internal friction for the flax-seed and buckwheat given in Table 1 are taken from the Polish Standard PN-89/B-03262, [167] for the amaranth seed the values of the angles were measured in the laboratory.

1.1.5. Results of the experiments

1.1.5.1. Stagnant zone boundaries

In [98], the author presented his experimental measurements of the stagnant zone boundary as a function of time obtained in a hemi-cylindrical bunker of diameter 650 mm fitted with a semi-circular orifice of 65 mm diameter. In [71], the author showed the predicted position of the stagnant boundary as a function of time. These two investigations indicate that the kinematic model considered by [71] and [98] gives an excellent prediction of the development of the stagnant zone boundary. Some differences were noticed close to the orifice, where the assumption of a point sink differs from the orifice of 65 mm diameter as used in experiments. Figure 1.2 presents the development of the stagnant boundary resulting from the present experiments in the plane model of silo with the angle to vertical 90° and compared with the results obtained by [98] and [71].

The picture shows the flow of amaranth seeds for one half of the model. The plug flow develops very quickly in the material. The flowing zone is similar to funnel flow – internal or pipe flow. Generally, the shape of the flowing zones of amaranth seeds in Figure 1.3 is converging in the intermediate phase of the flow similarly to that observed in the experiments carried out in [98] and in the predictions given by [71]. However, the lines of the stagnant boundaries in Figure 1.2 are closer to each other in their vertical parts. It indicates that the flowing region does not increase in its width as it was observed in [98] and [71]. After the initial time of 3.75 s the material flows gradually from the upper parts into the flowing zone and a stable funnel zone forms. It maintains its width till the end of the flow, contrary to the results given in [98] and [71] that show gradual widening of the flowing zone with time. It remains unclear as to whether an absence of the lateral expansion of the funnel flow is related to particle geometry or to difference in the initial packing density. In Figure 1.2, the horizontal axis is given as a normalised width of the model and the vertical axis as a normalized height of the model.

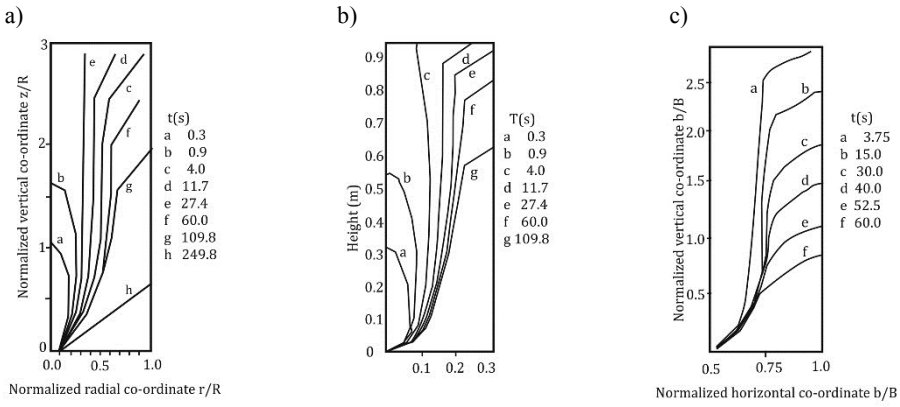

Figure 1.2. Experimental measurements of the stagnant boundary a) as a function of time, taken from [98], b) predicted position of stagnant zone boundary as a function of time by [71] c) present study – flow of amaranth seeds, [35].

1.1.5.2. Velocity distributions of the flowing grains

Figure 1.3 presents the velocity fields and velocity magnitude contours of the flowing amaranth obtained from the sequence of 315 images taken at the intervals of 0.2666 s, [35].

Evolution of the plug flow zone and development of a high velocity region (red colour contour) at the outlet is clearly visible. The stagnant zones are indicated by the blue colour of the velocity contour map.

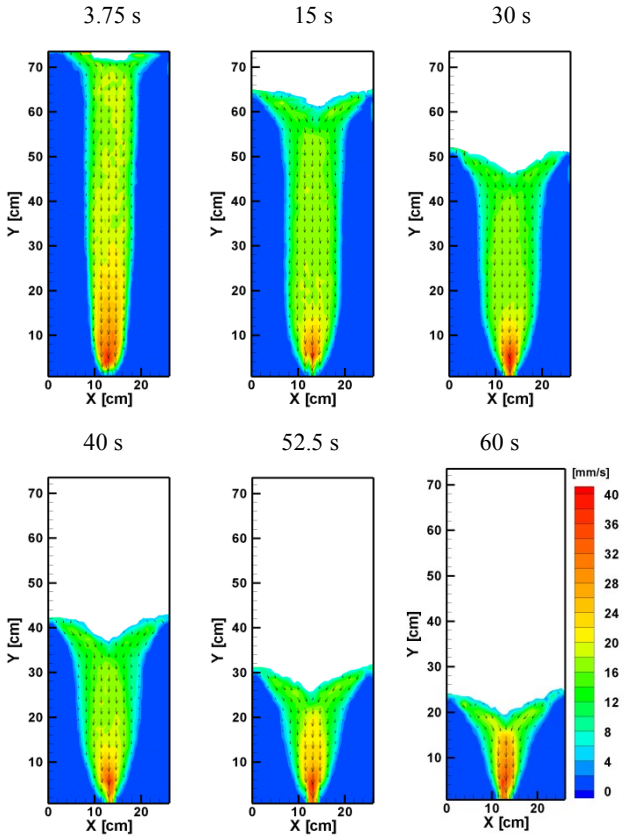

Figure 1.3. Velocity fields and velocity magnitude contours in the model with flowing amaranth seeds, [35].

1.1.5.3. Streamlines

Figure 1.4 presents selected streamlines calculated from the velocity field measured in the model for three flowing materials. The streamlines represent the motion of virtual particles, indicating the flow structure in the flowing zone. Figure 1.4a shows the streamlines, indicated with red vectors obtained for the flowing amaranth. The flow of the amaranth is symmetrical but some disturbances of the flow of single particles especially near the outlet can be seen. The black vectors denote the flowing region and the lengths of the vectors denote the velocity. In the stagnant zones there are points which denote vectors of zero value.

Near the outlet, where the velocity is the highest, convergence of the flow into the orifice is well illustrated by the streamlines. Local non-uniformities of the velocity field are well reflected in the asymmetry of the streamlines, observed in the flow regions. It appears that some degree of non-uniformity of the material is unavoidable in the experiments.

In Figure 1.4b, c the streamlines in the flowing flax seeds and buckwheat evaluated at the selected elevations are depicted with red colour lines. The total time flow of the amaranth seeds was 60 s, for the flax-seeds 103 s and for the buckwheat 122 s. All three flowing granular materials produce different flow structures as shown in Figure 1.4a, b and c. The outer streamlines are close to the boundary lines of the flowing zone. They are not always vertical or smooth. Some irregular lines result because both seeds were less homogeneous and contained some natural pollution. The shape of the grains and the kind of the seed surface influence also its flowing properties.

1.1.5.4. Velocity profiles

Other data obtained by the DPIV technique in experiments concerned velocity profiles. In Figure 1.5, the selected velocity profiles of the flowing amaranth seeds are shown, [35]. The profiles of the vertical velocity components across the cavity were obtained for different heights (indicated in the legend) and at time steps 3.75 s, 15 s, 30 s, 40 s, 52.5 s and 60 s after the beginning of experiment.

We observe a bunch of velocity profiles that have almost the same values. The shape of the profiles in the bunch is similar as well. This conclusion supports the other experimental observations (cf. [2, 74, 99]) that in symmetrical flow in plane bins the velocities of flowing materials above the outlet are constant and approximately vertical.

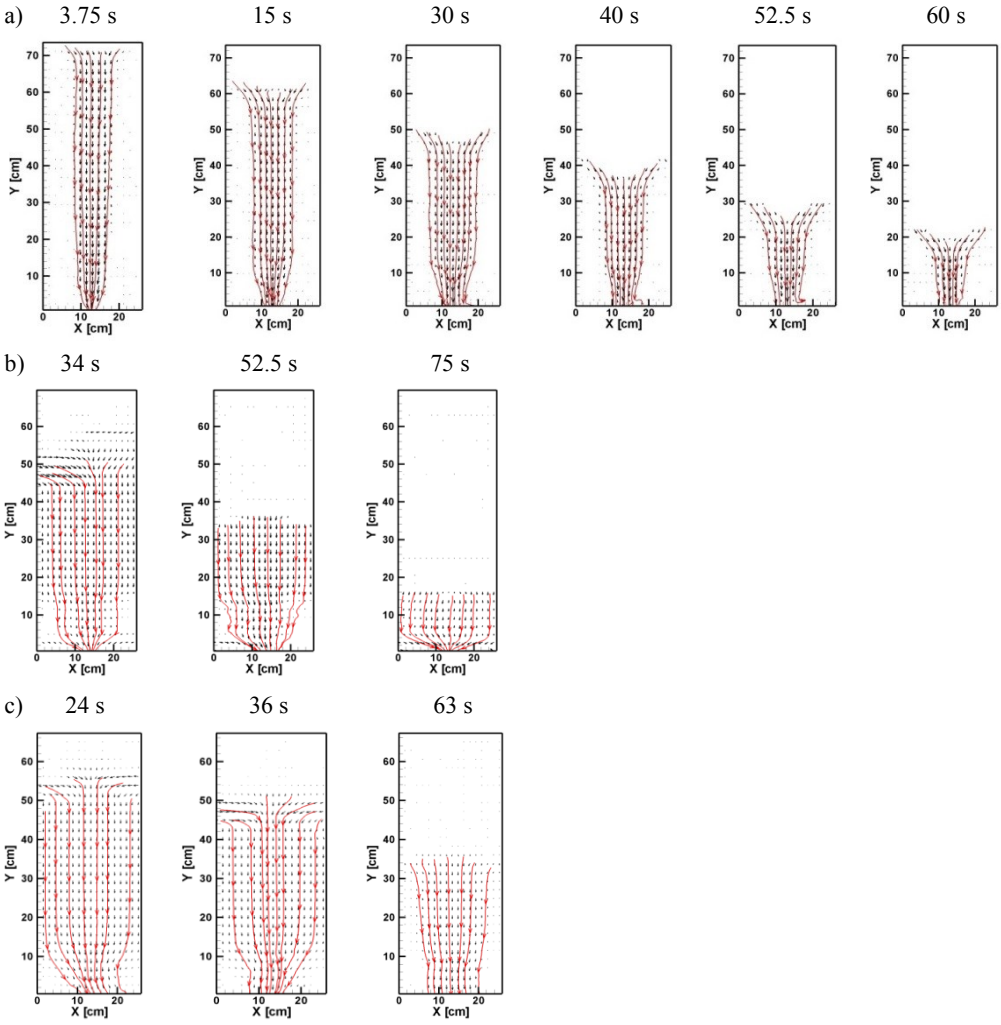

Figure 1.4. Streamlines in the flowing
a) amaranth seeds, b) flax-seeds, c) buckwheat, [35].

a) t=3.75 s

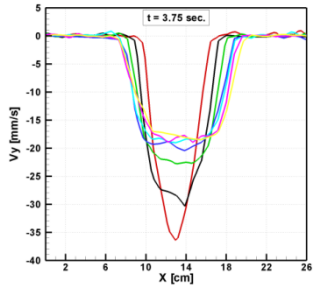

b) t=15 s

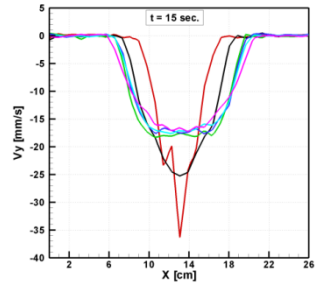

c) t=30 s

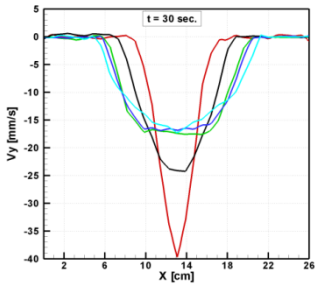

d) t=40 s

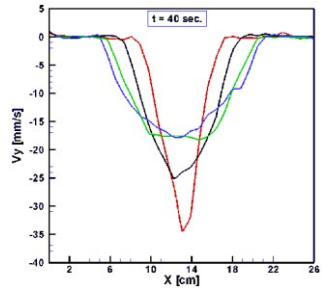

e) t=52.5 s

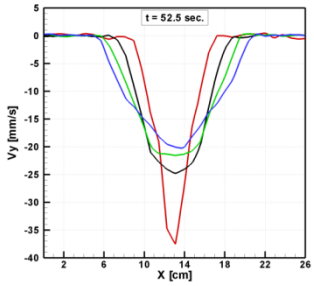

f) t=60 s

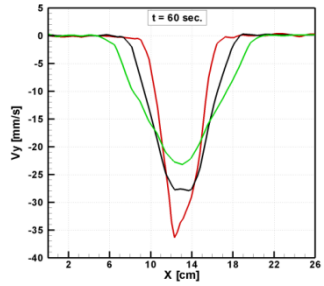

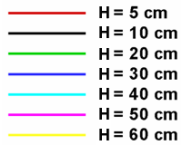

Legend to Figure 1.5 a-d

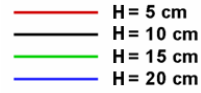

Legend to Figure 1.5 e-f

Figure 1.5. Velocity profiles of flowing amaranth seeds depicted in given time instants: a) t=3.75 s, b) t=15 s, c) t=30 s, d) t=40 s, e) t=52.5 s, f) t=60 s, (a, c, e [35]).

1.1.5.5. Evolution of velocities and plug flow zone

Variation in time of the volumetric discharge of granular materials is an important experimental parameter. It can be evaluated from the mean vertical flow velocity and the area of the flowing zone. Figures 1.6, 1.7 and 1.8 present the variation of the vertical velocities of particles V_y, height h and width $2b$ of the flowing zone of amaranth seeds as a function of time. Similar diagrams were presented in [28]. They observed that the maximum velocity of flowing crushed walnut shells was reached shortly after opening the outlet. Then the velocity rapidly decreased and from the 10th second of the flow the same velocity was registered. Similar behaviour was found in the present experiments.

"Main content of this chapter has been published in Chemical Engineering Science, 60, 2, 589-598, 2005".

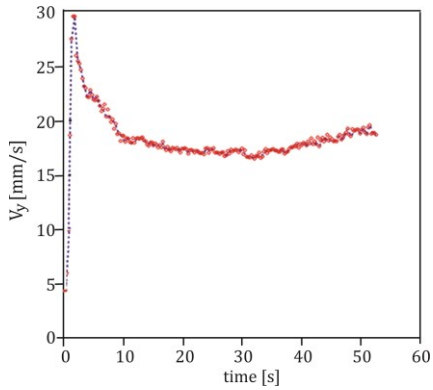

Figure 1.6. Evolution of the vertical velocity in the plug flow zone as a function of time, measured at the symmetry axis of the model flowing amaranth seeds, [35].

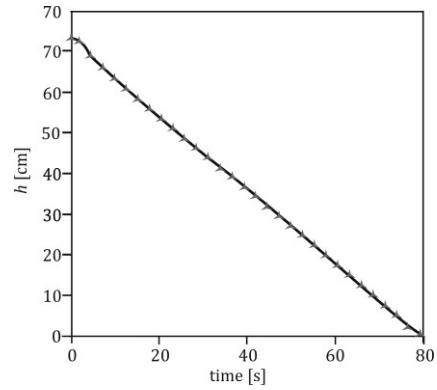

Figure 1.7. Evolution of the height of the plug flow zone as a function of time measured at the symmetry axis, flowing amaranth seeds, [35].

The observed evolution of the height of the plug flow zone is schematically shown in Figure 1.7 and the width of the plug flow at the level of 20 cm as a function of time in Figure 1.8.

The height of the plug flow zone was reported in [28] and [89]. They found that the plug flow zone reaches the height of the upper surface and then linearly decreases with time. Similar behaviour of the flowing zone was observed in the present experiments (cf. Figure 1.7). The evolution of the height of the plug flow can be approximated by almost a linear function of time.

Figure 1.8 displays evolution of the width of the plug flow zone as a function of time for the same experiment. This experimental analysis confirms the results obtained in [28], and reported the variation of the width of the flowing zone as a function of time for crushed walnut shells. It can be seen that the width of the plug flow zone varies with time and increases. The shape of the function in Figure 1.8 is similar to that in [28]. Comparing with the results obtained in [28] some differences can be encountered. They reported almost linear increase of the width of the plug flow zone in time. The disparity of the flowing material properties (crushed walnut shells against amaranth seeds used here) can be responsible for their different behaviour. Recently the authors in [89] showed the experimental results of the evolution of the half-width b of flowing crushed walnut-shells, however in [28] a heavier material was used, as a function of the percentage of mass discharged from a semi-cylindrical bin. They indicated that the variation of b is little effected by the initial height of the material and applies to the influence of outlet half-size. The functions showing the increase of the plug flow zone both in this analysis and in [28] and in [89] are in their general form similar.

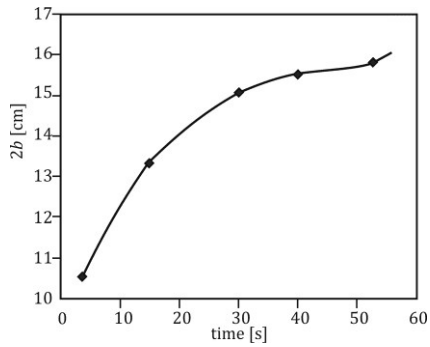

Figure 1.8. Evolution of the width of the plug flow zone as a function of time in the symmetry axis at the height 20 cm, flowing amaranth seeds; $2b$ – total width of the plug flow zone between stagnant boundaries, [35].

1.1.5.6. Wall stresses

The DPIV analysis yields velocity vectors for each point of the flow. This information can be used to predict the stresses in the flowing granular material. Calculating velocities in the flowing region, both derivatives of the obtained velocities as well as the stresses are calculated. In this experimental analysis such calculations were not made although it would be possible to extend this analysis in further work. As the issue of stresses both in the flowing material and on the silo walls is very important in the analysis of granular material flow, further investigations will be conducted and discussed later on. The accuracy of DPIV measurements seems sufficient to obtain velocity gradients inside the flowing zone. However, the evaluation of the stresses on the bin wall is still a challenging task. The velocity of the granular material near the wall is equal or close to zero and cannot be used to calculate the wall stresses. The velocity gradients measured on the boundary of the stagnant zone could offer useful values for calculating wall stresses. Such evaluation, combined with the stresses measured at the wall by electrical transducers, [30], could offer a possibility to verify theoretical descriptions of mechanical properties of granular media.

As stated above, wall stresses are significant parameter in silo design. Pressures in silos during discharge are quite different from those after filling. This difference is usually indicated as a main cause of silo failures [5, 100, 101, 102], so it is crucial to distinguish between filling and discharge pressures. It was already determined that filling pressures usually follow the Janssen pressure distribution, [103]. In Janssen's theory, the magnitude of introduced parameter k, the lateral pressure ratio, may be uncertain but was not defined. Moreover, if the filling is eccentric, this can lead to significant departures from the Janssen pressure distribution after filling process. The experimental analysis of discharge processes presented in sections 1.1, 1.2 and 1.3 indicates that behaviour of the flowing material during discharge is very complex.

To predict both the static wall pressures after initial filling and the quasi-static pressures during discharge we can use different classical theories. It is well known that after filling, the variation of pressure with depth is generally considered to be in the pattern of Janssen's theory (1895), and remains different about the form of the discharge pressure distribution. All known classical theories for both processes, present different approaches to the predicted pressure magnitudes which vary enormously in each theory, [103, 104, 105, 106, 107, 108, 109, 110, 111, 112]. Each theory introduces its own simplifying assumptions on the constitutive response of

the granular material, [2, 101]. Many of them were derived from plastic equilibrium considerations on the basis of different simplifying assumptions. Discussions of these theories and full descriptions may be found in [23, 112, 113, 114, 115, 116, 117].

1.1.5.6.1. Filling and storing pressures

The development of computational methods allowed overcoming the shortcomings of the classical theories. It was pointed in [23] that among many computational methods, especially the FEM (Finite Element Method) has some great advantages in being able to model complex geometries, sliding boundaries and complex material behaviour. But there is still a lack in producing realistic predictions. Filling pressures of the example given in [23] in classical approaches and comparison to the FEM analysis and the wall normal pressure distributions for the silo discussed in [23] are given in Figure 1.9.

In [23] the squat steel silo was studied for the condition after filling. The silo was of height H=10 m, aspect ratio H/D=1 and wall radius to thickness ratio R/t = 500. The stored solid had properties representative of cleaned Kentucky Paradise coal characterized by unit weight γ=10 kN/m^3, internal friction angle φ=42^o, Poisson's ratio ν=0.34, wall friction coefficient μ=0.44 and angle of repose of 25^o, [23, 118]. Figure 1.9b presents the values of design codes and the FEM predictions for this silo. Comparison of predictions of design codes and the FEM and for elastic-plastic solids shows that there is a different pressure value both at the beginning and at the end of the filling process.

In our investigations of wall pressures, the pea grains were used in the model with vertical walls. The pea grains were chosen for the analysis in order to verify the computational model in the DEM method which is presented in Chapter 2. The wall pressures were measured using a membrane sensor placed at three positions along the model wall, i.e., 8, 18 cm and 28 cm above the bottom calculating to the centre of the sensor. The sensor was round of 7 cm diameter made of duralumin; the membrane was of 4 cm diameter. The membrane sensor was placed in the hole made in the Plexiglas wall. In this case, the surface of the membrane coincided with the wall surface. The sensor was connected to the measurement system. The pea grains used in the experiments were of 0.8 cm diameter, and characterized by: unit weight γ=9 kN/m^3, internal friction angle φ=27.3^o, Poisson's ratio ν=0.26, wall friction coefficient μ=0.146 and the angle of repose of 21.5^o.

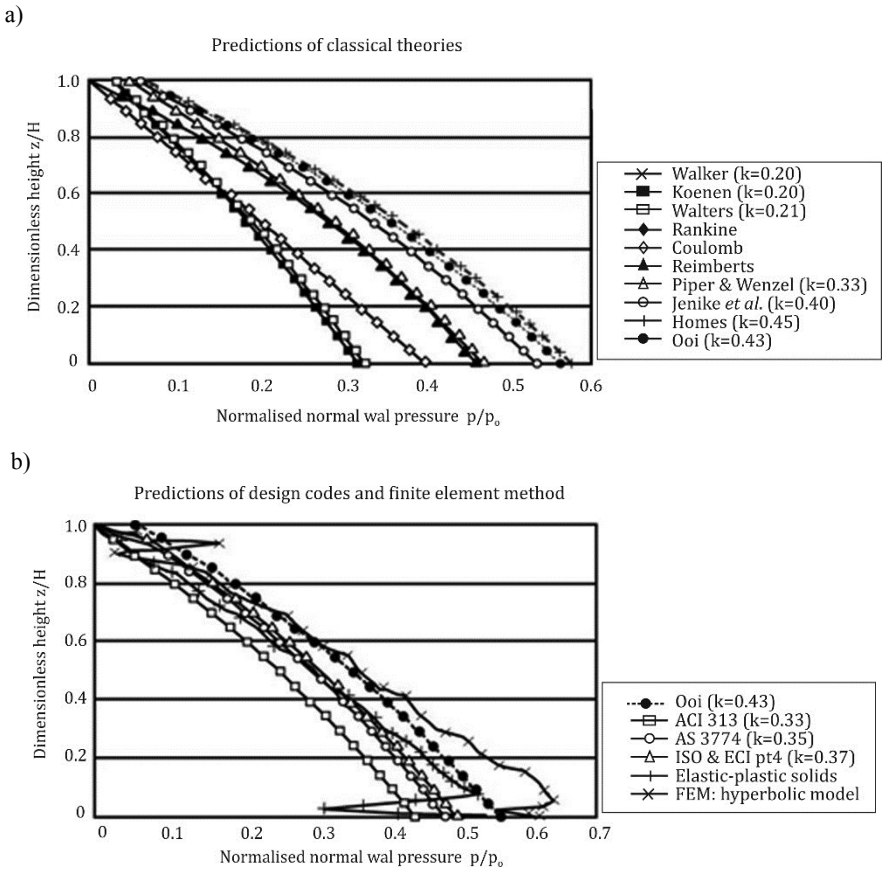

Figure 1.9. The normal wall pressure distributions in an example squat silo [23], a) Predictions of classical theories, b) Predictions of design codes and finite element method.

Discussing the results given in [23], it is seen that in the FEM solution there is a peak in wall pressure distribution both at the beginning of the filling and at the end of the filling. The same behaviour was registered in the case of the pea grains flow in the model. The first sensor indicated the rapid increase of the wall pressure and then there was no further increase of the wall pressure values. The filling time was 53 s. After filling the wall pressures in storing state were registered. A slight increase of the values was observed. The discharge started after the state of storing and a pick of significant increase of the wall pressures was registered. This investigation confirmed the experimental results obtained by the authors in [23]. Figure 1.10 presents the experimental measurements of wall pressures registered by

three varied positions of the sensor. Each diagram is divided by two vertical lines that indicate three processes: filling, storage and discharge.

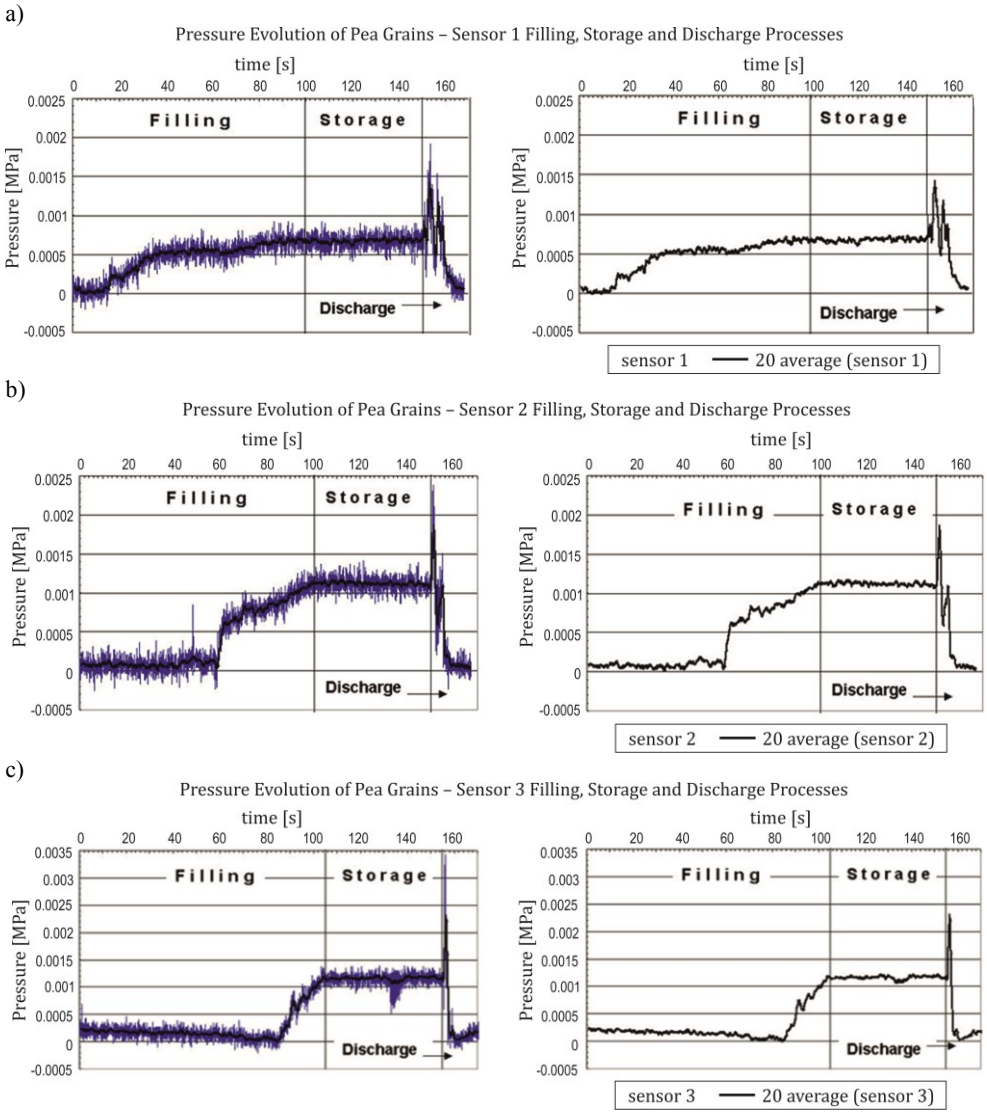

Figure 1.10. Measured wall stresses in the model filled with pea grains.

The results of wall pressures of the filling process presented in Figure 1.10 show the same tendency of the pressure distribution. For each case registered by each sensor the wall pressures present similar character.

1.1.5.6.2. Discharge pressures

The pressure distributions in the discharge process are more complex and unpredictable than those after filling. The problem of so called “switch” pressures and localized “patch” pressures is still a challenge to describe and produce codified rules for them. In [119], the author interpreted higher pressures during flow using the term “switch” from an active plastic stress field after filling to the passive field during discharge. This was discussed and modified by [3, 108, 109, 120].

In the experiments carried out in this work we notice the same phenomena. The filling pressures registered by three sensors indicated an increase followed the Janssen distribution with some peaks and pulsations, the discharge pressures increased rapidly after opening the outlet to the value about four times higher comparing the filling pressures and twice to the storing pressures. This rapidly increase is always dangerous to the silo structure. The increased pressures appear to be predominantly a rearrangement of the total pressure pattern from one part of the silo to another [121], rather than an overall symmetrical increase due to the lateral pressure ratio “switch”. In [101], the authors stated that Jenike’s minimum strain energy theory [109, 113, 122, 123] gained some acceptance but the theory is still not validated.

1.1.6. Theoretical analysis of vertical velocity

Investigations of granular material flows in the model with vertical walls were presented in Section 1.1. Several experimental and theoretical efforts have been directed mainly to the knowledge of velocity within the flow region: [88, 124, 125, 126, 127, 128, 129, 130, 131, 132, 133, 134]. Very few of those theoretical studies have shown an analysis of the whole velocity field in the steady-state of flow, [132] or in the time dependent flow, [129, 133]. Therefore, the experimental evaluation of the velocity appears necessary to obtain quantitative information of the gravity induced flow. We presented velocity field and velocity profiles in the two-dimensional model (depicted in Figures 1.5) and used in this theoretical analysis to describe the dependence of vertical velocity on some factors. We show a series of experimental results related to the non-steady granular flow and its spatial and temporal fluctuations. The whole velocity field has very interesting and complex properties. We characterize here the intensity of the velocity fluctuations at several heights from the bottom. The funnel flow was divided into three zones as it is shown

in Figure 1.11: the upper zone – *the inflow*, width of the model in the upper part and narrowing to the dimension of the central zone – *the steady state zone* with vertical boundaries and *the out flow zone*. Velocity vectors direct radially from the inflow zone into the central. In the central zone, velocity vectors pass vertically to *the outflow zone* with vectors passing radially to the outlet.

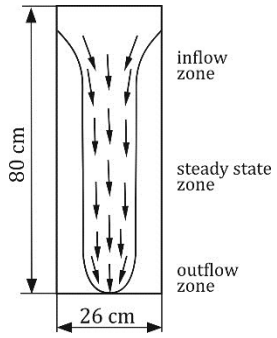

Figure 1.11. Flow zones in the model, [143].

In this section we analyze both the funnel flow on the basis of experimental measurements of velocities and whether the principles of conservation of mass and volume are preserved. According to [2] the density of the flowing material does not change. We provide here the analysis that the volume of the material is not constant during the flow and thus the density of the material.

1.1.6.1. Analysis of the experimental results

The readings taken from the vertical velocity profiles in Figure 1.5 are listed in Tables 1–6 given in Appendix 1. The velocity profiles show that velocities have different values at levels H=5 and 10 cm above the outlet during the whole period of the material flow. However, the other values of vertical velocity read from the profiles at levels higher than H=20 cm are almost uniform. In columns 1–7 in Tables 1–6 (Appendix 1) there are two lines of readings taken for time instants 3.75, 15, 30, 40, 52.5 and 60 s. The upper value relates to the left reading and the down number relates to the right reading from the symmetry axis, respectively.

1.1.6.2. Statistical analysis of experimental results

Applying the values given in Tables 1–6 (Appendix 1) the confidence intervals were determined for the analysed levels for the averages of velocities and listed in Tables 7–9, (Appendix 1), [135].

On the basis on the velocity profiles presented in Figures 1.5 and the data listed in Tables 1–9 (Appendix 1), an inconsiderable dependence of velocity on time has been found. In the further analysis, the average values of velocities calculated for the given levels, the distances from the symmetry axis and for various time instants have been applied.

In Tables 1–6 (Appendix 1) the results marked with were removed using statistics *K* criteria, [136]:

$$K = \frac{\left|V_{y_i} - \bar{V}_y\right|_{max}}{S}, \tag{1.3}$$

where V_{y_i} – is the *i-th* reading taken from the experiments for all time instants, $\bar{V}_y$ – the average value of experimental readings.

Table 1.2. Values of statistics *K* and critical values

Distance from the symmetry axis *x* [cm]	0		1		2		3		4	
Level *H* [cm]	*K*	critical value	*K*	critical value	*K*	critical value	*K*	critical value	*K*	critical value
5	-	-	-	-	2.925	3.387	-	-	-	-
10	-	-	-	-	-	-	-	-	2.640	2.387
20 and higher levels	2.8	2.461	3.163	2.749	3.056	2.749	-	-	-	-

If the value of statistics *K* exceeds the critical value then velocity V_{y_i} should be rejected. The values of statistics *K* calculated from formula (1.3) and Tables 1–6, (Appendix 1) are listed in Table 1.2 where the critical values are also given according to [136].

1.1.6.3. Empirical description of vertical velocity V_y by the parabolic function

At the beginning of the analysis we investigated the distributions of the measured velocities in order to choose the proper function to describe the velocity. If those distributions were linear then the functions of velocity $V_y(z)$ could be applied in a form of $f(1/z)$ or $f\left(1/\sqrt{z}\right)$. Figure 1.12 presents the values of velocities that are not distributed linear. Therefore, we could not take the functions of distribution mentioned above but we proposed another function to describe velocities of the flowing particles.

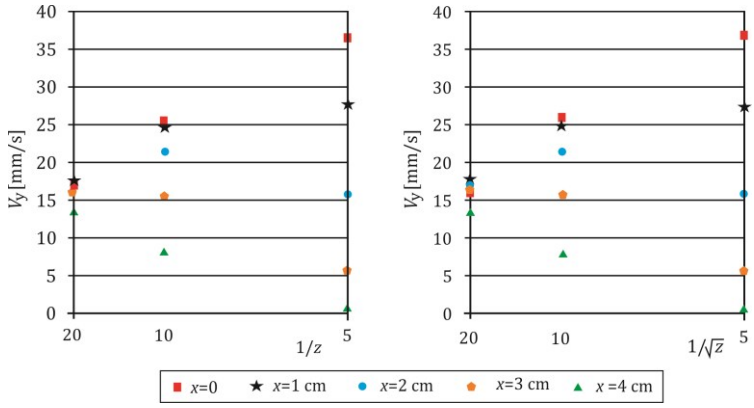

Figure 1.12. The character of distributions of velocities.

Empirical description of vertical velocity V_y calculated in millimetres per second was proposed according to the function:

$$V_y = V_0\left[1 - A\left(\frac{x}{c}\right)^{\alpha}\right], \tag{1.4}$$

where: V_0 is the initial velocity calculated in millimetres per second, x – the distance from the symmetry axis calculated in centimetres, c – half of the width of the model, A and α – certain parameters, determined by the least squares method and presented in Table 1.3.

Table 1.3. Values of the symbols given in formula (1.4)

Readings taken from level H [cm]	A	α	V_0 [mm/s]
5	4.745	1.162	36.92
10	10.913	2.295	25.75
20 and higher	5.373	2.678	17.77

According to the values given in Table 1.3, parameters A, α, and V_0 (given in Formula 1.4) depend on the location of the levels, where the velocities were calculated. We introduce variable z to define the location of the proper level. Parameters A, α, and V_0 were determined for i=0, 1, 2 according to the relations:

$$\begin{aligned} A_i &= A_0 + A_1 z + A_2 z^2, \\ \alpha_i &= \alpha_0 + \alpha_1 z + \alpha_2 z^2, \\ \mathrm{V}_{0_i} &= \mathrm{V}_{0_o} + \mathrm{V}_{0_1} z + \mathrm{V}_{0_2} z^2, \end{aligned} \tag{1.5}$$

and a parabola was drawn across three points of coordinates $(z_0, f(z_0)), (z_1, f(z_1)), (z_2, f(z_2))$ using the Lagrange formula:

$$\begin{aligned} f(z) = {} & \frac{(z-z_1)(z-z_2)}{(z_0-z_1)(z_0-z_2)} f(z_0) + \frac{(z-z_0)(z-z_2)}{(z_1-z_{01})(z_1-z_2)} f(z_1) + \\ & + \frac{(z-z_0)(z-z_1)}{(z_2-z_0)(z_2-z_1)} f(z_2), \end{aligned} \tag{1.6}$$

where $f(z) = A(z)\ or\ f(z) = \alpha(z)\ or\ f(z) = V_o(z)$.

Following formula (1.6), parameters A, α, and V_0 were finally determined and $f(z_i)$ are the values of parameters A_i, α_i, and V_{0i}, for i=0, 1, 2 for levels z=5, 10, 20 cm in the model. The values of these parameters are presented in Table 1.4. They are valid only for the range of the height from H=5 cm up to H=20 cm. For coorinate "z" from interval $z \in \langle 20, 50 \rangle$ some constant values of these parameters were taken, the same like at the level H=20 cm what is denoted by a broken line in Figures 1.13–1.15.

Table 1.4. Parameter values in formula (1.5)

Parameter	i=0	i=1	i=2
A_i	- 7.382	3.021	- 0,1192
α_i	- 0,5987	0,4149	- 0,01255
V_{0_i}	52.88	- 3,67	0,09573

Basing on the data given in Table 3 the distribution of parameters A, α, and V_0 are presented in Figures 1.13–1.15.

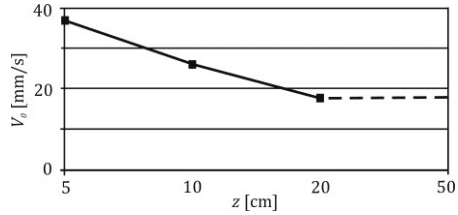

Figure 1.13. Parabolic distribution of velocity V_0.

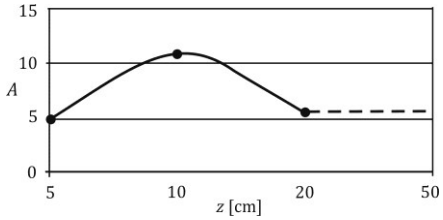

Figure 1.14. Parabolic distribution of parameter A.

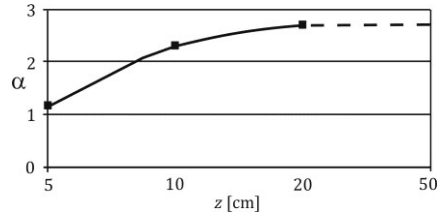

Figure 1.15. Parabolic distribution of parameter α.

Using formulas (1.4) and (1.5) and the values from Table 4 the empirical values of vertical velocity were determined and presented in Tables 1.5–1.7 where the experimental values for comparison are also given.

Another empirical analysis of vertical velocity V_y was conducted at level H=10 cm. The initial vertical velocity was much lower than at level H=5 cm. It was 25.58 mm/s. The values of vertical velocity V_y were measured at five points: x=0 and x=1, 2, 3, 4 cm located from the symmetry axis. The empirical model also presents good agreement with the measured values of the vertical velocity. The velocity profiles presented in Figures 1.5 showed that vertical velocities V_y at level H=20 cm located above the outlet, were almost uniform. Thus, the empirical model for the higher levels was created like for level H=20 cm.

Table 1.5. Values of vertical velocity V_y at level H=5 cm

Distance from the symmetry axis x [cm]	Empirical values [mm/s]	Average experimental values of velocity V_y [mm/s] (red profile)
0	36.92	36.92
1	28.03	28.17
2	17.03	16.27
3	5.04	5.83

Table 1.6. Values of vertical velocity V_y at level H=10 cm

Distance from the symmetry axis x [cm]	Empirical values [mm/s]	Average experimental values of V_y [mm/s] (black profile)
0	25.75	25.75
1	24.97	25.00
2	21.92	21.66
3	16.04	15.75
4	6.96	8.0

Table 1.7. Values of vertical velocity V_y at level H=20 cm and the higher levels

Distance from the symmetry axis x [cm]	Empirical values [mm/s]	Average experimental values of V_y [mm/s]
0	17.77	17.77
1	17.67	17.65
2	17.14	17.15
3	15.89	16.38
4	13.70	13.54
5	10.38	8.68
6	5.73	4.27

Applying the data given in Tables 1.5–1.7 a comparison of the average experimental results with the empirical description is presented in Figures 1.16–1.18.

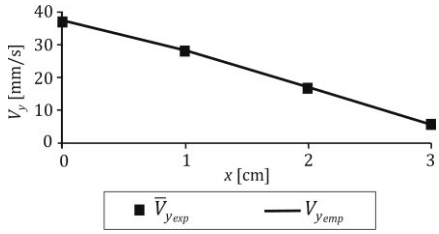

Figure 1.16. Agreement of the mathematical model with the average experimental values of V_y at level H=5 cm.

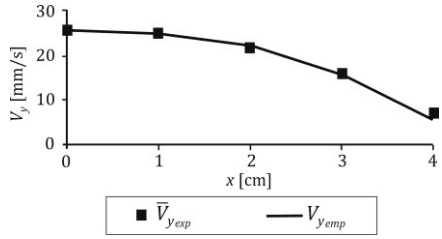

Figure 1.17. Agreement of the mathematical model with the average experimental values of V_y at level H=10 cm.

For the velocities in Figure 1.17 agreement of the experimental measurements to the empirical model was good up to the 4th cm from the symmetry axis. At the 5th and 6th cm the predicted values of vertical velocity by the empirical model were not so convergent as shown in Figure 1.18. At the higher levels, i.e. above level H=20 cm the velocities were uniform and the empirical description could be referred to all higher levels.

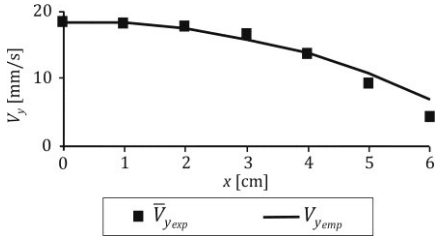

Figure 1.18. Agreement of the mathematical model with the average experimental values of V_y at level H=20 cm and the higher levels.

Agreement of the empirical model and average experimental measurements are presented in Figures 1.16–1.18, that show also the dependence of vertical velocity V_y on the distance x measured from the symmetry axis in the model. The symmetry axis of the model was determined as x=0. Points x=1, 2, 3 cm etc. were measured subsequently 1 cm from the symmetry axis. As it is seen the vertical velocity V_y decreased the more the further the measurement point was located from the symmetry axis. The measurement points were read in the symmetry axis, x=0, and at x=1, 2, 3 cm. The readings at x=4 cm were not taken into account because empirical values calculated for x=4 cm would be negative. The influence of the distance from the symmetry axis to the vertical velocity is shown in Figures 1.16–1.18.

1.1.6.3.1. Relation between velocities in the model

Here we present the relations between velocities at different levels in the model during the discharge process. Both relations $V_{H=10cm}/V_{H=5cm}$ and $V_{Higher\ levels}/V_{H=5cm}$ increase up to measurement point x=2 cm from the symmetry axis. These relations are inverse for distance x=3 cm. It means that vertical velocities increase at levels located higher than H=10 cm and at points located further than x=3 cm from the symmetry axis. The relations between velocities at different analysed levels are presented in Table 1.8.

Table 1.8. Relations between velocities at different levels

Vertical velocities V_y [mm/s]				
Level H [cm]	x=0 cm	x=1 cm	x=2 cm	x=3 cm
5	36.92	28.16	16.92	5.83
10	25.75	25.0	21.66	15.75
Higher levels	17.77	17.84	17.32	16.38
$\boldsymbol{V_{H=10cm}/V_{H=5cm}}$	**0.7**	**0.88**	**1.28**	**2.7**
$\boldsymbol{V_{Higher}/V_{H=5cm}}$	**0.48**	**0.63**	**1.02**	**2.8**

1.1.6.3.2. Theoretical investigations of flow rate

On the basis of formula (1.4) the values of abscissas x were determined only for velocity $V_y \geq 0$. The abscissas x were determined from the relation:

$$x_{max} = ce^{-\frac{\ln A}{\alpha}} x_{min} = 0, \tag{1.7}$$

where c=13 cm which constitutes half of the width of the model and parameters A and α are taken from Table 1.3. The values of x_{max} for various levels calculated for z=5 cm up to z=20 cm in formula (1.7) are listed in Table 1.9.

Table 1.9. Values of limits of integration x_{max} in formula (1.7)

Level H [cm]	5	6	7	8	9	10	12.5	15	17.5	20 and higher
x_{max}	3.397	3.560	3.822	4.224	4.354	4.587	5.087	5.503	5.967	6.939

The flow rate Q per unit thickness in the model at given levels was calculated from formula (1.4) as an area limited by the following function:

$$Q = 2\int_0^{x_{max}} V_y \,\mathrm{dx} = 2V_0\left[x_{max} - \frac{A}{c^{\alpha}(\alpha+1)}x_{max}^{\alpha+1}\right], \tag{1.8}$$

and its values are presented in Table 1.10.

Table 1.10. Values of flow rate Q

Level H [cm]	**5**	6	7	8	9	**10**	12.5	15	17.5	20 cm and higher levels
Flow rate Q [cm^2/s]	**13.51**	14.404	15.315	15.641	16.330	**16.46**	16.184	15.708	15.830	**17.955**

On the basis of the values of flow rate Q listed in Table 1.10, it is seen that the variation of the flow rate is significant and thus the volume and density of the material also change. In [2], the author found that the density of the flowing material does not change in the model. According to values given in Table 1.10 we have found that the volume of the flowing material changes at various levels especially between level H=5 cm and H=10 cm. It increases again but between H=10 cm and H=20 cm the volume of the flowing material decreases and at the level H=20 cm it again increases to value 17.955 cm^2/s. Because we analyzed the velocity profiles only till up the level H=20 cm we can state that above this level the assumption presented in [2] is valid and the density between the level H=20 cm and higher is constant in the model because velocities are almost similar.

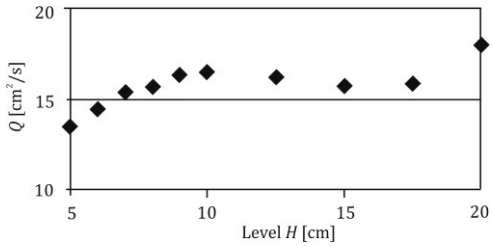

Figure 1.19. Variation of the volume of the flowing material in the model at the analysed levels.

1.1.6.4. Empirical description of the width of the funnel flow *2a*

In this analysis the width of the funnel flow was also determined and compared with the experimental values. Using the values of the readings from Figure 1.3 the width of the funnel flow at various levels and time steps was determined and presented in Table 1.11 (the upper values with no brackets).

Table 1.11. Widths of the funnel flow at various levels in the model

Width of the flow channel ***2a*** [cm]						
Time [s]	*H*=5 cm	*H*=10 cm	*H*=20 cm	*H*=30 cm	*H*=40 cm	*H*=50 cm
3.75	5.6 (**5.97**)	7.6 (**7.48**)	9.0 (**8.63**)	10.0 (**9.61**)	10.0 (**10.37**)	10.5 (**11.0**)
15	6.6 (**7.22**)	9.3 (**8.84**)	11.3 (**10.23**)	11.3 (**11.32**)	11.3 (**12.17**)	12.6 (**12.81**)
30	6.3 (**6.73**)	9.3 **(9.05)**	12.3 (**11.26**)	12.5 (**13.09**)	14.0 (**14.56**)	no reading
40	7.3 (**7.28**)	9.8 (**9.83**)	13.2 (**12.22**)	14.2 (**14.23**)	no reading	no reading
52.5	6.9 **(6.4)**	10.1 **(9.9)**	13.6 (**12.79**)	no reading	no reading	no reading
60	6.8 **(5.6)**	9.5 **(7.3)**	no reading	no reading	no reading	no reading
Empirical values are typed in **bold**						

The empirical description of the width of the funnel was proposed according to the function:

$$y = Ax^B, \tag{1.9}$$

where y=2a, and 2a – is the width of the funnel flow calculated in centimetres, taken from experimental measurements, and x is the distance from the symmetry axis also given in centimetres, (cf. Figure 1.3).

Parameters A and B were determined by the least squares method using the values from Table 1.11 and presented in Table 1.12.

Table 1.12. Values of parameters *A* and *B* in formula (1.9)

Flow time [s]	Parameter *A*	Parameter *B*
3.75	3.500	0.265
15	4.821	0.251
30	3.706	0.371
40	3.987	0.376
52.5	2.861	0.50
60	3.019	0.383

The calculated values in formula (1.9) and Table 1.8 are shown in Table 1.12.

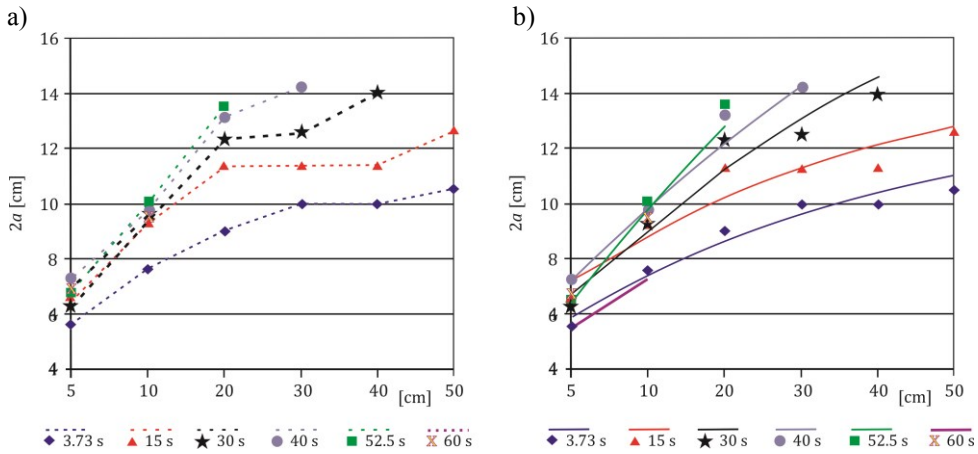

Figure 1.20. Variation of the funnel flow in the model, a) parallel sections denote the similar width of the funnel flow; b) empirical description of the funnel flow.

Variation of the funnel flow in time is presented in Figure 1.20. As can be seen the proposed function has good agreement with the experimental results marked by the coloured points and the continuous lines refer to the empirical model. In Figure 1.20 there are points of the same value of 2*a*. It means that the width of the funnel flow is constant and refers to the central zone. The heights of the each zone are changeable in time. In the initial phase of the flow the height of the outflow zone is the highest. After the first 15 seconds of the flow, the limit between the outflow zone and the central zone passed down and remained on the level 20 cm. The central zone has the same width till 30th s of the flow. In Figure 1.20, we can see that the limits between

the marked zones change their position due to time of the flow. The empirical description presented in Figure 1.20b can be compared with evolution of the width of the plug flow zone presented in Figure 1.8.

Up to level H=10 cm the funnel formed at the beginning of the flow remains uniform but above level H=10 cm it widens and its width remains constant and then widens again.

1.1.6.5. Theoretical description of the plug flow zone

During the discharge process after opening the outlet a region of the highest velocity formed in the vicinity of the outlet. This region called "plug flow" has a range that is difficult to describe by any mathematical relation. Table 1.13 presents the readings of the plug flow zone taken from the velocity contour distributions, (cf. Figure 1.3). There are two regions in the plug flow zone, the highest marked with the red colour and the orange surrounding the red one.

Table 1.13. Widths of the plug flow zone in the region at levels H=5 and 10 cm above the outlet

Time [s]	Widths of the plug flow zone at two levels in the model			
	H=5 cm		H=10 cm	
	Velocity 24–40 mm/s, (red zone)	Velocity 20–24 mm/s, (orange zone)	Velocity 24–40 mm/s, (red zone)	Velocity 20–24 mm/s, (orange zone)
3.75	3.0	4.0	4.0	5.7
15	1.33	3.8	2.16	4.7
30	2.66	3.8	2.33	4.2
40	2.33	3.0	2.0	4.3
52.5	2.33	3.0	2.16	5.2
60	2.83	3.5	2.5	4.6

Velocities in the plug flow zone present unsteady flow in the region from the outlet up to level H=10 cm above the outlet.

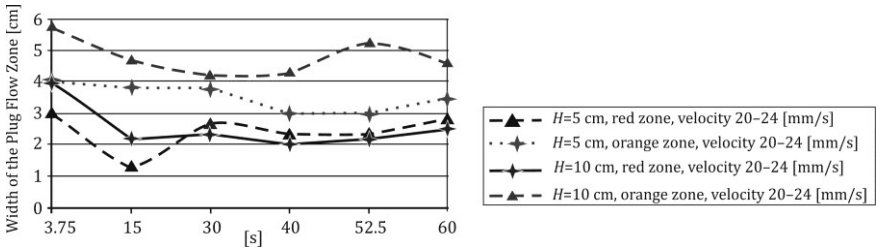

Figure 1.21. Variation of the widths of the plug flow zone in the vicinity of the outlet, at two levels, *H*=5 and 10 cm.

1.1.6.6. Kinematic model

We measured the flow of granular materials inside a quasi-two dimensional silo model and compared the obtained data with the kinematic model. The tracks of the particles registered by the Digital Particle Image Velocimetry technique provided data in both space and time to obtain their velocities. Almost all velocity profiles presented in this Chapter were smooth and free of the shock-like discontinuities.

The velocity field of the flow inside the silo models has been described by two different approaches. One based on the critical state theory of soil mechanics relates stress and density to predict velocity field or mass flow rate, [128]. The other approach considers a purely kinematic description of the velocity profiles first presented by Litwiniszyn in [83, 84], who discussed the stochastic model and random walks through available cages. Later, the author in [85, 86] proposed his stochastic model in terms of voids and extensively developed the continuum limit, where the diffusion equation arises. In [137], the authors analysed the void model and implemented its explicitly in computer simulations on a triangle lattice. Another solution as an alternative to the void model was proposed in [87] and [138]. They derived the same continuum equation using the constitutive law relating both horizontal and downward velocities gradients. The proposed model was very simple because it predicted velocity fields with only one free parameter that has been observed to be proportional to grain diameter in all experiments but the constant of proportionality does not agree, [87] and [138, 139]. Furthermore, the works [25, 26] analysed the flow using the PIV technique and have reported that the kinematic parameter varies in a non-linear form in the silo. In fact, recent experiments have rejected the void hypothesis and a new stochastic description – the spot model, [140] roughly preserves the mean flow profile of the kinematic model consistent with experiments.

In [87, 138], the authors proposed a model based on the constitutive law relating velocity components:

$$u = b\frac{\partial \nu}{\partial x}, \tag{1.10}$$

where u denotes the horizontal velocity that is proportional to the horizontal gradient of the downward velocity v. Combining Eq. (1.10) with the incompressibility condition

$$\frac{\partial u}{\partial x} + \frac{\partial \nu}{\partial z} = 0. \tag{1.11}$$

Works [87, 138] applied an equation for the downward velocity:

$$\frac{\partial \nu}{\partial z} = -b\frac{\partial^2 \nu}{\partial x^2}. \tag{1.12}$$

In Eq. (1.12) (compare formula 1.1) that has a form of a diffusion equation, time is replaced by the vertical coordinate z.

1.1.6.7. Empirical description of velocities by the Gaussian function

Empirical description of velocities in the model with vertical walls was made by the Gauss function in two phases. In section 1.6.7.1, we present the analysis of the velocity using the formula presented in [141]. In section 1.6.7.2, a modification of that solution has been proposed. We refer to the constant of proportionality b in Eq. (1.10), called "diffusion length" by [141].

1.1.6.7.1. Analysis of velocities

In [128] and in [141] a similar solution of Eq. (1.12) for velocity for a semi-infinite quasi-two-dimensional system $(-\alpha < x < +\alpha)$ with a point-like orifice at z=0 which acts as a source of velocity was presented:

$$\nu(x, y) = \frac{Q}{\sqrt{4\pi bz}} e^{-x^2/4bz}, \tag{1.13}$$

where Q – is the flow rate per unit thickness of the silo. In [141], the model was of length L=20 cm, height H=90 cm and thickness D=2.5 cm. The thickness of the silo

D is large enough that finite-size effects are not significant. The model in our analysis has the thickness 10 cm and the grain diameter is 1 mm. Thus the increased dimension of the orifice made it possible to obtain similar results for both velocity and diffusion.

The kinematic model predicts velocity fields with only one free parameter. As it was stated above the free parameter was determined to be proportional to the grain diameter. The kinematic model was tested experimentally and parameter b was measured by a number of researchers. For example, [138] determined $b \approx 2.24d$ for various particle sizes, in [139] $b \approx 2d$ for iron ore particles, [25, 26] found that diffusion length varies from $b \approx 1.5d$ to $b \approx 4d$. In [142], the authors proposed $b \approx 3.5d$ for monodisperse glass beads. It was also stated that a single fitting parameter b suffices to reproduce the entire flow field and it should be viewed as a major success of the kinematic model, [141].

Analysing velocities of the flowing material we propose the following function:

$$V_y(x) = Ae^{Bx^2}, \tag{1.14}$$

where A and B are the coefficients dependent on height H, constant for the proper levels, determined by the least squares method and listed in Table 1.14. In formula (1.14), the distance x from the symmetry axis is introduced in centimetres and $V_y(x)$ in millimetres per second.

Table 1.14. Parameters *A, B* in formula (1.14)

Parameter value	*A*	*B*	*R-coefficient of correlation*
H=5 cm	40.13	- 0.242	- 0.9942
H=10 cm	30.86	- 0.1008	- 0.9763
H=20 cm and higher levels	22.82	- 0.0508	- 0.9628

Taking the values from Table 1.14, parameters A and B were depended on the position of level z, at which the velocities are calculated in the following form:

$$\begin{aligned} A_i &= A_0 + A_1 z + A_2 z^2, \\ B_i &= B_0 + B_1 z + B_2 z^2. \end{aligned} \tag{1.15}$$

The values of parameters A_i and B_i for i=0, 1, 2 are listed in Table 1.15. They were determined using the approximation of the second order polynomial of the Lagrange type.

Table 1.15. Values of parameters A_i and B_i

Parameters	i=0	i=1	i=2
A_i	52.9	-2.904	0.07
$-B_i$	0.4607	-0.05148	0.001549

Distributions of parameters A and B according to Table 1.14 are presented in Figures 1.22 and 1.23.

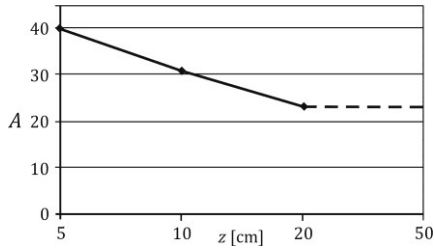

Figure 1.22. Distribution of parameter A.

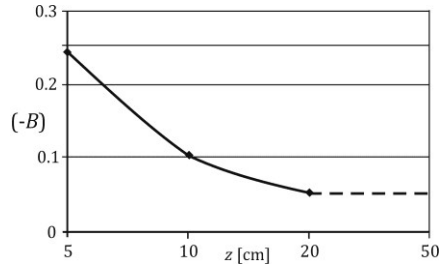

Figure 1.23. Distribution of parameter B.

For values $z \in \langle 20, 50 \rangle$ parameters A and B were taken as for level H=20 cm. The theoretical values of velocities were calculated from formula (1.14) using the values from Table 1.14 and presented in Tables 1.16–1.18.

Table 1.16. Empirical and average experimental values of velocity V_y at level H=5 cm

Distance from the symmetry axis x [cm]	Empirical values of velocity [mm/s]		Average experimental values of velocity [mm/s]
	Gaussian by [141]	Modified model	
0	40.13	36.17	36.92
1	31.50	29.52	28.17
2	15.23	16.06	16.27
3	4.54	5.82	5.83
4	0.83	1.41	0.71

Table 1.17. Empirical and average experimental values of velocity V_y at level H=10 cm

Distance from the symmetry axis x [cm]	Empirical values of velocity [mm/s]		Average experimental values of velocity [mm/s]
	Gaussian by [141]	Modified model	
0	30.86	27.05	25.75
1	27.90	25.15	25.0
2	20.62	20.21	21.66
3	12.45	14.05	15.75
4	6.15	8.44	8.0
5	2.48	4.38	1.92

Table 1.18. Empirical and average experimental values of velocity V_y at level H=20 cm and higher levels

Distance from the symmetry axis x [cm]	Empirical values of velocity [mm/s]		Average experimental values of velocity [mm/s]
	Gaussian by [141]	Modified model	
0	22.82	18.96	17.77
1	21.69	18.40	17.65
2	18.62	16.83	17.15
3	14.45	14.50	16.38
4	10.12	11.77	13.54
5	6.41	9.0	8.68
6	3.67	6.48	4.27

Using the values from Tables 1.16–1.18, the description of velocity by the Gaussian function is presented in Figures 1.24–1.26 (dashed line).

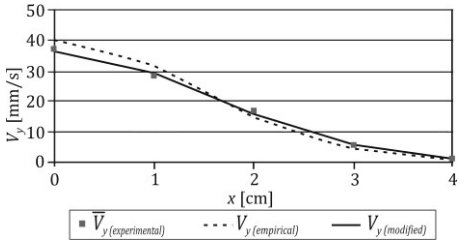

Figure 1.24. Function of Gaussian type for level H=5 cm.

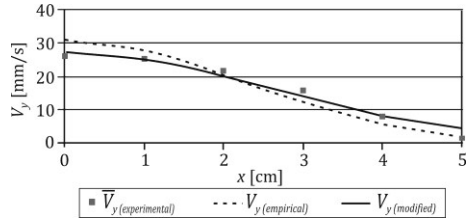

Figure 1.25. Function of Gaussian type for level H=10 cm.

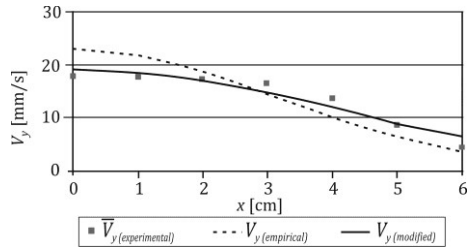

Figure 1.26. Function of Gaussian type for level H=20 cm and higher levels.

It is seen that the curves created by the Gaussian empirical model (dashed line) cover the experimental points with quite good accuracy. Better theoretical description comparing with the experimental values will be obtained by the modified model presented in section 1.6.7.2.

1.1.6.7.2. Modification of kinematic model

The kinematic model presented by formula (1.14) in section 1.1.6.7.1 has been modified and the modification was proposed as the following function:

$$V_y = A\left(e^{-Bx^2} + e^{-Cx^2}\right). \tag{1.16}$$

Using the non-linear regression (the Gauss-Newton method) parameters *A, B* and *C* in formula (1.16) were determined and listed in Table 1.19. In each case, velocity V_y is calculated in millimetres per second and the distance x in centimetres.

Table 1.19. Parameters from formula (1.16).

Position of the level [cm]	*A*	*B*	*C*
5	18.083	0.203	0.203
10	13.523	0.073	0.073
20 and higher levels	9.480	0.0304	0.0304

On the base of formula (1.16) and the values given in Table 1.19, the velocities were calculated and listed in the columns in Tables 1.16–1.18. Verification of the model described by formula (1.14) showed that the given description (1.16) practically is reduced to formula (1.14). The above can be proved by the obtained values of parameters *B* and *C* in formula (1.16) listed in Table 1.19. They all are equal. It follows that the model presented in [141] and our description given in formula (1.14) provide sufficient accuracy of the empirical description. Some better results obtained from the modified model (given in formula (1.16)), are derived from the method of determining the parameters *A, B* and *C* (non-linear regression) and not

from the term added in formula (1.16). The parabola in formula (1.16) was created using the non-linear regression, whereas formula (1.14) was transformed into the linear regression. The curves of the modified model are presented in Figures 1.24––1.26 with the solid line. It is clearly seen that the solid lines cover the experimental values of velocity with better accuracy than the Gaussian model according to [141].

1.1.6.7.3. Evaluation of kinematic parameter *b*

The structure of the patterns of velocity profiles obtained by the PIV technique does not change with the height. The kinematic model in [87] showed a good fit. Taking into account formulas (1.13)–(1.15) and the values given in Table 1.13 the parameter b was evaluated for the analysed levels comparing the corresponding coefficients in formulas (1.13) and (1.14) to each other.

For level H=5 cm (or z=5 cm) above the outlet parameter b equals:

$$b = -\frac{1}{4Bz} = -\frac{1}{4(-0.242)5} = 0.2066 \text{ [cm]},$$

or b=2,066d, where d=1 mm is the diameter of the particle. For level H=10 cm, parameter b=0.244 in centimetres or b=2.44d, for level H=20 cm and the higher levels b=0.247 in centimetres or b=2.47d. The "diffusion length" b becomes larger when z increases as some previous reports have also shown, [25, 26, 128].

In [25, 26] the authors presented velocity profiles obtained by the PIV technique, well fitted by the correlations obtained through the kinematic model, i.e., the average value of the vertical velocity was given in the form:

$$\overline{V} = \overline{V_0} exp\left(-\frac{\left(\hat{x}-\frac{1}{2}\right)^2}{4B\hat{z}}\right), \tag{1.17}$$

and

$$\overline{U} = -B\frac{\partial \hat{v}}{\partial \hat{x}} = \frac{\overline{V_0}\left(\hat{x}-\frac{1}{2}\right)}{2\hat{z}} exp\left(-\frac{\left(\hat{x}-\frac{1}{2}\right)^2}{4B\hat{z}}\right), \tag{1.18}$$

where $\overline{V_0}$ is the dimensionless average vertical velocity, B is a dimensionless fitting parameter, $\hat{x} = x/W$, $\hat{z} = z/W$ and z is the vertical coordinate, measured from the

bottom of the silo. The experiments were performed in a vertical glass-walled silo model of 100 cm height, W=30 cm width and 3.8 mm deep, filled up to H=82 cm with monodisperse granular material composed of spherical glass beads with mean diameter d=3.15$\pm$0.04 mm.

In our analysis the average vertical velocity is determined by formula (1.14). If we substitute x=0 to formula (1.15) then we obtain the calculated initial value of vertical velocity $\hat{V}_{y_0}$ and we assume that this value is close to the average experimental value. In [25, 26], the authors considered the variation of kinematic parameter B at height H=6 cm and up to H=20 cm above the bottom of the model. The distribution of parameter B was given as a non-linear increasing function. If we extrapolated this function above level H=20 cm in the model it would be continuously increasing. It would denote that kinematic parameter B would change continuously with the height in a non-linear form. In our analysis, the parameter b stabilizes from height H=10 cm, as it is shown in Figure 1.27.

The presented values confirm the fact that the kinematic parameter b is not a constant value but it varies depending on the height in the model. Like other authors [25, 26, 88, 131], we also have found that the kinematic parameter b changes with the height in a non-linear form but its significant increase about 18% is observed up to level H=10 cm and above this level the kinematic parameter increases only about 1%. We can say that its value stabilizes above level H=10 cm. A quite reverse situation was described by [25, 26], (cf. Figure 1.28).

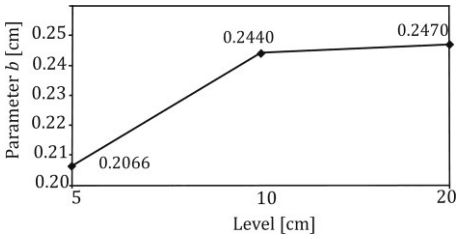

Figure 1.27. Variation of kinematic parameter b in the presented analysis, [143].

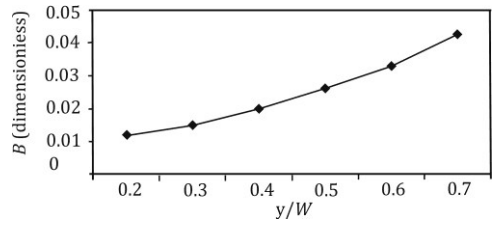

Figure 1.28. Variation of kinematic parameter B in the model by [25, 26].

On the base of formulas (1.17–1.18) and the formula given in [25, 26] the kinematic parameter B depends on $\hat{z}$ as:

$$B = 0.07exp(2.6\hat{z}). \tag{1.19}$$

The curve presenting the value B is shown in Figure 1.28.

1.1.6.8. Theoretical description of the flow rate

The flow rate is a very important data in technological processes occurring in silos. We present a theoretical analysis of flow rate Q based on empirical descriptions given by the Gaussian function. For the area limited by the function described in formula (1.14), the limits of integration were taken from Table 1.9. The flow rate for the unit thickness was calculated according to the formula:

$$Q = 2\int_{0}^{x_{max}} Ae^{Bx^2}\mathrm{dx}. \tag{1.20}$$

This integration was calculated numerically at each level in the model and the values of flow rate Q are listed in Table 1.20.

Table 1.20. Values of flow rate Q calculated using the limits of integration given in Table 1.9

Level z [cm]		5	10	20 and higher levels
Flow rate Q [cm^2/s]	Gaussian model	14.197	16.549	17.461
	Modified model	13.795	16.329	17.828

Comparing the parabolic solution given by formula (1.4), using the limits of integration x_{max}=4, 5, 7 cm, flow rate Q was also calculated and the values are given in Table 1.9. Applying these limits of integration the values of the flow rate are listed in Table 1.21.

Table 1.21. Values of the flow rate calculated by applying the limits of integration x_{max}=4, 5, 7 cm

Level z [cm]		5	10	20 and higher levels
Flow rate Q [cm^2/s]	Gaussian model	14.38	16.801	17.485
	Modified model	14.074	16.748	17.876

1.1.6.9. Verification of accuracy of the applied models

In Table 1.22 a comparison of the sums of the squares of the differences of the empirical and experimental values of velocities is given. On the base of Figures 1.24–1.26 and the values given in Table 1.22 it is seen that the better description is obtained using the modified model because the listed numbers are lower.

In fact both models are almost identical but the applied method of determining the parameters plays a significant role in accuracy of the solution.

Table 1.22. The sums of the squares of the differences of velocities

Model	$\Sigma(V_{yemp} - \bar{V}_{yexp})^2$		
	Level H [cm]		
	5	10	20 and higher
Model of Choi et *al.* [141]	25.95	50.23	59.35
Modified model	3.82	12.95	13.73

1.1.7. Conclusions

In this section the flow of granular materials in a flat model with vertical walls registered by the DPIV technique was presented. The recorded images were analyzed and we obtained both qualitative as well as quantitative data on the flow. The theoretical analysis of velocities in the model was presented in two parts: the first as a parabolic description and as the Gaussian function. In the latter description, two versions of the model have been investigated: according to assumptions given by [141] and also the modification of this model has been made. The chosen method appeared to be the main factor for the accuracy of the solution. The value of kinematic parameter $B(b)$ has been determined and we stated that it depends on the height in the model. Above level H=10 cm its value stabilized that is quite diverse result as given in [25, 26].

The regions of the highest velocities which are dangerous for the silo structure were investigated. It may cause silo vibrations and failure of the structure. The highest velocity region appears just above the model bottom. Higher, the velocities of the flowing materials have almost identical values in the whole flowing stream. This observation is significant for silo designers and for silo users. The flow modes

recognized during the experiments depend on different factors. Designed for funnel flow the silo structure cannot withstand another flow mode. And vice versa. The wall stresses will change their values active and passive, as it was stated by [144] with the change of the flow mode. Also the character of wall stresses were measured for filling, storage and discharge processes for the pea grains. The selection of the pea grains was based on the future comparison to the DEM simulation presented in Chapter 2 of this book.

"Main content of this chapter has been published in Biosystems Engineering, 108, 334-344, 2011".

1.2. Experimental analysis of granular flow in the converging model using the DPIV technique

1.2.1. Introduction

Numerous theoretical expressions are derived for velocity distributions in a granular material discharging from converging hoppers: wedge-shaped or conical in form.

In theoretical models of granular flow, the assumption of incompressibility throughout the hopper is an essential element in the predictions of velocities and flow boundaries.

In this section, the investigation of the flow in a converging model using the DPIV technique is presented in [36]. The technique uses a direct or FFT-based cross--correlation of two sequential flow images. Evaluation of the correlation peak and estimation of its location in the image plane reveals a mean displacement of the flowing material. It is obtained for each interrogated image sections. By using known time intervals between correlated images a mean velocity vector is calculated. The method is quite sensitive to image partitioning, seeding uniformity, and correct matching of section sizes to time intervals between correlated images. The DPIV based on the Optical Flow (OF) approach may use several images of the sequence. The OF-DPIV algorithm seeks geometrical transformations that match intensity patterns of the images in an iterative manner. Having these transformations, displacements are evaluated directly for each image pixel. The achieved accuracy of measured displacements is about 0.5 pixel size for an evaluation procedure with

two-image sequences and 0.2 pixel for three-image sequences. In [36, 38], the authors reported that an application of the DPIV technique to granular flow in converging hoppers appears to be very promising and offers a unique possibility to obtain full field transient velocity fields, and, by applying standard mechanical relations, offers a possibility to evaluate distribution of shear stresses in the material. The flow in converging models runs quite differently than in the models with vertical walls. The surface between the flowing region and the stagnant zones forms a stair-like shear zone.

1.2.2. Literature review

Experimental investigations of flow patterns in converging hoppers were presented in numerous publications, e.g. [46, 48, 75, 77, 145, 146, 147, 148]. In [149], the author investigated stress and velocity fields in two- and three-dimensional hoppers. In [47], the authors presented experiments in a plane parallel/converging bunker. In [150], the author measured the granular material flow in a wedge-shaped hopper with transparent walls. Insightful experimental investigations devoted to granular flow in conical hoppers are reported in literature, among others, by [96, 151]. In spite of the fact that results obtained from theoretical models may appear uncertain, researchers are still looking for a better way to recognize flow patterns using models and to predict the flow mode of the material stored in the hopper. The flow patterns occurring in the hopper have strong influence on wall pressure; strongly depend on silo geometry and granular material properties. They may vary in a non-linear manner according to the stress state which is quite different in a model and in a full scale hopper. The stress state varies consequently with different flow patterns, usually being different in model investigations and full scale hoppers. Therefore, the experimental validation of theoretical models appears to be the very necessary task.

Investigations concerning stress and velocity fields reported in [1, 95, 152], gave evidence that for plane strain and axial symmetry, the stress field requires a solution in a form of a system of two hyperbolic partial differential equations. The velocity field could then be computed by solving another system of two linear homogeneous partial differential equations of the hyperbolic type. The radial stress field is assumed to be particularly important for straight conical channels because all general fields tend to approach the radial stress fields in the vicinity of the vertex. These ideas were further developed by several other researches, for example in [2, 72, 149, 153, 154, 155].

In [88] the authors presented a review article with all the experimental methods that were used to measure velocities in a granular material. The paper also considered extension of the plasticity theory, well established for the predictions of small displacements in granular materials to the effectively infinite strains found in flowing systems. This was compared with alternative methods of predicting velocity distributions based on the kinematic or stress free models of [83, 84, 85, 139]. The details of experimental measurements of velocity distributions and comparisons with the theoretical predictions were presented. In the review article [88], the authors discussed both two and three dimensional flow and both wedge-shaped and conical hoppers. Although other authors reported the existence of discontinuities in velocity fields, a series of X-ray pictures and ultrasonic measurements presented practically uniform density of the flowing material. In most of the theoretical models, the velocity field analysis was restricted to the advanced stage of flow, which was treated as a pseudo-steady process. A theoretical description of the kinematics of the advanced phase of the flow is based on the plane plastic flow theory of an incompressible material coupled with the radial stress field. It reveals realistic velocity field, particularly in hoppers with smooth walls. A similar strategy of solving kinematics in hoppers was proposed in [145]. In [47], the authors presented experimental results of flow patterns in a plane, wedge-shaped hopper, and also an approach to a theoretical description of discharge. A non-steady discontinuous velocity field was measured using a stereo photographic technique.

Stress and velocity fields in two- and three-dimensional hoppers were also considered in the steady-state flow of an incompressible, cohesionless granular material by [149]. He presented a computational method for solving the equations governing the flow of a granular material, extending his solution to three-dimensional hoppers. In [156], the authors proposed a calculation method which gave a good prediction for the velocity distribution in mass flow hoppers (wedge-shaped and conical). The method was based on the classical plasticity theory. The results given in [157] supported the assumptions about distribution of the stress components made by Walker's differential slice model [106]. In [151], the author presented a new technique for measuring the velocity distributions in conical hoppers. Marker particles were released in the already-flowing material. The velocity distributions were deduced from the measured times of passage. A minor effect of the size and density of the marker particles was shown and the velocity of the particles adequately represents the velocity of granular material. The theoretical predictions given by [152], and among others, by [158], were reviewed and two

original modifications were presented. In [159], the author analysed behaviour of granular medium in a silo using a numerical Cosserat approach. The method introduced by [151] showed that the marker particles move with the same velocity as the surrounding material and this assumption was confirmed by the experimental results. The only small dependence of the time of passage on the size and density of the marker particles showed that there was no need to match the marker and bulk particles closely. By integrating the velocity profiles, the flow rate was calculated. It proved to be in good agreement with the flow rate measured independently, giving confidence in accuracy of the method. Theoretical predictions made for granular flow in wedge-shaped hoppers do not give a satisfactory approach to the radial stress and velocity fields. Calculations in conical geometries only appeared successful for either materials of unrealistic angles of friction, or for circumstances in which the stresses at the top surface were close to those predicted by the radial stress field. Experiments reported by [72, 155] showed that the velocities in the lower half of a conical hopper are radial with magnitudes similar to those predicted from the radial velocity field.

In [96], the authors used the method of characteristics to predict the exact stress and velocity fields in an incompressible, cohesionless Coulomb material discharging from a conical hopper for a great variety of boundary conditions imposed on the upper surface. They found that in all cases, stress and velocity tend to approach the radial stress and velocity fields, and that convergence was achieved about half way down the hopper. The velocity fields show the regions of more or less constant velocity separated by velocity discontinuities. This statement made by [96] justified the assumption in Drescher's method [2] of predicting velocity distributions. In [160] the author investigated behaviour of a granular medium in a plane silo with convergent walls and also dynamical phenomena in silos during discharge, [161]. In [70], the author used the finite element analysis to calculate steady-state velocity in a cohesionless granular material discharging from a planar flat-bottomed silo. The relationship between the horizontal velocity and the horizontal gradient of the vertical velocity was the basic assumption in the analysis. In [147], the authors investigated two-phase flow of interstitial air in a moving bed of granular solids in a mass flow hopper. In [148], the authors compared DEM simulation of granular material flow in two- and three-dimensional hoppers to imaging data from conventional photography and gamma-ray tomography. Deformation rate, velocity fields, and stress distributions were calculated in a model of converging silo by [32], where the finite element method based on Euler's reference frame was used.

The flow profiles were investigated and the stress evolution was obtained, e.g. a stress alter ation on the way from the outlet for the conical and the cylindrical section of the silo.

The focus of this section is to elucidate the character of the flow in converging models. It is set to demonstrate the ability of the novel DPIV technique to measure velocity fields for the cohesionless granular material flowing in wedge-shaped hoppers and to obtain quantitative and qualitative data on the flow evolution.

1.2.3. Experimental procedure

Experiments described in this section were conducted in a plane converging model made of Plexiglas and presented in detail in [36]. Figure 1.29 presents a schematic view of the experimental setup. The model wall has a shape of an isosceles triangle with the height 80 cm. The depth of the model is 10 cm with the inclination value of the walls to the vertical 30^o. The lower vertex of the triangle is cut off to a form of 1 cm broad outlet. The flow analysis was limited to the area above the bottom Plexiglas box attached above the outlet (cf. Figure 1.32). Its position defines the "bottom line", i.e. beginning of the coordinate system used to describe measured velocity fields.

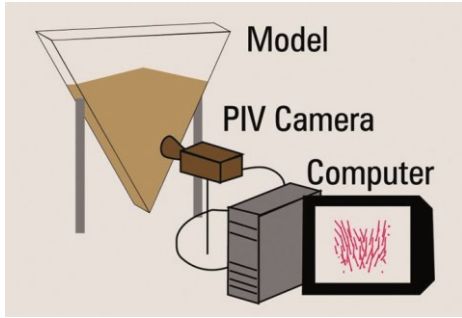

Figure 1.29. Experimental setup.

The amaranth seeds were used in the experiments. Its properties were presented in Table 1.1 given in section 1.1.4. To present more material properties, the angle of internal friction of densely packed material was measured and it varied from $\varphi_e = 40^\circ$ at normal stresses 3.8 kPa to $\varphi_e = 31^\circ$ at normal stresses 21.6 kPa. The value of wall friction against Plexiglas was determined experimentally. Moisture of

the grains was found to be 10.2%. Granular material density was also measured in two cases with zero-free fall.

Before each experiment the discharge rate was measured every 30 s on a digital scale. Reproducibility of the discharge process was very good, allowing assuming that the same discharge level is suitable to describe recorded flow images.

1.2.4. Mechanics of the flow

Upon opening the outlet, the material sets in motion and a narrow plug flow zone propagates upward. The material moves into the flowing zone from the upper parts in an avalanche manner. In fact, there is a flow channel formed at the symmetry axis. In the lower parts the boundaries of the flow region are almost vertical; at higher levels the flowing zone widens and finally reaches the walls of the model. The velocity vectors in the upper part of the flowing material are directed radially to the flow channel and the assumption of Jenike radial flow is thus confirmed. In the flow zone the velocity vectors are mostly vertical, placed along the flow channel. The formation of a narrow plug flow zone and its propagation upward during the discharge process is quantitatively evaluated. This effect is associated with other interesting phenomena of the flow – shear zones and discontinuities of vector fields. It is found that the size of the observed flow region increases with time and shear zones are formed between the flowing and the stagnant material. These shear boundaries have a form of steps. The flowing zone widens and the evolution of "the shear stairs" boundaries is shown in the consecutive time steps of the flow. The shear zones in the flowing material are further presented in Figures 1.31. The density of the flowing material is distinctly lower than in the surrounding material packed in the stagnant zones. It was also found in the velocity magnitude contours obtained for models with vertical walls, as reported by [30, 31, 36]. The material, after filling, formed the upper free surface of a constant slope at an angle equal to the material angle of response. With a progressing discharge the upper surface lowers and changes its shape. The evolution of the upper surface of the flowing amaranth seeds is shown in Figures 1.30. The left column of Figure 1.30 presents vector fields evaluated for the flowing material by the DPIV method. It is seen that the width of the plug flow zone increases rapidly. The narrow stagnant zones can be observed exclusively near the walls. The points denote velocities equal to zero, regions of material stagnation. The vectors located near the upper surface are directed towards the flow region, indicating radial direction of the flow. The depicted vector fields

indicate that instantaneous velocities at various locations of the flow region appear to be nearly vertical and constant within this region and that the mean velocity (length of the vectors) decreases with time. In the right column of Figure 1.30, the evolution of the upper surface of the flowing amaranth seeds is shown. Just after opening the outlet, one can observe the development of a flow channel, where the material density becomes rapidly lower than in the surrounding material. Some strongly asymmetric, local behaviours and an avalanche mode of the flow are observed in the vector fields. Although the filling of the model is symmetric, the material flow is not in fully symmetric. This fact may be due to a misalignment of the model. Disparity of the material flow from the left or the right wall into the flow channel creates sloshing motions. These sloshing motions give evidence of flow instabilities generated by dynamic changes of the material density and variations in the material friction coefficient. As the time of the flow elapses, the flow region broadens and finally almost the whole material is in motion. In the flow region the vectors are directed vertically to the outlet, radial flow component is present only in the avalanche part of the flow in the vicinity of the surface.

1.2.4.1. Velocity fields

The observed vector field reveals two different flow regions. One is visible in the radial avalanche flow mode and the other is represented by the uniform channel flow in the vertical direction. Such state of flow exists till 120th s of the flow. Then, because there is less and less material in the model, the radial velocity field connects to the vertical vector field. A curved boundary indicating rapid changes in the flow direction are identified in the vector field. In the subsequent flow time both regions merge and only the radial velocity field is observed, (cf. Figure 1.30). In [2, 46, 145, 162, 163], the authors described their experimental observations concerning velocities and discontinuities occurred in a mass flow model hopper. It was also stated that the velocities varied significantly across the hopper width and the radial direction of the flow was observed, [2, 47, 164].

a) Vector field after 7th s of the flow

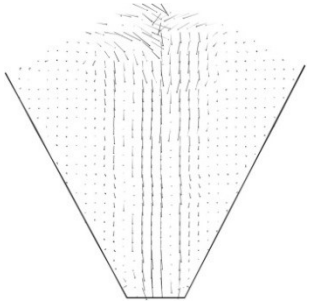

b) Shape of the upper surface after 7th s

c) Vector field after 45th s of the flow

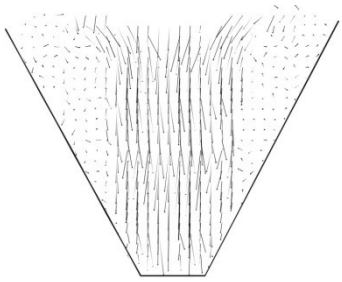

d) Shape of the upper surface after 45th s

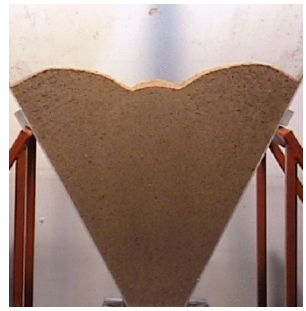

e) Vector field after 95th s of the flow

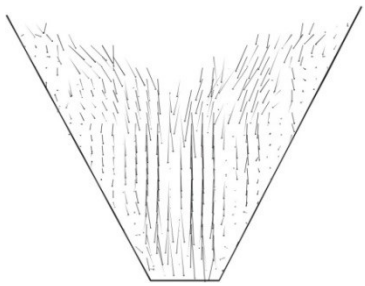

f) Shape of the upper surface after 95th s

Figure 1.30. DPIV evaluated velocity vector fields (left column) and observed evolution of the upper surface in flowing amaranth seeds (right column) for six time steps.7th s, 45th s, 95th s, 120th s, 180th s and 214th s after opening the outlet, [36]

[*Continued figure on next page*].

g) Vector field after 120th s of the flow

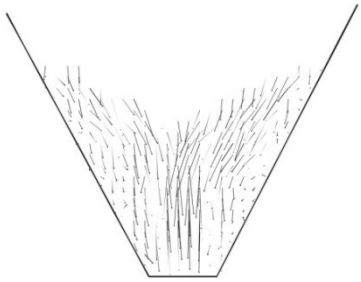

h) Shape of the upper surface after 120th s

i) Vector field after 180th s of the flow

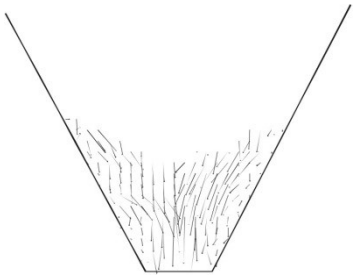

j) Shape of the upper surface after 180th s

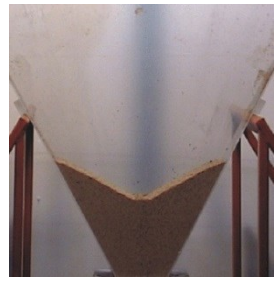

k) Vector field after 214th s of the flow

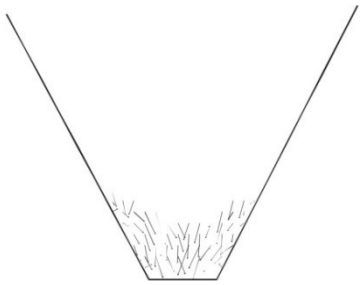

l) Shape of the upper surface after 214th s

Figure 1.30. DPIV evaluated velocity vector fields (left column) and observed evolution of the upper surface in flowing amaranth seeds (right column) for six time steps: 7th s, 45th s, 95th s, 120th s, 180th s and 214th s after opening the outlet, [36].

1.2.4.2. Streamlines in the flowing material

Figures 1.31 present velocities and streamlines measured in the flowing amaranth seeds in the initial phase of the flow, at 45th s, 95th s and 195th s of the flow time. To depict transient development of different flow regions, the velocity vector field is overlaid with contours of the velocity magnitude in Figure 1.31 (left column). The right column in Figure 1.31 shows flow streamlines, i.e. flow paths obtained by integrating the DPIV velocity vector field. In [35], the term "trace of selected particles" was introduced instead of streamlines. However, it should be noted that these lines do not represent paths of individual particles, but rather indicate instantaneous motion of the bulk material. If it represented a path of a single particle it would be called "pathline". The vertical channel of the high velocity region develops in the middle part of the flowing material (cf. Figures 1.31a–d) and it propagates quickly upward. Its shape does not change much with time. Only after reaching the free surface it starts to propagate down, into the inlet. The shape of the vertical channel is almost the same in the whole analysed flow time. Figures 1.31b, d, f show that in the flow region located in the middle part of the model material moves nearly vertically to the outlet. The radial velocity field is visible only in the upper part of the flowing material, where the avalanche type of flow develops. It is indicated by the curvature of streamlines near the upper surface (cf. Figures 1.31b, d, f). After 120th s the flow velocity decreases (cf. velocity contours in Figures 1.31a, c, e). Some asymmetry of the flow pattern is noticed. These local phenomena are clearly visible in the velocity profiles shown in the following figures. The shear zones occurring in the flowing material may be a source of avalanche-like flow and arch formations when the moisture of the flowing material is high enough.

1.2.4.3. Velocity profiles

Full velocity field measurements allow extracting velocity profiles at a selected cross-section in the model. It helps to identify the shape of the flow channel and make quantitative comparison of different flow regimes. Five horizontal cross-sections have been selected for the analysis at: H=9.5 cm, H=19 cm, H=28.5 cm, H=38 cm and H=57 cm from the beginning of our coordinate system, i.e. above the bottom line shown in Figure 1.32. It corresponds approximately to 0.20, 0.41, 0.54, 0.67, and 0.94 of the initial material height. Figure 1.32 shows the location of only three selected levels in the model. Below, in Figures 1.33–1.40 the profiles of

the vertical velocity component V_y extracted across the channel from appropriate vector fields are presented. Negative velocity values indicate flow direction down to

a) Velocity vectors and velocity contours for the time *t*=45 s

b) Streamlines for the time *t*=45 s

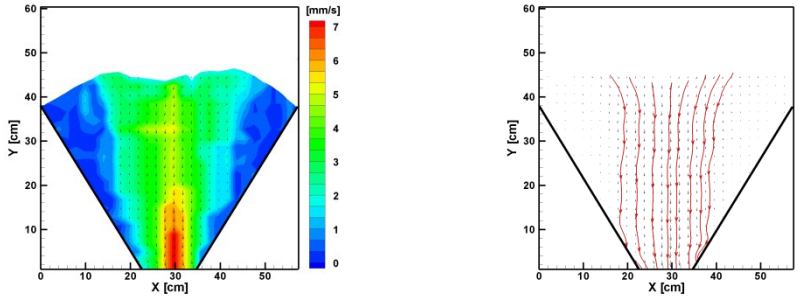

c) Velocity vectors and velocity contours for the time *t*=95 s

d) Streamlines for the time *t*=95 s

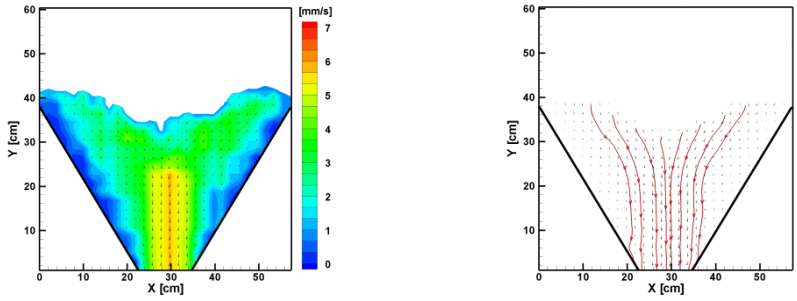

e) Velocity vectors and velocity contours for the time *t*=195 s

f) Streamlines for the time *t*=195 s

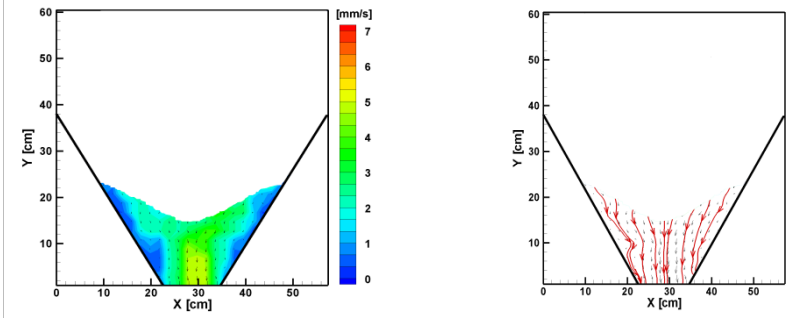

Figure 1.31. Flow velocity vector field and velocity magnitude contours in the flowing amaranth seeds (left column); flow streamlines calculated from the velocity field (right column), evaluated for three time steps at: 45th s, 95th s and 195th s after opening the outlet, [36].

the bottom. After extracting the velocity values the curves are smoothed using the cubic-spline method. It may create small artefacts, especially close to the walls and at the flow axis, where strong velocity gradients are present. On the other hand the smoothed profiles are necessary to compare them at different time steps and to detect the asymmetry of the flow.

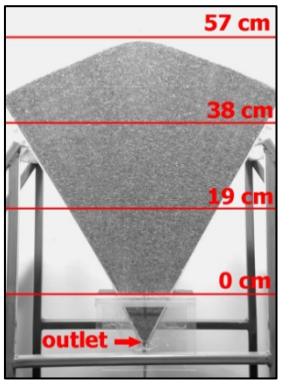

Figure 1.32. Location of the selected cross-sections used to evaluate velocity profiles: H=19 cm, H=38 cm, and H=57 cm from the bottom line (H=0 cm) of the model. Elapsed flow time is 10 s, [36].

It is worth noting that the material is removed from the model as time passes. Hence, depending on the time step and the profile location, only part of the model is filled with the seeds. Therefore, some velocity profiles shown in the figures exhibit broken lines or they disappear at later time steps.

Figure 1.33a shows velocity profiles extracted form DPIV vector field evaluated at the time step t=7th s. It is the first analysed moment of the flow. The highest location (H=57 cm) is partly filled with the seeds and only a short section of the profile is shown. Nevertheless, the initial asymmetry of the flow is clearly visible, indicating beginning of the sloshing motion for the avalanche flow regime at the surface. This asymmetry is present for the mid-height profiles (H=28.5 cm and H=38 cm) as well, but it almost disappears at the bottom (H=19 cm). It means that when the material starts to flow, not only the plug flow zone develops but a slight lateral motion of the packed material is also present from very beginning. By comparing maximum values of the velocity we can find that the plug flow slightly accelerates for the mid-height (H=28.5 cm and H=38 cm), and decelerates closer to the bottom (H=9.5 cm and H=19 cm). Figure 1.34 presents the velocity profiles obtained at the later time step t=23 s. The plug flow is well developed and velocity profiles at four locations nearly overlap. Initial asymmetry of the flow observed in

Figure 1.33 smoothed out for the mid-profile (H=28.5 cm and H=38 cm), but apparently appeared at the lower location.

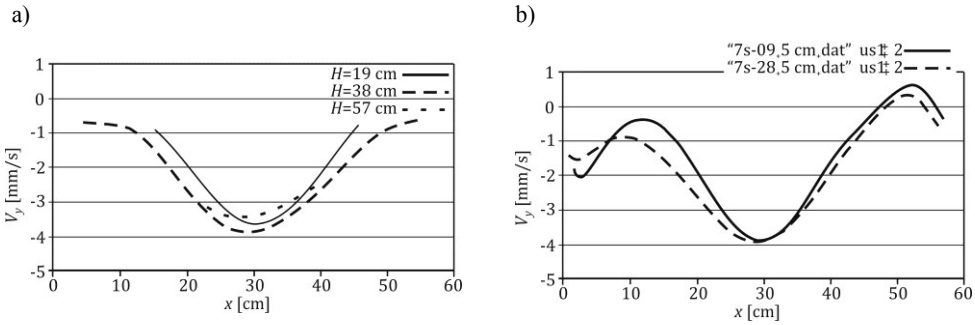

Figure 1.33. Vertical velocity component V_y measured across the channel at various analyzed levels: a) H=19 cm, H=38 cm, and H=57 cm, [36]; b) H=9.5 cm, H=28.5 cm. Time step t=7th s after opening the outlet.

Figure 1.35 shows the velocity profiles extracted at the time step of 45th s. As expected in converging models, the flow is nearly symmetrical for the higher level, but the asymmetry near the bottom developed earlier remains, (cf. Figure 1.34). Velocity distribution at H=19 cm relates to the narrower flow region than at the location H=38 cm, where the flow region is considerably wider. Whereas maximum velocity at the lower level (H=19 cm) remains constant, at the higher location, the vertical velocity component evidently diminishes at H=38 cm.

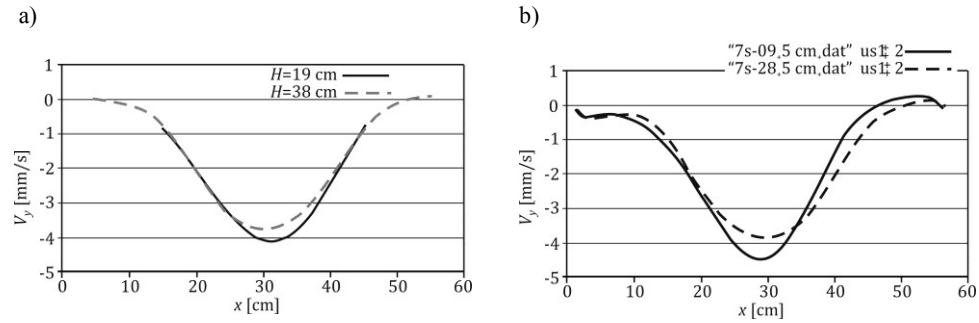

Figure 1.34. Vertical velocity component V_y measured across the channel at various analyzed levels: a) H=19 cm, H=38 cm, [36]; b) H=9.5 cm, H=28.5 cm. Time step t=23rd s after opening the outlet.

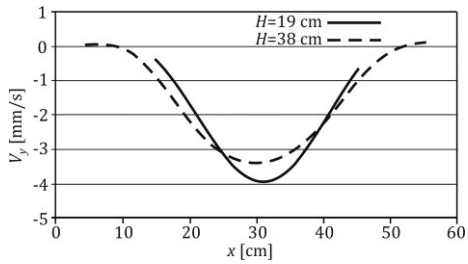

Figure 1.35. Vertical velocity component measured across the channel at H=19 cm and H=38 cm. Time step t=45th s after opening the outlet, [36].

a)

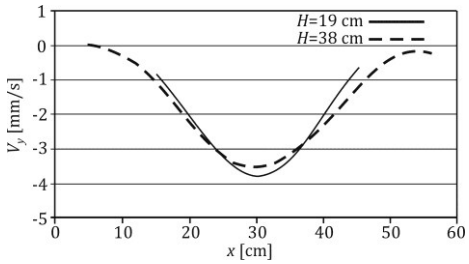

b)

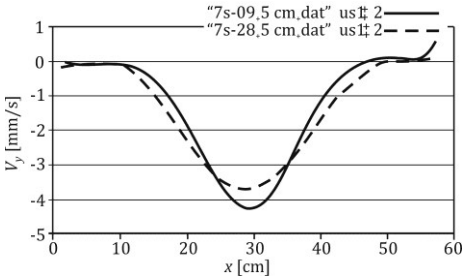

Figure 1.36. Vertical velocity component measured across the channel at:
a) H=19 cm, H=38 cm, [36]; b) H=9.5 cm, H=28.5 cm.
Time step t=53rd s after opening the outlet.

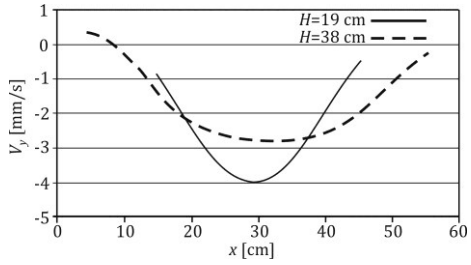

Figure 1.37. Vertical velocity component measured across the channel at H=19 cm and H=38 cm. Time step t=70th s after opening the outlet, [36].

The transient change of the converging flow is observed during the consecutive stages of the flow. The profiles depicted at the time step t=53rd s, (cf. Figure 1.36) indicate slight decrease of the plug flow velocity and further smoothing of the asymmetry present before. This nearly uniform plug flow mode suddenly changes for the next time step at 70th s of the flow, (cf. Figure 1.37). In the upper region, the avalanche flow mode dominates now. The value of the vertical velocity component is higher at H=9.5 cm and H=19 cm and much lower at H=28.5 cm and H=38 cm. Comparing with Figure 1.36 where the vertical velocity component for two analysed

levels has almost the same values, now velocities at H=28.5 cm and H=38 cm rapidly diminish. This type of flow regenerates flow asymmetry at the upper surface. Next two figures (cf. Figures 1.38–1.39) show velocity profiles in the material after a funnel-like void area developed at the model axis, (cf. Figures 1.30f, h). Only small regions close to the side walls are filled with the seeds at the upper level (H=28.5 cm and H=38 cm). The avalanche type of flow is mainly parallel to the walls, hence, its vertical velocity component evidently diminished. It is evident in the profiles shown at the level H=28.5 cm and H=38 cm, (cf. Figures 1.38–1.39). It is worth noting that at the lower level (H=9.5 cm and H=19 cm) the velocity profile remains nearly unchanged at the time step t=87th s, (cf. Figure 1.38), and only slight acceleration of the material for this level is seen at the next time step 107th s, (cf. Figure 1.39). Flow remains nearly symmetrical at this location and for the time t=87th s, but some disturbance appears at the next time step, (cf. Figure 1.39).

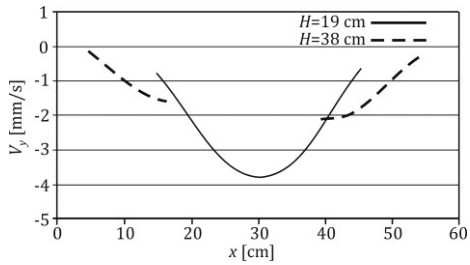

Figure 1.38. Vertical velocity component measured across the channel at H=19 cm and H=38 cm. Time step t=87th s after opening the outlet, [36].

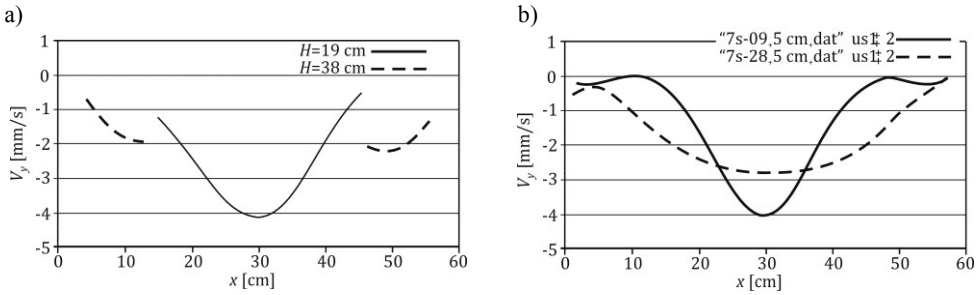

Figure 1.39. Vertical velocity component measured across the channel at a) H=19 cm and H=38 cm, [36]; b) H=9.5 cm and H=28.5 cm. Time step t=107th s after opening the outlet.

The last figure of the sequence (cf. Figure 1.40) shows the velocity profile obtained for the final stage of the process (t=154th s). There is only one profile available for the lower level (H=19 cm). It depicts an irregular avalanche type flow with a strong asymmetry of the vertical velocity component. In fact, most of the material slides along the side walls converging into the outlet, (cf. Figures 1.31e, f).

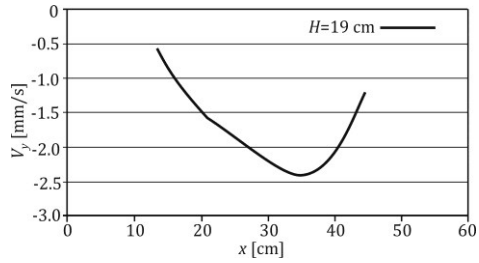

Figure 1.40. Vertical velocity component measured across the channel at H = 19 cm. Time step t = 154th s after opening the outlet, [36].

The transient changes of the flow pattern are illustrated in Figure 1.41, where velocity profiles measured at the location H=19 cm are collected for three time steps. All three velocity profiles have a very similar shape which indicates the same pattern of the flow in this period of time. Velocities reach their maximum values at the axis of symmetry of the model.

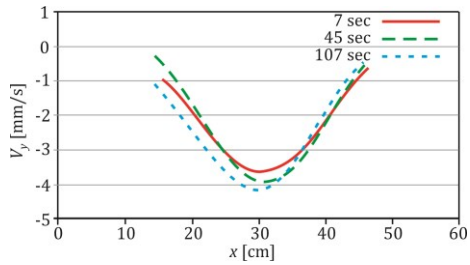

Figure 1.41. Velocity profiles of the vertical component V_y for location H=19 cm measured at time steps 7th s, 45th s, and 107th s, [36].

Figure 1.42 shows evolution of the height of the plug flow as a function of time. After opening the outlet a plug flow zone rapidly forms in the material and reaches the free surface of the packed material during the first 10 seconds after beginning of the flow. Till about 170th s of the flow, the evolution of the plug flow zone is represented by a slightly concave line and relates to a nonlinear relation.

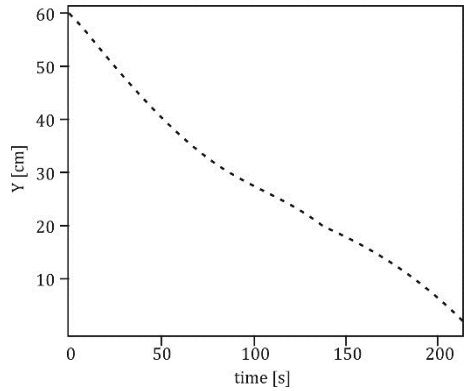

Figure 1.42. Evolution of the height of plug flow zone measured in the symmetry axis, [36].

1.2.4.4. Discharge flow rate

The total discharge time for the amaranth seeds was found to be 234 s. For the first 150 s the mass discharge rate was constant and equal 74.3 g/s. After this time, the discharge rate rapidly decreased to the value of 58.3 g/s at 180th s, and 45.0 g/s at 210th s. For the material density equal 832.5 kg/m^3 it corresponds to the volumetric discharge rates of 89.3 cm^3/s, 70.1 cm^3/s and 54.1 cm^3/s, respectively. The abrupt decrease of the discharge flow rate is explained by the fact that the material in the model had considerably lower bulk density in the later phase of the flow. This observation is confirmed by independent measurements of the volumetric flow rate, (cf. Figure 1.43).

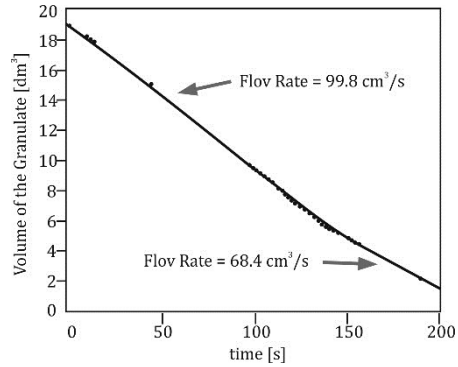

Figure 1.43. Volumetric discharge flow rate for the amaranth seeds calculated from the images of the material in the model, [36].

To verify the accuracy of these measurements several images of the seed flow collected during the experiments were evaluated and the areas filled with the material were used to calculate its volume. This image processing procedure is very reliable and permits to track instantaneous flow rate with accuracy 1%. In Figure 1.43, we present the results of the evaluation. The points showing the calculated volume of the material indicate almost the linear variation until about 150 s. This flow regime was approximated by linear regression shown in Figure 1.43. The slope of the line indicates the flow rate equal 99.8 cm^3/s. After about 130th s the flow rate abruptly diminishes and is equal to 68.4 cm^3/s, approximately. This behaviour confirms the tendency noticed by the direct measurements of the discharge rate. The evaluated flow rate values are generally in accordance with the direct, weight based measurements. The observed differences, mainly in the initial flow rate, can be due to the differences in the packing ratio of the material. The flow observations are limited to the wall vicinity only. One may expect that the assumption of an ideal two-dimensional flow can be violated and the calculated material volume needs correction. To verify such a possibility a three-dimensional imaging of the material interface is necessary in the future.

"Main content of this chapter has been published in Chemical Engineering Science, 61, 5307-5317, 2006".

1.2.5. Empirical description of vertical velocity of moving particles

In this section we present the theoretical analysis of velocities of flowing amaranth seeds in the converging model. The analysis was made for the initial phase of the flow, i.e. the first 53 seconds of the flow. The total discharge time was 234 seconds.

1.2.5.1. Experimental readings taken from velocity profiles

The readings taken from the vertical velocity profiles (cf. Figures 1.33, 1.34, 1.36) are presented in Tables 1–4, (Appendix 2).

1.2.5.2. Statistical analysis of the experimental results

Applying the values given in Tables 1–4, (Appendix 2) the confidence intervals were determined for the analysed levels for the averages of velocities and listed in

Tables 1.5–1.8, [135]. Calculating the values in Tables 5–8, (Appendix 2) the time was not taken into account. On the base of velocity profiles presented in Figures 1.33, 1.34, 1.36 and the data listed in Tables 1–8, (Appendix 2), an inconsiderable dependence of the velocity on time has been found. In the further analysis, the average values of velocities calculated both for the given levels, distances from the symmetry axis and for various time instants, have been applied.

1.2.5.3. Statistical verification of dependence of velocity on height *H*

Figure 1.44 presents the dependence of velocity on the location of the analyzed levels H for various distances from the symmetry axis. An insignificant dependence of velocity on the height $V_y(H)$ follows from this Figure.

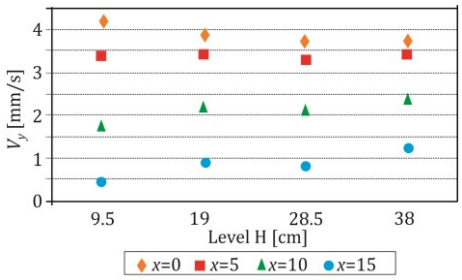

Figure 1.44. Dependence of the velocity V_y on the position of the level, [165].

The analysis of variance at singular classification for measurement points located at x=0, 5, 10, 15 cm was performed to show the dependence of velocity V_y on the height and is presented in Appendix 2.

On the base of the values listed in Table 11 and published in Appendix 2 we can state that coefficient b=0 in all measurement points except x=15 cm. It confirms the conclusion that the velocity does not depend on the height at points x=0, 5 and 10 cm but depends on the height at x=15 cm.

1.2.5.4. Empirical description of velocities by the parabolic function

In spite of the conclusion drawn above that the velocity depends insignificantly on the height at the measurement points located at x=0, 5 and 10 cm, in the analysis presented below we depend velocity V_y on the distance x and the height z. Empirical description of vertical velocity V_y calculated in the units of millimetres per second

was proposed according to the function given in formula 1.4. For this case we relate to formula 1.4 and we introduce into it parameters as follows:

$$V_y = V_0\left[1 - A\left(\frac{x}{c}\right)^{\alpha}\right] \tag{1.21}$$

V_0 is the initial velocity calculated in the units of millimetres per second, x – the distance from the symmetry axis calculated in the units of centimetres, $c = 1$ cm, A and α – are certain parameters determined by the least squares method and presented in Table 1.23.

Table 1.23. Values of the symbols given in formula (1.21)

Readings taken at level H [cm]	A	α	V_0 [mm/s]
9.5	0.0192	1.443	4.17
19.0	0.0101	1.620	3.9
28.5	0.00628	1.811	3.7
38.0	0.00366	1.940	3.7

According to the values given in Table 1.23, the parameters A, α, and V_0 (given in formula 1.21) were depended on the position of the levels, where the velocities were calculated. These parameters were determined according to the relations:

$$\begin{aligned} A_i &= A_o + A_1 z + A_2 z^2, \\ \alpha_i &= \alpha_o + \alpha_1 z + \alpha_2 z^2, \\ V_{0_i} &= V_{0_0} + V_{0_1} z + V_{0_2} z^2. \end{aligned} \tag{1.22}$$

Parameters A_i, α_i and V_{0i} for i=0, 1, 2 were determined by the least squares method using the values listed in Table 1.23 and presented in Table 1.24.

Table 1.24. Parameter values in formula (1.22)

Parameter	i=0	i=1	i=2
A_i	0.0305	$-1.384 \cdot 10^{-3}$	$1.795 \cdot 10^{-5}$
α_i	1.254	0.0205	$-6.52 \cdot 10^{-5}$
V_{0_i}	4.608	- 0.0525	$7.479 \cdot 10^{-4}$

On the base of formula (1.22) and the values given in Table 1.24, parameters A, α and V_0 were calculated and their distributions presented in Figures 1.45–1.47.

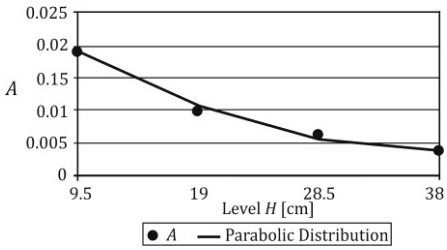

Figure 1.45. Parabolic distribution of parameter A, [165].

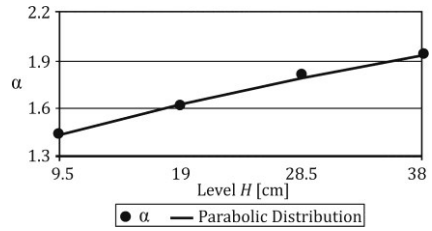

Figure 1.46. Parabolic distribution of parameter α, [165].

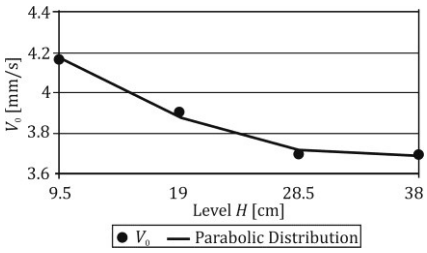

Figure 1.47. Parabolic distribution of velocity V_0, [165].

In Figures 1.45–1.47 the values from Table 1.23 are depicted – the points. The distributions of the parameters are plotted by the curves.

Empirical values of velocity V_y calculated from formula (1.21) using formula (1.22) and values from Table 1.24 are listed in Table 1.25.

Table 1.25. Average experimental and empirical values of velocity

Level [cm]	Distance from the symmetry axis x [cm]							
	0		5		10		15	
	$\bar{V}_y$	$\hat{V}_y$	$\bar{V}_y$	$\hat{V}_y$	$\bar{V}_y$	$\hat{V}_y$	$\bar{V}_y$	$\hat{V}_y$
9.5	4.17	4.18	3.38	3.37	1.72	1.98	0.42	0.23
19.0	3.9	3.88	3.38	3.32	2.15	2.15	0.88	0.54
28.5	3.7	3.72	3.28	3.35	2.13	2.43	0.65	1.06
38.0	3.7	3.69	3.4	3.37	2.43	2.45	1.22	0.77

In Table 1.25, $\bar{V}_y$ denotes the average and $\hat{V}_y$ empirical values of vertical velocity. On the basis of the values listed in Table 25, the empirical description of vertical velocity in dependence on the distance x and height z was presented. Agreement of the empirical model with the average experimental values is shown in Figures 1.48––1.51.

From this empirical analysis we can draw a few conclusions. Comparing the values listed in Tables 1–4 and 5–8 (enclosed in Appendix 2) it is seen that the velocity does not depend on time. But in Figure 1.44 we can notice an insignificant dependence of velocity on level H. The pattern of this dependence varies according to the distance from the symmetry axis, decreasing for x=0 and increasing for x=10 and 15 cm. For x=5 cm velocities have practically the same values. Performing the analysis of variance for the significance level α=0.05 (results are listed in Table 10 in Appendix 2) it is seen that the velocity depends on the height only at x=15 cm. This conclusion is confirmed by the results presented in Table 11 in Appendix 2. In spite of this insignificant dependence on the height, the parameters in formula (1.21) depend on the height that is seen in Figures 1.45–1.47. The results of the analysis are presented in Figures 1.48–1.51.

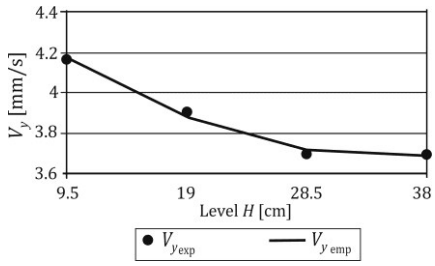

Figure 1.48. Agreement of the experimental values with the empirical description at x=0 cm, [165].

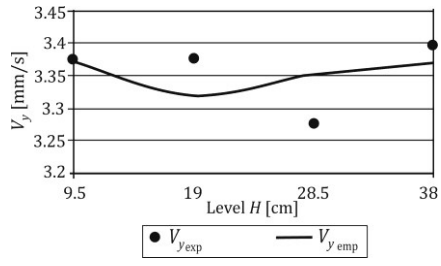

Figure 1.49. Agreement of the experimental values with the empirical description at x=5 cm, [165].

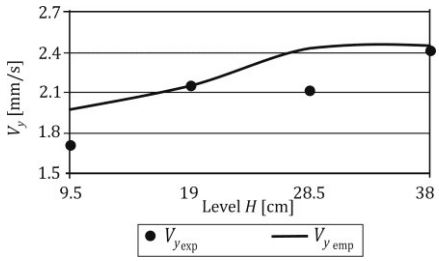

Figure 1.50. Agreement of the experimental values with the empirical description at x=10 cm, [165].

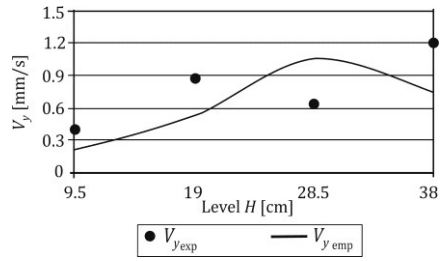

Figure 1.51. Agreement of the experimental values with the empirical description at x=15 cm, [165].

1.2.5.5. Theoretical investigation of the flow rate

On the basis of formula (1.21) the values of abscissas x were determined only for velocity $V_y \geq 0$ according to the relation:

$$x_{max} = ce^{\frac{\ln A}{\alpha}} \cdot x_{min} = 0, \tag{1.23}$$

where c = 1 cm. Parameters A and α taken from formula (1.21) are listed in Table 1.24. Values of x_{max} are given in Table 1.26.

Table 1.26. Values of limits of integration x_{max} from formula (1.23)

Level H [cm]	9.5	19.0	28.5	38.0
x_{max} [cm]	15.58	16.46	18.10	17.53

The flow rate Q per unit thickness in the model at a given level was calculated from formula (1.21) as an area limited by the following function:

$$Q = 2\int_0^{x_{max}} V_y \mathrm{d}x = 2V_0\left[x_{max} - \frac{A}{c^{\alpha}(\alpha+1)}x_{max}^{\alpha+1}\right], \tag{1.24}$$

and its values are presented in Table 1.27.

Table 1.27. Values of flow rate Q

Level H [cm]	9.5	19.0	28.5	38.0
Flow rate Q [cm^2/s]	7.698	7.898	8.635	8.542

1.2.5.6. Empirical description of velocities by the Gaussian function

Empirical description of velocities in the converging model was also made by the Gaussian function. We present the analysis of the velocity using the formula presented in [128] and [141]. Modification of the solution has not been performed because of the conclusions drawn in section 1.1.6.7.2.

1.2.5.6.1. Analysis of velocities given in [128] and [141]

In this section we apply a mathematical model presented in [128] and [141], (as a solution of Eq. (1.12) given in section 1.1.6.7.1)

$$v(x,z) = \frac{Q}{\sqrt{4\pi bz}} e^{-x^2/4bz}, \tag{1.25}$$

where Q – is the flow rate per unit thickness of the silo. In our analysis, we refer to the constant of proportionality b in Eq. (1.10), called "diffusion length" by [141].

Analysing velocities in the flowing material we apply the following function:

$$V_y(x) = Ae^{Bx^2}, \tag{1.26}$$

where A and B are certain parameters determined by the least squares method and put into Table 1.28. In formula (1.26), the distance x from the symmetry axis is introduced in centimetres and $V_y(x)$ in millimetres per second.

Table 1.28. Parameters *A, B* in formula (1.26)

Levels *H* [cm]	*A*	*B*	*R-coefficient of correlation*
9.5	4.3756	- 0.01024	- 0.9981
19.0	3.9937	- 0.006635	- 0.9989
28.5	4.1423	- 0.008334	- 0.997
38.0	3.6029	- 0.00455	- 0.9912

According to the values listed in Table 1.28, parameters *A* and *B* given in formula (1.26) were depended on the position of the level. These parameters were determined according to the relations:

$$A_i = A_{0_i} + A_1 z + A_2 z^2,$$
$$B_i = B_{0_i} + B_1 z + B_2 z^2. \tag{1.27}$$

Parameters A_i and B_i for i=0, 1, 2 were determined by the least squares method using the values listed in Table 1.28 and presented in Table 1.29.

Table 1.29. Values of parameters in formula (1.27)

Parameter	*i*=0	*i*=1	*i*=2
A_i	4.3741	- 0.0021132	- 0.0004362
B_i	- 0.01106	0.00013825	$4.95845\ 10^{-7}$

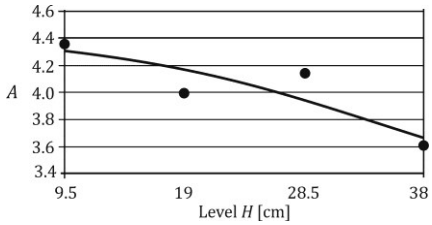

Figure 1.52. Distribution of parameter *A*, [165].

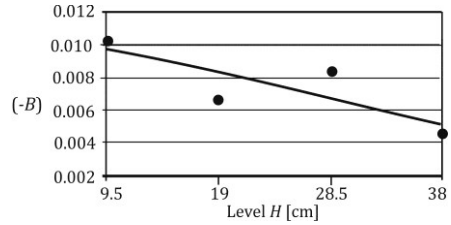

Figure 1.53. Distribution of parameter *B*, [165].

The values from Table 1.28 are also depicted in Figures 1.52–1.53 (points).

Empirical values of velocity V_y calculated from formula (1.26), using formula (1.27) and the values from Table 1.29, are listed in Table 1.30.

Table 1.30. Empirical values of velocity

Level H [cm]	Distance from the symmetry axis x [cm]							
	0		5		10		15	
	$\bar{V}_y$	$\hat{V}_y$	$\bar{V}_y$	$\hat{V}_y$	$\bar{V}_y$	$\hat{V}_y$	$\bar{V}_y$	$\hat{V}_y$
9.5	4.17	4.31	3.38	3.39	1.72	1.64	0.42	0.49
19.0	3.9	4.18	3.38	3.40	2.15	1.83	0.88	0.65
28.5	3.7	3.96	3.28	3.35	2.13	2.02	0.65	0.87
38.0	3.7	3.66	3.4	3.23	2.43	2.20	1.22	1.17

On the basis of the data given in Table 1.30, we present the comparison of the empirical values $\hat{V}_y$ with average experimental results that are depicted in Figures 1.54–1.57.

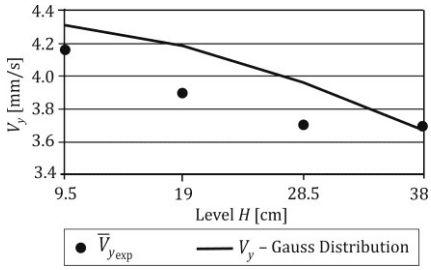

Figure 1.54. Agreement of experimental and empirical values of velocity at the measurement point x=0 cm, [165].

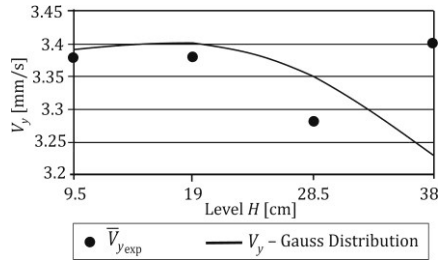

Figure 1.55. Agreement of experimental and empirical values of velocity, at the measurement point x=5 cm, [165].

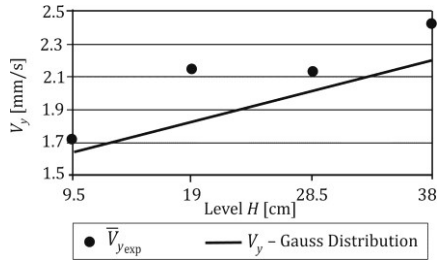

Figure 1.56. Agreement of experimental and empirical values of velocity at the measurement point x=10 cm, [165].

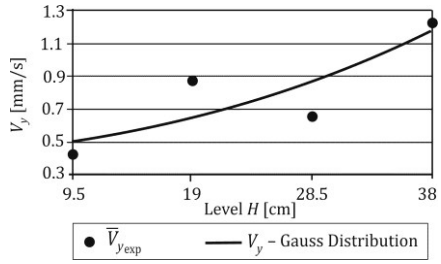

Figure 1.57. Agreement of experimental and empirical values of velocity at the measurement point x=15 cm, [165].

1.2.5.6.2. Evaluation of kinematic parameter b

The shape of velocity profiles obtained by the DPIV technique does not change with the height. Taking into account formulas (1.25–1.27) and the values given in Table 1.28, the kinematic parameter b was evaluated for the analysed levels comparing the corresponding coefficients in formulas (1.25) and (1.26).

For level H=9.5 cm above the outlet parameter b equals:

$$b = -\frac{1}{4Bz} = -\frac{1}{4(-0.01024)9.5} = 2.57 \text{ [cm]}.$$

For level H=19 cm, parameter b=1.983 in centimetres, for level H=28.5 cm b=1.053 in centimetres and for level H=38 cm b=1.446 in centimetres. Figure 1.58 presents distribution of parameter b in the model.

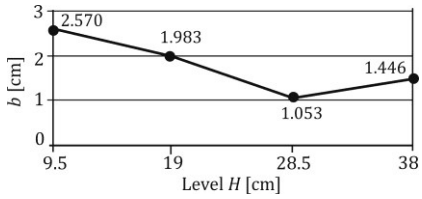

Figure 1.58. Variation of kinematic parameter b in the converging model, [165].

It reaches the highest value very close to the outlet. Then it decreases up to the level H=28.5 cm but the decrease between the level 9.5 cm and 19 cm is about 20% and between level H=19 cm and 28.5 cm is about 90%. From the level 28.5 cm, parameter b increases again and the increase is about 40%.

1.2.5.6.3. Comparison of flow rate value *Q* by the parabolic and Gaussian solution

On the basis of formula (1.21) the values of x_{max} were determined and listed in Table 1.31 where the parameters A and α calculated in formula (1.22) using the values from Table (1.24) are listed.

Table 1.31. Values of flow rate (parabolic solution)

Level [cm]	A	α	V_0 [mm/s]	x_{max} [cm]	Q [cm^2/s]
9.5	0.019	1.443	4.18	15.58	7.698
19.0	0.0107	1.62	3.88	16.46	7.898
28.5	0.00567	1.786	3.72	18.10	8.635
38.0	0.00386	1.94	3.69	17.53	8.542

In the Gaussian solution the flow rate per the unit thickness of the model was calculated according to the formula:

$$Q = 2\int_0^{x_{max}} Ae^{Bx^2}\,\mathrm{dx}. \tag{1.28}$$

This integration was calculated numerically using the limits of integration given in Table 1.32 at each level in the model and the values of flow rate Q are also listed in Table 1.32.

Table 1.32. Values of the flow rate (Gaussian solution)

Level [cm]	A	B	x_{max} [cm]	Q [cm^2/s]
9.5	4.315	- 0.009701	15.58	7.599
19.0	4.177	- 0.008253	16.46	7.869
28.5	3.96	- 0.006716	18.10	8.257
38	3.664	- 0.005089	17.53	8.403

The comparison of the flow rates calculated in the parabolic and the Gaussian solution is presented in Figure 1.59.

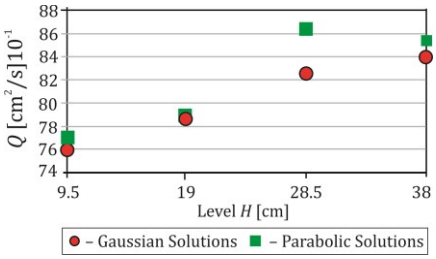

Figure 1.59. Comparison of the flow rate obtained in two solutions; parabolic and the Gaussian type, [165].

Analysing the flow rate obtained both in the parabolic and Gaussian solution (cf. Tables 1.31, 1.32) it is clearly seen that the Drescher's assumption (1991) of the constant density in the hopper is not preserved.

1.2.5.7. Radial Flow Departure

The radial flow in converging hoppers is described by the relation presenting velocity vector along radius r for the wedge-shaped hopper, [2]:

$$v_r = -\frac{A_1}{r}, \tag{1.29}$$

and for the conical hopper:

$$v_r = -\frac{A_2}{r^2}, \tag{1.30}$$

where A_1, A_2 are certain constant values, [2]. Formula (1.29) is applied when the density of the flowing material does not change in the hopper.

Using the profiles obtained in the DPIV technique it was possible to verify vertical velocity values and their dependence on variable r.

1.2.5.7.1. Verification of the Radial Flow Assumption

To verify this assumption the values of the readings of velocity components V_y obtained in the DPIV technique from the profiles presented in Figures 1.33, 1.34 and 1.36 were used in the analysis. The values of readings were put into Tables 1–4 published in Appendix 2.

Now we assume that the vertical velocity is described by the following relation:

$$v_r = -\frac{A}{r^B}. \tag{1.31}$$

If parameter B is equal or almost equal "1" then the relation describing the velocity of the radial flow given by [2] is valid. If parameter $B \neq 1$ considerable then the theory given in [2] is not possible to apply and the assumption of the radial flow cannot be used.

In our analysis it was found that if parameter $B=1$ and parameter A would be calculated then the errors of the description would reach several hundred percents. In such conditions the Drescher's model could not be applied to describe velocity for each measurement point value x and for each level z. Analysing the values given in Table 1.33 it is noticeable that it is possible to determine a certain region of velocity and then for high values of x and z, the Drescher's model describes velocity in a proper way. Assume $B=1$ and calculate A by the least squares method but the description is not adequate.

In fact, the vector fields, (cf. Figure 1.30) do not show the radial nature of the flow. The vectors located in the funnel flow that formed in the middle of the hopper, indicate the vertical direction of the moving particles. Only in the upper part of the flowing material there are regions where the vectors direct radially to the funnel. Also in the vicinity of the outlet velocity vectors pass radially to the outlet. There are staircase-like boundaries between the flowing material and the stagnant portions.

The least squares method with applying the nonlinear regression was used to determine parameters A and B. Coefficient of correlation R and coefficient of determination R^2 were also calculated. In the current analysis we do not introduce velocity as a dependent value on time as it was proved in the previous section. Values of parameters A and B are listed in Table 1.33.

Table 1.33. Values of parameters A and B in formula (1.31)

Level [cm]	A
9.5	$4.0178\ 10^{17}$
19.0	$1.8031\ 10^{23}$
28.5	$1.3088\ 10^{52}$
38.0	$4.2448\ 10^{45}$

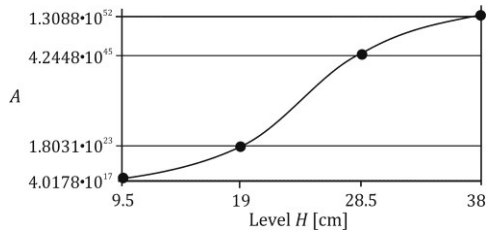

Figure 1.60. Values of parameter *A*.

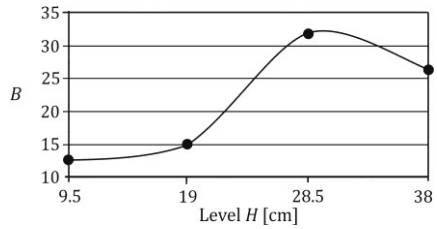

Figure 1.61. Values of parameter *B*.

It is seen in Figure 1.60 that the analysis can be performed using the polynomial although not the second order but the polynomial of the third order. Parameter *B* can be also described by the parabola of the third order using the Lagrange polynomial for four points.

$$\begin{aligned} f(z) = {} & \frac{(z-z_1)(z-z_2)(z-z_3)}{(z_0-z_1)(z_0-z_2)(z_0-z_3)} f(z_0) + \\ & + \frac{(z-z_0)(z-z_2)(z-z_3)}{(z_1-z_0)(z_1-z_2)(z_1-z_3)} f(z_1) + \\ & + \frac{(z-z_0)(z-z_1)(z-z_3)}{(z_2-z_0)(z_2-z_1)(z_2-z_3)} f(z_2) + \\ & + \frac{(z-z_0)(z-z_1)(z-z_2)}{(z_3-z_0)(z_3-z_1)(z_3-z_2)} f(z_3), \end{aligned} \tag{1.32}$$

where $f(z) = A(z)$ or $f(z) = B(z)$.

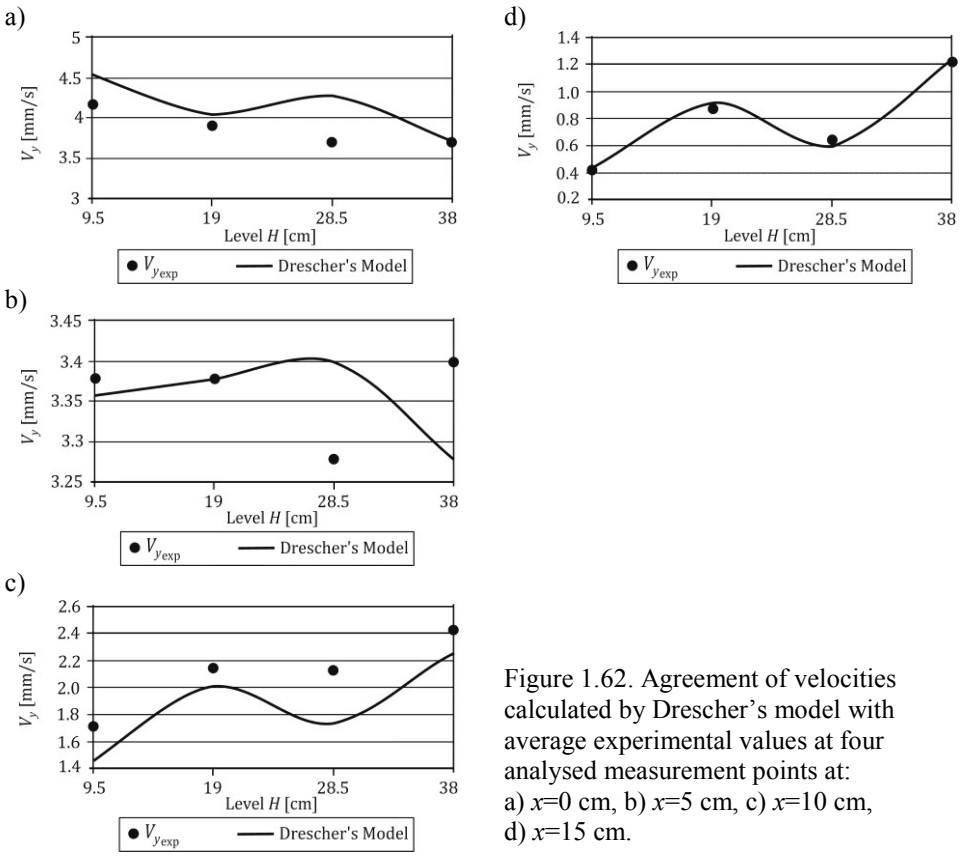

Figure 1.62. Agreement of velocities calculated by Drescher's model with average experimental values at four analysed measurement points at: a) x=0 cm, b) x=5 cm, c) x=10 cm, d) x=15 cm.

The calculated velocities by Drescher's model give good agreement to the experimental values but only for the measurement points located far from both the symmetry axis (x) and the outlet (z). In Figure 1.62 one can compare and analyse the differences between the calculated velocities by Drescher's model and the experimenttal values.

1.2.5.7.2. Verification of accuracy of the applied methods

We also verified the accuracy of the applied methods. In Table 1.34 there are sums of the squares of the differences of velocities in three applied methods.

Table 1.34. Sums of the squares of the differences of velocities measured at the points located from the symmetry axis

Method	Sums of the squares of differences of velocities measured at the points located from the symmetry axis x $\sum(\hat{V}_{emp} - \bar{V}_{yexp})^2$				
	0	5 cm	10 cm	15 cm	$\sum\sum(\hat{V}_{emp} - \bar{V}_{yexp})^2$
Parabolic solution	0.001	0.010	0.158	0.382	0.551
Gaussian solution	0.167	0.034	0.174	0.109	0.484
Drescher's model	0.485	0.029	0.263	0.004	0.781

Table 1.35. Sums of the squares of the differences of velocities measured at the analysed levels

Method	Sums of the squares of differences of velocities measured at the levels located from the outlet $\sum(\hat{V}_{emp} - \bar{V}_{yexp})^2$				
	9.5 cm	19.0 cm	28.5 cm	38.0 cm	$\sum\sum(\hat{V}_{emp} - \bar{V}_{yexp})^2$
Parabolic solution	0.104	0.120	0.263	0.078	0.551
Gaussian solution	0.031	0.234	0.133	0.086	0.484
Drescher's model	0.201	0.049	0.493	0.044	0.781

1.2.6. Conclusions

Comparing the values of the sums of the squares listed in Tables 1.34–1.35 it is seen that there is no method that decrypts the velocities in an adequate way both at all measurements points and at all analysed levels, thus in the whole flow region. The parabolic solution gives good agreement to the experimental results at the measurements points at x=0, 5 and 10 cm. But at x=15 cm and at the level H=38 cm Drescher's solution decrypts the velocities decidedly the best for the points located far from the outlet. In the vicinity of the outlet the Drescher's assumption of density ρ=*const* cannot be applied. This assumption can be used but in the steady state region of the flow located far from the outlet as it is indicated in Figure 1.62d. This conclusion confirms the fact that the region of the flow in the vicinity of the outlet presents an unsteady state of flow with density $\rho \neq const$. The Gaussian solution

presents the best empirical values of velocities for the levels located very close to the vicinity of the outlet.

As a conclusion of the analysis of the radial flow applied in the theoretical investigations we can state that in fact the assumption given by [1] and [2] does not describe adequately the radial flow in converging hoppers. The flow does not run radially in the whole hopper. At the symmetry axis the velocity vectors indicate vertical flow channel. Material located in the upper part of the hopper (where velocity vectors indicate a radial nature of the flow) moves to this vertical flow channel. So we can call the flow – combined or mixed flow. This kind of flow was observed during the whole process of discharge in the converging model.

"Main content of this chapter has been published in Biosystems Engineering, 106, 412-422, 2010".

1.3. Experimental analysis of eccentric flow in the plane model by the DPIV technique

1.3.1. Introduction

In this section experiments of eccentric filling and discharge already presented by [34] are analysed. In practice, the eccentricity of filling or discharge processes occur very often and it may lead to quite an unexpected behaviour of the structure. During asymmetrical processes, flow patterns and wall stresses may be quite different. It is therefore crucial to identify the flow developed in the material during eccentric filling or discharge, and to determine important flow parameters.

1.3.2. Literature review

International Standards usually relate to axial symmetric states of stresses and even avoid defining discharge pressures and flow patterns because of continuing uncertainties. In Standard EN 1991-4 [166] the flow channel geometry and wall pressures under eccentric discharge are defined. The Polish Standard PN-89/B-03262 [167], titled „Silosy żelbetowe na materiały sypkie. Obliczenia statyczne", proposes the values of increased coefficients of horizontal pressure during eccentric discharge. There are codes and guides that include eccentric discharge but they treat it in a different way: [168, 169, 170]. Also a few theoretical solutions have been

proposed for design of silos under eccentric discharge [171, 172, 173]. The European Standard ENV 1991-4, [174] includes a comment on the eccentricity of the outlet, the definition of the flow channel geometry and wall pressure under eccentric discharge. Eccentric filling is described as a condition in which the top of the heap at the top of the stored solids at any stage of the filling process is not located on the vertical centreline of the silo. Eccentric discharge is described as flow pattern in the stored solid arising from moving solid being asymmetrically distributed relative to the vertical centreline of the silo. This normally arises as a result of an eccentrically located outlet but can be caused by other asymmetrical phenomena which are not clearly defined. Calculations for flow channel geometry are required for only one size of flow channel contact with the wall, which should be determined for $\Theta_C = 35^{\circ}$.

Other methods of predicting flow channel dimensions may be also used. Wall pressures under eccentric discharge are defined as the pressure on the vertical zone. The pressure depends on the distance "z" below the equivalent solid surface and the frictional traction on the wall at level "z". So far a few approaches have been developed for the design of bins under eccentric discharge, [173, 175]. The issue of eccentricity has also been found to be one of major causes of hopper failures, given in [5]. Eccentricity of the flow to the silo axis causes the pressure patterns to become much more complex than in the centric case. In the field of silo investigations three main issues are analysed: pressures under eccentric discharge, flow patterns in eccentric discharge and stagnant zone boundaries. Works on eccentric discharge have been published for many years and a few researchers have dealt with this complicated problem. In [176] Anon presented eccentric discharge silo loads and wall loads as a function of discharge rate. In [177], the authors measured wall loads in a corrugated model grain bin when unloaded eccentrically and the effect of eccentric unloading in a model bin for different unloading rates. In [178], the authors investigated the effect of eccentricity draw off and flow rate in a model grain bin. In [179, 180], the authors investigated ways of discharge in silos, further [181] and [182] analysed wall pressures under eccentric discharge. In [183] the author investigated eccentric discharge and the calculation of bending moments in circular silos. They made an experimental study of certain effects of the interaction in the full scale silo between the reinforced concrete silo walls and a free flowing medium. In [184], the authors dealt with post-tensioned circular silos for modern industry and presented irregularities of pressure intensity caused by flow problems, eccentric discharge, or multiple discharge openings. In [185], the authors discussed

experiments with buckling failure problems in which the wall stresses were directly induced by stored solids. In [186], the author studied flow patterns in a silo with concentric and eccentric outlet, and also a steel silo with two types of outlets and its susceptibility to buckling. He found that a thin-walled silo with concentric outlet tends to be well behaved, and whereas the other one with eccentric outlet was susceptible to buckling and collapse. It was also stated that none of the existing theories adequately addressed the issue of buckling of eccentrically-emptied silos. In [187], the author investigated the bahavior of two steel silos under eccentric discharge. In [188], the authors presented experimental results of pressure measurements in the wall in a full-scale silo under eccentric discharge. In [189], the authors analysed eccentric discharge in silos and reduction of the dynamic flow pressures in grain silo by using discharge tubes. In [175], the authors investigated discharge and the eccentricity of the hopper influence on silo wall pressures. In [190], the authors presented investigations on bin loads by both central and eccentric filling and discharge of grains in a model of silo. In the analysis given in [191, 192], the authors using the kinematic model, proposed by [87], constructed a boundary-value problem.

The results consist of measurements of circumferential shell wall deformation for various load histories as a function given service cycles: filling and discharge – centrally and eccentrically. In [191, 192], the authors investigated granular flow in a two-dimensional flat-bottomed hopper with eccentric discharge. In [193] the authors presented computational analysis of wall pressures in silos with concentric and eccentric hoppers. In [144], the authors made some experiments in a two-dimensional flat-bottomed model and identified flow patterns and stresses on the wall during centric and eccentric discharge. The flowing material was recorded using a digital camcorder and the normal and shear stresses were measured using pressure gauges. In [194], the authors measured experimentally the heights of the stagnant zones for two kinds of granular materials after hopper eccentric and centric discharge. In [195], the authors applied FEM modelling in the analysis of influence of hopper eccentricity on wall pressures. In the proposed model the distribution of plastic areas according to eccentricity was analysed. In [196], the authors analysed the results in FEM of a buckling strength of steel silo subject to code-specified pressures for eccentric discharge with the wall loads predicted by four codes where the pressure asymmetry was determined by local pressure increases or reductions and described by the authors as patch loads. In [197], the authors presented a study of localized deformation pattern in granular materials, investigating shear

localizations in granular materials numerically, with the use of a Cosserat continuum approach, and compared the obtained results to experimental data. In [159, 198, 199, 200], the authors also presented a numerical Cosserat approach to bahavior of granular medium in a silo.

The latest paper on the flow pattern measurement however, in a full scale silo not in a model, was presented in [6]. One can find a long list of references concerning investigation of eccentric discharge there.

1.3.3. Experimental procedure

In this section the images of the flowing material registered by DPIV technique in a plane flat-bottomed silo model with central and eccentric filling and discharge are investigated. The experimental setup used in the experiments was presented in Figure 1.1. To investigate the effects of eccentricity the model was filled centrally at the symmetry axis and close to the left or to the right edge of the silo. The discharge opening was also located centrally or eccentrically, (cf. Figure 1.63). To analyse the effects of wall roughness, the side walls of the model were lined with sand paper and the experiments were compared with analogous tests made for the model with smooth lateral walls. The degree of roughness was varied by the use of two different sand papers. To obtain medium rough walls ARBATEX X P60A 194 sand paper was used and in the model with very rough lateral walls, the paper ARBATEX X P16A 432.

1.3.4. Experimental results

There are some attempts to codify rules for eccentric filling and discharge and some investigations on silo wall pressures have been recently completed. The flows of amaranth seeds and of flax seeds have been investigated in different configurations, (cf. Figure 1.63). Discharge was investigated in three positions of the outlet, from the left, from the right and in the symmetry axis. Only some of the results, such as velocity profiles and velocity distributions are presented here to show the evolution of the flow in all discussed cases. The influence of both the position of the outlet and the roughness of the wall on the flow pattern was observed and registered. The eccentricity of the filling pipe and the outlet led to several flow irregularities not observed before. Therefore, it is difficult to relate the results obtained in this analysis to any previous investigation. Figure 1.63 presents a scheme of six investigated filling and discharge variants.

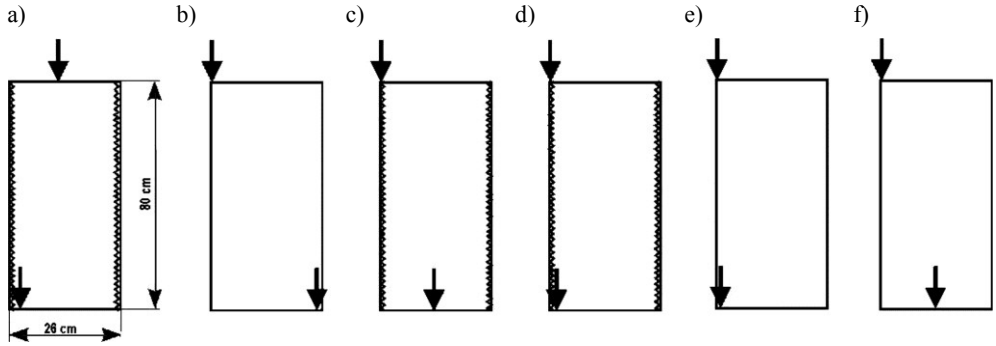

Figure 1.63. Schematic images of filling and discharge modes: a) amaranth seeds in the model with rough walls, b) amaranth and flax seeds in the model with smooth walls, c) flax seeds in the model with medium rough walls, d) flax seeds in the model with rough walls, e-f) flax seeds in the model with smooth walls.

1.3.4.1. Velocities of the flowing amaranth seeds. The model with rough walls

Figure 1.64 illustrates velocity contours for the eccentric flow with the model filled with the amaranth seeds in the symmetry axis and discharged eccentrically from the left. The walls of the model were rough. The discharge outlet was situated 0.8 cm from the left lateral wall in the model. The total time of the flow was found to be 68 s. The total mass of the grains was 18.6 kg and the moisture of the grains 10.2%.

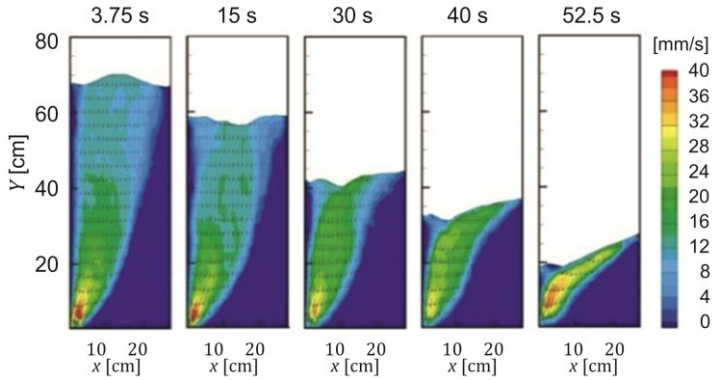

Figure 1.64. Velocity distributions and vector fields for central filling and eccentric discharge located at the left wall. Amaranth seeds through the outlet situated 0.8 cm from the left edge in the model with rough walls,
after: 3.75th s, 15th s, 30th s, 40 s, 52.5 s.

After the silo had been filled centrally, the grains formed a natural angle of repose. The total height of the packed material was 78 cm at the symmetry axis. The free surface natural angle collapses along the symmetry axis. Soon after the flow initiation a nearly uniform flow channel for the entire height of the silo and the highest velocity ("plug flow") are formed. Intensity of the "green region" in the flowing stream remains uniform till 40th s of the flow. The stagnant zones with nearly zero velocity are indicated by the blue colour. During the flow, the free surface changes its shape, becomes more and more concave but not regularly. It collapses, but a depression forms in the symmetry axis and slowly passes to the left edge of the model. The material uniformly feeds the flowing stream from the stagnant zones. The stagnant zone forms near the left rough wall but it becomes narrow. Its width is about 2 cm in the upper part and it almost vanishes in its bottom part. The stream of the flowing material has rather sharp boundaries. The rough model walls cause the material near the lateral wall to adhere to it, creating a zone of higher density. The rough wall behaves like a "brake" holding the lateral parts of the material.

Velocity vectors of the plug flow indicated in Figure 1.64 are no longer aligned vertically. However, in the initial phase of the flow, in the upper part the velocity vectors are less inclined than in the lower part of the flowing material. The flow evidently accelerates; the velocity vectors in the initial phase of the flow are shorter than in the advanced phase of the flow.

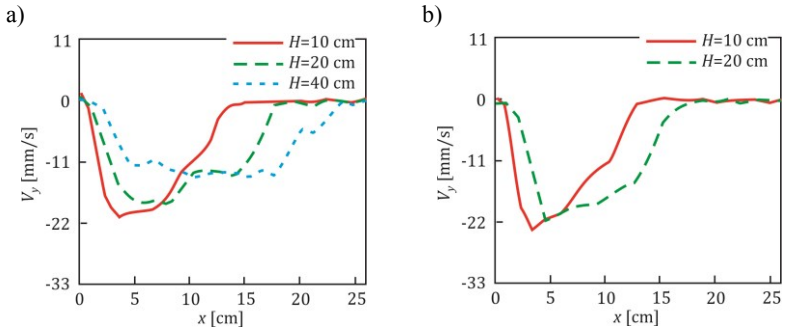

Figure 1.65. Velocity profiles for the flow of amaranth seeds, central filling and discharge from the left in the model with rough walls, at a) 15th s and b) 40th s of the flow.

Full field velocity measurements were used to extract selected velocity profiles. Figure 1.65 presents velocity profiles obtained for the flowing amaranth seeds in the model with rough walls. The velocities form a bunch of profiles, almost of the same

shape, with their maximum values displaced to the left side of the model. At the higher level (40 cm) the velocity maximum decreases and the velocity profile becomes nearly flat in the centre. The profile lines are not smooth in their central part; however near the rough wall the profiles are smooth. Such behaviour of the flowing material near the rough wall may be explained by the fact that the rough wall acts like a brake. High velocity gradients "keep" ordered structure of the granular material being in the area close to the rough wall. The flowing material slides along the border between the stagnant zone and the flowing stream. In the plug region local, fluctuations of the material density, due to the weaker horizontal stresses between grains, are probably responsible for the observed velocity non-uniformities.

1.3.4.2. Velocities of the flowing amaranth seeds. The model with smooth walls

Another round of experiments was made in the model with smooth walls to elucidate effects of the wall roughness. The flow of the same amaranth seeds was investigated for eccentric location of the feeding tube (left) and discharge opening located in the opposite corner (right). The total time of the flow was found to be 78 s. The discharge outlet was situated 1.4 cm from the right lateral wall in the model. The set of pictures in Figure 1.66 presents the flow after 15th and 40th s and at three heights 10, 20 and 40 cm above the outlet, (cf. Figure 1.67).

After eccentric filling from the left, the free surface was formed in the natural angle of repose but the way of filling blocked forming the whole repose. The total height of the packed material was 78 cm measured near the left wall of the model. After the flow starts, the flowing stream forms immediately in the material and the free surface collapses shortly after that. The stagnant zone formed near the right wall is rather small and visible only in the initial flow stages. In fact, it quickly vanishes and the flowing stream just slides along the right lateral wall. The plug flow zone, formed in the initial phase of the flow, vanishes in the advanced phase of the flow. The material moves into the flowing stream from the stagnant zones at a uniform rate. After 40th s of the flow the deeper depression in the free surface slides from the upper surface into the area between the rough wall and the flowing stream.

The depression slides on the upper border of the flowing material. Velocity vectors indicated in Figure 1.66 are not vertically orientated. Only in the initial phase of the flow, the velocity vectors observed in the upper parts are less inclined than in the lower parts of the flowing material.

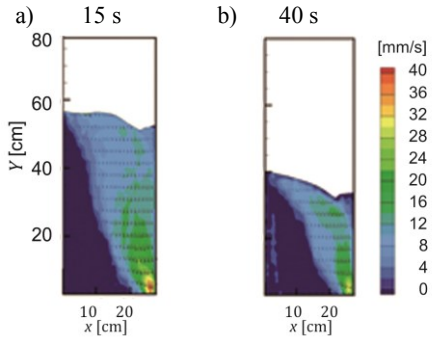

Figure 1.66. Velocity distributions and vector fields for discussed cases of the flow of amaranth seeds in the model with smooth walls, after a) 15th s, b) 40th s of the flow.

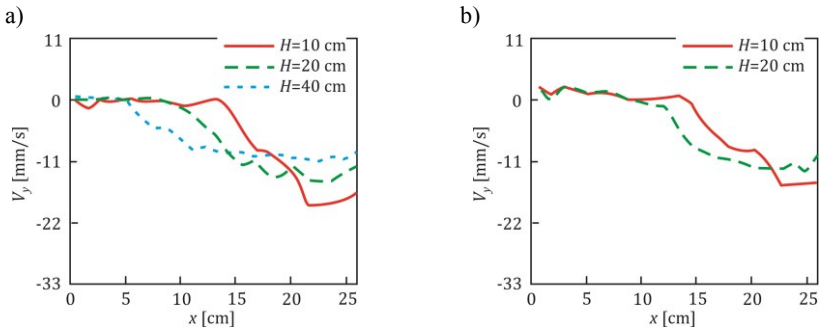

Figure 1.67. Velocity profiles for the flow of amaranth seeds: filling from the left and discharge from the right in the model with smooth walls, after a) 15th s and b) 40th s of the flow.

The velocities form a bunch of profiles, of a little different shape, with their maximum values displaced to the right. The velocity profiles obtained closer to the bottom (red and the green lines) exhibit values about 0–1 mm/s in the 10 cm broad area adjacent to the left wall. Closer to the bin axis the flow velocity increases, reaching about 9 mm/s in the relatively flat maximum close to the right wall. There are positive velocity values recorded for the 8 cm broad area near the left wall. The material flow is obviously directed upwards. The main flowing stream directed to the right (cf. Figure 1.66b) pushes the material into the stagnant zone so forcefully that the upper parts of the material in the stagnant zone is moved upwards.

1.3.4.3. The flow of the flax-seeds in the model with medium-rough walls

To elucidate the effects of the wall roughness other experimental tests were made in the model with medium-rough walls (sand paper P60A194), (section 1.3.4.4). These

results are compared with the flow of the flax-seeds in the model with smooth walls, presented in the previous section. Here the recorded images of the flow of the flax-seeds in the case of eccentric filling and central discharge (cf. Figure 1.68), and also eccentric filling and eccentric discharge from the left (cf. Figure 1.70) are presented. The total time of the flow in the case of the model with medium-rough walls was found to be 88 s, and in the model with rough walls – 125 s. The velocities in the model with medium wall roughness are much lower than in the model with smooth walls, (cf. Figure 1.90 and 1.91). For the same feeding-discharge locations the material flowing forms a well visible channel in the centre of the model (cf. Figure 1.90), whereas in Figure 1.68 the broad mass flow of the material is observed. There is no narrow flow channel but there is a plug flow of similar intensity during the flow.

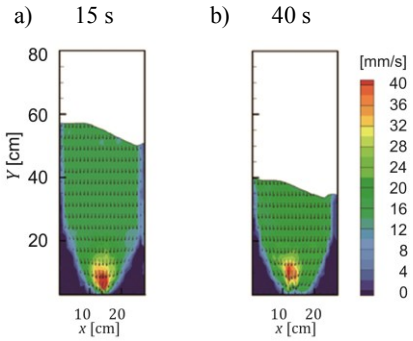

Figure 1.68. Velocity distributions and vector fields for filling from the left and central discharge of the flax seeds in the model with medium-rough walls.

The velocity profiles shown in Figure 1.69 confirm the mass flow in the model with medium-rough walls. The blue and the green line present the constant velocities. Near the left wall, a stagnant zone forms but it is a little wider than on the right wall.

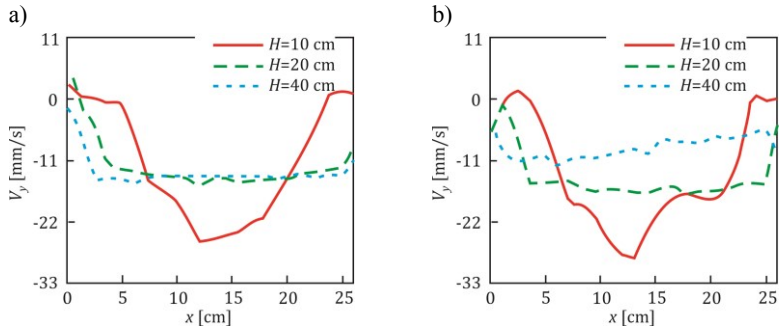

Figure 1.69. Velocity profiles for the flow of the flax seeds in the filling from the left and central discharge in the model with medium-rough walls, a) 15 th s of flow, b) 40 th s of flow.

1.3.4.4. The flow of the flax-seeds in the model with rough walls

In the model filled and discharged eccentrically with rough walls with the flowing flax-seeds a clear flow channel, (cf. Figure 1.70) is registered in contrast to the previous case discussed in Figure 1.68. The total time of the flow, (cf. Figure 1.70) is much longer, i.e. 125 s, comparing with 88 s, (cf. Figure 1.68). In such cases, the free surface is formed in the natural angle of repose but the left wall blocks the formations of the whole slope. After about 15 s of the flow the free surface collapses with a centre in the flowing stream of the material. The depression moves on the upper border of the flowing stream to the stagnant zone.

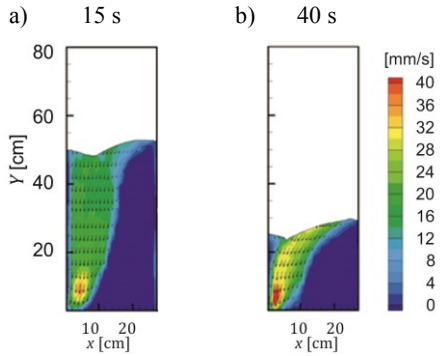

Figure 1.70. Velocity distributions and vector fields for filling and discharge from the left of the flax seeds in the model with rough walls, a) 15 th s of flow, b) 40 th s of flow.

The velocity profiles depicted in Figure 1.71 confirm the velocity values presented in the velocity contours, (cf. Figure 1.70). In the stagnant zone close to the right wall, all three profiles indicate velocities equal to zero. In Figure 1.71a, the green velocity profile indicates the velocity of a positive value. It means that the velocity vectors are directed upward. In the flowing region, the material presses the material stored close to the left wall so hard that it moves upwards. The flowing material exerts an unexpected high pressure onto the model wall.

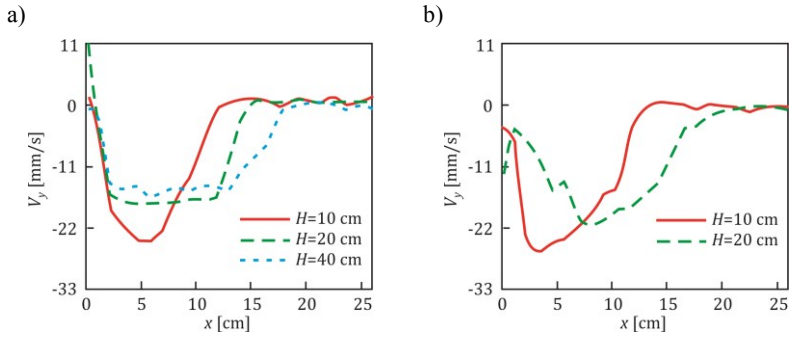

Figure 1.71. Velocity profiles for the flow of the flax seeds for the filling and discharge from the left in the model with rough walls, a) 15 th s of flow, b) 40 th s of flow.

1.3.4.5. Empirical analysis of the flow of the flax seeds in the model with smooth walls. Discharge from the right

In this section we present the theoretical analysis of velocities in asymmetric flow of flax seeds in the model with vertical and smooth walls with outlet located close to the right wall. We consider the case discussed in Figure 1.72. The model has the depth of 5 cm.

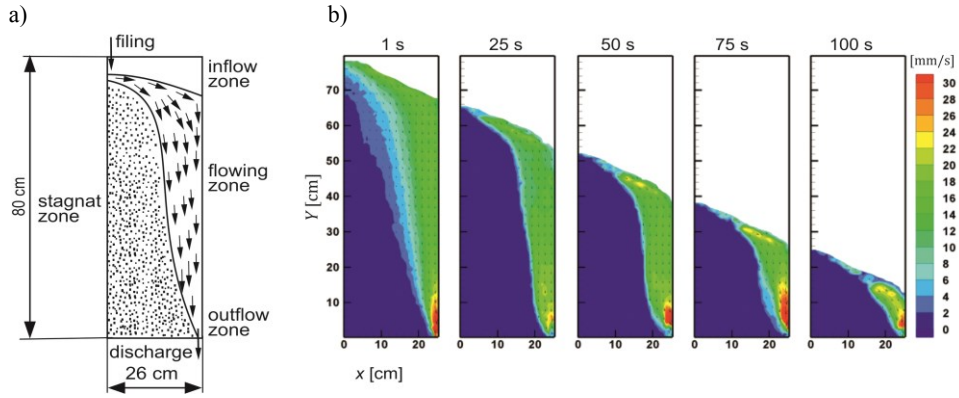

Figure 1.72. Eccentric flow of flax seeds: filling from the left and discharge from the right, a) flow mode formed in the model, b) velocity contours, [201].

The readings taken form the velocity profiles presented in Figure 1.73 are listed in Tables 1–7 published in Appendix 3.

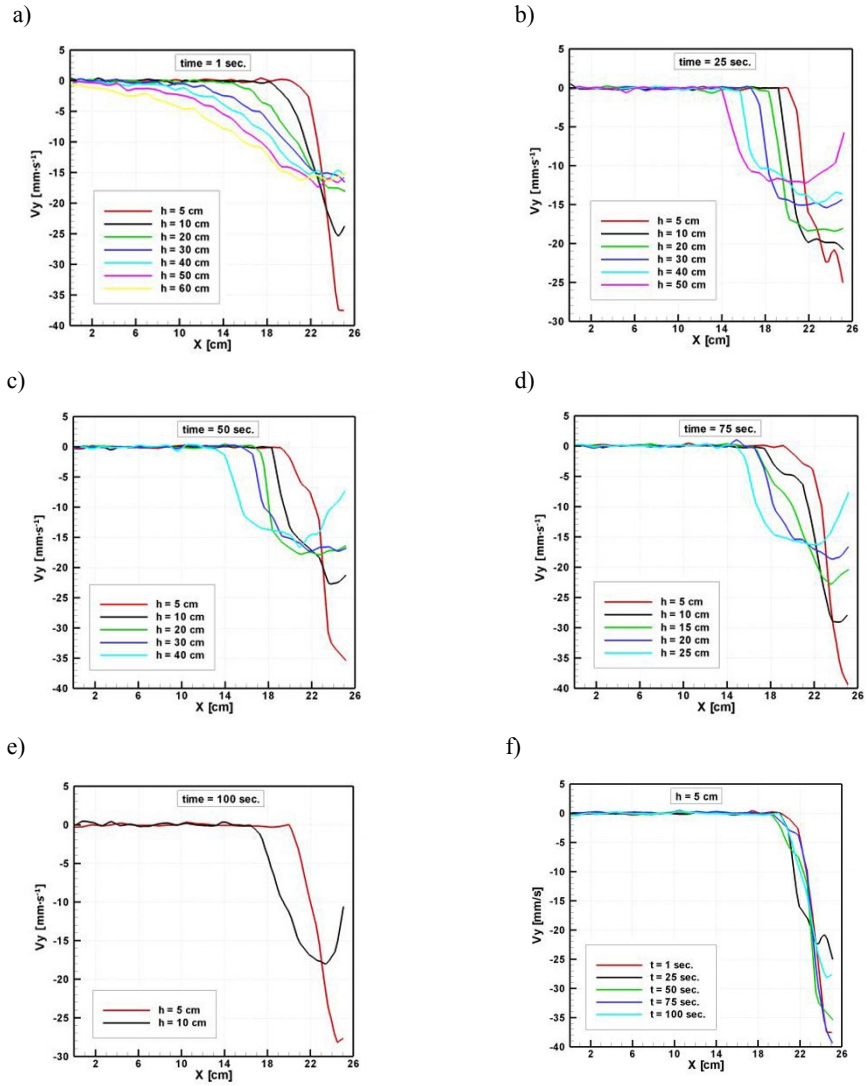

Figure 1.73. Velocity profiles of flax seeds flow at: various time instants (a–e) and levels f–j, k) velocity distribution in time, [201]
[*Continued figure on next page*].

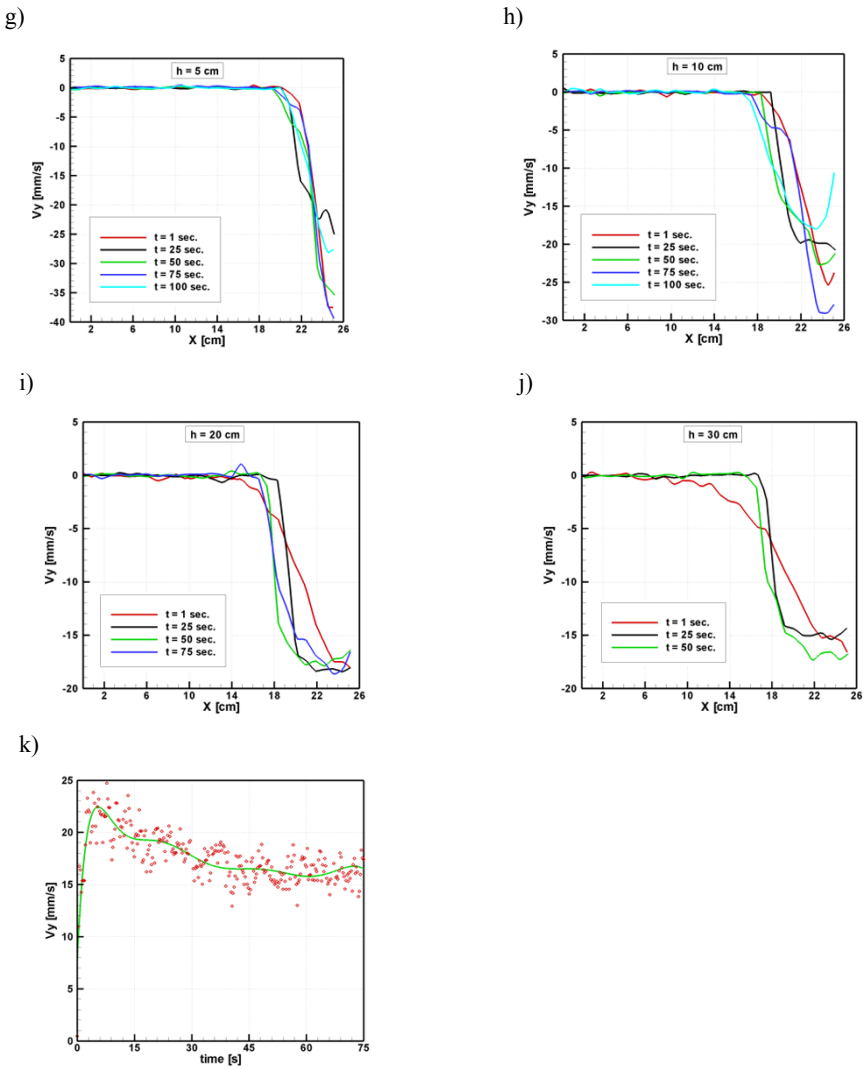

Figure 1.73. Velocity profiles of flax seeds flow at: various time instants (a–e) and levels f–j, k) velocity distribution in time, [201].

Also the statistical analysis of the experimental results was done.

Applying the values given in Tables 1–7 (given in Appendix 3) the confidence intervals were determined for the analysed levels for the averages of velocities and listed in Tables 8–13 published in Appendix 3, [135]. In the calculations, time was not taken into account. In this analysis, there are no readings that were removed from the data set.

1.3.4.5.1. Description of velocities by the exponential function (modified, the Gaussian type)

In this section we depend velocity V_y on the distance x – location of the measurement points and on various heights z. There is no method to obtain directly a function with two variables $V_y(x,z)$. We present here the method how to approach the function with two variables. The type of the function applied in empirical description of vertical velocity V_y calculated in millimetres per second was proposed as:

$$V_y = e^{A+Bx+Cx^2}, \tag{1.33}$$

where parameters A, B and C were determined by the least squares method (*the first regression*), listed in Table 1.36 and presented as points in Figure 1.74. The solid lines show the empirical description of these parameters at various analysed levels.

Table 1.36. Values of the symbols given in formula (1.33), (*1st regression*)

Level H [cm]	A	B	C
5	3.501	0.07521	- 0.10105
10	3.029	0.10732	- 0.04708
20	2.623	0.2970	- 0.05453
30	2.721	0.08002	- 0.02084
40	2.416	0.13908	- 0.01892
50	2.608	0.009943	- 0.006805
60	2.820	-0.006486	- 0.0048328

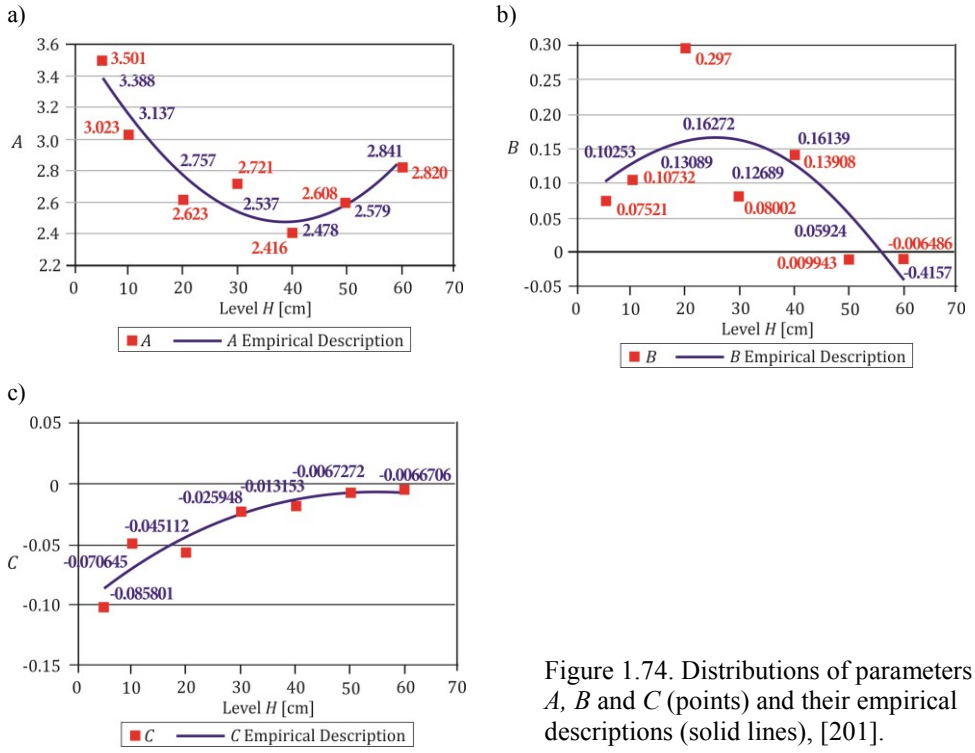

Figure 1.74. Distributions of parameters *A, B* and *C* (points) and their empirical descriptions (solid lines), [201].

Because parameters *A, B* and *C* are depended on the height z in the model (especially parameter *B*) in the form presented in formula (1.34), thus we expect the second regression results to be less agreed with the experimental results, (cf. Figure 1.75). However, calculating the second regression we determined the form of the function to describe velocity V_y by the multiple regressions.

$$\begin{aligned} \hat{A} &= A_0 + A_1 z + A_2 z^2, \\ \hat{B} &= B_0 + B_1 z + B_2 z^2, \\ \hat{C} &= C_0 + C_1 z + C_2 z^2. \end{aligned} \tag{1.34}$$

Parameters A_i, B_i, C_i for i=0, 1, 2 were determined by the least squares method by formula (1.34) and listed in Table 1.37.

Table 1.37. Values of the symbols given in formula (1.34)

Parameters	*i*=0	*i*=1	*i*=2
A_i	3.679	-0.062143	0.000803132
B_i	0.065893	0.0081573	-0.000165805
C_i	-0.10255	0.0035087	- 0.000031846

On the basis of formulas (1.33), (1.34) and values listed in Table 1.37 velocity distributions were drawn. Figure 1.75 presents the comparison of average experimental results $\bar{V}_{yexp}$ with empirical values $\hat{V}_{yemp}$ after the 1st regression (the velocity depends on distance *x* from the symmetry axis), after the 2nd regression $\hat{\hat{V}}_{yemp}$, depending the velocity both on distance *x* and on height *z,* and after the multiple regression $\hat{\hat{\hat{V}}}_y$ that is discussed in the next section.

1.3.4.5.2. Description of velocities by the multiple regression

Applying the 1st and 2nd regression, the description of vertical velocity was assumed in the form of the following function:

$$V_y = exp(a_o + a_1x_1 + a_2x_2 + a_3x_3 + a_4x_4 + a_5x_5 + a_6x_6 + a_7x_7 + a_8x_8), \quad (1.35)$$

where

$$x_1 = z, x_2 = z^2, x_3 = x, x_4 = xz, x_5 = xz^2, x_6 = x^2, x_7 = zx^2, x_8 = z^2x x^2,$$

and *x* denotes the distance from the left wall, *z* – is the height in the model, measured in centimetres.

The coefficients a_i where *i*=0, 1…8 were calculated using the least squares method, and listed in Table 1.38. We define the calculations accurately using the multiple regression. There is a possibility to determine the parameters by the non-linear regression, that would define the description more accurately, but it is a very time--consuming task.

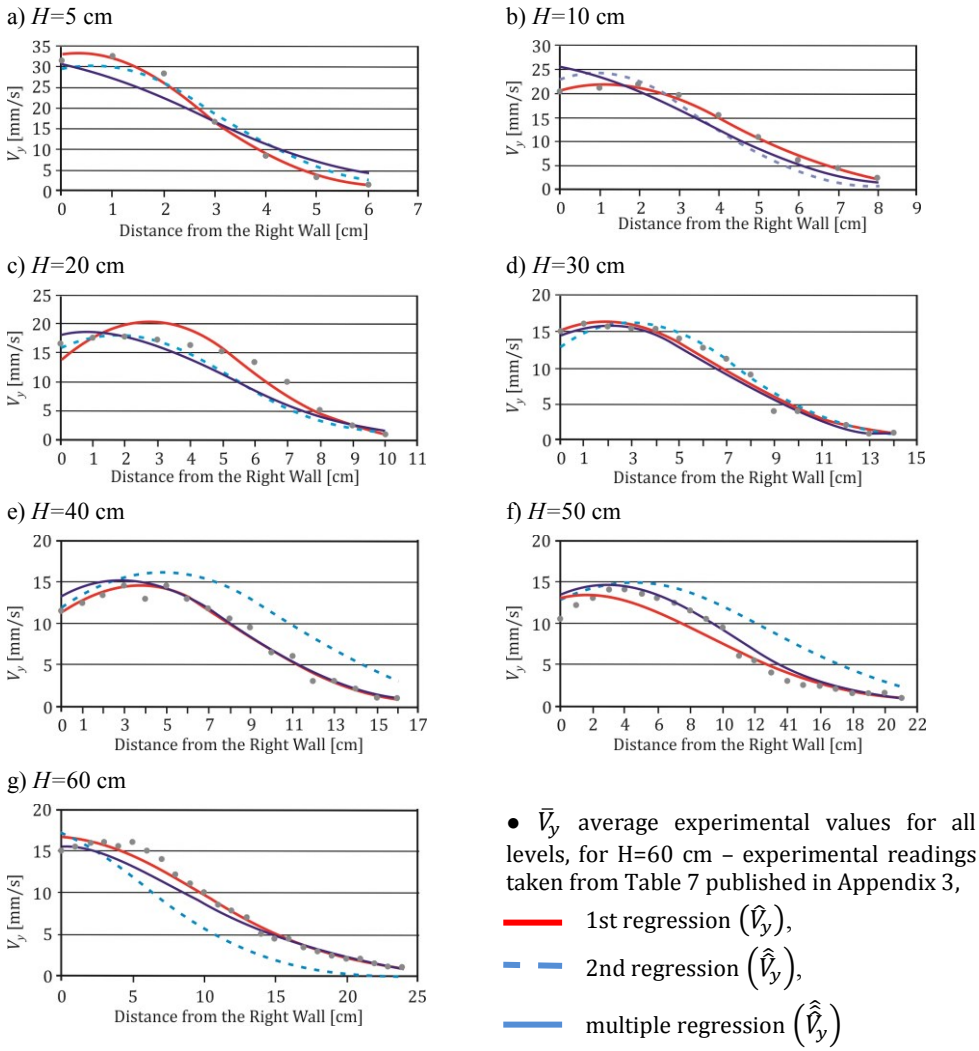

Figure 1.75. Velocity distributions: average experimental results compared with the 1st, 2nd and the multiple regression, [201].

Table 1.38. Values of coefficients α_i in formula (1.35)

a_0	a_1	a_2	a_3	a_4	a_5	a_6	a_7	a_8	*R-coefficient of correlation*
3.663	-49.92 10^{-3}	0.577 10^{-3}	-143.42 10^{-3}	3.159 10^{-3}	-0.184 10^{-3}	-45.704 10^{-3}	0.886 10^{-3}	-0.003 10^{-3}	0.9714

On the basis of formula (1.35) and data listed in Table 1.38, the values of vertical velocity $\hat{\hat{V}}_y$ were calculated by the multiple regressions. Three approaches of describing the velocity in the model presented above are shown in Figure 1.75. The points denotes average values of experimental measurements and the solid lines represent the functional descriptions of velocity after the 1st $(\hat{V}_y)$, the 2nd $\left(\hat{\hat{V}}_y\right)$ and the multiple regression $\left(\hat{\hat{V}}_y\right)$.

As it is seen in Figure 1.75 there is no empirical function which values agree accurately with the average experimental results both at all measurement points and all levels. We have found the best description of velocities at the lowest levels for H=5 cm and H=10 cm. The higher the considered level is located the higher regression should be applied to describe the velocities. But it is not a rule. This is changing at the middle levels. Velocity distributions (cf. Figure 1.75) confirm the aptness of the applied function for the multiple regression.

1.3.4.5.3. Description of velocities by ***ch*** function

In this section we propose another empirical description of velocity by the ***ch*** function in the following form:

$$V_y = ch(A + Bx + Cx^2). \quad (1.36)$$

The notation ***ch*** means cosh function. In the analysis, the velocity was depended on distance x using the 1st regression. Parameters *A, B* and *C* in the empirical description were calculated by the least squares method and listed in Table 1.39.

Table 1.39. Parameters *A, B* and *C* in formula (1.36), the 1st regression

Level *H* [cm]	*A*	*B*	*C*
5	4.1800	0.10689	- 0.10904
10	3.7170	0.11379	- 0.048339
20	3.2350	0.38199	- 0.066509
30	3.3078	0.15780	- 0.028827
40	3.0010	0.20549	- 0.024767
50	3.2337	0.040317	- 0.0088796
60	3.4154	0.031379	- 0.0070211

Parameters *A, B* and *C* in formula (1.34) are depended on height *z* as was presented in formula (1.34). Coefficients A_i, B_i and C_i calculated by the least squares method are listed in Table 1.39. Their parabolic descriptions are presented in Figure 1.76.
Applying formula (1.34) and (1.36) and values listed in Table 1.40 we obtain the description of velocity dependent on distance *x* and height *z* after the second regression.

Table 1.40. Values of the parameters in formula (1.34)

Parameters	*i*=0	*i*=1	*i*=2
A_i	4.39600	-0.0682080	0.00087487
B_i	0.06613	0.0124850	- 0.00023117
C_i	-0.10702	0.0032341	- 2.62531 10^{-5}

On the basis of the 1st and 2nd regression we assumed the vertical velocity in the following form:

$$V_y = ch(a_o + a_1x_1 + a_2x_2 + a_3x_3 + a_4x_4 + a_5x_5 + a_6x_6 + a_7x_7 + a_8x_8). \quad (1.37)$$

The values of parameters a_i where i=0, 1, 2…8 were calculated using the least squares method, and listed in Table 1.41. Variables x_1, x_2, x_3, x_4, x_5, x_6, x_7, x_8 are applied like in formula (1.35).

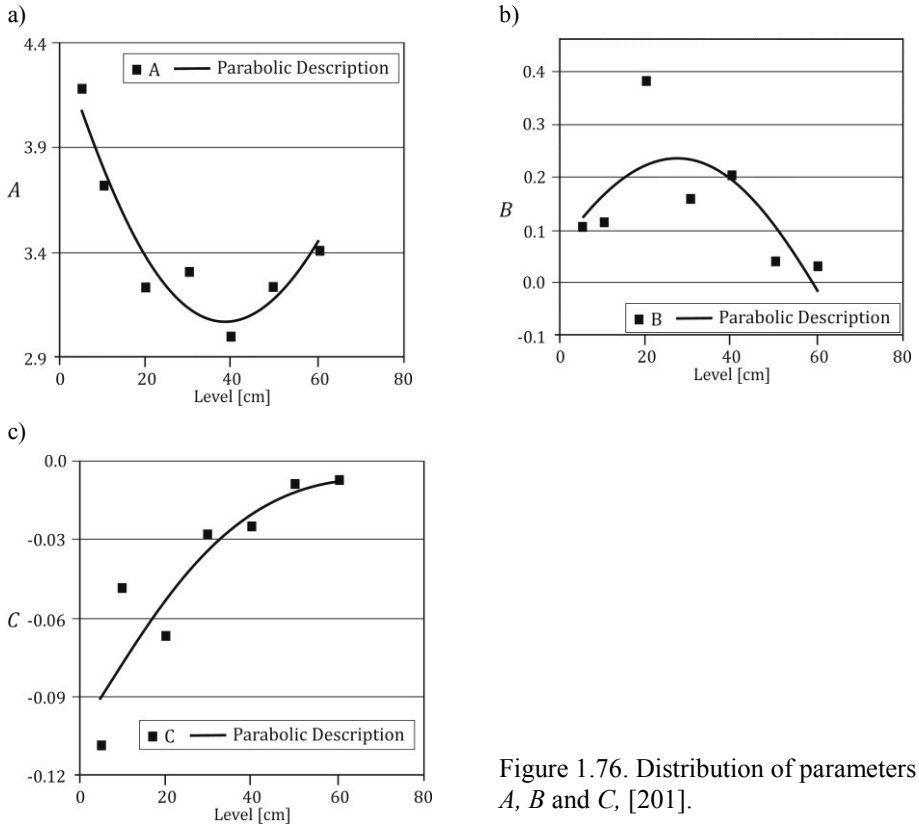

Figure 1.76. Distribution of parameters *A, B* and *C,* [201].

Table 1.41. Values of coefficients α_i in formula (1.37)

a_0	a_1	a_2	a_3	a_4	a_5	a_6	a_7	a_8	*R-coefficient of correlation*
4.2904	-0.04908	0.000552	-0.052342	0.01143	-0.00017	-0.062328	0.001345	-0.000007	0.9695

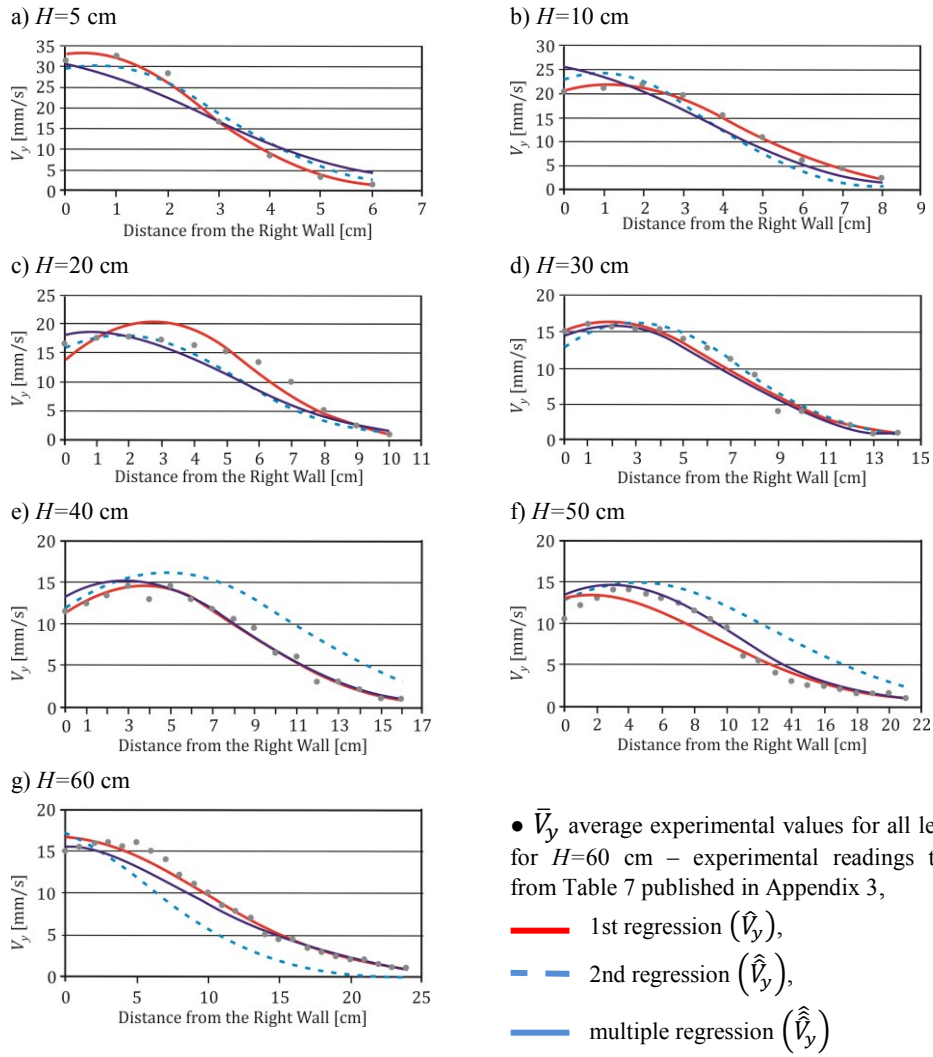

Figure 1.77. Vertical velocity descriptions by the three applied methods, [201].

Applying the approaches presented above we show the vertical velocity distributions in Figure 1.77. Description of velocities by the ***ch*** function also proved that at the higher levels the best agreement of the experimental and empirical results was obtained by the first and the multiple regressions. The second regression was only needed to predict the type of the function to describe velocity.

1.3.4.5.4. Verification of accuracy of the applied descriptions

We also verified accuracy of the applied descriptions. In Table 1.42, the sums of the squares of the differences of velocities in three applied approaches by the Gaussian description and by the ***ch*** function are listed.

As it is seen the best description of velocities was found using the ***ch*** function because the sum of the sums of the squares is lower, both in the used regressions and at the analysed levels.

1.3.4.5.5. Flow rate

The flow rate Q was calculated for two presented descriptions of velocities. In the solution given by the Gaussian exponential function the flow rate was calculated according to the following formula:

$$Q = \int_0^{x_n} e^{A+Bx+Cx^2} \mathrm{dx}, \tag{1.38}$$

and the values Q are listed in Table 1.43. In formula (1.38) and (1.39) the limit of integration x_n denotes the distance of the last measurement point calculated from the right wall taken from the experimental readings for various analysed levels, (cf. Tables 1–7 published in Appendix 3). The flow rate was described by the following parabolic function:

$$\tilde{Q} = \tilde{A}_1 + \tilde{B}_1 z + \tilde{C}_1 z^2, \tag{1.39}$$

where parameters $\tilde{A}_1 = 110.54, \tilde{B}_1 = -0.20605, \tilde{C}_1 = 0.026017$ were calculated by the least squares method using the values listed in Table 1.43. On the basis of the values of parameters $\tilde{A}_1$, $\tilde{B}_1$, $\tilde{C}_1$, the values of the flow rate $\tilde{Q}$ were determined and these values were used to calculate the sums of the squares of the differences that are also listed in Table 1.43.

In the description of velocities by the ***ch*** function, the flow rate was calculated according to the formula:

Table 1.42. Sums of the squares of the differences of velocities

Regression	Sums of the squares of the differences of velocities measured at the analysed levels $\sum(V_{emp} - \bar{V}_{exp})^2$							
	5 cm	10 cm	20 cm	30 cm	40 cm	50 cm	60 cm	$\sum\sum(V_{emp} - \bar{V}_{exp})^2$
	Gaussian description							
1st	10.208	3.490	40.234	10.959	6.118	39.354	11.496	121.85
2nd	35.304	62.223	136.29	17.591	170.465	198.620	169.803	790.30
Multiple	101.645	63.307	70.573	14.221	18.828	30.752	38.005	337.33
$\sum\sum$	147.157	129.020	247.097	42.771	195.411	268.726	219.294	1249.48
	Description by the ***ch*** function							
1st	6.299	3.153	76.849	13.041	9.213	22.865	4.992	136.41
2nd	31.151	50.542	63.660	32.277	136.013	147.475	150.124	611.24
Multiple	95.186	38.688	64.369	18.055	12.628	24.568	29.405	282.90
$\sum\sum$	132.636	92.383	204.878	63.373	157.854	194.908	184.521	1030.55

$$Q = \int_0^{x_{max}} ch(A + Bx + Cx^2)\mathrm{dx}, \tag{1.40}$$

and the values listed in Table 1.43. The limit of integration x_{max} was used like in formula (1.38).

The flow rate $\tilde{Q}$ was also described by the parabolic function given in formula (1.39) and parameters $\tilde{A}_2 = 110.18, \tilde{B}_2 = -0.076199, \tilde{C}_2 = 0.024345$ were determined by the least squares method using the values listed in Table 43. On the basis of the values of parameters $\tilde{A}_2, \tilde{B}_2, \tilde{C}_2$, the values of the flow rate $\tilde{Q}$ were calculated and used to determine the sums of the squares of the differences of velocities that are also listed in Table 1.43.

Table 1.43. Values of the flow rate (integrated)

Level H [cm]	x_n [cm]	Q [cm^2/s]		Sums of the squares of differences $\Sigma(Q_{\text{emp}} - \bar{Q})^2$	
		Gaussian description	Description by the ***ch*** function	Gaussian description (x 10^{-2})	Description by the ***ch*** function (x 10^{-2})
5	6	10.51	10.565	25.6036	22.6576
10	8	11.116	11.120	0.0064	0.4356
20	10	12.655	12.859	94.4784	103.8361
30	14	13.007	13.229	5.2441	6.1504
40	16	14.06	14.301	11.0889	9.4864
50	21	15.363	15.467	135.7225	158.0049
60	24	19.979	20.165	63.2025	302.4121
			∑∑	335.3464	602.9831

In both solutions the parameters $\tilde{A}_i, \tilde{B}_i, \tilde{C}_i$ for i=1, 2, were introduced into the analysis after the 1st regression, from Table 1.36 and 1.39, respectively. The best description of the flow rate was obtained by the Gaussian function, because the sum of the sums of the differences of velocities given in Table 1.43 is lower than in the case of the description made by the ***ch*** function.

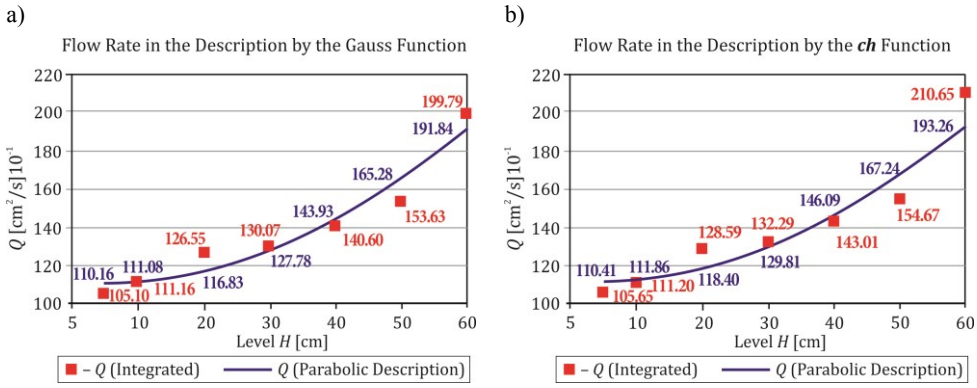

Figure 1.78. Comparison of the flow rate calculated by: a) the function of the Gaussian type, b) the ***ch*** function, [201].

In two cases the calculated values of the flow rate Q [cm^2/s] are almost similar, both in the empiric description (by parabolic function) and by integrated values by formulas 1.38 and 1.39, respectively. In the region between the level H=5 cm and the level H=10 cm where the flow channel is the narrowest (cf. Figure 1.72), the increase of the flow rate reaches approximately the similar values. From this level the increase of the flow rate is rapid. From level H=20 cm up and higher the increase of the flow rate is not constant. As a result of differentiating formula 1.39 we obtain the linear increment of the velocity of the flow rate at different levels. The difference of the flow rate reaches 0.352 cm^2/s between levels H=20 cm and H=30 cm and 1.053 cm^2/s between levels H=30 cm and H=40 cm, respectively. But higher than H=40 cm the flow rate increases more rapidly because the flow channel widens thus more material flows into it and the velocity is higher. The increase of the flow rate between level H=40 cm and H=50 cm is again lower 1.303 cm^2/s and between level H=50 cm and H=60 cm is already 4.616 cm^2/s. The flow channel at level H=50 cm is so wide that the flow rate reached more than 15.0 cm^2/s.

"Main content of this chapter has been published in Powder Technology, 198, 381-394, 2010".

1.3.4.6. Empirical description of the flax seed flow in the model with smooth walls. Discharge from the left

In this section we discuss another empirical description of eccentric flow with filling and discharge located near the left wall. Figure 1.79 presents velocity distributions and Figure 1.80 velocity profiles that were used to statistical analysis. The readings taken from velocity profiles (cf. Fig. 1.80) are given in Tables 1–7 in Appendix 4.

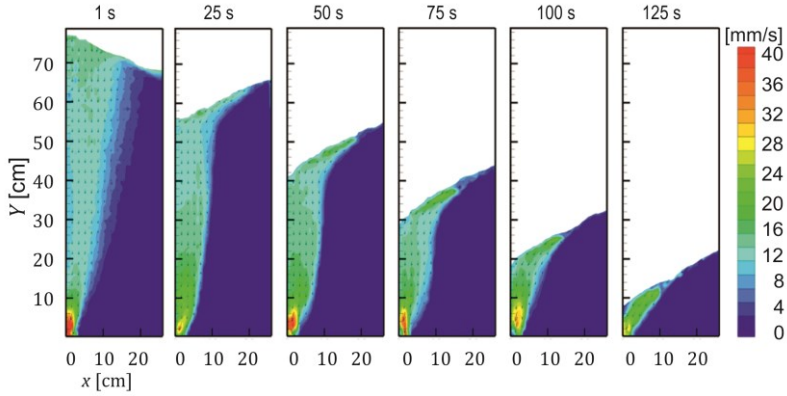

Figure 1.79. Velocity distributions in the flowing flax seeds in the model, [202].

Also the statistical analysis of the experimental results was done.

Applying the values given in Tables 1–7 (Appendix 4) the confidence intervals were determined for the analysed levels for the averages of velocities, [135] and listed in Tables 8–13 in Appendix 4. Calculating the values to Tables 8–13 (Appendix 4) the time was not taken into account. In this analysis, there are no readings that were removed from the data set.

Velocity distributions at analysed levels (H=5, 10, 20, 30, 40 and 50 cm) are made on the basis of the values of average velocities given in Tables 8–13 in Appendix 4. For level H=60 cm velocity distribution was made using the experimental readings listed in Table 7 in Appendix 4.

On the basis of velocity profiles presented in Figure 1.80 and the data listed in Tables 1–7 (Appendix 4), an inconsiderable dependence of the velocity on time and on the height of the measurement points has been found, especially for time 1 s and the height H=5 cm above the bottom of the model. In the further analysis, the average values of velocities calculated both for the given levels and for the distances

from the symmetry axis have been applied. The data presented in Tables 8–13 (Appendix 4) confirmed the independence of the analysed velocities on time. In fact, we can find the measurement points, located i.e. at x=7 cm and x=8 cm and levels H=30, 40 and 50 cm where velocities are similar and they can be described by one curve or the parameters of the curves should be similar.

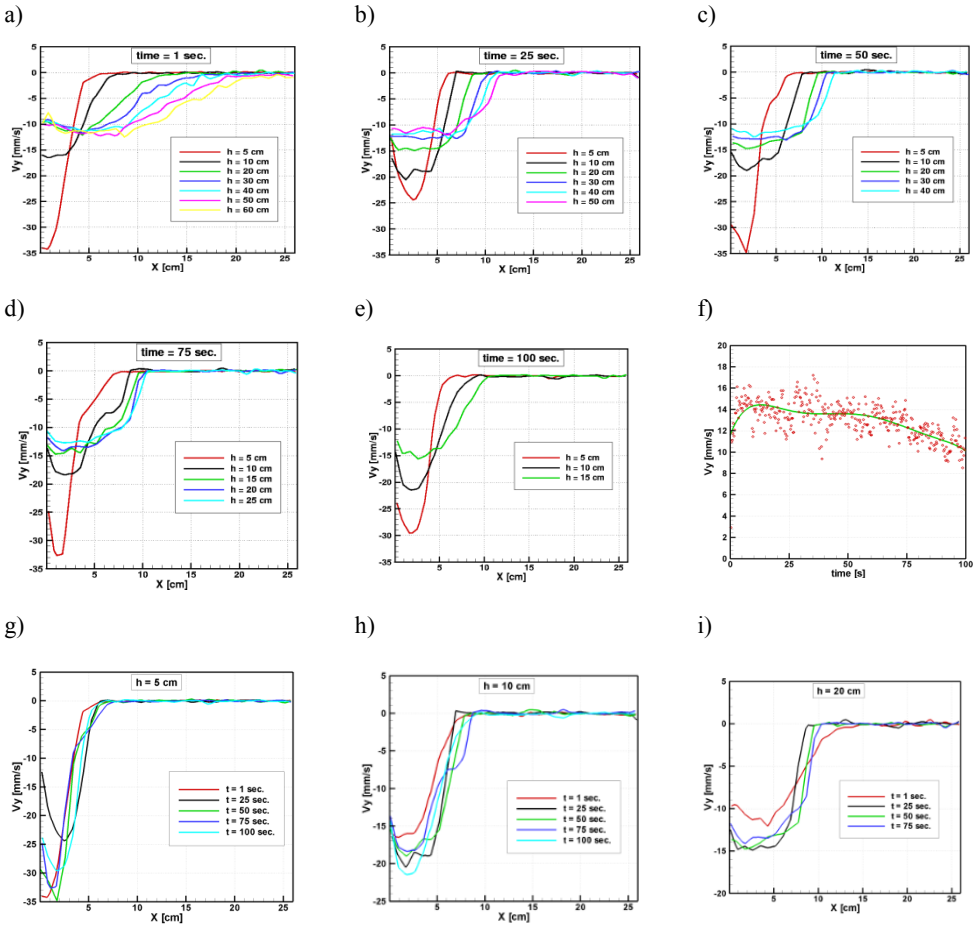

Figure 1.80. a–e) Velocity profiles of flax seed flow at various time instants, f) velocity distribution in time; g–i) velocity distribution on the analysed levels, [202].

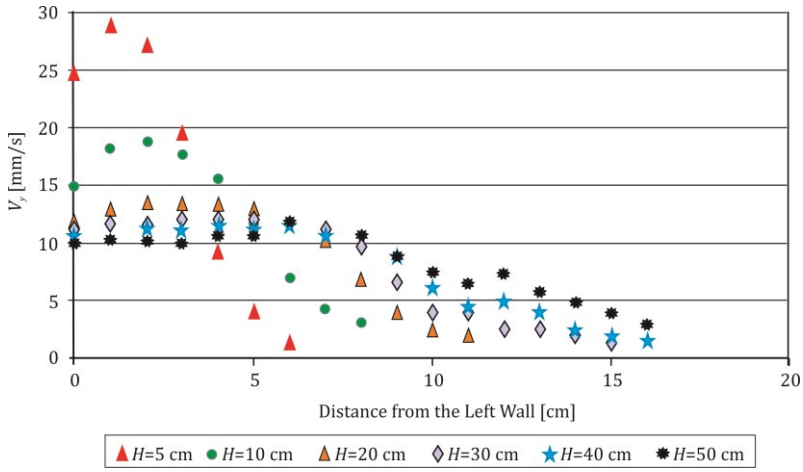

Figure 1.81. Average velocities at various analysed levels in the model.

1.3.4.6.1. Description of velocities by the exponential function (modified, the Gaussian type)

In the analysis presented below we depend V_y on the distance x and for various heights z (or levels marked with H). Empirical description of vertical velocity V_y calculated in the units of millimetres per second was proposed according to the function:

$$V_y = Ae^{Bx+Cx^2}, \tag{1.41}$$

where parameters A, B and C were determined by the least squares method (*the first regression*) and listed in Table 1.44.

Table 1.44. Values of the symbols given in formula (1.41), (*1st regression*)

Level H [cm]	A	B	C
5	25.381	0.2623	- 0.1239
10	15.690	0.1873	- 0.04985
20	11.078	0.1943	- 0.03269
30	11. 577	0.06821	- 0.01433
40	10.157	0.09630	- 0.01359
50	9.412	0.09173	- 0.01022
60	8.719	0.1087	- 0.009013

Distributions of parameters *A, B* and *C* after the 1st regression are shown in Figure 1.82. The points denotes the values of the parameters and the solid lines the empirical description of the parameters at various analysed levels.

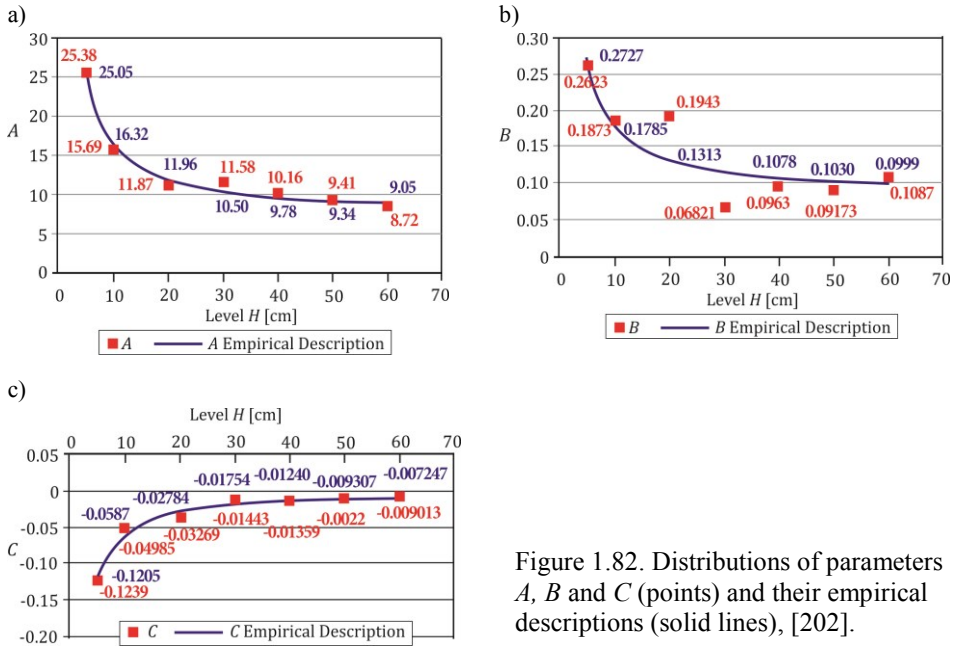

Figure 1.82. Distributions of parameters *A, B* and *C* (points) and their empirical descriptions (solid lines), [202].

In the further analysis, parameters *A, B* and *C* were depended on the height *z* in the model in the following form:

$$\hat{A} = A_0 + A_1/z$$
$$\hat{B} = B_0 + B_1/z \qquad (1.42)$$
$$\hat{C} = C_0 + C_1/z$$

and their values A_i, B_i, C_i for i=0,1 were determined by the least squares method (*the 2nd regression)* and listed in Table 1.45.

Velocity distributions were made on the basis of formulas (1.41), (1.42) and values listed in Tables 1.44 and 1.45. Figure 1.83 presents the average experimental results $\bar{V}_{yexp}$ and the empirical values $\hat{V}_{yemp}$ after the 1st regression (after depending the velocity on the distance from the symmetry axis *x* and after the 2nd regression $\hat{\hat{V}}_{yemp}$, depending the velocity both on the distance *x* and on the height *z*.

Table 1.45. Values of the symbols given in formula (1.42), (*2nd regression*)

Parameters	*i*=0	*i*=1	*R-coefficient of correlation*
A_i	7.596	87.267	0.9934
B_i	0.08419	0.9427	0.8823
C_i	0.003051	- 0.61786	- 0.9937

On the basis of the 1st and 2nd regression the description of vertical velocity was assumed in the form of the following function:

$$V_y = exp(a_o + a_1x_1 + a_2x_2 + a_3x_3 + a_4x_4 + a_5x_5), \tag{1.43}$$

where $x_1 = \frac{1}{z}$, $x_2 = x$, $x_3 = \frac{x}{z}$, $x_4 = x^2$, $x_5 = \frac{x^2}{z}$, and x denotes the distance from the left wall, z – is the due height in the model, measured in centimetres.

The coefficients a_i where i=0, 1…5 are calculated using the least squares method, and listed in Table 1.46. We define the calculations accurately using the multiple regression. There is a possibility to determine the parameters by the nonlinear regression as it was stated in the previous section, that would define the description more accurately, but it is a very time-consuming task.

Table 1.46. Values of coefficients a_i in formula (1.43)

a_0	a_1	a_2	a_3	a_4	a_5
2.2055	5.3965	0.0799	0.4510	- 0.000585	- 0.4743

On the basis of formula (1.43) and data listed in Table 1.46, the values of vertical velocity $\hat{\hat{\hat{V}}}_y$ were calculated using the multiple regression. Three approaches of describing the velocity in the model presented above are shown in Figure 1.83. The points denotes average values of experimental measurements and the solid lines represent the functional descriptions of velocity after the 1st $(\hat{V}_y)$, the 2nd $\left(\hat{\hat{V}}_y\right)$ and the multiple regression $\left(\hat{\hat{\hat{V}}}_y\right)$.

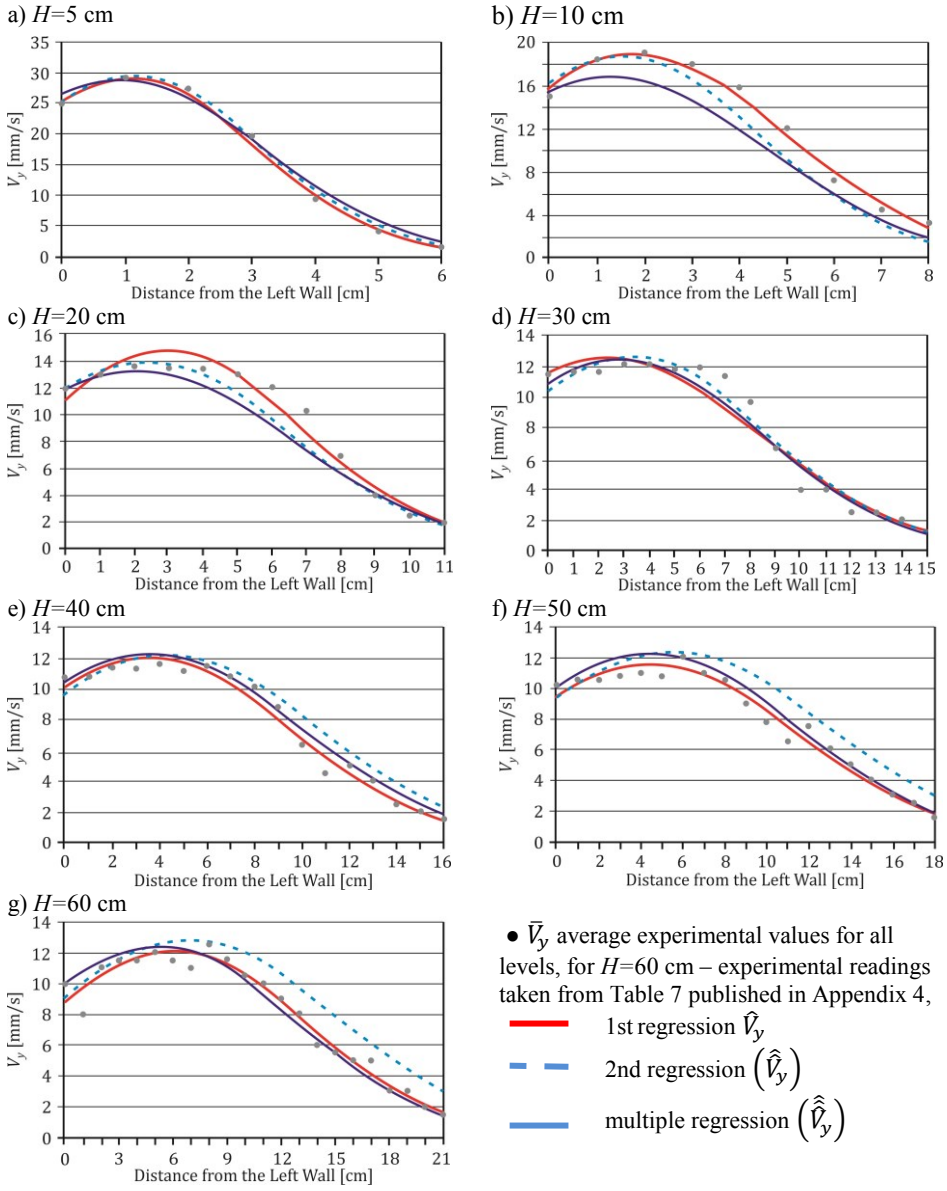

Figure 1.83. Velocity distributions: average experimental results compared with the 1st, the 2nd and the multiple regressions, [202].

1.3.4.6.2. Description of velocities by ***ch*** function

In our analysis we search the best description of velocities that were measured during experiments. Another description of velocity was proposed by the ***ch*** function in the following form:

$$V_y = ch(A + Bx + Cx^2). \tag{1.44}$$

Using the 1st regression the velocity was depended on the distance *x*. The parameters *A, B* and *C* were calculated by the least squares method and listed in Table 1.47.

Table 1.47. Parameters *A, B* and *C* from formula (1.44), the 1st regression

Level *H* [cm]	*A*	*B*	*C*
5	3.914	0.2935	- 0.1318
10	3.443	0.1913	- 0.05063
20	3.088	0.2028	- 0.03386
30	3.127	0.07823	- 0.01538
40	2.994	0.1055	- 0.01437
50	2.918	0.09999	- 0.01086
60	2.841	0.1159	- 0.009498

Using the 2nd regression according to formula (1.42) the velocity was depended both on the distance *x* measured from the left wall and on the height *z*. Parameters *A, B* and *C* were calculated by the least squares method and given in Table 1.48.

Table 1.48. Values of the symbols given in formula (1.42), (*2nd regression*)

Parameters	*i*=0	*i*=1	*R-coefficient of correlation*
A_i	2.83800	5.5240	0.9853
B_i	0.08839	1.0528	0.9094
C_i	3.55620	- 0.6546	- 0.9920

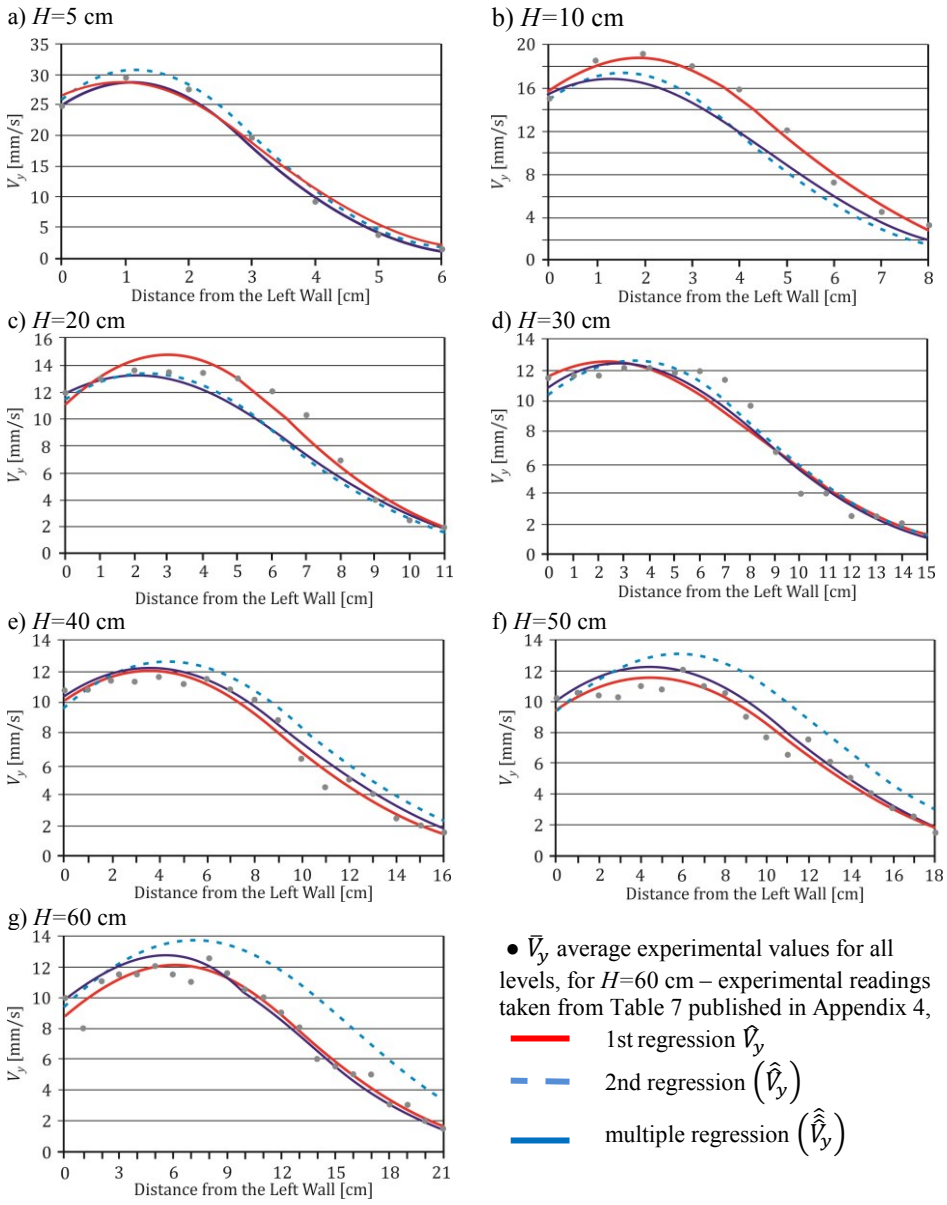

Figure 1.84. Vertical velocity descriptions by the three applied methods, [202].

On the basis of the 1st and 2nd regression we assumed the description of vertical velocity as a following function:

$$V_y = ch(a_o + a_1x_1 + a_2x_2 + a_3x_3 + a_4x_4 + a_5x_5). \quad (1.45)$$

The values of parameters a_i (where i=0, 1…5) were calculated using the least squares method and listed in Table 1.49. Variables x_1, x_2, x_3, x_4, x_5 are applied like in formula (1.43).

Table 1.49. Values of coefficients a_i in formula (1.45)

a_0	a_1	a_2	a_3	a_4	a_5
2.8743	5.5093	0.0903	0.4736	- 0.000817	- 0.4980

Applying all three approaches we present both the empirical description of vertical velocity by the ***ch*** function and the distributions of velocity in Figure 1.84.

1.3.4.6.3. Verification of accuracy of the applied descriptions

We also verified accuracy of the applied descriptions. In Table 1.50, the sums of the squares of the differences of velocities in three applied approaches by the Gaussian description and by the ***ch*** function are listed.

The 1st and the multiple regressions in both descriptions of velocities (by the function of the Gaussian type and by the ***ch*** function) provide the similar results that indicate the right choice of the functions. The 2nd regression gives better agreement to the experimental results by the Gaussian description, but the regression was only applied to determine the type of the function. In fact, we search the multiple regression. If we calculated the 1st and the multiple regressions we would see that both descriptions of velocities are almost similar. This fact can be analysed in Figures 1.83 and 1.84 comparing the proper curves.

Table 1.50. Sums of the squares of the differences of velocities

Regression	Sums of the squares of the differences of velocities measured at the analysed levels $\sum(V_{emp} - \bar{V}_{exp})^2$							
	5 cm	10 cm	20 cm	30 cm	40 cm	50 cm	60 cm	$\sum\sum(V_{emp} - \bar{V}_{exp})^2$
	Gaussian description							
1st	4.128	2.790	8.132	14.195	5.423	6.250	8.962	49.88
2nd	4.002	26.504	16.378	10.058	20.533	40.901	50.936	169.31
Multiple	16.001	49.529	24.520	11.554	7.969	12.557	15.311	137.44
$\sum\sum$	24.131	78.823	49.030	35.807	33.925	59.708	75.209	356.63
	Description by the ***ch*** function							
1st	2.431	2.737	8.843	12.875	5.503	6.780	9.280	48.45
2nd	8.717	51.069	24.526	9.920	28.413	72.162	108.568	303.37
Multiple	13.218	50.413	24.037	10.691	8.857	15.478	15.303	138.00
$\sum\sum$	24.366	104.219	57.406	33.486	42.773	94.420	133.151	489.82

1.3.4.6.4. Flow rate

The flow rate Q was calculated for two presented descriptions of velocities. In the solution given by the Gaussian exponential function, the flow rate was calculated according to the following formula:

$$Q = \int_0^{x_{max}} e^{Bx+Cx^2}\mathrm{dx}, \tag{1.46}$$

and the values are listed in Table 1.51. In formulae (1.46) and (1.47), the limit of integration x_{max} denotes the number and position of the last measurement point calculated from the left wall taken from the experimental readings for various analysed levels, (cf. Tables 1–7 in Appendix 4). The flow rate was described by the following parabolic function:

$$\tilde{Q} = \tilde{A}_1 + \tilde{B}_1 z + \tilde{C}_1 z^2, \tag{1.47}$$

where parameters $\tilde{A}_1 = 104.03, \tilde{B}_1 = -0.2808, \tilde{C}_1 = 0.0233$ were calculated by the least squares method using the values listed in Table 1.51. Using the parameters $\tilde{A}_1, \tilde{B}_1, \tilde{C}_1$, the values of the flow rate $\tilde{Q}$ were determined and these values were used to calculate the sums of the squares of the differences of velocities that are listed in Table 1.51.

In the description of velocities by the ***ch*** function, the flow rate was obtained by calculating the following integral:

$$Q = \int_0^{x_{max}} ch(A + Bx + Cx^2)dx, \tag{1.48}$$

and the values listed in Table 1.51. The limit of integration x_{max} was used like in formula (1.46).

The flow rate $\tilde{Q}$ was also described by the parabolic function:

$$\tilde{Q} = \tilde{A}_2 + \tilde{B}_2 z + \tilde{C}_2 z^2, \tag{1.49}$$

where parameters $\tilde{A}_2 = 104.39, \tilde{B}_2 = -0.2902, \tilde{C}_2 = 0.02346$ were determined by the least squares method using the values listed in Table 1.51. Using the parameters $\tilde{A}_2, \tilde{B}_2, \tilde{C}_2$, the values of the flow rate $\tilde{Q}$ were calculated and used to determine the sums of the squares of the differences of velocities that are also listed in Table 1.51.

Table 1.51.Values of the flow rate (integrated)

Level H [cm]	x_{max} [cm]	Q [cm^2/s]			Sums of the squares of the differences $\Sigma(Q_{emp} - \tilde{Q})^2 \times 10^{-2}$		
		Gaussian description	Description by the ***ch*** function	Joined functions	Gaussian description	Description by the ***ch*** function	Joined functions
5	6	10.190	10.247	10.268	1.7161	1.1236	2.2500
10	8	10.349	10.356	10.460	0.0036	0.0784	0.0441
20	11	10.962	10.967	10.959	3.5721	2.8900	1.7689
30	15	11.901	11.918	12.016	5.9049	5.6644	11.6281
40	16	12.829	12.880	12.819	3.2041	2.3104	2.6896
50	18	14.450	14.480	14.254	14.0625	13.9129	24.9001
60	21	17.366	17.392	17.303	6.7600	6.2001	10.2400
				∑∑	35.2233	32.1798	53.5208

In both solutions the parameters $\tilde{A}_i, \tilde{B}_i, \tilde{C}_i$, for i=1, 2, were introduced into the analysis after the 1st regression, from Table 1.44 and 1.47, respectively.

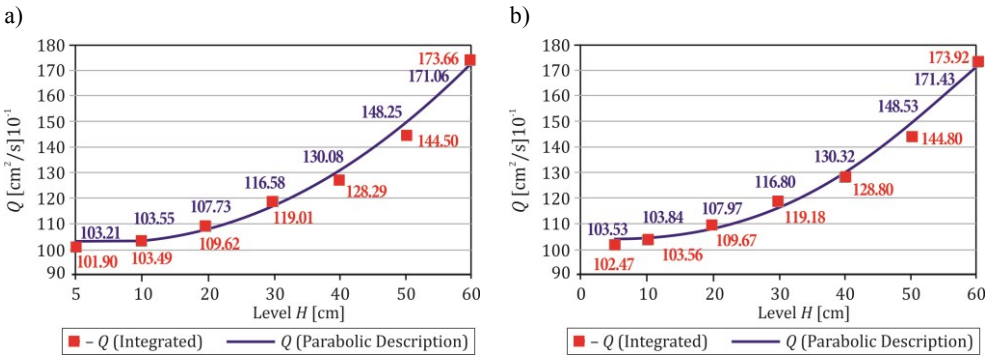

Figure 1.85. Comparison of the flow rate calculated by: a) the function of the Gaussian type, b) the ***ch*** function, [202].

In two cases, the calculated values of the flow rate Q [cm^2/s] are almost similar, both in the empiric description by the parabolic function and as integrated values. It is noticeable that in the region between the level H=5 cm and the level H=10 cm the increase of the flow rate reaches approximately the similar values. From level H=20 cm and higher the increase of the flow rate is not constant. As a result of differentiating formula (1.47) we obtain the linear relation of the increment velocity of the flow rate of different velocities at different levels. The difference of the flow

rate reaches 0.939 cm^2/s between levels H=20 cm and H=30 cm and 0.928 cm^2/s between levels H=30 cm and H=40 cm, respectively. But higher than H=40 cm the flow rate increases rapidly because the flow channel widens and more material flows into it. The increase between level H=40 cm and H=50 cm is already 1.621 cm^2/s and between level H=50 cm and H=60 cm reaches 2.916 cm^2/s. Here we analysed the integrated values in the description by the Gaussian function. The similar situation occurs in the calculations of the flow rate in the description by the ***ch*** function.

1.3.4.6.5. Empirical description of velocities using "the joined functions"

Analysing the results of the description of velocities in the previous section especially the 1st regression presented in Figures 1.83 and 1.84, we notice that good agreement to the average experimental results is given both by the function of the Gaussian type as well as by the ***ch*** function.

Because of the specific nature of the flow in the asymmetric configuration we discuss here another description of velocities by functions of the same type but with various parameters in two different regions. One part of the velocity profile curve is described by one function and the other part by another function.

In the analysis, we divide the set x into two subsets: the first with $x \in < 0, x_{\frac{n}{2}} >$ for even points and $x \in < 0, x_{\frac{n+1}{2}} >$ for odd points and the second subset with $x \in < x_{\frac{n}{2}}, x_n >$ for even points and $x \in < x_{\frac{n+1}{2}}, x_n >$ for odd points. Figures 1.86 and 1.87 present the area limited by any velocity profile and the coordinate system with functions ascribed to the due parts of the curves.

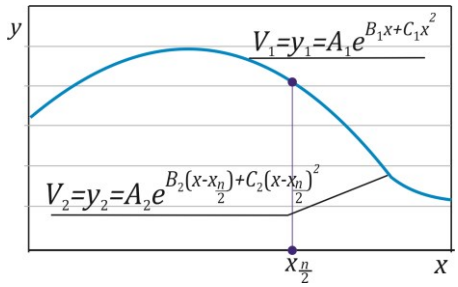

Figure 1.86. Velocity profile and its description by two functions, for even points, [202].

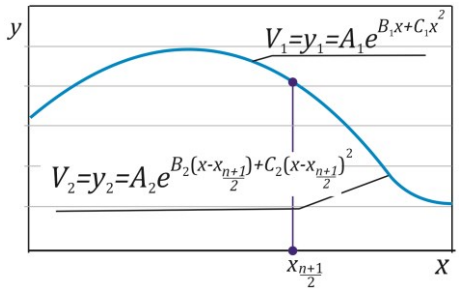

Figure 1.87. Velocity profile and its description by two functions, for odd points, [202].

The first part of the velocity profile is described by the following function:

$$\hat{V}_{y_1} = y_1 = A_1 e^{B_1 x + C_1 x^2}, \tag{1.50}$$

and the other part of the curve by the function:

$$\hat{V}_{y_2} = y_2 = A_2 e^{B_2\left(x - x_{\frac{n}{2}}\right) + C_2\left(x - x_{\frac{n}{2}}\right)^2}, \tag{1.51}$$

if the number of measurement points n is even.

In the case if the number of measurement points is odd then the velocity profile is described by function (1.50) and the following function in the due parts:

$$\hat{V}_{y_2} = y_2 = A_2 e^{B_2\left(x - x_{\frac{n+1}{2}}\right) + C_2\left(x - x_{\frac{n+1}{2}}\right)^2}, \tag{1.52}$$

where $A_2 = \hat{y}_1\left(x_{\frac{n}{2}}\right)$ for even points and $A_2 = \hat{y}_1\left(x_{\frac{n+1}{2}}\right)$ for odd points. Parameters A_1, B_1, C_1 and B_2, C_2 were determined by the least squares method. In Figure 1.88 vertical velocity descriptions by "the joined functions" are presented.

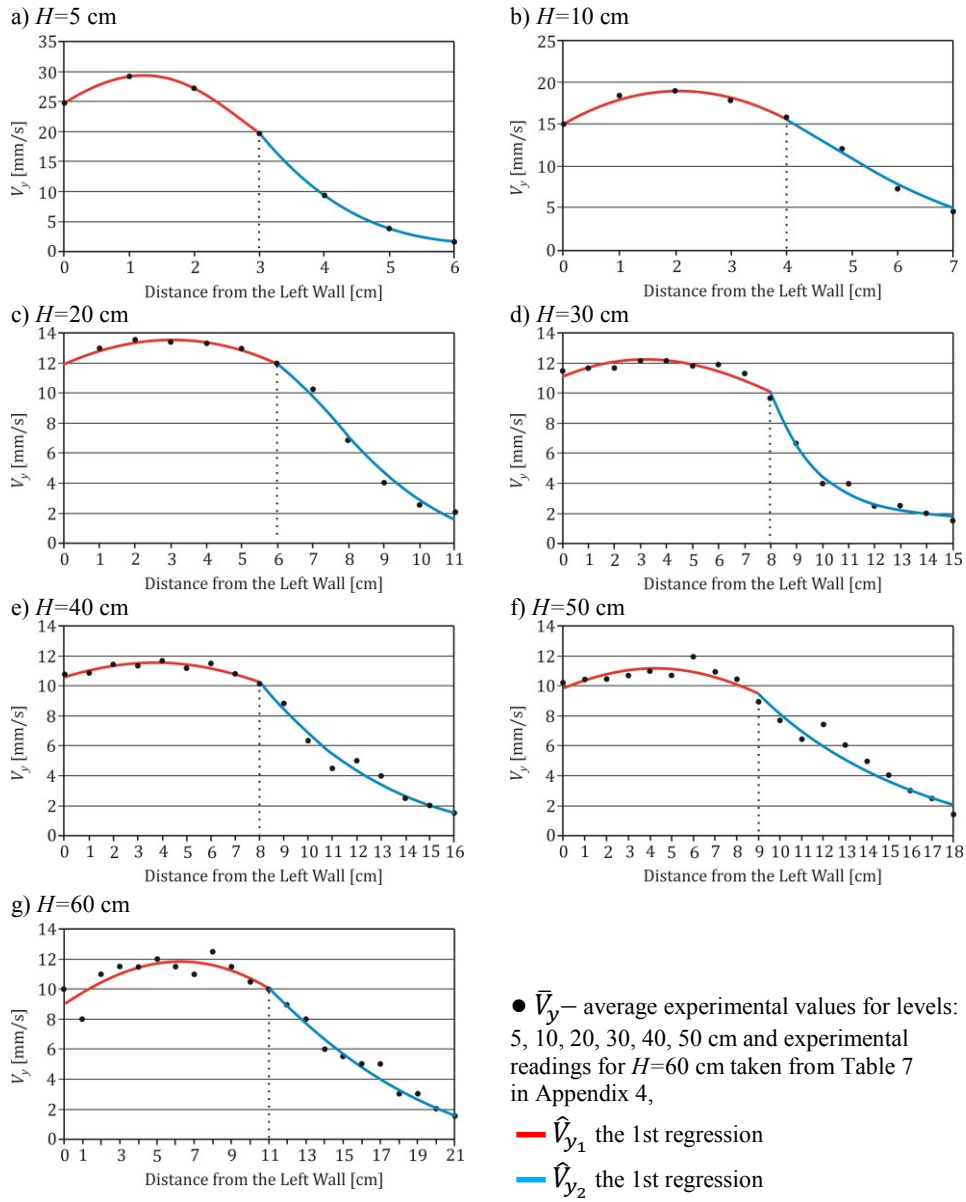

Figure 1.88. Vertical velocity descriptions by "the joined functions", [202].

1.3.4.6.6. Verification of accuracy of the solution by "the joined functions"

Accuracy of the applied method was investigated by calculating the sums of the squares of differences of velocities. The results from Table 1.52 can be compared with data given in Table 1.50. The description made by "the joined functions" gives the least sum of the squares of the differences of velocities. But we can state that in such specific flow there are no method to describe velocities in an accurate way both at all analysed levels and at all measurement points. Thus if the description of velocities is due at lower levels then it does not describe velocities accurate at higher levels. And vice versa.

Table 1.52. Sums of the squares of the differences of velocities

Description method	Sums of the squares of the differences of velocities measured at the analyzed levels $\Sigma(\hat{V}_{y_i} - \bar{V}_{y\,exp})^2$ (i=1, 2)							
	5 cm	10 cm	20 cm	30 cm	40 cm	50 cm	60 cm	$\Sigma\Sigma(\hat{V}_{y_i} - \bar{V}_{y\,exp})^2$
"Joined functions"	0.0117	1.3702	1.2453	1.8206	2.4789	6.6774	8.3527	21.96

1.3.4.6.7. Flow rate calculated by "the joined functions"

In the description of velocities the flow rate Q was calculated as integrals both for even and for odd points:

– for even points:

$$Q = \int_0^{x_{\frac{n}{2}}} \hat{V}_{y_1}\,\mathrm{d}x + \int_{x_{\frac{n}{2}}}^{x_n} \hat{V}_{y_2}\,\mathrm{d}x, \tag{1.53}$$

– and for odd points

$$Q = \int_0^{x_{\frac{n+1}{2}}} \hat{V}_{y_1}\,\mathrm{d}x + \int_{x_{\frac{n+1}{2}}}^{x_n} \hat{V}_{y_2}\,\mathrm{d}x,$$

where: n denotes the abscissa x at which the given functions join to each other and x_{max} is the last measurement point for velocity profiles. The flow rate was described by the parabolic function according to formula (1.47). Parameters $\tilde{A} = 105.12, \tilde{B} = -0.3033$ and $\tilde{C} = 0.02303$ were calculated by the least squares method. The values of the flow rate Q [cm^2/s] are listed in Table 1.51.

Figure 1.89 presents the graphical distribution of the flow rate. It is noticeable that in the region between level H=5 cm and H=10 cm again the flow increment is 0.192 cm^2/s and between H=10 cm and H=20 cm already reaches 0.499 cm^2/s, respectively. From level H=20 cm and higher the increase of the flow rate is not constant and increases rapidly. The linear increment of velocity of the flow rate at different levels can be obtained as a result of differentiating formula 1.47. The difference of the flow rate reaches 1.057 cm^2/s between levels H=20 cm and H=30 cm and 0.803 cm^2/s between levels H=30 cm and H=40 cm, respectively. But higher than H=40 cm the flow rate increases rapidly. The increase between level H=40 cm and H=50 cm is already 1.435 cm^2/s and between level H=50 cm and H=60 cm reaches 3.049 cm^2/s, respectively.

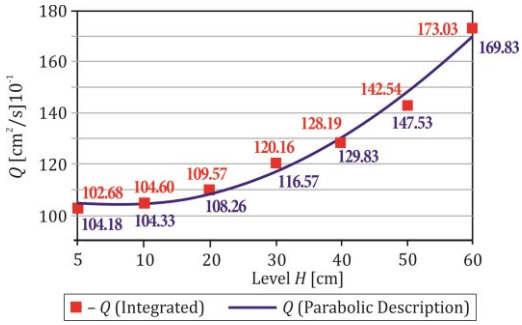

Figure 1.89. Flow rate calculated by "the joined functions", [202].

The values of the flow rate calculated by "the joined functions" approximate the values calculated by the methods presented in section 1.3.4.6.4. As a conclusion of the analysis we can state that there are levels at which more accurate descriptions have been found and levels with not so good descriptions. General the all applied methods provide almost the same values.

"Main content of this chapter has been published in Powder Technology, 212, 38-56, 2011".

1.3.4.6.8. Conclusions

The effect of the two filling-discharge locations was discussed in section 1.3.4.5 and 1.3.4.6. The total time of flow for the flax-seeds was found to be 123 s in the case presented in section 1.3.4.5 and 146 s in the case shown in section 3.4.6. Another eccentric flow mode we investigate in section 1.3.4.7 when the outlet is located in the centre of the bottom. In this case, the total time flow was 142 s.

Presented empirical descriptions provided theoretical analysis of velocities in eccentric flow. We found that all applied methods appear approximately due to describe velocities in such complex flow.

1.3.4.7. Eccentric filling. Discharge in the centre of the bottom

The third discussed case was also with eccentric filling but the position of the outlet was symmetrical located as shown in Figure 1.90. This location of the outlet produces a very interesting flow mode of the material, becoming symmetrical very quickly after opening the outlet. Despite eccentric feeding, just after 25th s of the flow, the material tends to form a symmetric flow. Soon after the initiation it is possible to observe nearly uniform flow channel for the entire height of the silo. In the plug flow region, the velocity vectors in the initial phase of flow are still not vertical but soon they pass directly and vertically to the outlet. In the upper part of the flow, the velocity vectors indicate converging lateral flow towards the flowing zone. It seems that the central outlet induced the formation of the central plug flow.

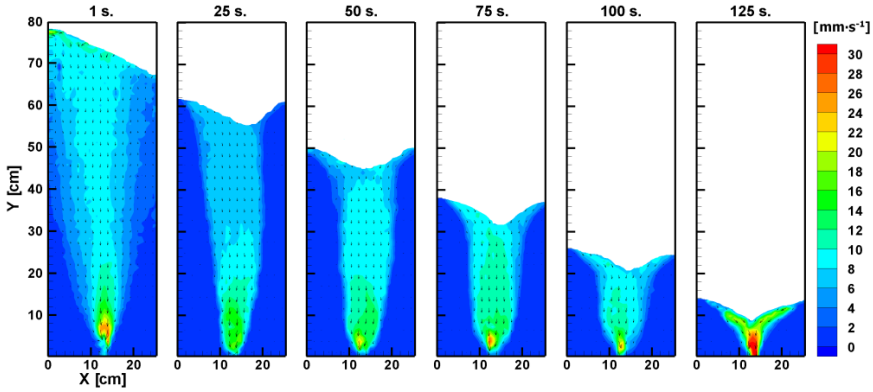

Figure 1. 90. Velocity distributions in the model with smooth walls. Eccentric filling on the left. Discharge in the centre, [34].

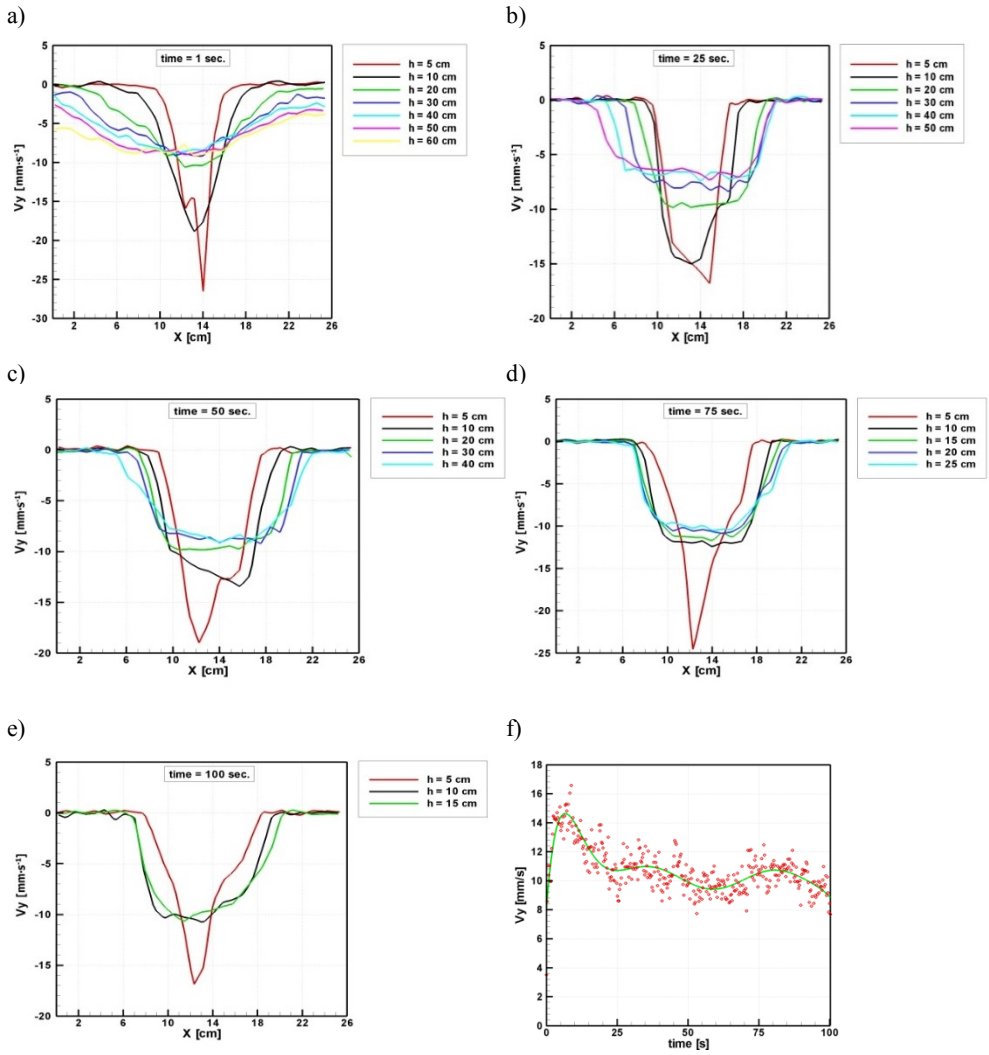

Figure 1.91a-e) Velocity profiles for the flow of flax-seeds obtained for a) eccentric filling on the left and discharge in the central part of the bottom; f) variation of velocity, distribution in time, [34].

The technique DPIV provides wide possibilities to obtain various data on the flow. We also present velocity distributions on the various levels in the model, (cf. Figure 1.92).

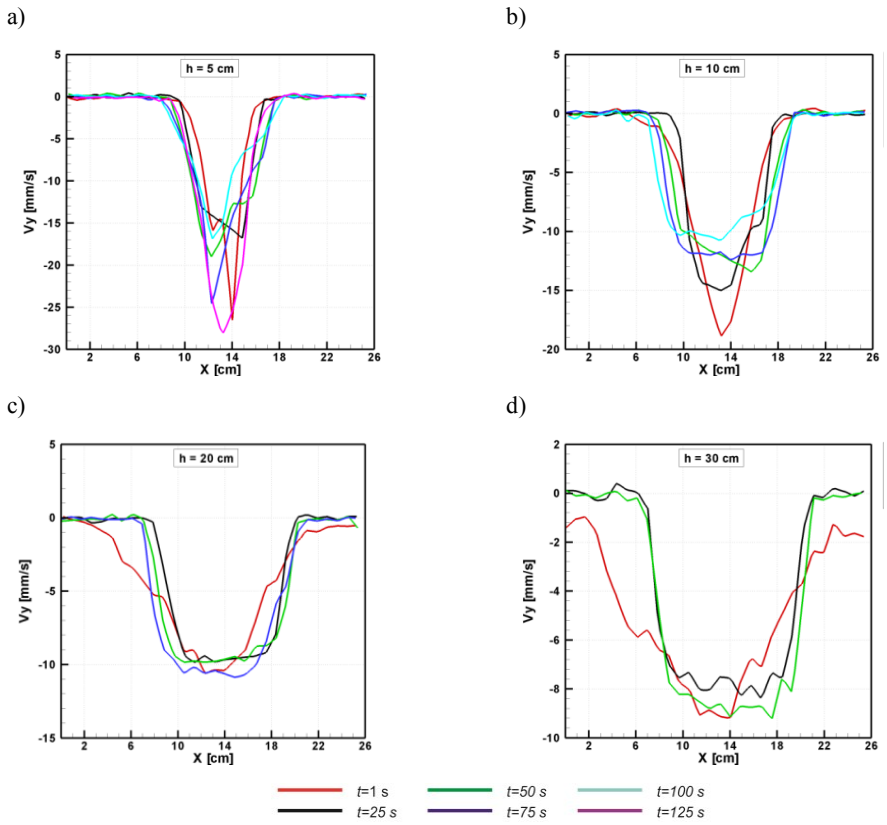

Figure 1.92. Velocity profiles obtained at analyzed levels in the model, [34].

The profiles of the vertical velocity components across the cavity are obtained at different heights (indicated in the legend, Figure 1.92) and at time steps of 1 s, 25 s, 50 s, 75 s, 100 s and 125 s after the beginning of the experiment. In Figure 1.92a, at H=5 cm above the outlet (the red line) one can observe the shape of the velocity profile. This profile is a special one because in each case discussed in the thesis it behaves individually especially at the beginning of the flow. The other profiles form a bunch of functions on the due levels. In the case of central discharge, this velocity profile reaches its maximum value in the flowing zone and becomes symmetric. It means that the central position of the outlet makes the flow symmetric soon after the flow starts. The filling feed does not play a significant role.

1.3.4.8. Stagnant zone boundary measurements in the model with smooth walls. Deformations in the material

Unfortunately there are only a few studies on eccentric flow zone boundaries in the literature, so it seems to be worth-while to undertake this challenge and try to investigate flow evolution in this complex case. Two eccentric cases were discussed in detail. Their empirical descriptions were also provided in the analyses. The third case with central location of the outlet was not discussed in detail because the velocity profiles obtained by the DPIV technique showed the symmetrical tendency of the flow. Here we present the stagnant zone boundaries (cf. Figure 1.93) depicted at various time instants. Figure 1.93 presents evolution in time of the stagnant zone boundaries for three discussed cases.

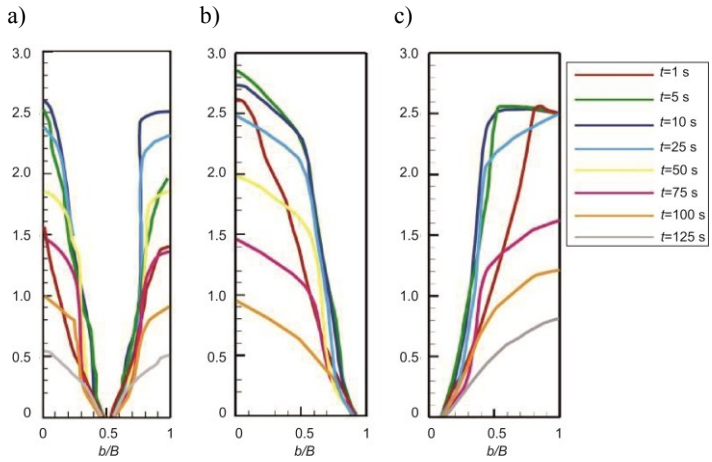

Figure 1.93. Experi-mental measurements of the stagnant zone boundaries in the flowing flax seeds in the case of eccentric filling and discharge a) central, b) on the right, c) on the left, [34].

The DPIV technique provided data on the velocity field in the whole analysed area. It is possible to obtain such data for each pixel of a single image, i.e. for each point of the analysed flow. Having the dense velocity vector field, one may evaluate velocity gradients and calculate strains in the flowing material. The strain tensor is calculated in terms of partial derivatives $^{\mathrm{du}}/_{\mathrm{dx}}$, where u denotes a velocity component and x a coordinate. Measuring the displacement field $\mathrm{u_i}(x, y)$, the strain component is calculated, namely the Green strain tensor:

$$\varepsilon_{ij} = \frac{1}{2}\left(\frac{\partial u_i}{\partial \mathrm{x}_j} + \frac{\partial u_j}{\partial \mathrm{x}_i} + \frac{\partial u_k}{\partial \mathrm{x}_i}\frac{\partial u_k}{\partial \mathrm{x}_i}\right). \tag{1.54}$$

Figures 1.94–1.96 show evaluated deformation profiles of the flax seeds recorded after the first second, 50th s and 100th s of the flow. The flow took place in the model with smooth walls and the feeding was performed eccentrically at the left side. The legend (blue, red and green lines) relates to the three investigated configurations: discharge on the left side, in the centre and on the right side. For the presented time steps there are no significant disturbances of the deformation profiles obtained close to the bottom (cf. Figures 1.94a, 1.95a and 1.96a). At the higher locations, i.e. at 30 and 50 cm above the outlet (cf. Figure 1.94 b, c) we can well recognize the location of the shear zones in the flowing material in the three analysed modes of the flow, whereas, the flow runs rather quietly in the first second of the flow at the height of 5 cm above the outlet. In [198, 199, 200], the authors published interesting results on modelling of shear localisations in granular bodies.

a) time=1 s, *h*=5 cm

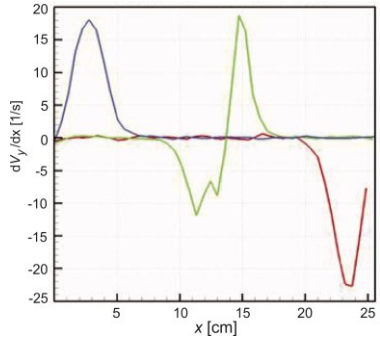

b) time=1 s, *h*=30 cm

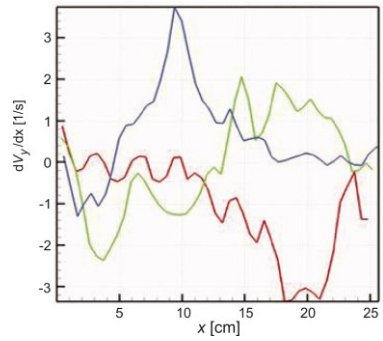

c) time=1 s, *h*=50 cm

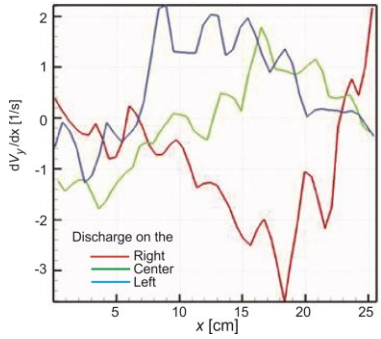

Figure 1.94. Deformation profiles evaluated for the flowing flax seeds in the case of eccentric filling for three discharge locations (cf. the legend), and observed for the initial flow time (1st s) at three levels: a) 5 cm, b) 30 cm, c) 50 cm above the bottom of the model, [34].

a) time=50 s, *h*=5 cm

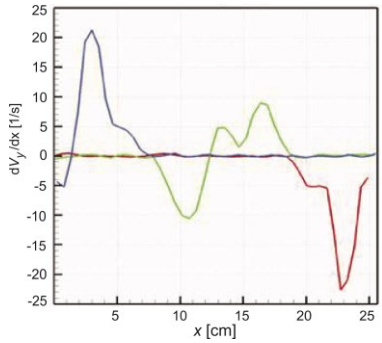

b) time=50 s, *h*=20 cm

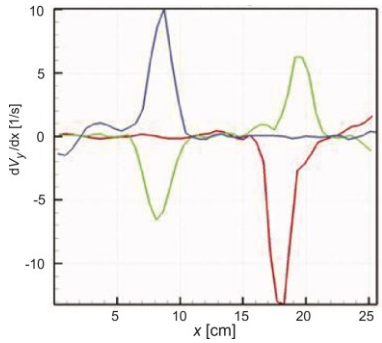

c) time=50 s, h=40 cm

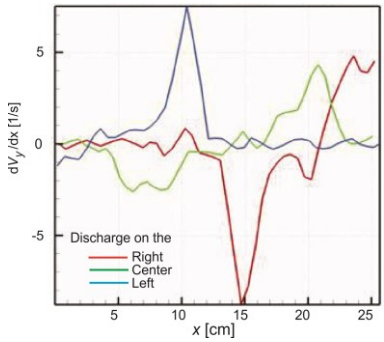

Figure 1.95. Deformation profiles evaluated for the flowing flax seeds in eccentric filling for three discharge locations (cf. the legend), and observed after 50th s of the flow at three levels: a) 5 cm, b) 20 cm, c) 40 cm above the bottom, [34].

a) time=100 s, *h*=5 cm

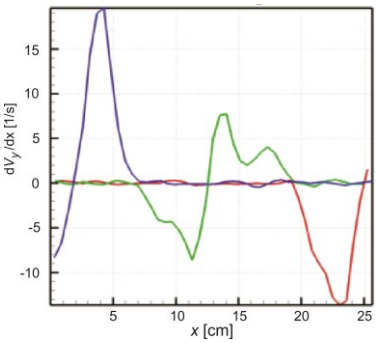

b) time=100 s, *h*=10 cm

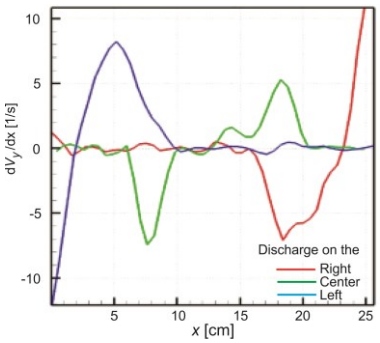

Figure 1.96. Deformation profiles evaluated for the flowing flax seeds in the case of eccentric filling for three discharge locations (cf. the legend), and observed after 100th s at two levels: a) 5 cm, b) 10 cm above the bottom, [34].

In the advanced phase of the flow, further development of the stagnant and shear zones (cf. Figures 1.95 and 1.96) are identified and more clearly shown in Figures 1.97–1.99 where one can also see directions of deformations. The analysis provides real images of the flow in consecutive stages and variations of velocities.

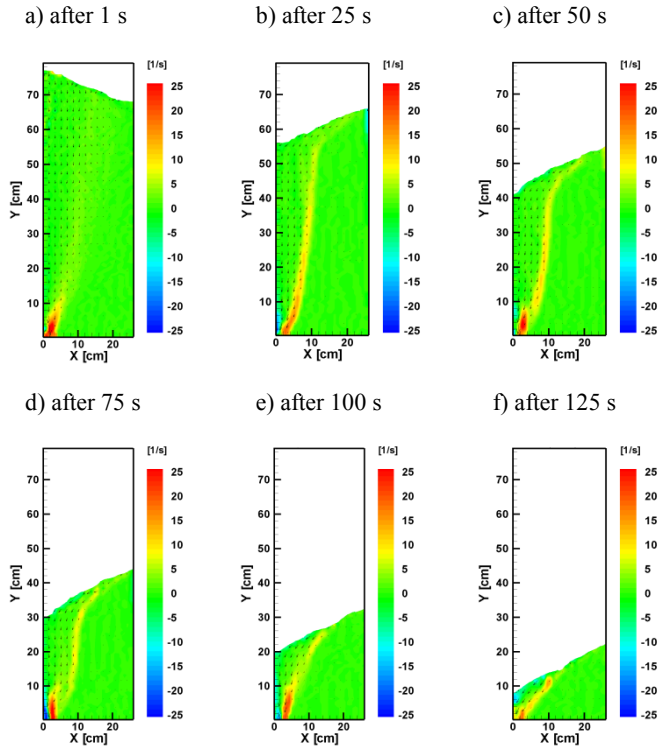

Figure 1.97. Deformations in the flowing material (discharge on the left), [34].

Three analysed eccentric flows are very complex, as it was investigated in previous sections, especially due to appearance of localisation of deformation between flowing and stationary solid, (cf. Figures 1.97–1.99). These narrow zones are of intense shearing. Our investigation was performed in the model with smooth walls thus the shear zones do not form close to the wall. They can also occur between the wall and the stagnant material but in the case when the wall is rough. Such investigation of flow in models with different wall roughness was made by [203, 204]. In [37], the authors mentioned a few significant factors on which the width of shear zone depends. Among others they are: "initial solid density, mean grain diameter of solid, wall roughness, pressure level, direction of deformation and flow

velocity". The authors in [37] referred to works of [33, 204, 205, 206, 207, 208, 209, 210]. In [211], the authors made finite deformation analysis of motion of granular materials in a silo. In this section the registered deformation fields in the flowing flax seeds in three plane models during eccentric flow and obtained directions of deformation provided valuable information on the mechanism of the granular behaviour inside the silo. The knowledge of the range of deformation fields is the reason to perform theoretical description of shear localisation in flow processes. And this can be presented in our future works.

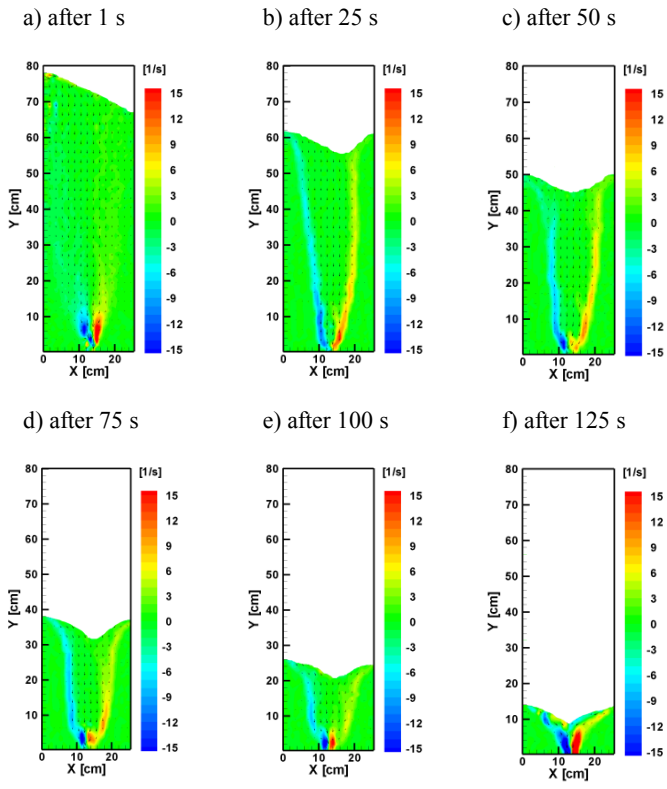

Figure 1.98. Deformations in the flowing material (discharge in the centre of the model), [34].

In Figures 1.97–1.99, the green fields denote regions of low similar deformations registered during the flow. There are also clearly visible blue and red bands between the flowing material and the stagnant zone. The highest deformations occurred in the case of discharge on the left, about 25 1/s, the lower 15 1/s during the central discharge and the lowest 10 1/s when the outlet was located close to the right wall.

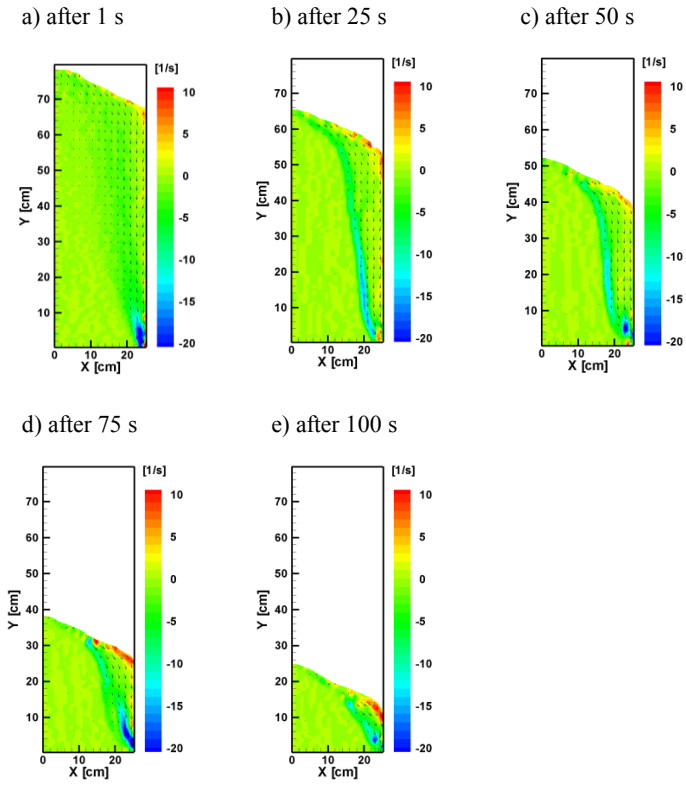

Figure 1.99. Deformations in the flowing material (discharge on the right), [34].

"Main content of this chapter has been published in Engineering Transactions, 53, 2, 195-227, 2005".

1.3.5. Final conclusions

In this Chapter the experiments on granular materials in various flat models and with different wall roughness have been presented. The great potential of the DPIV technique has made it possible to observe the flow in detail. The regions of the highest velocities were identified. They were found to be dangerous for the silo structure as they might cause silo vibrations and failure of the structure. The highest velocity appears just above the model bottom. At higher levels the velocities have almost identical values in the whole flowing stream. This observation is significant both for silo designers and for silo users. The flow modes determined during the experiments depend on different factors. Here the influence of wall roughness is investigated. After many cycles of filling and discharge the inner surface of the silo wall changes its roughness. The rougher the wall is, the higher possibility of the flow mode change occurs. Designed for funnel flow the silo structure cannot withstand another flow mode, and vice versa. The wall stresses will change their active and passive values as it was stated by [144] with the change of the flow mode.

We also presented the theoretical analysis of velocities and flow rates both in symmetric and asymmetric flow of amaranth and flax seeds in two models: with vertical and smooth walls and in the converging. Evaluation of kinematic parameter b was conducted and also verification of the radial flow departure in the converging model was performed. As a final conclusion we can state that the DPIV technique appeared a useful diagnostic tool in investigation of granular material flow. It provides quite new possibilities to analyse the flow field and obtain both quantitative and qualitative data on the flow. Unfortunately the method can be applied only for 2D structures. We can register the picture just through the transparent wall. It is not possible to track the flow inside the model. Silos are round structures and it would be useful to register the flow inside to recognise all phenomena. But nowdays researchers perform experiments only in flat models. In spite of this limiatation phenomena in flowing materials are well recognised and the results may be applied in practice.

2. Simulations of granular material flow by the Discrete Element Method

2.1. Discrete element method: a tool for investigation of the granular material flow processes in silos

2.1.1. Introduction

The flow of granular materials through an orifice has been extensively studied in recent decades due to the great interest for industrial applications. The phenomena related to compaction, dilation, and segregation, are particularly relevant to the granular material flow during the operation period of silo systems containing bins, hoppers, etc. A unified theory encompassing these phenomena has not been developed, while the well-known approaches are usually restricted, primarily due to the incomplete complex rheological description of granular media caused by the fluctuations in the bulk material properties during the material flow.

This Chapter presents a discrete element technique in the modelling of filling and discharge processes in the three-dimensional silo systems of various shapes.

The main focus of the Chapter is the investigation on the single particle properties contribution to the observable macro-phenomena in time dependent flow processes in a silo. The analysis defined is also devoted to a proper understanding of the granular material behaviour within the silo throughout the qualitative/quantitative predictions, indications and experimental measurements. It should also stress that the research presented may be useful for an ongoing development of DEM methodology in granular flow analysis.

2.1.2. Theoretical approaches to granular material simulations

Theoretical understanding of granular flow is largely empirical since the evaluation of the influence of individual particle micro-properties on the dynamic behaviour of the whole granular material is highly complicated. The existing theories of continuum mechanics or statistical physics have only limited applications for the description of granular media, and an unified theory encompassing all the granular phenomena is still missing, [212, 213].

The field of analytical modelling of stresses in a granular material stored in silo/hoppers has undergone significant theoretical development since the days of Janssen, when the best-known slice method for calculating the wall pressure after filling was introduced. Models relying on the linear elastic Hooke's law as well as the perfectly plastic relations with the Coulomb yield condition and the associated or non-associated flow rules (or those based on the assumption of density hardening with the varying cohesion dependent on the material density) can be found in literature, e.g. [128, 214, 215]. Analytical models for the evaluation of filling and, especially, discharge states of the elastic and elastic-plastic matter is presented by among others in [158, 216] or [217].

To simulate the computational treatments of the granular flow based on the continuum approach are largely demonstrated in literature by the application of the method of characteristics by e.g. [218, 219]. Computational studies were particularly performed by using the FEM technique within the elasto-plastic Cosserat type theory [220], the Drucker-Prager yield condition [195], visco-elasto-plastic models [221], the non-associated viscoplasticity, [222], the polar-hypoplasticity, [223].

It is well known, the continuum-based approaches have serious difficulties in capturing the discrete nature of granular material. In particular, the effects of microstructure of granular material during filling and discharge are in most cases neglected by assuming simplified constitutive laws. As demonstrated by [224], the particle shape has the significant influence on the material flow in the bin; however, the classical continuum approach is not able to take into account this effect.

On the other hand, the continuous finite element mesh should be specifically treated or rearranged to generate any possible discrete nature of the granular material. In this case, the bulk properties of granular matter are mostly assumed to be constant within the entire material and independent of the grain properties such as shape, size and friction. The distribution of velocity fields within the flowing granular material

is usually approximated as a certain function established *a priori* relying on the experimental test data captured on the bulk flow behaviour. Consequently, the continuum-based techniques are useful for predicting the stress field within the hopper, especially on its walls, at the end of filling and can hardly be used in the discharge state modelling, where a transition from the unsteady to the steady flow is required. In addition, the granular material packing characteristics, such as the bulk material density and the initial filling height (which are always obtained after filling only), are assumed to be a set of initial parameters in the continuum-based analysis.

Unlike the above methods, the discrete element method (DEM) enables simulating the dynamical behaviour of granular material directly introspecting the physical effects of individual grains on the resulting behaviour of the static and flowing granular material without any global assumptions. Therein, a granular material is modelled as an assembly of spherical particles and all dynamical parameters (position, velocity, etc.) as well as inter-particle contact forces between the particles are tracked during simulation.

2.1.3. Review of Discrete Element Method in modelling the silo systems

In [225] and later in [226] the authors first introduced the discrete element method into geomechanics and they are considered to be pioneers of the solid particle modelling. Further, the method was extended to wide range applications and, among others, to the analysis of the flow of granular media. In [227, 228, 229], the authors were the first to apply the discrete element method to the silo flow problems. In these simulations, a limited number of particles were used and, in spite of this fact, [229] obtained some interesting results concerning the flow rate and velocity profiles.

Discrete particle simulations of granular material flow phenomena in hoppers were considered in a number of works by Langston and co-authors. In particular, internal stress and flow fields in granular funnel flow in two- and three-dimensional hoppers were investigated by [230, 231, 232] accounting for spherical particles. The DEM model used was validated by comparing the wall stress and outflow parameters with the classical macroscopic predictions. A comparison of computational results with the data obtained by conventional photography and gamma-ray-tomography was also presented in [148]. The cohesive (capillary) bonds at particle contacts were studied by [233, 234, 235] along with experimental measurements.

A comprehensive study of filling and discharge processes in flat-bottomed plane model of silo using DEM was performed by [236]. Wall pressure distribution and comparison with the analytical and FEM results, velocity and stress distribution fields, contact forces transmission within the material of different elasticity and roughness have enabled the authors to obtain a global view on a quasi-static as well as steady-state flow response of granular material. In [237], the authors obtained results of wall forces and wall roughness consistent with those in [236]. A systematic computational study on filling and the unsteady/steady discharge processes in 3D wedge-shaped hopper has been recently performed by [238]. They thoroughly analysed friction effects, contributing to the behaviour of granular material in terms of microscopic variables, such as inter-particle contact forces and particle velocities, as well as macroscopic parameters, such as the system kinetic energy, porosity fields, wall pressures, material stresses, and discharge rates.

Rather than apply non-spherical particles, [239] used spherical particles by imposing an additional elastic spring, dashpot and a slider resisting the rotation on granular flow during the discharge from a flat-bottomed silo in 2D discrete particle simulation. In this way, the flow patterns were investigated. This variety of simulations was also considered by [240] to capture shear bounds localization during triaxial compression test.

The functional dependencies of the orifice size on the discharge flow rates and outflow velocities under a steady state conditions in 3D cylindrical rough-walled silo were studied by [241]. DEM modelling of granular flows involving parallel computing was performed by [242]. They investigated the effect of particle shape on hopper discharge describing the methodology of constructing and modelling of geometrically complex industrial applications in 3D cases. DEM analysis was also used by [243] to study particle circulations in a 3D spouted bed.

The developments of DEM were also aimed to simulate granular flow using elliptical particles [244], non-spherical discs and cylinders [245], sphero-discs [246] and irregular polygons [247, 248] and grains built as the multi-spherical particles, [249, 250, 251].

Recently, DEM simulation of the steady and unsteady states of granular flow in three dimensional cylindrical hopper with flat bottom was presented by [252, 253, 254]. They have used averaging procedures to transfer the microscopic results from discrete-particle simulations into a corresponding continuum system. Consequently, the local variables were averaged over the considered domain and time taking into

account weighting functions based on simplified S_B distribution function and the extension of unvaried distribution to three variants. The multi-objective approach for optimization of visco-elastic frictional granular material flow parameters implementing the discrete concept and a numerical discrete element method was proposed in [255]. The discharge time and discharge flow rate were taken to be the optimization criteria, while the discharge mass of material and the shape of the hopper were considered as design variables.

The DEM suffers, however, from serious disadvantages in comparison with the above mentioned methods i.e. insufficient computational capabilities limited by a huge number of particles and relatively small time integration step. The visualization of granular material flow is also extremely difficult because the common visualization programs unable to distinguish the particles needed to be drawn and rendered and also the particles that are not visible. It is clear that parallel DEM simulations (e.g., [256, 257]) involving millions of particles induce an immense requirement to their visualizations, [242, 258]. In addition, there are significant difficulties related to identification of the bulk material properties from the microscopic parameters of the particles. Moreover, measurements of the latter require scrupulous laboratory tests.

Another field of investigation is the DEM comparison with experiments, especially, in wall pressure, velocity patterns measurements. A 2D DEM simulation of the outflow rate of mono-sized particles has been validated experimentally for 3D Plexiglas hoppers of different outlet sizes and wall inclination angles, [259]. They selected particle material properties from the literature, while a transition from 2D to 3D case was defined via the scale factor.

A hybrid computational 2D model, based on finite and discrete element methods, has been verified experimentally for wall pressure analysis under the plane strain state, [260]. The rectangular bin with a hopper and an adjustable wall slope at the outlet was considered. The single-particle material properties were established experimentally. In spite of the limited number of particles and the simulation time selected, computer simulations successfully matched most of the observed features of the wall pressure measured at the intersection of the bin and the hopper.

The granular flow is a complex phenomenon, and the examination of DEM vs. the experimental results cannot be limited to the validation in terms of a single parameter. Investigation relying on two interrelated parameters has been demonstrated by [250]. That study particularly emphasised that the experimental

discharge time for the converging hopper may capture well but a comparison of the discharged material repose angles resulted in poor agreement. Those results underscore the necessity to measure at least two flow parameters.

In conclusion, one of the most serious drawbacks of the DEM simulations is attributed to validation of models by experiments, and the majority of the aforementioned simulations have been mainly associated with the qualitative analyses rather than of quantitative predictions. It is important to note that a DEM validation of the experimental results concerning wall pressure is absent in the published literature except for one article, [260].

Recently, the comparison of measured wall pressures and outflow rates with the DEM-based results has been presented by [261]. Meanwhile, the mean bulk density at the end of filling phase, the discharge rate, and the flow patterns filmed using a high speed during the discharge from a small model silo were compared with the DEM results by [262].

Currently, a comparison of the experimentally measured wall stresses and those produced by a DEM model, relying on the material data established experimentally at the microscopic and bulk scales, is strongly required and appears to be one rigorous way of validating DEM-based predictions. The present study is particularly aimed to achieve such a comparison, along with material stress analysis and outflow rate measurements. The qualitative analysis is also presented to replicate the different observations from the continuum-based predictions.

2.1.4. A discrete concept

Instead of the continuum approach, we adopt a discrete concept in a treatment of the granular media. Thereby, the granular material is assumed to be composed of a set of spherical (or approximately round) particles. Each particle may be treated as a body, with the description of its physical state and geometric representation. A physical state is defined by a constitutive description of particle material properties, while the geometric representation is provided throughout the description of the location of the particle centre of gravity and its radius. Any particle in the system is allowed to execute translational and rotational motions due to gravity acceleration, as well as forces and torques that originate from visco-elastic, non-cohesive, frictional contacts with some rolling resistance between particles or

a particle and walls. The walls may define the geometric description of the bin and serve as the basis for mathematical specification of boundary conditions.

The particles are assumed to be deformable entities. Instead of using the sophisticated modelling of real deformation of the sphere by a computational continuum-approach, we approximate deformation of the spheres in contact by the overlap. In other words, we assume that one sphere shape overlapping another approximately as a real deformation of spheres in contact. This assumption simply allows for the application of the contact mechanics laws of a single particle (Hooke or Hertzian spring analogy, the simplified Mindlin and Deresiewicz theory), [266]. In addition, we consider an isolated contact, i.e. the disturbances due to wave propagation within the contacting spheres are assumed to have neglecting influence on the contact velocity. We also classically suppose that the area/radius of contact is much smaller than the characteristic radius of the body.

Finally, the evaluation of the inter-particle as well as particle-wall contact forces and torques follows Newton's laws of classical mechanics and Poisson's hypothesis. In this case, the motion of the granular media is time-dependent and defined by Newton's second law. The resultant forces and torques acting on particles are collected from the action of the gravity and contact forces, torques as well. The contact search algorithm to check the contact between the particles is provided.

2.1.5. A modelling technique

The time-driven discrete element method presented by [244] and later considered by [263] is used as the main theoretical basis to investigate the behaviour of a granular material in the three dimensional silo systems.

Contact geometry and kinematics. Thus, in mathematical model, the granular material is assumed to be composed of a set of N discrete spherical particles. Geometry of a particle i ($i = 1, N$) is defined by radius R_i in terms of the specified grain size distribution. As the mentioned previously, any particle in the system is allowed to execute translational and rotational motions due to gravity acceleration, as well as forces and torques originated from visco-elastic, non-cohesive and frictional contacts with portion of the rolling resistance between particles or the particle with walls.

Two spherical particles in contact, i and j, are defined by positions $\mathbf{x}_i$ and $\mathbf{x}_j$ of the centres of gravity O_i and O_j of the particles and by translation velocities $\mathbf{v}_i$ and $\mathbf{v}_j$, and rotation velocities $\boldsymbol{\omega}_i$ and $\boldsymbol{\omega}_j$, (cf. Figure 2.1).

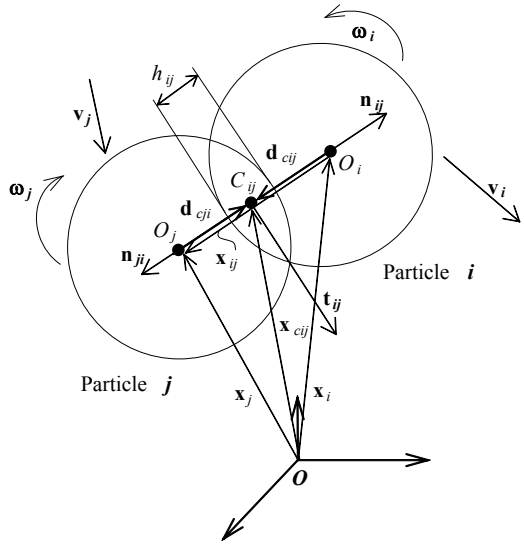

Figure 2.1. Representation of main geometrical and kinematical parameters in contact of two spheres.

The kinematics and contact geometry parameters are considered by a normal component acting in the normal direction (i.e. along the line connecting the centres of gravity of a pair of colliding particles) denoted by subscript n and the tangential component denoted by subscript t. The terms involved in describing the contact are clearly illustrated in Figure 2.1. An explicit evaluation of these terms was given elsewhere in [263].

Equations of motion. During the granular material flow the particles are generally undergone the large displacements, while the composition of the media becomes a time-dependent because individual particles change their position due to motion. In this case, the classical equations of motion are feasible. Thus, the motion of i-th particle within the granular aggregate may be calculated from the resultant of forces and moments according to Newton's second law:

$$m_i \frac{\mathrm{d}^2 \mathbf{x}_\mathrm{i}(t)}{\mathrm{d}t^2} = \sum_{j=1, j\neq i}^{N} \mathbf{F}_{ij} + m_i \mathbf{g}. \tag{2.1}$$

$$I_i \frac{\mathrm{d}\boldsymbol{\omega}_i(t)}{\mathrm{d}t} = \sum_{j=1, j\neq i}^{N} \mathbf{d}_{cij} \times \mathbf{F}_{ij} + \mathbf{T}_{ij}^{roll}, \tag{2.2}$$

where $\mathbf{x}_i$ and $\boldsymbol{\omega}_i$ are vectors of position and rotational velocity of the centre of gravity (cf. Figure 2.1.), $\mathbf{d}_{cij} = -\mathbf{d}_{cji}$ are vectors specifying the position of the contact point with respect to the centres of the particles (cf. Figure 2.1), $\mathbf{g}$ is the vector of gravity acceleration, m_i is mass and $I_i = 2/5 m_i R_i^2$ is the inertia moment of the sphere i with radius R_i (i = 1, N).

Contact forces. The evaluation of the inter-particle as well as particle-wall contact forces $\mathbf{F}_{ij}$ is performed following the third Newton's law implementing visco-elastic contact model. Hence, contact force $\mathbf{F}_{ij}$ found between two particles i and j is expressed in terms of normal and the tangential components $\mathbf{F}_{n,ij}$ and $\mathbf{F}_{t,ij}$

$$\mathbf{F}_{ij} = \mathbf{F}_{n,ij} + \mathbf{F}_{t,ij}. \tag{2.3}$$

The normal component of contact force $\mathbf{F}_{ij}$ depends on the contact geometry as well as on physical properties of the particulate material and is described by Hooke or by Hertzian springs taking into consideration the non-conservative viscous damping response during the collision, [244].

$$\mathbf{F}_{n,ij} = \frac{4}{3} \cdot \frac{E_i E_j}{E_i\left(1-\nu_j^2\right) + E_j\left(1-\nu_j^2\right)} R_{ij}^{2-\alpha} h_{ij}^{\alpha} \mathbf{n}_{ij} - \gamma_n m_{ij} \mathbf{v}_{n,ij}, \tag{2.4}$$

where $m_{ij} = \frac{m_i m_j}{m_i + m_j}$ and $R_{ij} = \frac{R_i R_j}{R_i + R_j}$ present the reduced mass and reduced radius of particles i and j, E_i and E_j are elasticity moduli and ν_i and ν_j are Poisson's ratios, $h_{ij} = R_i + R_j - \left|\mathbf{x}_{ij}\right|$ is the overlap between contacting particles i and j (cf. Figure 2.1), where $\mathbf{x}_{ij}$ is the vector of the relative position (cf. Figure 2.1); $\mathbf{n}_{ij}$ is the unit vector normal to the contact surface and directed towards the particle i (cf. Figure 2.1), $\mathbf{v}_{n,ij} = \left(\mathbf{v}_{ij} \cdot \mathbf{n}_{ij}\right)\mathbf{n}_{ij}$ and $\mathbf{v}_{t,ij} = \mathbf{v}_{ij} - \mathbf{v}_{n,ij}$ are the normal and tangential component of contact relative velocity, [263], where

$\mathbf{v}_{ij} = \mathbf{v}_i + \boldsymbol{\omega}_i \times \mathbf{d}_{cij} - \mathbf{v}_j - \boldsymbol{\omega}_j \times \mathbf{d}_{cji}$,

whilst $\mathbf{v}_i, \mathbf{v}_j$ and $\boldsymbol{\omega}_i, \boldsymbol{\omega}_j$ are the translational and rotational velocities of the particles *i* and *j*, respectively; γ_n is viscous damping coefficient in normal direction. For the Hertzian contact model, the power is of $\alpha = 3/2$, while, for Hooke's law, it is provided as $\alpha = 1$, [244].

For the above force model, a viscous damping coefficient in the normal direction γ_n is a phenomenological constant that may be conventionally determined from the restitution coefficient measured in the grain collision experiment.

A simple illustration on a time-dependent behaviour of an oscillating spring predicted by Eq. 2.4 and accounting for the different viscous damping constant γ_n is shown in Figure 2.2 by using the reasonable ratio with γ_t. Here, the values on the damping coefficient are selected a priori. When the restitution coefficient e_n is known from the experimental measurement, γ_n value can be numerically fitted to obtain the experimental value of this coefficient as a ratio between the rebound velocity and velocity at the contact engagement of the sphere (see also, Section 2.3.3.1). For the Hooke's spring, γ_n resolves analytically, i.e., $\gamma_n = -\sqrt{\frac{k_n}{m_i}}\frac{\ln e_n}{\sqrt{\ln^2 e_n + \pi^2}}$ (where $k_n = \frac{4}{3}\cdot\frac{E_i E_j}{E_i\left(1-\nu_j^2\right)+E_j\left(1-\nu_i^2\right)}R_{ij}h_{ij}$ is the spring stiffness), while for the Hertz's non-linear spring only the numerical solution is feasible. The restitution coefficient in tangentional direction is difficult to measure, hence γ_t is basically in Figure 2.2 the oscillating spring behaviour is considered with viscous damping coefficient values γ_n of 0, 1 and 20 s^{-1}. The motion was induced by initial velocity, the same for all viscous damping cases. For $\gamma_n = 0$, the spring force-displacement path represents a loading/unloading/reloading function linearly changing from its positive to negative values (cf. Figure 2.2a). For $\gamma_n > 0$, the loading/unloading/ /reloading loops develop. In the *p-q* phase space (cf. Figure 2.2b), the classical curve of the Hamiltonian mechanics (for $\gamma_n = 0$), meaning the symmetrical interchange of *p* (momentum) and *q* (coordinate), turns into a spiral-like shape, for $\gamma_n > 0$, manifesting the energy dissipation due to viscous damping. The constant Hamiltonian function *H* (cf. Figure 2.2c) represents the energy of the system (provided that there are no external forces, or additional energy added to the system). In this case, the system kinetic and potency energies interchange do to viscous damping to hold the energy conservation).

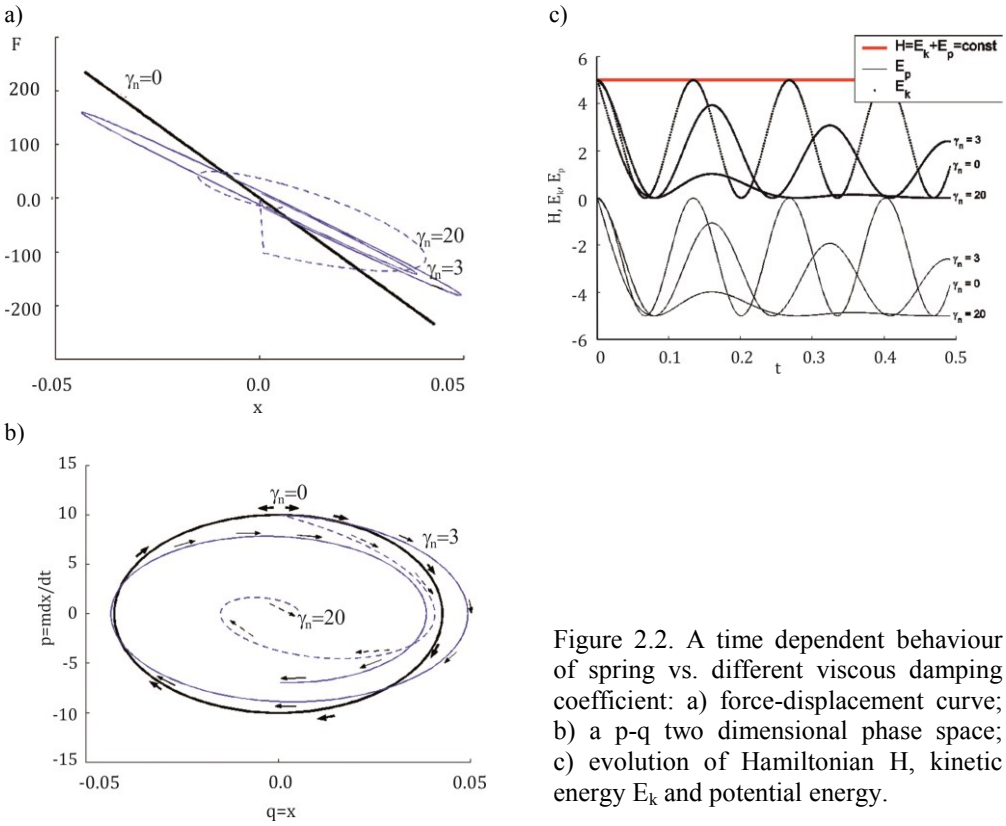

Figure 2.2. A time dependent behaviour of spring vs. different viscous damping coefficient: a) force-displacement curve; b) a p-q two dimensional phase space; c) evolution of Hamiltonian H, kinetic energy E_k and potential energy.

Considering the frictional behaviour of the grains, we adopted one of the most popular approaches comprising the evolution of tangential force $\mathbf{F}_{t,ij}$ consisting of the static, $\mathbf{F}_{t,ij,static}$ (ie., slip) or dynamic friction, $\mathbf{F}_{t,ij,dynamic}$ (i.e., sliding). In particular, the static friction force describes the friction in terms of approximate account for the slip, while the dynamic friction force corresponds to the sliding. The most general form of the static friction was proposed by [264, 265] simplifying Mindlin's theory [266]

$$\mathbf{F}_{n,ij,static} = -\frac{16}{3} \cdot \frac{G_i G_j \sqrt{R_{ij} h_{ij}}}{G_i\left(2-\nu_j\right) + G_j\left(2-\nu_i\right)} \boldsymbol{\delta}_{t,ij} - \gamma_t m_{ij} \mathbf{v}_{t,ij}, \tag{2.5}$$

where

$$\boldsymbol{\delta}_{t,ij} = \int \mathbf{v}_{t,ij}(t)\mathrm{d}t, \text{ when } \left|\mathbf{F}_{t,ij,static}\right| < \left|\mathbf{F}_{t,ij,dynamic}\right|, \tag{2.6}$$

is the tangential displacement vector (for $\mathbf{v}_{t,ij} \to 0, \boldsymbol{\delta}_{t,ij}$ specifies also the unit vector of the tangential direction), G_i and G_j are the shear moduli, respectively, $\mathbf{v}_{t,ij} = \mathbf{v}_{ij} - \mathbf{v}_{n,ij}$ is the tangential velocity of colliding particles i and j, γ_t is the viscous damping coefficient in tangential direction.

The dynamic friction force describes the friction after gross sliding and is expressed by Coulomb law

$$\mathbf{F}_{t,ij,dynamic} = -\mu\left|\mathbf{F}_{n,ij}\right|\mathbf{t}_{ij}, \tag{2.7}$$

where μ is the particle-particle or particle-wall friction coefficient, $\mathbf{t}_{ij} = \left\{\frac{\mathbf{v}_{t,ij}}{|\mathbf{v}_{t,ij}|}, \left|\mathbf{v}_{t,ij}\right| \neq 0\right.$ is a unit vector specifying the action of tangential contact force vector, [244]. Particularly, if the tangential component of contact velocity vector length $\left|\mathbf{v}_{ij}\right|$ is not equal to zero, then the unit vector $\left|\mathbf{v}_{ij}\right|$ of the tangential contact direction is directed along $\mathbf{v}_{t,ij}$. If $\left|\mathbf{v}_{ij}\right|$ is equal to zero, $\mathbf{t}_{ij}$ has the same direction in which the slip occurs. Otherwise, $\mathbf{t}_{ij}$ is equal to zero if lengths of $\mathbf{v}_{t,ij}$ and $\boldsymbol{\delta}_{t,ij}$ are equal to zero.

In order to evaluate which static or dynamic friction act on the contact surface, we use one of the most popular approaches comprising the evolution of tangential force $\mathbf{F}_{t,ij}$ as

$$\mathbf{F}_{t,ij} = -\mathbf{t}_{ij}\min\left(\left|\mathbf{F}_{t,ij,static}\right|, \left|\mathbf{F}_{t,ij,dynamic}\right|\right), \tag{2.8}$$

Rolling resistance. In early experiments on the shear strength of a random assembly of spherical particles, the researchers observed interesting phenomena: the shear strength need not necessary vary when the interparticle friction coefficient changes. In [267], the author conducted the shear strength tests for 1 mm glass ballotini with wet (high friction regime) and dry (low friction regime) spheres. In spite of the fact that the interparticle friction coefficients differ by about 5 times for wet and dry grains, the overall shapes of the force-displacement curves were similar with the same peak strength and almost the same energy being dissipated for both specimens. Since the interparticle friction was 5 times different, the author probably the first concluded that the type of particle motion must also be different for both specimens, and the particle can move relative to its neighbours only by two ways, i.e. by sliding

or by rolling. He also supposed that the sliding of the grains is a predominant feature in the low friction regime, and, when the interparticle friction is raised; more particles should roll rather than slide, in order to keep the energy balance the same. In [268] the author also concluded that the dynamical angle of reposes in rotating drum increase in proportion to the interparticle friction coefficient only when the values of this coefficient were very low. The higher values of interparticle friction coefficient allowed for the rotational motion of the particles and the angle of repose did not increase. Finally, to handle this issue, the simple computational concept of rolling resistance (or rolling friction) was firstly applied by [240] to successfully capture the shear bands in DEM analysis for the triaxial compression test of spherical particles. Recently, the importance of rolling resistance in promoting shear band formation in granular materials has been discussed in [269].

Formally, the rolling behaviour could describe a standard approach in terms of force-displacement, in this case, the rolling torque-rotation, relationship. Actually, the dynamics of pure rolling of deformable bodies is quite complicated and is not clearly understood, but it has been extensively studied theoretically and experimentally. Fundamentally, it is difficult to resolve analytically the contact traction and the contact zone evolution, [270, 271, 272], with account for slip and rolling modes.

Probably the first model for the rolling resistance between cylindrical particles was introduced and implemented by [273]. Generally, rolling is coupled with frictional sliding and is very complex phenomenon, where the role of rolling parameters is still under discussion, [249, 250, 274, 275, 276, 277, 278, 279]. The validation and/or calibration of the grain level parameters and contact models by conducting an experiment or parametric simulation is required to reflect the macroscopically observable phenomena of a granular material.

Accuracy and capturing the reality by these models is quite different. Hence, in a recent review of rolling friction, [276], the main models were extensively analysed by special benchmark tests. Meanwhile, a theoretical investigation on the equilibrium, stability for pure rolling problem of a sphere moving on a flat plane relying on several force models was analysed by [280]. It was particularly found that the sphere can roll on the hard plane without sliding only when both the tangential force and torque acting on the sphere are zero.

The rolling friction model can probably be adapted to imitate the effects related with the particle shape. The technique to capture the dynamical behaviour of the non-

spherical particles assembly by using the perfect spheres with the modified coefficient of rolling friction was discussed by [281]. They computed the coefficient of rolling friction from the ratio of the normalised average eccentricity of a contact to the rolling radius of an idealised sphere representing the particle. As pointed out by the authors, in spite of similar behaviour observed comparing idealised non-spherical particles and spherical particles subject to rolling friction, the technique, in some cases, was not entirely successful.

During the rotational motion of the grains the contact between two grains occurs not at a single contact point, but generally on a finite contact surface. The friction model (2.8) cannot induce any resistance on the sphere rolling over a rough surface or other contacting sphere, if the relative tangential velocity at the contact point is zero. It may induce the rolling torque $\mathbf{T}_{ij}^{roll}$ counteracting the relative rotation between two contacting spheres, manifesting the asymmetry of the normal traction distribution on the contact surface and causing a gradual slowdown in the rotational motion.

The main objective of rolling resistance approaches is attributed to define the additional rolling torque $\mathbf{T}_{ij}^{roll}$ to the torque produced by the contact friction forces, $\sum_{j=1,\, j\neq i}^{N} \mathbf{d}_{cij} \times \mathbf{F}_{ij}$. Relying on the mentioned references, we can develop a simple approach to account for the rolling friction in the granular material flow from the flat-bottomed bin.

Thus, as for the above sliding friction model, we can similarly define $\mathbf{T}_{ij}^{roll}$ in terms of the torque supplied by the elastic rotational spring/roller combination. An elastic spring suppresses the rotation prior to the rolling and causes the rolling friction torque that may be specified as:

$$\mathbf{T}_{ij,st}^{roll} = k_r \boldsymbol{\Theta}_{ij}^{roll}, \tag{2.9}$$

where $k_r = k_t r_{ij}^2$ is the rolling stiffness according to [280], approach, $r_{ij} = \min(R_i, R_j)$ is the effective radius of the contacting particles, k_t is the tangential spring stiffness, $\boldsymbol{\Theta}_{ij}^{roll}$ is a vector of rolling angle.

The angle of rolling is specified by relative rotational velocity $\boldsymbol{\omega}_{ij} = \boldsymbol{\omega}_i - \boldsymbol{\omega}_j$ acting at the contact point (cf. Figure 2.1) (where $\boldsymbol{\omega}_i$ and $\boldsymbol{\omega}_j$ are the rotational velocities at the centres of the particles *i* and *j*, respectively), thus

$$\boldsymbol{\omega}_{ij} = \frac{\mathrm{d}\boldsymbol{\Theta}_{ij}^{roll}}{\mathrm{d}t}. \tag{2.10}$$

By integrating via trapezoidal rule, we can get:

$$\int_{\boldsymbol{\Theta}_{ij}^{roll}(t)}^{\boldsymbol{\Theta}_{ij}^{roll}(t+\Delta t)} \mathrm{d}\boldsymbol{\Theta}_{ij}^{roll} = \frac{\Delta t}{2}\Big(\boldsymbol{\omega}_{ij}(t) + \boldsymbol{\omega}_{ij}(t+\Delta t)\Big). \tag{2.11}$$

For a small time increment, it is reasonable to assume that

$$\begin{gathered}\boldsymbol{\omega}_{ij}(t+\Delta t) \approx \frac{1}{2}\Big(\boldsymbol{\omega}_{ij}(t) + \boldsymbol{\omega}_{ij}(t+\Delta t)\Big), \text{hence} \\ \boldsymbol{\Theta}_{ij}^{roll}(t+\Delta t) = \boldsymbol{\Theta}_{ij}^{roll}(t) + \boldsymbol{\omega}_{ij}(t+\Delta t)\Delta t,\end{gathered} \tag{2.12}$$

and, using (2.9) we finally define formula for the elastic torque suppressing the rotation prior to rolling, thus:

$$\mathbf{T}_{ij,st}^{roll}(t+\Delta t) = k_r\big(\boldsymbol{\Theta}_{ij}^{roll}(t) + \boldsymbol{\omega}_{ij}(t+\Delta t)\Delta t\big). \tag{2.13}$$

When the particles start to roll relative to each other, the elastic torque reaches its limit value characterizing the rolling resistance. In this case, the rolling torque magnitude may define emulating the Coulomb's law for the case of rolling friction. Thus, the rolling resistance is specified as follows

$$T_{ij,0}^{roll} = \mu_R r_{ij}\left|\mathbf{F}_{n,ij}\right|, \tag{2.14}$$

where $\mu_R = \tan(\alpha)$ is the coefficient of rolling friction provided by the tangent of the asperity contact angle α.

The rolling friction torque magnitude $T_{ij,dyn}^{roll}$ is now rearranged into a vector form in terms of the unit vector of the relative rotational velocity as follows:

$$\mathbf{T}_{ij,dyn}^{roll} = T_{ij,0}^{roll}\frac{\boldsymbol{\omega}_{ij}(t+\Delta t)}{\left|\boldsymbol{\omega}_{ij}(t+\Delta t)\right|}. \tag{2.15}$$

A final decision, which torque produces the rolling resistance on the contacting spheres rotational motion at $t+\Delta t$, may define the following condition:

$$\mathbf{T}_{ij}^{roll} = -\begin{cases} \mathbf{T}_{ij,st}^{roll}, & \left|\mathbf{T}_{ij,st}^{roll}\right| < T_{ij,0}^{roll} \\ \mathbf{T}_{ij,dyn}^{roll}, & \left|\mathbf{T}_{ij,st}^{roll}\right| \geq T_{ij,0}^{roll} \end{cases}. \tag{2.16}$$

When the rolling angle fully mobilizes and the particle rolls under the constant torque $T_{ij,0}^{roll}$, the rolling angle vector should grow up and this effect may be predicted via condition of $\left|\mathbf{T}_{ij,st}^{roll}\right| = T_{ij,0}^{roll}$, thus:

$$\mathbf{\Theta}_{ij}^{roll}(t+\Delta t) = \frac{T_{ij,0}^{roll}}{k_r} \frac{\boldsymbol{\omega}_{ij}(t+\Delta t)}{\left|\boldsymbol{\omega}_{ij}(t+\Delta t)\right|}. \tag{2.17}$$

Note, at the initiation of the rolling angle mobilization, the direction of torque $\mathbf{T}_{ij,dyn}^{roll}$ is still under influence of $\mathbf{\Theta}_{ij}^{roll}(t+\Delta t)$, hence, instead of Eq. (2.15) $\mathbf{T}_{ij,dyn}^{roll}$ is determined as:

$$\mathbf{T}_{ij,dyn}^{roll} = T_{ij,0}^{roll} \frac{\mathbf{\Theta}_{ij}^{roll}(t+\Delta t)}{\left|\mathbf{\Theta}_{ij}^{roll}(t+\Delta t)\right|}. \tag{2.18}$$

Now, some final remarks on the above model could be mentioned. In particular, condition (2.16) with combination of expression (2.12) preserve zero rolling friction torque at time $t+\Delta t$, when two particles are subjected to zero translational velocity and oppositely directed angular velocity of the same magnitude, $|\boldsymbol{\omega}_i| = \left|\boldsymbol{\omega}_j\right|$. In addition, instead of integration of Eq. (2.10), this expression may be rearranged into an incremental form, i.e., rate of $\dot{\mathbf{T}}_{ij,st}^{roll} = k_r$, yielding the formula $\mathbf{T}_{ij,st}^{roll}(t+\Delta t) = \mathbf{T}_{ij,st}^{roll}(t) + k_r\left(\mathbf{\Theta}_{ij}^{roll}(t+\Delta t) - \mathbf{\Theta}_{ij}^{roll}(t)\right)$ that was found in [276], (see, Eqs. 11–12 there). This expression with additional account for the damping terms worked very well in their benchmark tests including the rolling back behaviour of the particle.

On the other hand, the above rolling friction model operates with less parameters over the simulation than the incremental form. In the silo discharge process, the effect of rolling back behaviour is minimal. We also use the limited number of variables involving one basic parameter, namely the rolling friction coefficient, in order to avoid the complications to deal with multiple model parameters which prediction or physical meaning are quite obscure.

Numerical integration. For a many body problem, the state of all particles at time *t* is obtained by the numerical integration of Eqs. (2.1-2) and calculation of particle forces (2.3-7) using a constant time step Δt. The numerical solution of these equations is obtained by the 5*th – order Gear's predictor-corrector* scheme, [282].

Firstly, particles positions $\mathbf{x}_i^p$,velocities $\mathbf{v}_i^p$ accelerations $\mathbf{a}_i^p$ and higher order derivatives $\mathbf{b}_{ni}^p = \frac{\mathrm{d}^n \mathbf{x} \Delta t^n}{\mathrm{d}t^n} \frac{\Delta t^n}{n!}$ (for *n* = 3, 4, 5), denoted by superscript *p* therein, are predicted by the following expressions:

$$\mathbf{x}_i^p(t+\Delta t) = \mathbf{x}_i(t) + \Delta t \mathbf{v}_i(t) + \frac{1}{2}\Delta t^2 \mathbf{a}_i(t) + \mathbf{b}_{3i}(t) + \mathbf{b}_{4i}(t) + \mathbf{b}_{5i}(t). \tag{2.19}$$

$$\mathbf{v}_i^p(t+\Delta t) = \mathbf{v}_i(t) + \Delta t \mathbf{a}_i(t) + \frac{1}{\Delta t}\left(3\mathbf{b}_{3i}(t) + 4\mathbf{b}_{4i}(t) + 5\mathbf{b}_{5i}(t)\right). \tag{2.20}$$

$$\mathbf{a}_i^p(t+\Delta t) = \mathbf{a}_i(t) + \frac{2}{\Delta t^2}\left(3\mathbf{b}_{3i}(t) + 6\mathbf{b}_{4i}(t) + 10\mathbf{b}_{5i}(t)\right). \tag{2.21}$$

$$\mathbf{b}_{3i}^p(t+\Delta t) = \mathbf{b}_{3i}(t) + 4\mathbf{b}_{4i}(t) + 10\mathbf{b}_{5i}(t). \tag{2.22}$$

$$\mathbf{b}_{4i}^p(t+\Delta t) = \mathbf{b}_{4i}(t) + 5\mathbf{b}_{5i}(t). \tag{2.23}$$

$$\mathbf{b}_{5i}^p(t+\Delta t) = \mathbf{b}_{5i}(t)\,. \tag{2.24}$$

When the positions and velocities are preliminary computed, the corrector step (denoted by superscript c) refines the initial approximations in terms of acceleration, accordingly:

$$\mathbf{a}_i^c(t+\Delta t) = \frac{\mathbf{F}_i\left(\mathbf{x}_i^p, \mathbf{v}_i^p\right)}{m_i}. \tag{2.25}$$

$$\Delta \mathbf{a}_i(t+\Delta t) = \mathbf{a}_i^c(t+\Delta t) - \mathbf{a}_i^p(t+\Delta t). \tag{2.26}$$

$$\begin{pmatrix} \mathbf{x}_i^c(t+\Delta t) \\ \mathbf{v}_i^c(t+\Delta t) \\ \mathbf{a}_i^c(t+\Delta t) \\ \mathbf{b}_{3i}^c(t+\Delta t) \\ \mathbf{b}_{4i}^c(t+\Delta t) \\ \mathbf{b}_{5i}^c(t+\Delta t) \end{pmatrix} = \begin{pmatrix} \mathbf{x}_i^p(t+\Delta t) \\ \mathbf{v}_i^p(t+\Delta t) \\ \mathbf{a}_i^p(t+\Delta t) \\ \mathbf{b}_{3i}^p(t+\Delta t) \\ \mathbf{b}_{4i}^p(t+\Delta t) \\ \mathbf{b}_{5i}^p(t+\Delta t) \end{pmatrix} + \begin{pmatrix} 0.5c_o\Delta t^2 \\ 0.5c_1\Delta t^2 \\ c_2 \\ 0.5c_3\Delta t^2 \\ 0.5c_4\Delta t^2 \\ 0.5c_5\Delta t^2 \end{pmatrix} \Delta\mathbf{a}_i(t+\Delta t). \qquad (2.27)$$

The values of the constants c_i depend on the desired accuracy, and, for a second order of differential equation, are as follows: $c_0 = 3/16$, $c_1 = 251/360$, $c_2 = 1.0$, $c_3 = 11/18$, $c_4 = 1/6$ and $c_5 = 1/60$, [282].

Rotational variables of the particles described by Eq. (2.2) are determined in the same way. The performance of the above scheme producing a low artificial damping may be briefly illustrated.

In particular, to achieve the accuracy of numerical integration schemes, unidirectional two particles motion tests were checked and the results were compared with analytical solutions, [283]. Generally, an assertion of [284] has shown that an accurate simulation requires $\Delta t \sim T_c/50$ (T_c is the time of collision between two particles). However, the authors often use a larger time step in order to achieve faster simulations.

The evaluation of the accuracy of the above-mentioned schemes and the dependency of the ratio, Δt / T_c on the numerical errors are considered below. To test the particle – particle collision, the particle i with the radius, $R = 0.05$ m, and mass, $m = 10$ kg, moving at the initial velocity $v_0 = 1$ m/s and hitting a stationary particle j were simulated. The modulus of elasticity E and Poisson's ratio ν were assumed to be $3 \cdot 10^5$ Pa and 0.3, respectively, while the normal viscous damping parameter is equal to $\gamma_n = 10\ \mathrm{s}^{-1}$. The collision in normal direction was considered only accounting for:

- Test 1: normal elastic force;
- Test 2: normal elastic and damping forces;
- Test 3: normal elastic, damping and gravity forces.

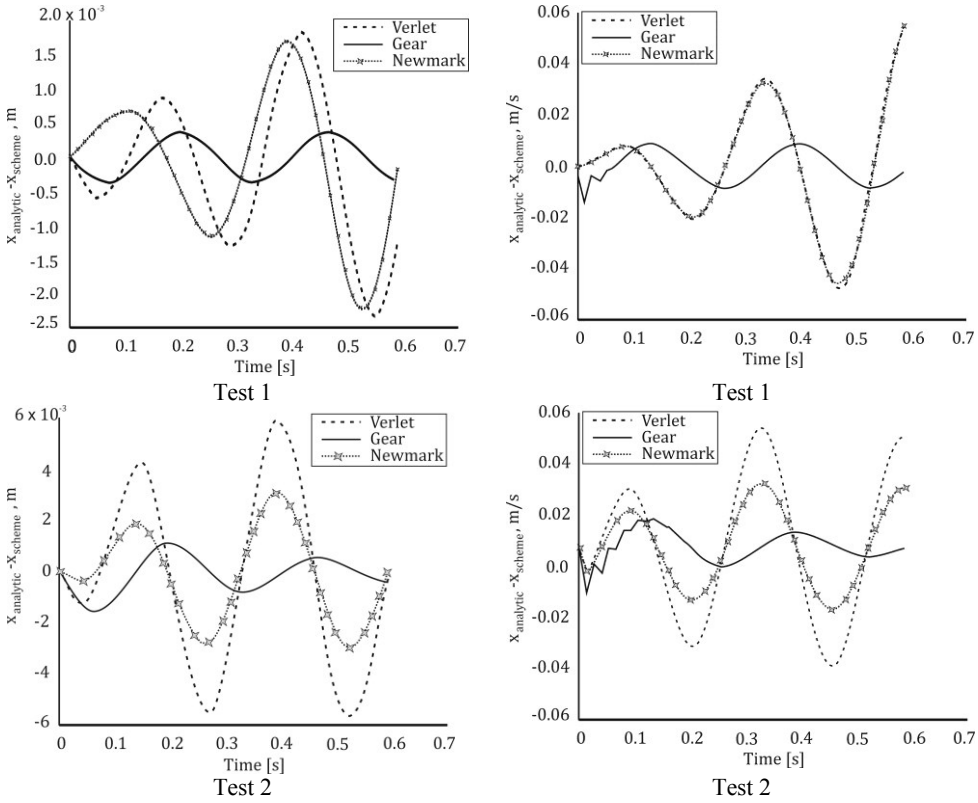

Figure 2.3. Numerical errors vs. time, when $\Delta t \sim T_c/10$.

The time-evolution of simulation errors for the particles overlap, $x_{analytic}$-x_{scheme}, as well as for the velocity, $v_{analytic}$-v_{scheme}, magnitudes versus the different time integration step, Δt, are shown in Figure 2.3 and Figure 2.4.

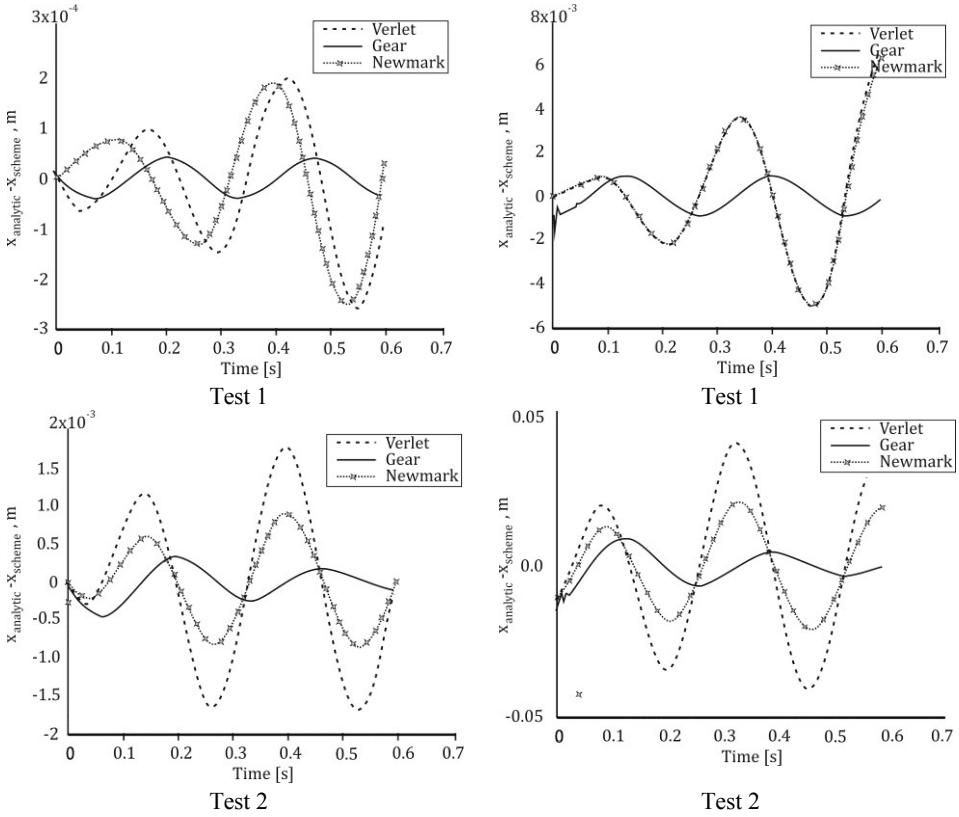

Figure 2.4. Numerical errors vs. time, $\Delta t \sim T_c/30$.

As it can see from these graphs, the simulation accuracy mainly depends on the number of the acting particle forces. One can clearly see that the lowest numerical errors provide the 5^{th} *– order Gear predictor-corrector* time integration scheme.

In order to estimate the artificial damping of these time-integration schemes, the evolution of relative errors is computed:

$$\Delta_x(t) = \left| \frac{x_{analytic}(t) - x_{scheme}(t)}{x_{analytic}(t)} \right|, x_{analytic}(t) \neq 0. \qquad (2.28)$$

To estimate statistically the sample of simulation errors, $\Delta_x(t)$, obtained within the entire time of simulation for each scheme the mean and standard deviation (STD) are computed. The uncertainty of the schemes is due to either random errors (STD) or systematic errors $\Delta_x(t)$.

The results of adequacy tests of analytical and numerical solutions for different time integration schemes, depending on time steps, Δt, and the time of collision, T_c, are presented in Table 2.1.

According to Table 2.1, the *5th – order Gear predictor-corrector* scheme results in the lowest average relative error and standard deviation of these errors varying over the range of 0.8 and 4.2%, and 0.07–2.92%, respectively. The *Newmark* time integration scheme provides much more value of average relative errors ranging from 3% to 15%. The standard deviation of these errors is also grater than Gear's scheme, i.e. 3.8–22%. These values are picked out from Table 2.1, for the ratio $\Delta t/T_c$=10 and the error tends to vanish with the increasing $\Delta t/T_c$. The *Velocity Verlet* algorithm resulted in more significant errors in comparison with the above-mentioned schemes, whereas the *Taylor Expansion Series* expansion leads to considerably high artificial damping.

Finally, to obtain sufficiently accurate computational simulations, the *5th – order Gear predictor-corrector* scheme can be reliably used in DEM simulations. This scheme provides sufficiently accurate results for time integration $\Delta t = T_c/10$, while other considered schemes require considerably smaller integration step $\Delta t = T_c/30$.

Contact search. In order to evaluate forces $\mathbf{F}_{ij}$ all contacts between the particles and their neighbours must be detected. In a system containing N particles, a general contact detection problem is of the size $O(N^2)$, when the neighbour particles search algorithm is applied sequentially. In order to reduce the number of all particle pair combinations, one of the simplest *zoning* algorithm [285] to find the neighbours was used for the contact detection. The lists of neighbouring particles as well as for the walls reduce the computational effort required for determining the contact forces, [255].

All the particles, whose centres of gravity are within the cells, are referenced by using the ceiling of the components of vector $\mathbf{x}_i$, the size of the cell and the geometric data of the domain of granular media. Thus, the referenced particles indices, cells indices and the number of particles per cell are stored in the memory. After referencing the *neighbour list of particles* is constructed by assembling particles indices from the neighbouring cells which are around the

reference cell. In a 3D case, the reference cell includes up to 27 neighbouring cells, while for a 2D case the reference cell has up to 9 neighbouring cells. The neighbouring cells include also the boundary zones. The *boundary neighbour list of particles* was constructed in the manner described above. Finally, the contact detection procedure is done by a sequentially checking for the contacts distinguishing the particle-particle from particle-walls and particle-walls and is performed by using particle indices obtained from the *neighbour list of particles* and the *boundary neighbour list of particles*. Detailed information was given by [255, 286].

Table 2.1. Statistical results of relative errors for time integration schemes

Scheme	Statistical parameters of relative error, $\Delta_x(t)$			
	$\Delta t = T_c/10$		$\Delta t = T_c/30$	
	Mean	STD	Mean	STD
	Test 1:			
5th – order Gear predictor-corrector	0.0085	0.0007	0.0009	0.00002
Newmark predictor-corector	0.0351	0.0389	0.0057	0.0091
Velocity Verlet	0.0383	0.0434	0.0060	0.0094
Taylor Expansion Series	0.6397	0.5428	0.1846	0.1369
	Test 2:			
5th – order Gear predictor-corrector	0.0424	0.0021	0.0121	0.0006
Newmark predictor-corector	0.1505	0.2002	0.0703	0.1226
Velocity Verlet	0.2980	0.3867	0.1376	0.2397
Taylor Expansion Series	1.3214	1.7983	0.3746	0.5642
	Test 3:			
5th – order Gear predictor-corrector	0.0216	0.0292	0.0129	0.0403
Newmark predictor-corector	0.1494	0.2275	0.0653	0.2975
Velocity Verlet	0.2664	0.3762	0.1223	0.5175
Taylor Expansion Series	0.8178	1.0426	0.2165	0.3787

Boundary conditions. The boundary conditions are described by using the rectangular planes of a finite size with own local coordinate system (cf. Figure 2.5) enabling to obtain the different shapes of the hopper.

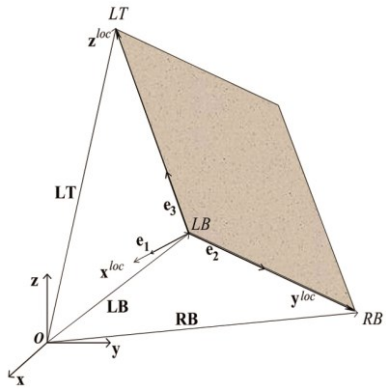

Figure 2.5. Geometry of wall as boundary condition, [238].

The geometry of each boundary surfaces in the global coordinates system is sketched by using three plane corner vectors **LT** (left top), **LB** (left bottom), **RB** (right bottom) utilizing them to define local coordinate frame $(xyz)^{loc}$ of the wall specified by unit vectors $\mathbf{e}_1$, $\mathbf{e}_2$, $\mathbf{e}_3$:

$$\mathbf{e}_2 = \frac{\mathbf{y}^{loc}}{|\mathbf{y}^{loc}|}, \mathbf{e}_3 = \frac{\mathbf{z}^{loc}}{|\mathbf{z}^{loc}|}, \ \mathbf{e}_1 = \mathbf{e}_2 \times \mathbf{e}_3, \tag{2.29}$$

where $\mathbf{z}^{loc} = \mathbf{LT}–\mathbf{LB}$, $\mathbf{y}^{loc} = \mathbf{RB}–\mathbf{LB}$.

Unilateral constraint orientation restricting the motion of the particle in outward direction of the wall is defined by using the orientation of the unit vector $\mathbf{e}_1$. Transition form any vector in local $\mathbf{P}^{loc}$ and global **P** coordinate systems may be defined as

$$\mathbf{P}^{loc} = \begin{bmatrix} e_{1x} & e_{1y} & e_{1z} \\ e_{2x} & e_{2y} & e_{2z} \\ e_{3x} & e_{3y} & e_{3z} \end{bmatrix} (\mathbf{P} - \mathbf{LB}) = [\mathbf{A}](\mathbf{P} - \mathbf{LB}). \tag{2.30}$$

Detection of the particle and the wall contact interaction is performed by creating locally oriented boundary cells and the checking of the contact possibilities with the plane of the wall and its edges in the local coordinate frame. In the case of the contact between the particle and the wall, the interaction forces are defined treating the plane as the particle with infinite radius and mass. The external action of the wall is induced by using the kinematics boundary conditions.

The above concept is implemented into code *DEMMAT,* [255, 286]. The parallel version was also developed, [257].

2.2. Qualitative predictions of granular material flow in silos, hoppers of different shapes

2.2.1. Introduction

This Chapter presents the application of the discrete element method to model the granular material flow in silos and hoppers where the models were of different shape. Before comparison of DEM results with the experimental data the qualitative predictions are aimed to study the abilities of the above presented mathematical model to capture qualitatively the main indications observed in granular material flow throughout the orifices during the filling and discharge processes. As preliminary investigation of real grain materials, instead of using large models operating with huge amount of spherical particles, qualitative characterization of flow will test adopting the relatively rough models with small number of particles investigating the consistency of micro and macro-phenomena in the time dependent flow process.

Simulations via DEM are very time consuming. The in most CPU time is wasted on contact searching between grains. As demonstrated in [255, 257, 286, 287], the CPU time increases when the polydispersity of spheres increases; beside, the CPU extremely grows up with increasing the number of particles. The most efficient work of the contact searching procedure is when the polyderspisity of spheres is mild, since the size of cells in zoning of the calculation domain can be selected equal to diameter of the sphere. Thus, in order to speed up the simulations the qualitative analysis will be performed artificially selecting a small number of spheres and using small polydispersivity of the grains.

The evolution of granular flow, internal forces and densification (rarefaction) will characterize macroscopic parameters such as the discharge rates, the porosity fields and the wall pressures as well as microscopic evaluations in terms of coordination number, velocity patterns and inter-particle contact forces. The results obtained are based on [238, 288, 289].

2.2.2. Microscopic and macroscopic analysis of granular material behaviour in 3D flat bottomed hopper

2.2.2.1. Computational model

The geometry of flat-bottomed hopper is depicted in Figure 2.6. The characteristic dimension of outlet D is assumed to be related to maximal diameter d of the particle as $D = 10d$. The thickness of the hopper at the bottom is assumed to be $b = 5d$. The dimension of the top hopper edge is $L = 2.33D$, while the overall height of the hopper is $H = 3.33D$. Assuming that $d = 0.06$ m, the main geometrical parameters of the hoppers are defined as: $b = 0.3$ m, $H = 2.0$ m, $L = 1.4$ m, $D = 0.6$ m.

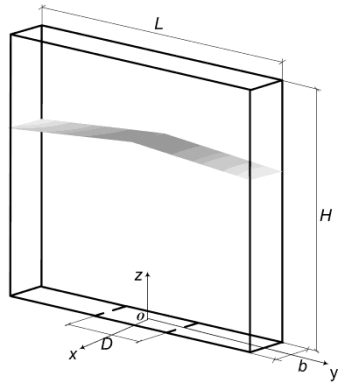

Figure 2.6. Geometry of the hopper, [288].

The granular material is modelled as an assembly of $N = 1{,}980$ particles. The values of the particle radii R_i varying over the range of 0.03 and 0.035 m are generated having a uniform distribution. The particle's physical data for artificially assumed as the visco-elastic material are given in Table 2.2. The assumed value of the normal viscous damping coefficient constitutes about 10% of the critical damping coefficient in collision of two particles. Inter-particle and particle-wall friction is specified by the same friction coefficient μ, indicating the case of fully rough walls. The hopper walls (including the bottom) are assumed to be rigid and are considered as the fixed boundaries possessing friction.

In general, filling comprises the settling of the material into the hopper. The discharge means flow of material from the hopper due to the orifice opening. Processes of the filling and discharge can perform different simulation scenarios which can affect the stress transmission within granular matter as well as the

geometry of granular structure. The choice of simulation scenario must highlight an attempt to achieve as close as possible situation encountered in real hoppers as well as to save the computation time needed.

Table 2.2. Basic data of granular material

Quantity	Symbol	Value
Density, kg/m^3	ρ	500
Poisson's ratio	ν	0.30
Elasticity modulus, Pa	E	$0.3 \cdot 10^6$
Shear modulus, Pa	G	$0.11 \cdot 10^6$
Rolling friction coefficient	μ_R	0
Normal viscous damping coefficient, 1/s	γ_n	60.0
Tangential viscous damping coefficient, 1/s	γ_t	10.0

To obtain the compromise between these requirements, the filling is simulated by the sedimentation of particles *en masse*, i.e., all particles start to fall due to gravity acceleration and to mix up when the initial particle velocities are also artificially imposed. During the particles settling on the bottom in the filling process, the orifice is kept closed until a quasi-static state occurs. The discharge process begins after an instantly opening of the orifice. During the discharge no material re-supply from above is made.

By following this scenario, the initial state for commencing of the filling is generated in the following manner. The space within and above the hopper was divided into the cubic cells as an orthogonal and uniform 3D grid of 0.1 m. Initially, at time $t = 0$, the particles are embedded free of contact into the centres of these cells. The fields of initial velocities are defined randomly with uniform distribution with their magnitude varying in the range from 0 to 0.3 m/s.

The behaviour of a granular material during filling was controlled by the evolution of the total kinetic energy of granular material expressed as the sum of all particle energies due to translational and rotational motion. The evolution of the kinetic energy to zero value is assumed to be a stabilization indicator of the filling process of granular material allowing de facto to interrupt the simulation.

The time-evolution of kinetic energy reflects a sophisticated integral behaviour of the flow. Generally, frictional particles lose energy not only due to material viscous damping but additionally due to friction. In this case, the particles start to rotate,

affecting the translational motion. The effect of friction is manifested throughout the competing between static and dynamic friction forces. This competition leads to significant fluctuation of relative inter-particle contact velocities $\mathbf{v}_{t,ij}$, particle velocities $\mathbf{v}_i$ and, in turn, the evolution of the total kinetic energy. Frictionless material is subjected, however, to a higher fluctuation since particles are able to dissipate the kinetic energy only due to the damping in the normal direction. Stabilization of the total kinetic energy means that most of particles have dropped on the bottom and cannot essentially change the positions relatively to their neighbours.

Stabilization of the granular flow is a rather hypothetical state which may achieve within the limits of the required tolerance. On the basis of computational experience, the state of rest is indicated by the level of total kinetic energy equal to $0.3 \cdot 10^{-6}$ J which specifies the average particles flow velocity equal to 10^{-6} m/s and practically negligible small average acceleration. It is indicated as time instant t_1 required for interrupting of filling. It depends on the friction coefficient value. Hereby, the end of filling is defined as t_1=10 s for the frictionless material (μ=0) and t_1=6.59 s for frictional (μ=0.3) and t_1=6.09 s for highly frictional materials (μ=0.6), respectively.

Consequently, all dynamical parameters of particles obtained at the end of the filling process are assumed to be the initial conditions for the simulation of the discharge process, while a new time scale referred to initial discharge time $t = 0$ is employed for the sake of comparison.

2.2.2.2. A microscopic analysis

The implementation of the discrete element method for the analysis of the filling and discharge processes provides the basis for detailed microscopic-macroscopic analysis of granular material phenomenon in hand. In the framework of current approach, microscopic analysis comprises investigation of a time-evolution of the mean coordination number of the particle material during filling, variation of the inter-particle contact forces within granular material and the analysis of the particle velocity fields.

The coordination number is the number of contacts for the given particle. It represents a microscopic parameter of granular material and the number has widely been used for the characterization of homogeneity of granular structure. The mean value of the number characterizes an assembly of particles and is computed as the

sum of all particle contacts divided by the number of particles. The time evolution of this characteristic during filling is plotted in Figure 2.7.

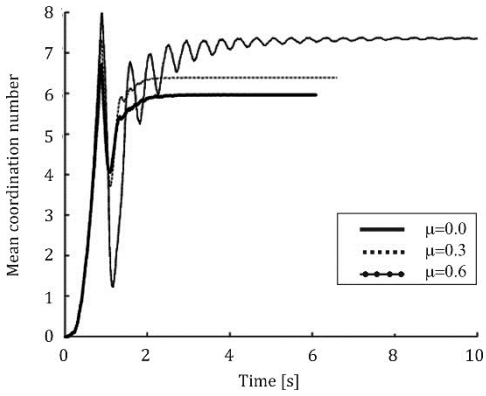

Figure 2.7. A time evolution of the mean coordination number of the material during filling, [288].

As it is seen in Figure 2.7, higher values of the coordination number are obtained for frictionless material, while for frictional media, this number decreases with an increase of the particle friction coefficient. The values of the mean coordination number fluctuate in time, and it should be noted that these fluctuations have considerable similarity to the total kinetic energy of particles.

The time evolution of the mean coordination number of the particle may classify arbitrary into three stages. The initial stage indicates the densification phase. It signifies that the particles gradually come into contact with each other transforming from the less contact of the particles settling indicated by "zero" coordination number up the maximal number indicating contact with the hopper's bottom. At time instant t=0 s, the "zero" coordination number indicates that before the application of gravity acceleration alloving to start the filling process the spheres are initially generated contact-free. It can see clearly on the graph Figure 2.7, where at time instant 1s the material is characterized by the maximum value of the coordination number in the range between 6.5 and 8, depending on the inter-particle friction coefficient.

The second stage indicates rarefaction phase. After a very short period of the contact, the particles rebound from the bottom leading to drastic material rarefaction

and decreasing the mean coordination number of the particle. In particular, for frictionless particles, this decreasing is up to 1.5, while the frictional assemblies are less sensitive to this loosening of packing (coordination number is about 4) since the particles additionally dissipate their energy due to friction and undergo the confined motion.

Starting from 2÷3 s the evolution of the mean coordination number of particle transforms into the stage of stabilization which is characterized by the values equal to {7.34, 6.38, 5.96} for μ={0, 0.3, 0.6} respectively, remaining almost constant until the end of the filling. In fact, the results obtained depend on the hopper parameters and filling scenario. However, in particular a lower connectivity of the granular structure formed by frictional particles can attribute to the formation of small arches within the material. It is noticeable, that the maximum values of the mean coordination number of the particle obtained before the first material rarefaction (due to the contact with the bottom) cannot reach this maximum value until the end of the filling process.

The microscopic state of the particles may be defined by contact forces acting on each individual particle while capturing the values of these forces render the quantitative information about the nature of granular structure. In the other case, the analysis of contact force network provides the qualitative information about the heterogeneity of granular structure. Consequently, applying the same methodology we consider contact force distribution obtained at the filling and the discharge.

Thus, the character of filling and discharge, indicating the transitional and final stage of the flow in hoppers, is illustrated in Figure 2.8. and Figure 2.9. The colour-bar plotted in these Figures quantitatively represents particle contact forces, $\sum_{i \neq j} |\mathbf{F}_{ij}|$. The transitional and the final stages for frictionless (μ=0) and frictionally during the filling process, (cf. Figure 2.8). It is easy to indicate the forming of material layers having a different contact force transmission within the hopper. In the upper layers of granular structure these forces are distributed more uniformly, while the layers above the bottom are characterized by non-uniformly distributed contact forces.

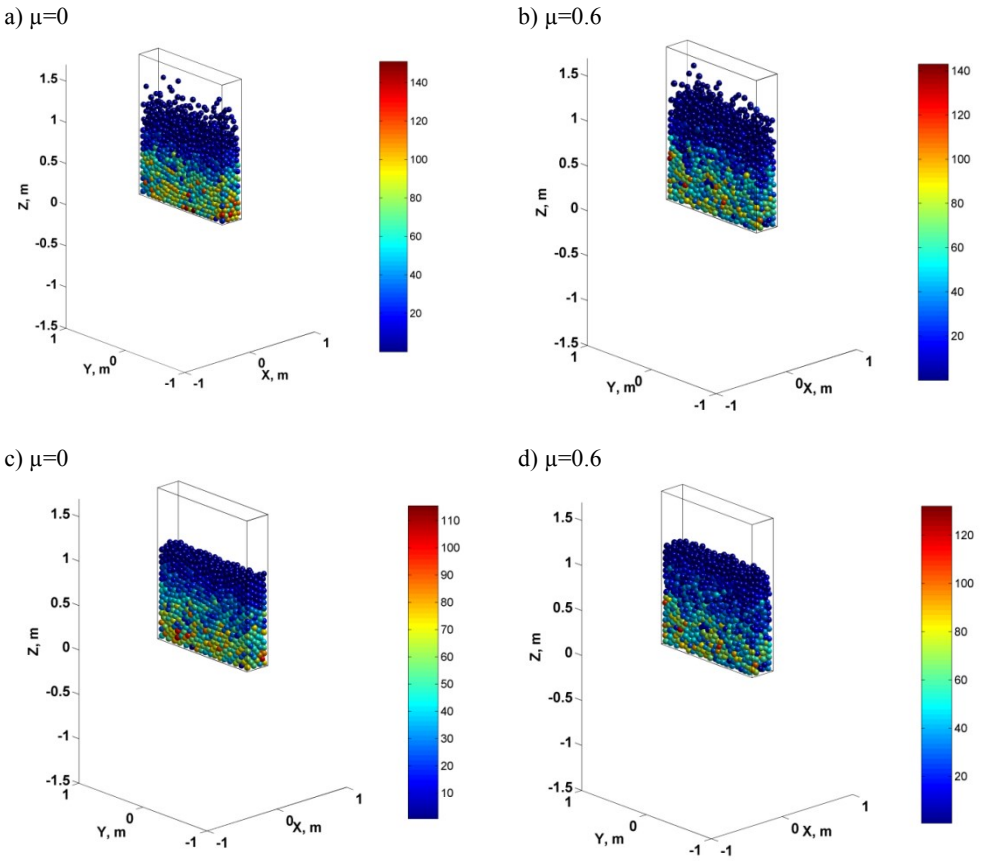

Figure 2.8. Filling flow and contact forces (measured in newtons):
a, b) transitional (t = 1 s); c, d) final stages, [288].

The magnitudes of contact forces at the top surface are much lower compared to those at the bottom layer since they grow towards the direction of gravity force. Comparing transitional and final stages, it can be seen that the particle acceleration during the filling flow affects the magnitudes of particle contact forces. In particular, the maximum value of these forces in the transitional state is higher than in the final stage. In the transitional state, it can also be seen that frictionless particles are subjected to a higher maximal contact force of the magnitude equal to 155 N as compared to frictional forces (140 N) since the last dissipate additional portion of kinetic energy during frictional contacts.

As it can also be seen, the particle friction produces an increase of the local heterogeneity of the particle contact force transmission which is higher for rough particles (μ=0.6) than for smooth ones (μ=0). It can be also demonstrated that there are some rough particles subjected to much higher contact forces in comparison with the smooth ones in the lower part of the hopper. It is also seen that due to the arching, rough particles located at the vertical wall (cf. Figure 2.8d) form unfilled voids unlike frictionless particles (cf. Figure 2.8c).

In general, the discharge process in flat bottomed hopper starts with progressing dilation wave that spreads up to the top surface of material. The depression zone above the orifice occurs at some material height and it deepens with continuation of the discharge process. Its sides become steeper and when the slope of these sides reaches the angle of repose, some of the particles cascade down to the central part of the material that moves faster. The nature of granular flow in the flat-bottomed hopper contains characteristic features of the funnel flow. For brevity, the transitional stages of the discharging flow for frictionless (μ=0) and for rough (μ=0.6) particles are captured at time instant t=0.2 s and it depicted in Figure 2.9.

a) μ=0 b) μ=0.6

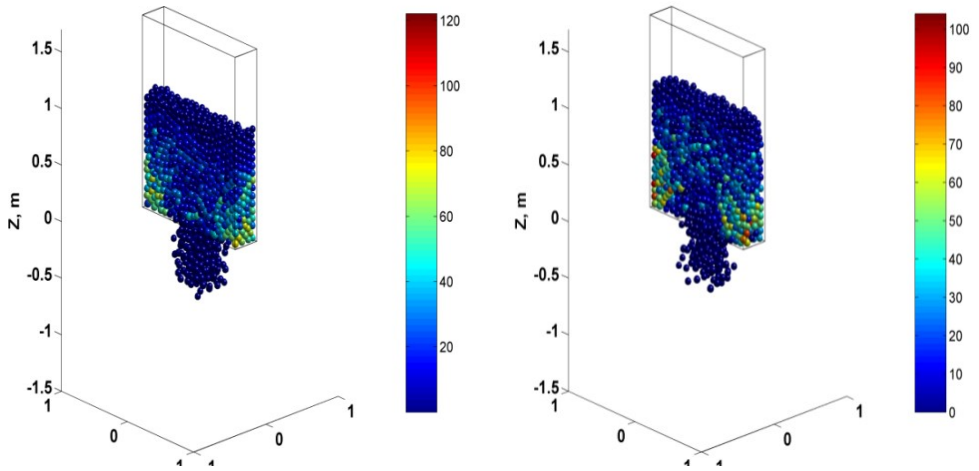

Figure 2.9. Discharge flow and contact forces at time instant t = 0.2 s (forces measured in newtons), [288].

These plots demonstrate the described tendencies concerning the local heterogeneity of the particle contact force transmission within granular material. It is also indicated that there are much rougher particles subjected to higher contact forces in comparison with the smooth ones. A common feature of the discharge in flat--bottomed hopper can be observed, namely the particles located above the orifice up to the top surface of material are practically unloaded when the orifice is opened.

Significant information on particle connectivity and contact forces are obtained by considering particle contact forces network. Figure 2.10 and Figure 2.11 show such networks in the form of lines connecting the contacting particles. The thickness of these lines is scaled to the force magnitude that is determined by the magnitude of the maximum contact force. Hence, we can obtain only the qualitative comparison between the networks.

a) μ=0 b) μ=0.6

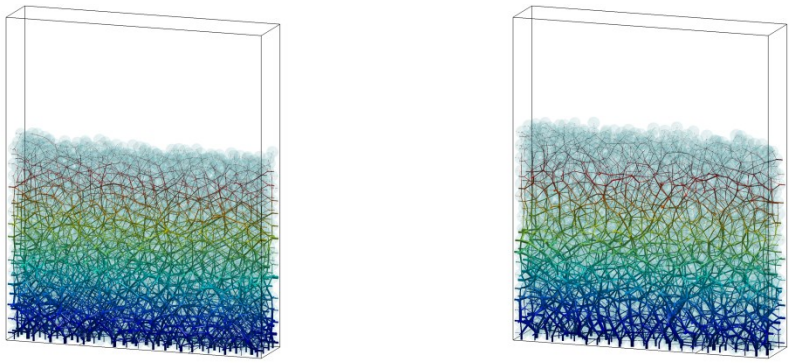

Figure 2.10. Contact forces network at the end of filling, [288].

As the graphs in Figure 2.8 and the plots in Figure 2.10 show, the particle contact forces tend towards the gravity force. For frictionless particles, the contact force magnitude network is quite uniform and isotropic within the material depth as well as over all particle contacts. The particle friction induces an increase of local heterogeneity in contact force transmission. Frictional contacts provide less connectivity; however, large contact forces can exist in the particles located in lower part of the material and close to the walls. Large contact forces are able to form stress arches leading to the material weight transmission towards the hopper's walls.

The spatial contact force evolution within material during the discharge is plotted in Figure 2.11. It can indicate that large forces are found in the particles located at the walls around the bottom corner. Particles located in the upper part have smaller contact forces. Small forces are also found in the particles located in a region of "a free-fall arch", which is adjacent to the orifice where particles can accelerate almost freely.

a) μ=0 b) μ=0.6

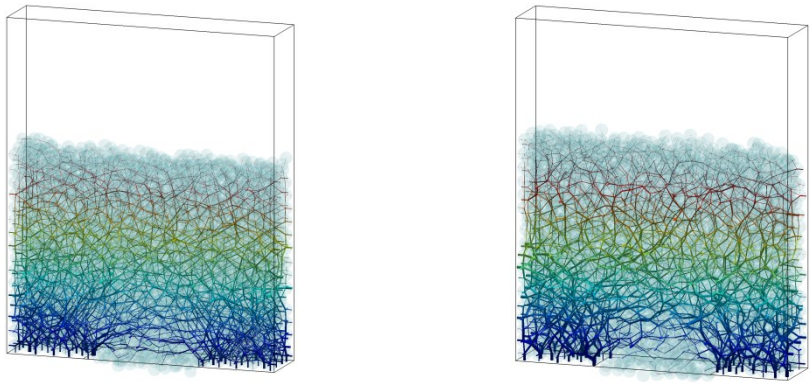

c) μ=0 d) μ=0.6

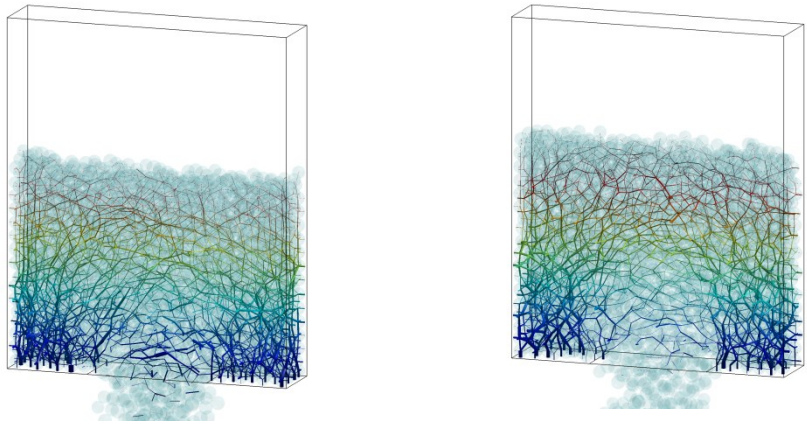

Figure 2.11. Contact forces network during discharge at: a, b) t = 0.04 s; c, d) t =0.2 s, [288].

From the plots depicted in Figure 2.11b, d it can evidently see that the height of "free-fall arch" region at the initiation of the discharge (t=0.04 s) is of the order of ½ the orifice width, D (cf. Figure 2.11b), while later, the arch remains constant and approximately equal to D. Above this region particles are packed together confining each other's motion while below. It can see that the particles fall almost without contacts. In the case of frictionless particles (cf. Figure 2.11a, c), it can demonstrate that the region of "free-fall arch" does not exist and particle outflow depends on the material's height.

Let us consider the discharge flow kinematics. The distribution of velocity fields has been extensively studied by the macroscopic experiments and simulations. However, the detailed motion of individual particles in the discharge flow is difficult to measure experimentally, particularly in 3D cases. Thus, according to the classical macroscopic description of the discharge flow, there are five zones of flow inside the flat-bottomed hopper: stagnant zones located at the bottom corners, a plug flow zone in the upper part, a converging flow zone, in the lower part, a transition zone from plug flow to converging flow (where particles move toward the orifice), and a free particle fall zone. From the initial transient stage (t=0.04 s) up to the pseudo-steady (t=0.4 s) flow, such flow patterns can be observed in Figure 2.12, where the velocity vectors of individual particles are presented.

The initial transient stage of the discharge runs in the same manner for frictionless and frictional particles (cf. Figure 2.12a, b), however the latter flow proceeds quite differently. Particularly, it is seen in Figure 2.12 (e, f) that the converging flow zone is enclosed from both sides by stagnant zone of material with "zero" particle velocities. Stagnant zones form two flow converging boundaries whose shape changes during the discharge. The inclination of these boundaries depends on the particle and wall friction. Noticeable, the frictionless particles have a less distinct flow convergence than particles with friction contacts, (cf. Figure 2.12e, f). It observes that plug flow zone in the case of frictionless particles runs almost vertically and can treat as mass flow zone, (cf. Figure 2.12c, e).

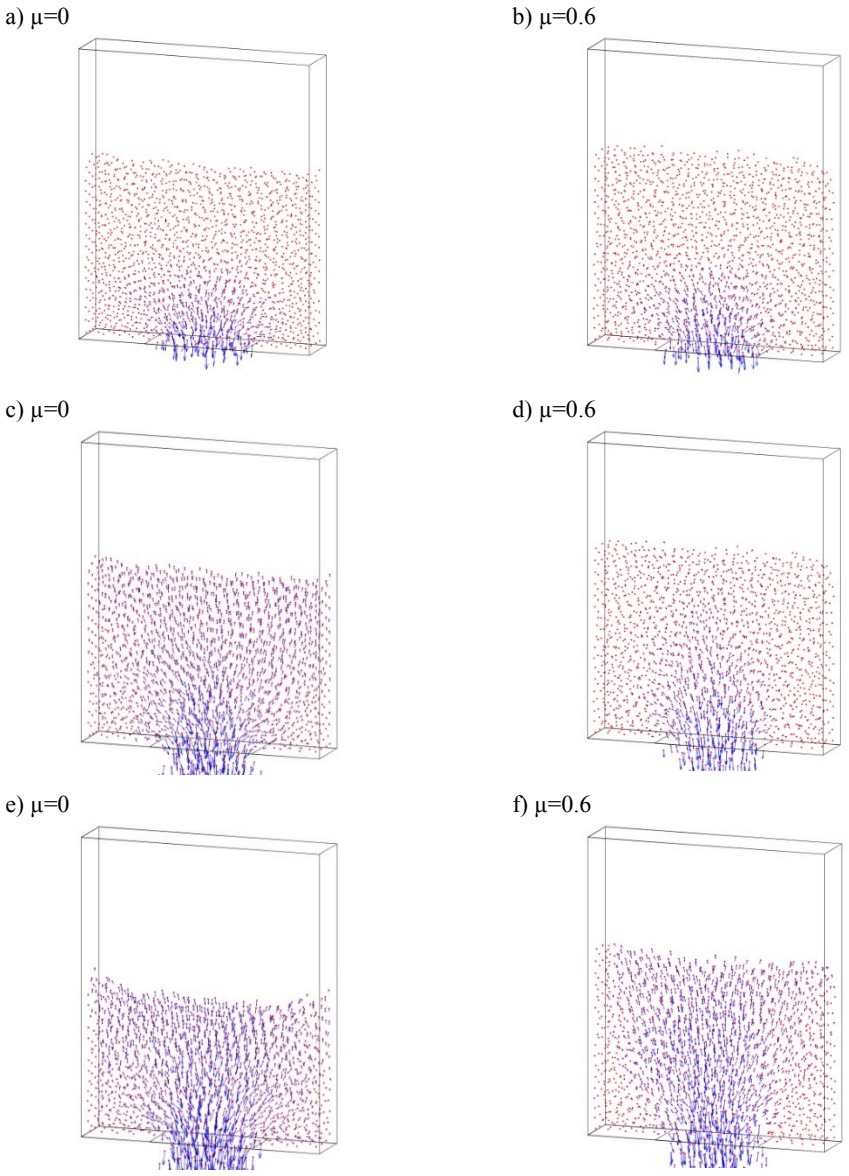

Figure 2.12. Particle velocity fields during discharge flow at: a, b) t = 0.04 s; c, d) t = 0.2 s; e, f) t = 0.4 s, [288].

2.2.2.3. A macroscopic analysis

When the contact forces acting within the granular material between the particles and those acting between particles and walls are known, the following simulation may be adopted to calculate the normal and shear stresses acting on the hopper walls. The values of the wall stresses at different heights are obtained by the averaging over the height equal approximately to four particle diameters. The results obtained are compared with well-known Janssen's analytical solution which is used in most standards for predicting the filling pressures in flat-bottomed section of hoppers. The identification of Janssen's macroscopic parameters from the simulation correspond to the bulk density values equal to 335, 325 and 320 kg/m^3 for cases of μ=0, μ=0.3 and μ=0.6, respectively. While internal friction angle, φ, following to [230], is determined by the angle of stagnant boundary zone assumed to be an internal slip plane. The internal friction angle values equal to $\varphi=6\div12^0$ are determined by specifying the angle of repose of granular heap in the additional experiments performed with the same composition of material but using a smaller orifice. These experiments are not demonstrated here. The wall pressure fields obtained at the end of the filling and Janssen's macroscopic prediction are shown Figure 2.13a. The pressure distribution captured during discharge is plotted in Figure 2.13b.

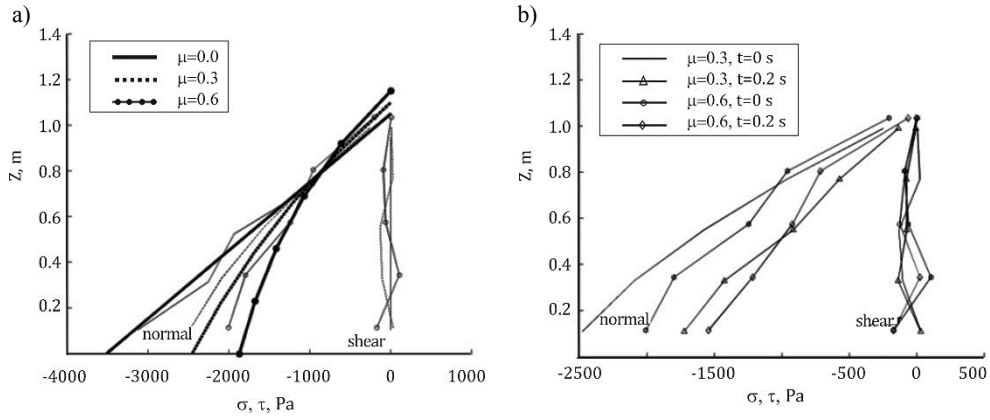

Figure 2.13. Evolution of wall pressure at the end of filling (a) and during discharge (b). bold line – Janssen's prediction, [288].

Despite a small number of particles used in simulation the obtained pressure dependence on material height is quite consistent with macroscopic prediction. As it can see in Figure 2.13a, the increased values of the friction coefficient results in a transition from fluid-like to granular material behaviour.

During the discharge (cf. Figure 2.13b), the wall pressure is lower than at the end of the filling. The overpressure during discharge is always very remarkable in the wedge shaped hopper, where due to the converging flow towards the orifice the passive stress state can develop, while in the flat-bottomed hopper this increase is lower and mainly depends on the hopper geometry and the angle of stagnant zone resulting in the converging flow. In our case, the drop in wall lateral pressure during discharge is mainly attributed to relatively large size of orifice and a squat shape of hopper resulting in a quick reduction of material weight and as well as its dilation upon orifice opening. The propagation of material dilation is studied below.

Thus, the dilation reduces the value of normal stress at the wall. The effects of material dilation are determined by the distribution of bulk material porosity fields within the hopper.

The macroscopic variable, such as the bulk porosity, reflecting the packing structure of the material within the hopper and directly affecting the bulk density can be considered in terms of the spatial distribution of the porosity fields within the granular material. The porosity is obtained by the averaging of particles volume within the chosen elementary volumes represented by spheres. The volume of the granular structure computed within the representative sphere is defined by excluding the overlaps of the particles. The volume of the representative sphere adjacent to the wall is also defined relying on the sphere-wall intersection geometry. Finally, the computed volumetric data of the porosity are displayed on a spatial grid, (cf. Figure 2.14).

In general, it has been well-established that the coordination number decreases with the porosity. Such correlation remains unchanged within the whole period of the material packing history. For brevity, the spatial evolution of the porosity within the hopper is restricted here for the frictionless particles with μ=0.6, (cf. Figure 2.7).

The obtained spatial distribution of the porosity at the end of filling is shown in Figure 2.14. Independently of the roughness of the particle, the formation of the densest assemblies is characterized by the lowest values of the porosity and is observed in the lower part of the hopper, while the loose granular structures are

located in the upper part, near the walls and in the narrow boundary layer above the bottom. Thus, in the case of the frictionless granular material (μ=0), the dominating porosity values are n=0.27÷0.3, while for μ=0.3 and for μ=0.6 these values are n=0.29÷0.32 and n=0.33÷0.36, respectively. The depth of the dominating porosity zones is spread up to the elevation of 0.7÷0.9 m.

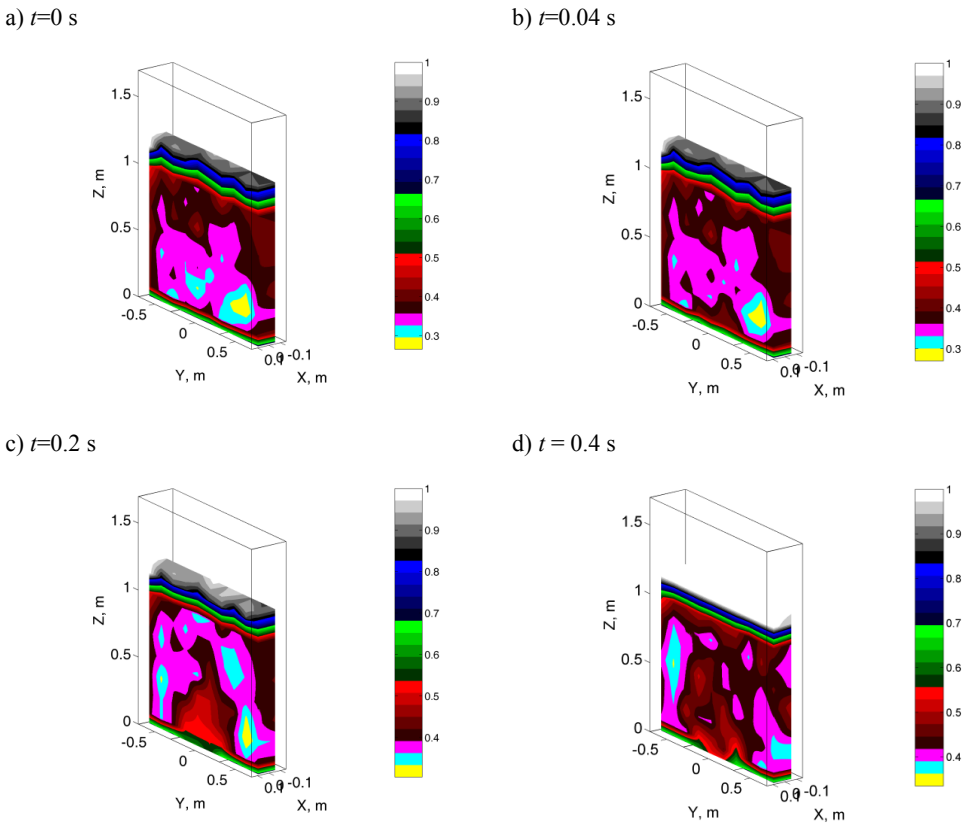

Figure 2.14. Time evolution of the porosity fields during discharge (μ=0.6), [288].

The captured evolution of the porosity fields (cf. Figure 2.14b–d) within the hopper clearly exhibits well known phenomenon that the orifice opening generates a dilation of the bulk material. In a short time instant after orifice opening (t=0.04 s), the zone of material rarefying with porosity n=0.39÷0.42 begins to form in the vicinity of the outlet, (cf. Figure 2.14 b). At time instant t=0.2 s this porosity wave reaches about 0.8 m of the material height, while the dilation above the orifice

increase up to the porosity values n=0.5÷0.53 (cf. Figure 2.14c). Later (at t=0.4 s), each zone of material up to the top of the filling is reached by this dilatancy wave, (cf. Figure 2.14d).

Considering the plots shown in Figure 2.14b–d and Figure 2.12b, d, e it is easy to note that high porosity corresponds to high velocities of the particle.

Let us examine discharge flow rate (i.e. mass discharged flux) through the orifice. By generalization of numerous empirical observations of the granular flow [128] the main conditions defining a constant discharge rate, when the rate is effectively independent of the quantity of material in the hopper characterized by material height z, were established: $z > 2D$; and $L > 2.5D$. Actually, these conditions highlight the fact about the sufficient material quantity within the hopper which allows obtaining a constant flow rate in time. Hence, for appropriate z and L the rate depends only on the bulk density, the orifice diameter, gravity acceleration and the material friction. In opposition to in-viscid liquid the discharge flow rate is proportional to $D^2\sqrt{2gz}$ (where g is the gravity acceleration). For the rectangular orifice, the discharge rate can be calculated by the following relation given in [128]:

$$\frac{\mathrm{d}m}{\mathrm{d}t} = \frac{8C}{\pi\sqrt{2}}\rho\sqrt{g}\frac{\left((D-kd)(b-kd)\right)^{3/2}}{(D+b-2kd)^{1/2}}, \tag{2.31}$$

where ρ is the bulk density of the whole material filled, kd is the width of the so-called "empty annulus", C is the material constant which is assumed to be 0.64 for exceptionally smooth spherical particles and 0.58, for the rough ones.

The empirical factor k is determined experimentally and is claimed to be derived from the region near the orifice surrounded by the particles obstructing the passage. This is consistent with the concept of "an empty annulus" proposed by [127]. Values of k may vary in a broad range, in particular, from 0.94 for the glass bed [141] up to 4 for the sand, [75].

The time evolution of particle flow through the orifice captured in Figure 2.15, clearly confirms the concept of "empty annulus". In these plots, the fewer particles can be detected adjacent to the orifice corners than in the central region. In particular, it can see that kd changes from zero to grain diameter (cf. Figure 2.15a), over the range of 0.5÷1 by about 2 (near 825 particles in Figure 2.15c). Hence, it is reasonably to ssume k=0.75.

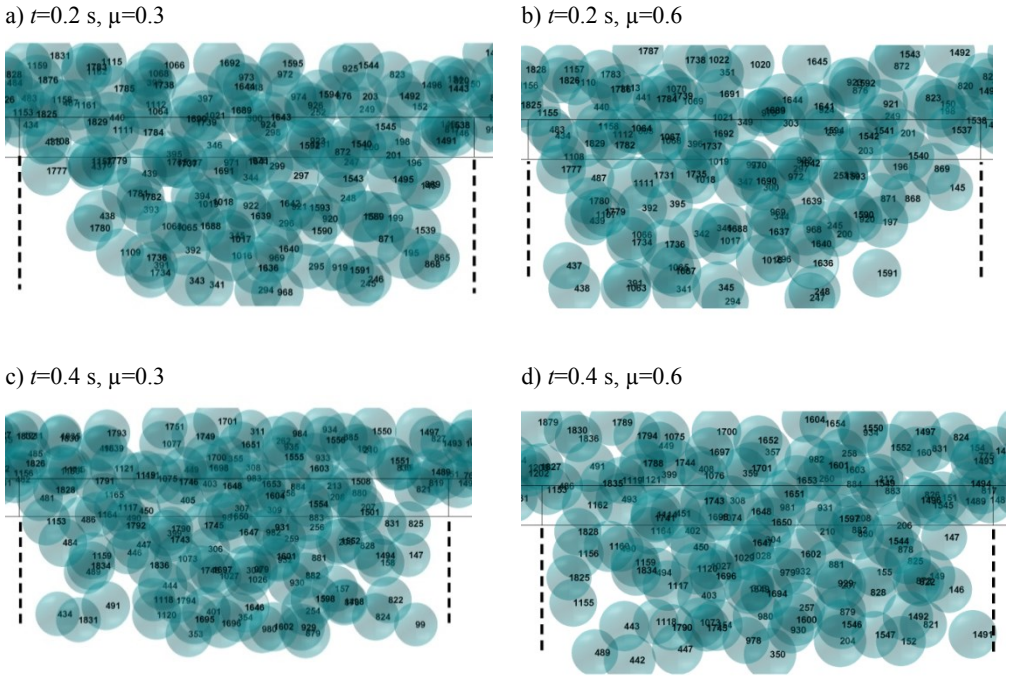

Figure 2.15. The time evolution of phenomenon "venna contracta" through the orifice, [288].

Thus, the material flow rate is measured in the discharge simulation and is compared with the theoretical prediction specified by Eq. (2.31), (cf. Figure 2.16). The bulk density is derived by the averaged porosity. In particular, values of 295, 270 and 260 kg/m^3, for cases of μ=0, μ=0.3 and μ=0.6 were obtained, respectively.

As it can see in Figure 2.16, the current simulation indicates the empirical evidence that an increase of the particle friction coefficient reduces the rate of discharge. It is seen that this reduction represents a mild function of the particle friction coefficient and is adequate to the experimental observations. For frictionless particles (μ=0), an expected nonlinear variation of mass discharged flux is observed. For frictional particles, the discharge rate has some disparities over time, however, in the case of μ=0.6 the constant rate can be observed in the time period from 0.2 s to 1 s.

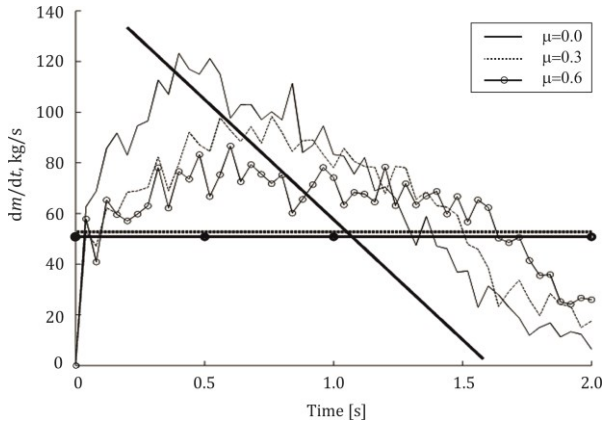

Figure 2.16. Evolution of the discharge rate. Bold line – macroscopic prediction by (2.31), [288].

The agreement between the prediction based on Eq. (2.31) and the results of the simulation would be closer, if the particle sizes were smaller resulting in a much greater number of particles and a closer approach to the continuum. Furthermore, the variation of the discharge flow rate in time is generally attributed to small height of the hopper. In such a case, the material discharged re-supplying into the hopper allows to obtain more steady discharge flow with fewer fluctuations, [128].

"Main content of this chapter has been published in Archives of Mechanics, 59, 3, 231-257, 2007".

2.2.2.4. Concluding remarks

Filling and discharge processes of the granular material in the flat bottomed rough-walled hopper are simulated by the three dimensional discrete element model. The model is based on a single particle contact mechanics constitutive laws with Hooke's spring interaction, static and dynamic frictions as well as viscous damping forces. The main focus of the paper was the qualitative illustration of the physical processes inside the time dependent flow of granular material and the consistency of micro and macro descriptions.

Generally, despite the small number of particles in the current analysis the consistency of micro and macro descriptions has been proved. The micromechanical aspect of the macroscopically observable phenomenon is additionally exhibited by introducing the microscopic variables, such as coordination number, inter-particle

contact forces or particle displacements and velocities defined at particle scale. The analysis performed shown that particle friction has a major influence on the material flow kinematics, the changes in porosity and stress fields. On the basis of computational simulation, the following conclusions may summarize as follows:

- The consistency between the obtained wall pressure and its macroscopic equivalent based on Janssen's formula was found considering the end of filling stage for frictional and frictionless particles. In the discharge, the obtained drop in pressure was affected due to squat shape of hopper and relatively large orifice inducing a sudden reduction of the material weight.
- Evolution of material packing during the filling illustrates that the final quasi--static state in the hopper is characterized by the lower coordination number as compared to the highest value reached by the first densification wave. Such aspect is relevant to the particle viscous damping/elasticity balance and filling scenario ensuring a close packing structure during particle settling in the hopper.
- The obtained spatial distribution of bulk porosity within granular material has demonstrated the fact about the propagation of the experimentally observed dilation wave occurring after opening of the orifice. During a short period this wave reaches the top material surface and occupies almost the whole material causing the decompression of particle contact forces, which in turn leads to the reduction of wall stresses.
- Microscopic motion of particles during the discharge illustrated by the velocity profiles corresponds qualitatively to macroscopic profiles experimentally observed in real funnel-flow hoppers. Time evolution of bulk porosity and the individual particle velocities simply demonstrate the fact that high porosity corresponds to high particle velocity.
- The obtained spatial distribution of the particle contact forces within flowing frictional particles demonstrated a decisive role of the inter-particle friction and exhibited fundamental differences between frictionless and frictional granular matter by characterization of the so called "free-fall arch" region.
- The concept of so-called „empty annulus" or "vena contracta" and a mild influence of particle friction on discharged mass flow rate have also been highlighted in the current analysis. The existing predictions of the steady-state discharged mass flow rate of the frictional material present slightly lower bounds of the computationally simulated evaluations.

The results obtained are considered as preliminary investigation of real grain materials. For more accurate simulation the aggregate of larger number of grains should be analyzed with a realistic grain size distribution function. This will constitute a subject of future studies.

2.2.3. Microscopic and macroscopic analysis of granular material behaviour in 3D wedge-shaped hopper

2.2.3.1. Mathematical model

The granular material is considered to be an assembly of N=20,400 spherical particles. The particle radii R_i are close-distributed ranging from 0.0128 to 0.017 m, with the coefficient of variation equal to 8.1% and are defined randomly by a uniform distribution. Hereby, such variation in particle radii may allow avoiding a crystal-like fabric produced by mono-sized material [290] and problems relevant to a spurious stress distribution near the walls, [230]. Three different values of the particle friction coefficients $\mu=\{0, 0.3, 0.6\}$ are introduced into the analysis. The physical particle data for artificially assumed material are the same as summarised in Table 2.2. Note, the value $\gamma_n = 150$ s^{-1} is used only in the case of frictionless particles.

The configuration of the hopper is presented as a three-dimensional wedge-shaped wall structure, (cf. Figure 2.17). The hopper walls are assumed to be rigid by treating them as fixed boundaries with friction (including the bottom). Friction and viscous damping coefficients of the walls are assumed to be the same as those for the particles. The characteristic dimension of the outlet, D, is assumed to be dependent on the maximal diameter d, where d=0.034 m. In general, the size of the orifice affects the material density, propagation of dilation wave during material flow and can cause material blockage. Thus, to prevent material blockage, the size of orifice is assumed to be $D = 17.7d$, provided that $D > (4 \div 6)\, d$, while $L = 3.3\, D$, and $H = 2.88\, D$. As a result, the half angle of the hopper is equal to $\alpha = 22°$. The thickness of the hopper is assumed to be $b = 8.8\, d$.

2.2.3.2. Mathematical modelling of the filling process

Granular flow in hoppers is a continuous process, hence, its simulation may consider at several stages, reflecting different physical as well as technological aspects of this

complex phenomenon. In general, filling comprises settling of the material in the hopper, while the discharge flow means the flow of the material out of the hopper, starting at the instant of opening the orifice. During the particle settling on the bottom in the process of filling, the orifice is kept closed until a quasi static state occurs.

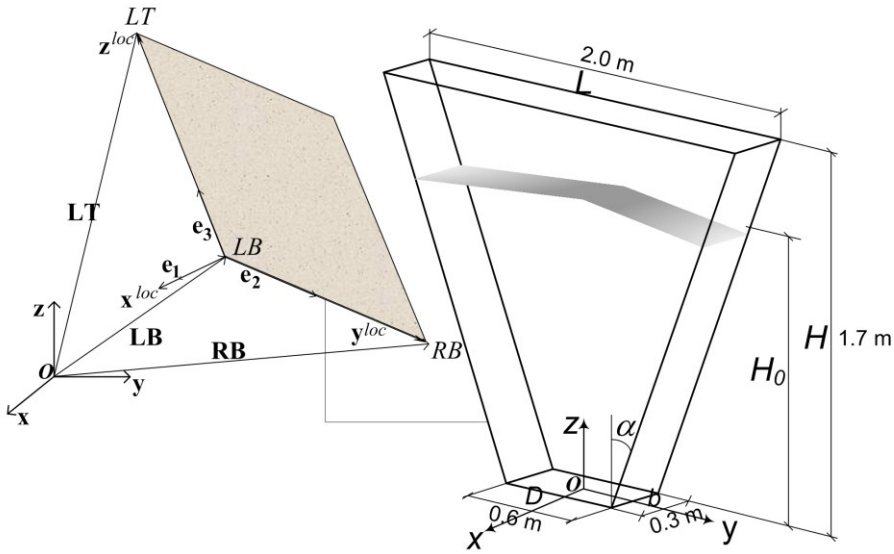

Figure 2.17. The main geometry of a wedge-shaped hopper, [238].

Theoretically, in the process of filling, the major compressive stresses in the hopper are directed downwards, since they are caused by the weight of bulk material. In the discharge process taking place in wedge-shaped hopper, the major stress is directed horizontally, since a convergent flow towards the orifice contracts horizontally and expands vertically the bulk material.

Analytical prediction of wall pressure at end of the filling process for 3D wedge--shaped hopper may be obtained by using a simple slice approach while the analytical prediction of the discharge pressure, when the velocity of the particles varies with time and with their location (i.e. unsteady discharge process), is a theoreticaly complicated task, [2, 128]. Thus, the computational wall pressure obtained after the filling process will verify with continuum-based analytical solution, while the discharge pressure comparison with analytical solution will be omitted.

In computational analysis, the state of the filling is induced by fall the particles *en masse* due to gravity force and random particle velocities imposed. For the time integration procedure, a constant time step, $\Delta t = 10^{-5}$ s, is chosen to be about 1500 times smaller than the time of the maximum overlap of two particles in the collision. The behaviour of granular material during filling was controlled by considering the evolution of the total as well as rotational kinetic energies which are expected to tend to zero indicating complete stabilization of motion of the granular material. The filling was interrupted at time $t = 10$ s by the so called "zero" total kinetic energy that is computed by summation of the particle energies produced by the rotational and the translational motions. After interruption, the average scalar flow velocity is equal to 10^{-6} m/s and 10^{-3} m/s is obtained, for frictional and frictionless particles, respectively. This state of the particles is treated as a quasi-static regime of the filling. Since a negligibly small average scalar accelerations varying over the range of $1–2 \cdot 10^{-3}$ m/s^2 is obtained, it is assumed that the stresses within the bulk material and on the walls can be induced due exclusively to particles own weight.

The evolution of the system's kinetic energy is depicted in Figure 2.18.

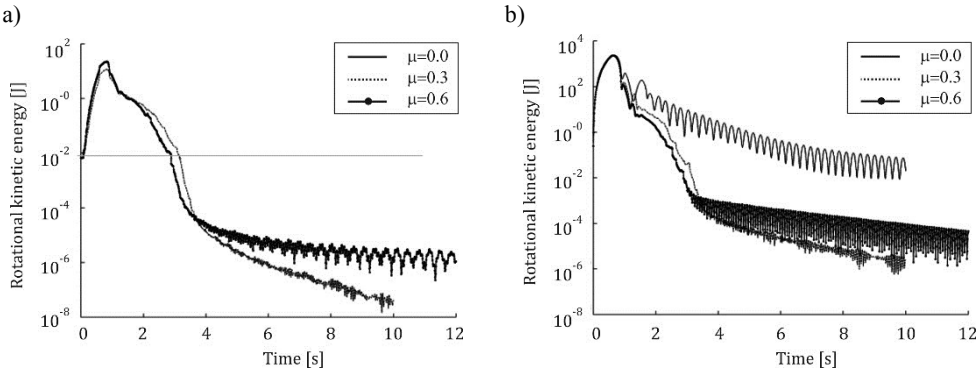

Figure 2.18. The evolution of rotational (a) and total kinetic energy (b) during the filling for particles with three values of the friction coefficient, [238].

Generally, the total kinetic energy depicted in Figure 2.18 can be treated as an integral characteristic of granular material flow. The rapid increase of the total kinetic energy (cf. Figure 2.18b) within 0.5 s presents the falling of particles into the hopper. The beginning of increasing of the particle rotational energy obtained at 0.1th s of the filling indicates the fact that the particles come first into contacts with each other and due to the friction start rotating gradually losing their own kinetic

energy. In contrast, frictionless particles are expected to avoid rotational motion during their collisions and this is found in graphs of the rotational energy, (cf. Figure 2.18a). A rapid decrease of the kinetic energy within 0.5–2.5 s means that most of the particles have fallen onto the bottom and cannot essentially change the positions relatively to their neighbours. For frictional particles at 3.5–4th s, the increased number of contacts induces the slowing down of particle fluctuations. Frictionless material at this time, however, is subjected to a higher fluctuation since the particles are able to dissipate the kinetic energy due only to the damping in the normal direction.

The maximal coordination number, i.e. the maximum number of particles in contact with another particle can be briefly considered for the indirect characterization of granular material structure packed in terms of the particle friction. In particular for frictionless particles, the maximal coordination number is equal to 12, while, for the frictional particles, this equivalent consists of 11 and 10 for μ=0.3 and μ=0.6, respectively. Whilst the coordination number for all walls is equal to 3381, for μ=0; 3377, for μ=0.3 and 3360, for μ=0.6, respectively. Accordingly, this parameter indirectly shows that the porosity of frictional material as well as the particles adjacent to the wall is higher than for frictionless particles.

The time evolution of total and rotational kinetic energies for particles with μ=0.6 has a different distributive character in comparison with the material consisting of the particles having μ=0.3. This can attribute to a relatively small shear dissipation coefficient γ_s used in the current simulation which, in the case of μ=0.6, leads to a more expressed competing between the static and the dynamic friction forces. The significantly smoother characteristics of total kinetic energy after the 4th s of the flow obtained in additional simulations performed with the increased value of γ_s.

The character of the total kinetic energy can also reflect by inspecting the time evolution of particle velocity vectors. The mid-plane fields of velocity vectors captured during a quasi-static state of the filling are presented in Figure 2.20 (vectors scale factor equals to ten). These fields are constructed by the velocity vector of the individual particles and provide a microscopic insight into a quasi-static regime that occurs during the filling. The frictional material was subjected to quasi static vortex-like velocity fields presented in Figure 2.20. In general, these patterns are similar to the turbulence velocity fields that occurred in fluid dynamics. On the other hand, a frictionless material is a subject to a radial nature of velocity distribution during quasi static conditions. Similar motion patterns were recognized

in compaction tests under high levels of deviatory strains in [291]. The presence of a vortex-like velocity patterns in a quasi-static behaviour of granular material, when the static friction prevails between contacting particle with others or with the walls, lead to a sophisticated functional dependency of $\mathbf{v}_{t,ij}(t)$ in Eq. (2.6) to obtain the tangential displacement of vector $\boldsymbol{\delta}_{t,ij}$ which affect the vector of the static friction force and in turn wall shear stresses.

The state of granular material, the distribution of porosity fields as well as the particle contact forces within the hopper, obtained at the end of filling, are depicted in Figure 2.19. The particles are colored by using a scalar, with $f_i = \sum_{i \neq j} |\mathbf{F}_{ij}|$ representing the sum of inter-particle contact forces acting on the particle (cf. Figure 2.19a-c). The macroscopically representative porosity fields within the material (cf. Figure 2.19d-f) are defined by averaging the volume of particles within the chosen representative volumes represented by spheres. The averaging process is performed by specifying the representative volume of the spheres having the size equal to 6–7 times the largest diameter of the particle. The volume of the granular structure within the representative sphere was corrected by excluding the overlaps of the particles. The volume of the representative sphere adjacent to the wall was defined taking into account the sphere-wall intersection geometry. Finally, the computed volumetric data of the porosity are displayed on the orthogonal grid of the midsection slice by using linear interpolation, (cf. Figure 2.19d-f). Implementation of the interpolation technique enables us to estimate the unknown values of the porosity that lie between the known data points of the representative spheres, as well as providing the smoothness of the data fit.

The obtained structure of granular material (cf. Figure 2.19a-c) at the end of filling indicates that the top surface of granular material is a flat and almost regular in the case of frictionless particles, while, in the case of frictional particles, this surface is less uniform (μ=0.3) and the material is piled up in a heap (μ=0.6). The variation of particle contact forces indicates that force transmission within the granular material varies, in particular, at the lower part of the hopper. It can observe that the particle friction induces an increase of the local heterogeneity of particle contact force transmission, which is higher for rough particles (μ=0.6) compared to smooth ones (μ=0.3). It can demonstrate that there are some rough particles subjected to much higher forces as compared to smooth particles in the lower part of the hopper. This fact may partially relate to local arching of rough particles at the lower part of the hopper at the end of filling.

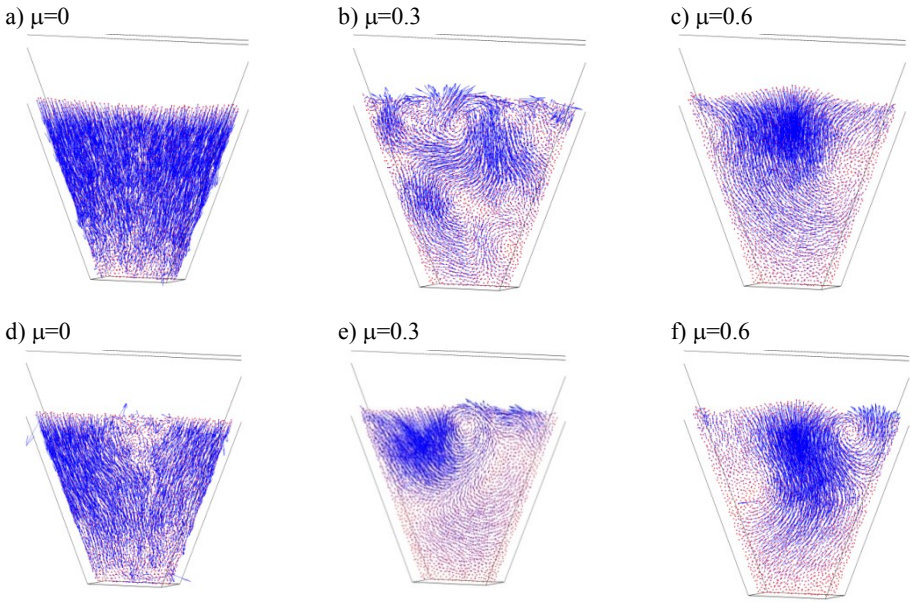

Figure 2.19. A quasi static particle velocity vectors in a mid-plane of the hopper when: μ=0 (a, d), μ=0.3 (b, e), μ=0.6 (c, f). Simulation time t=4 s (a–c) and t=8 s (d–f), [238].

The computed porosity fields, representing the degree of material compaction after the process of filling is over, are shown in Figure 2.19d-f. These fields quantitatively expose different packing of material caused by the frictional properties of the particles. Evidently, in all cases, the formation of the densest assemblies can observe at the lower part of the hopper, while loose granular structures are located at the upper hopper's part, as well as near the walls and the bottom. It should be noted that porosity profiles are spread symmetrically (some asymmetry can observe in the case of μ=0.6) with respect to the vertical axis z of the hopper, therefore, the symmetry of wall pressure can also be expected.

In general, for a frictionless granular material, the highest bulk density zone (with the lowest porosity coefficient n=0.24–0.27) can observe within the domain of approximately 0.5 m above the bottom. In the case of μ=0.3, the depth of this zone is almost the same, however, the porosity increases over the range of n=0.29–0.32 there. For particles with μ=0.6, the porosity of the densest zone is higher than that for particles characterized by μ=0.3, ranging from 0.27 to 0.3. However, but its

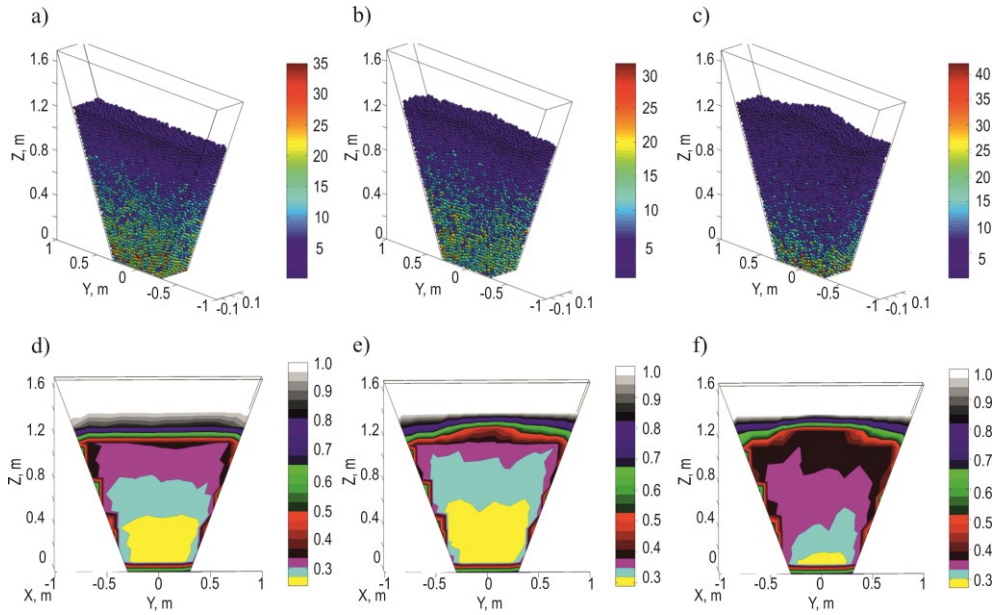

Figure 2.20. Illustration of granular material in the midsection at the end of filling for various friction coefficients: the state of material with inter-particle forces (expressed in newtons) for μ = 0 (a), for μ = 0.3 (b), for μ = 0.6 (c), and the porosity fields for μ = 0 (d), for μ = 0.3 (e) and μ = 0.6 (f), [238].

depth is quite small and does not exceed 0.1 m. In the dominant part of the hopper, i.e. within the levels ranging from 0.5 m to 1.2 m, the lower porosity fields prevail. In particular, for the case of μ=0, they vary in the range of 0.27÷0.33, while, for μ=0.3, n=0.32÷0.37 and, for μ=0.6, the porosity increases from n=0.3 to n=0.4. The higher porosity obtained with increasing particle friction can attribute to the formation of the arches within the granular material in the hopper. Considering horizontal profiles of the porosity distribution within the hopper, it can state that higher porosity is exhibited near the wall as compared to the central part of the hopper. Generally, the presence of wall friction produces a disordering effect, particularly, for μ=0.6, on the granular structure adjacent to the wall and, in turn, affects the contact force transmission between the particle and the wall.

Relying on the microscopic quantities of the discrete particles, such as contact forces and their contact locations, the macroscopic mean stress tensor can generally be found by using homogenization of these quantities over the given volume V, [292].

$$\sigma_{ij} = \frac{1}{V}\sum_{c\in V} F_i^c l_j^c, \tag{2.32}$$

where $\mathbf{F}^c$ and $\mathbf{l}^c$ are the contact force and the contact position vector at the contact c, while i (j) denotes the ith (jth) component of these vectors over the range i, j=1, 2, 3 (i.e. $i, j \equiv$ x, y, z).

In general, the stress tensor $\boldsymbol{\sigma}$ defines the three-dimensional state of stresses acting on three mutually perpendicular planes at a given position of granular matter. However, the experimental determination of $\boldsymbol{\sigma}$ within granular material is very complex, requiring non-invasive and precise contact force measurements.

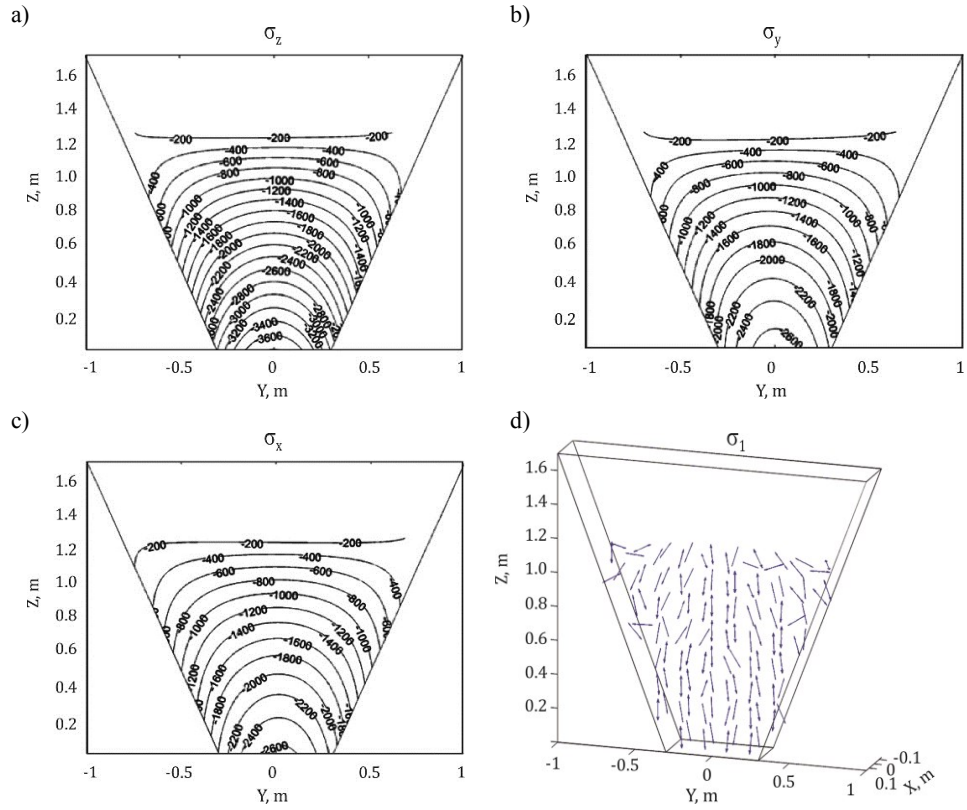

Figure 2.21. Illustration of stresses (expressed in Pa) found in the midsection at the end of filling for frictional material, μ = 0.3: (a) contour plot of normal components (a-c); trajectories of the major principal stresses σ_1 (d), [238].

Consider stress distribution within granular material calculated computationally. For this end, the whole volume of the material is divided into representative spheres, similar to the case of determining the porosity, and the particle microscopic quantities within these spheres are homogenized by using Eq. (2.31). A three-dimensional cubic spline interpolation/extrapolation procedure was implemented to compute the values of the spatial stress function at the intermediate and the external points of the grid. The obtained distribution of the midsection normal stresses for the case of μ=0.3 is depicted in Figure 2.21.

As follows from Figure 2.21 (a-c), the distribution of all stress components has a convex shape along y coordinates on YZ plane and their values are lower at the walls compared to the central part of the hopper. The same tendency and the convex distribution of stress were found in the continuum-based analysis of asymptotic bottom stress distribution, [2]. Additional inspection of stress fields on XZ plane has shown that they are constant over x coordinate and can treat as uniformly distributed on XZ plane. In the vertical direction, stresses gradually increase away from the top surface of material. The magnitudes of the horizontal stresses σ_x and σ_y are lower than the vertical stress σ_z, since the material partially transmits its own weight towards the wall due to friction. A similar tendency of stress distribution is observed for the case of μ=0.6. The trajectories of the major principal stresses σ_1 represented as the eigen vectors $\mathbf{n}_1$ are plotted in Figure 2.21d.

Based on the continuum-based analysis [2] it has been well established that, for the corresponding active stress state, the trajectories of σ_1 are approximately vertical (due to the weight of material), with a slight inclination towards the walls (due to shear stresses). The obtained computational results, shown in Figure 2.21d, are effectively consistent with this indication. In addition, some horizontally directed vectors at the upper surface indicate that the passive stress state can develop in the upper part of the hopper.

Let us consider wall stresses developed at the end of filing process. The normal and shear wall stresses versus the height of the stored material in the local axis $\mathbf{z}^{loc}$ are computed and depicted in Figure 2.22. The wall along its local axis $\mathbf{z}^{loc}$ is divided into representative segments of the height 0.14 m and the width equals to the hopper thickness, b=0.3 m. Hereby, the wall stresses are calculated in the local framework of the wall by summing up the particle-wall contact forces and averaging their resultant force over the representative wall segment. The sign of the normal wall stresses are specified by the direction of the axis $\mathbf{x}^{loc}$ while the shear wall stresses are

defined by the direction of the axis $\mathbf{z}^{loc}$. In particular, the wall normal stresses, $\sigma_n < 0$ means that the particles compress the wall while the shear wall stresses $\tau_n < 0$ show that particles slip downwards along the wall having their own friction force pointed upwards (according to the direction of the vector $\mathbf{z}^{loc}$); hence by the third Newton's law, the wall is subjected to negative reaction force.

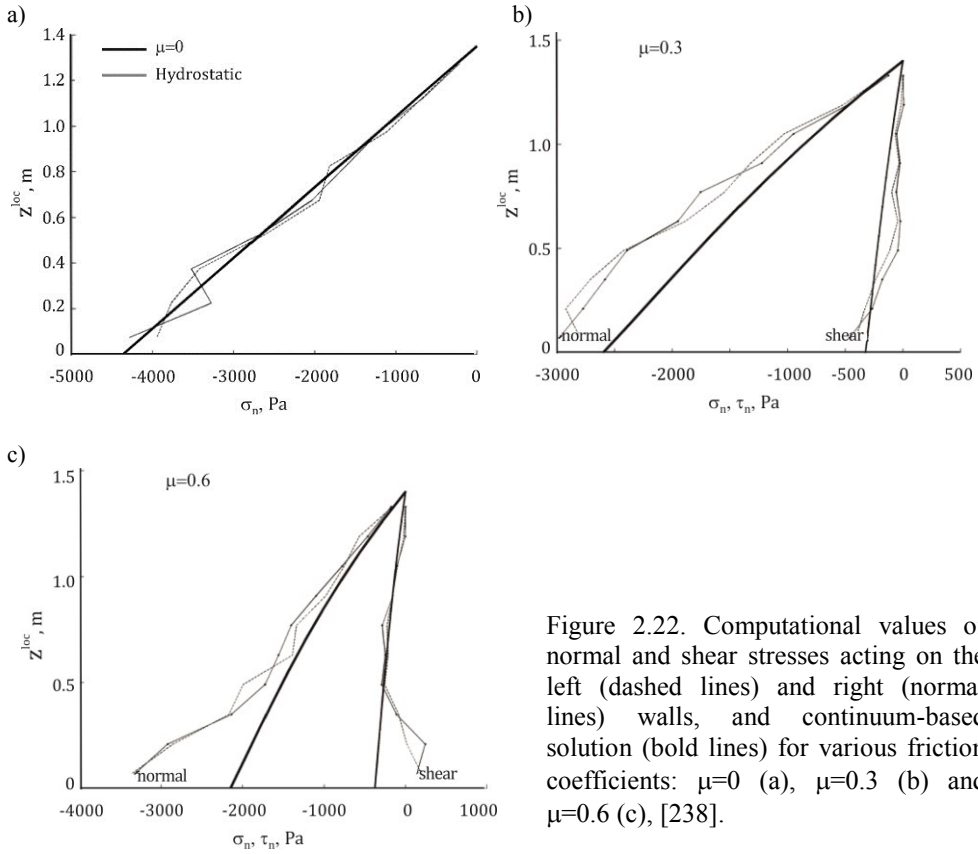

Figure 2.22. Computational values of normal and shear stresses acting on the left (dashed lines) and right (normal lines) walls, and continuum-based solution (bold lines) for various friction coefficients: μ=0 (a), μ=0.3 (b) and μ=0.6 (c), [238].

The perfectly smooth particles (μ=0) result in a quite linear profile of normal wall pressures for the left and the right which are close to the hydrostatic pressure. An increase of the friction coefficient induces an expected increase of the wall shear stresses which in turn decreases normal pressures relevant to load transfer of the bulk material weight towards the wall.

The DEM model results can compare with continuum based prediction. The method of the differential slice introduced by Janssen for the flat-bottomed hopper is often

used in various analyses when theoretical prediction of wall pressure is required. With a set of correction factors this approach was extended by Walker and Walters for the converging hoppers in [128]. However, these extensions were attributed to the plane strain hoppers and cannot be directly applied to 3D hopper. In this case, the simplified wall stress model based differential slice approach adopted for three-dimensional hopper along with the Coulomb yield condition was developed, [238].

A comparison of this model and DEM results for normal and shear stresses acting on the inclined walls at the end of the filling are depicted in Figure 2.22b, c. The bulk material weight is found by relation $\gamma_b = \rho g(1-n)$ (where n denotes the porosity coefficient) by the averaging porosity fields of granular material within the hopper (cf. Figure 2.19d-f). It was found that the weight of the bulk material at the end of the filling decreases with an increase of the particle friction coefficient. In particular, for frictionless particles (μ=0), it is established that the bulk material weight is equal to 3470 N/m^3, while for frictional particles (μ=0.3, μ=0.6), γ_b is obtained 3310 N/m^3, 3240 N/m^3, respectively.

The internal friction angle is determined by specifying the angle of repose of granular heap in the additional experiments performed. It has been found that μ=0.3 corresponds to internal friction angle φ, ranging approximately from 8° to 10°, while, for μ=0.6, $\varphi = 13 \div 15°$. Additional investigation of the macroscopic friction angle between bulk material and the wall was performed by confining the appropriate porosity (the similar as developed within the hopper) sample of granules to the box and tilting a horizontal wall until sliding occurs. Simulation has shown that this angle is close to internal friction angle and may simply define as $\mu_w = \tan(\varphi - \Delta), (\Delta = 1 \div 2^o)$.

A comparison of computationally simulated wall pressures (normal and shear) components and continuum-based solution is presented in Figure 2.22. For frictionless material the hydrostatic pressure prediction model was employed. Different computational solutions on the left (dashed lines) and the right (normal line) walls are also depicted there.

In spite of insignificant scattering of the obtained values of normal wall stresses, good agreement of these values with the hydrostatic pressure prediction data was obtained for frictionless particles (μ=0). Moreover, the balance between the left and right walls was observed (cf. Figure 2.22) for all cases of friction. For frictional particles, the agreement between the macroscopic pressure and DEM results may also treat as relatively accurate within the distance from the top surface of material

up to approximately 0.5 m over the bottom, whereas below this level, the greater values of normal and shear stresses are predicted by the discrete element method. In the case of μ=0.3, the prediction variation is not significant, while, in the case μ=0.6, the predicted normal wall pressures by DEM are considerably higher than in the case of the continuum model prediction. To improve these results, the additional simulations were performed. It was obtained that normal and shear stresses of the wall are actually not sensitive to the variation of particle damping parameters, representing up to 2% change in the stress magnitude. Furthermore, removing friction at the bottom level did not result in wall pressure variation.

In the case of μ=0.3, shear stresses of the wall act downwards (i.e. τ_n<0, since $\mathbf{z}^{loc}$ is pointed upwards) over the entire wall length, and this is in accordance with the continuum prediction. In the case of μ=0.6, the difference in shear stresses of the wall in the lower part of the hopper was found. This can be related to poor development of the direction of friction forces, acting upwardly at 0.2–0.3 m above the bottom, while above this elevation, the obtained shear stresses are pointed downwards similar to the continuum-based model prediction.

These results show some differences between the continuum approach and modelling based on the discrete particle model. In DEM model, the particle friction induces its rotational motion which affects the translational motion and, hence, contributes to changes in the direction of the resultant of particle-wall contact tangential forces as well as in the direction of the wall shear stresses. In continuum, the direction of the wall shear stress is defined a priori by Coulomb's dynamic friction force. In a quasi static response, the particle static friction forces prevail and form the stress bearing arches in the lower part of the hopper, transferring the material weight to the walls. In the case of static friction, the particle contact tangential stiffness is independent of the particle friction coefficient and remains almost the same for the cases of μ=0.3 and μ=0.6. However, in the case of μ=0.6, the dynamic friction force must be almost two times higher than that for μ=0.3 (assuming that the overlaps between the particles are similar in both cases). This shows that, in the case of μ=0.6, the tangential stiffness of the particles (in the vicinity of the bottom) is too small and requires about two times larger tangential contact displacement $\left|\boldsymbol{\delta}_{t,ij}\right|$ to develop the friction force corresponding to initiation of the slip.

The above-mentioned aspects partially explain the obtained differences. Thus, there is a balance between the particle's physical properties and contact laws, when dis-

crete particle simulation cannot adequately reproduce macroscopically representative wall pressure near the hopper bottom, if the particle friction coefficient increases. The attempt of modifying the tangential force model to produce much higher values of tangential contact stiffness can be found in [231].

2.2.3.3. Mathematical modelling of the discharge process

In general, the mechanics of discharge is strongly dependent on the geometry of the hopper, mechanical properties of bulk material, and interactions between the particles and the walls. The discharge process is modeled here by instantly opening the orifice and allowing for free fall of granular material with no control of its flow by a receiving assembly. Such a scenario of the discharge process has been attempted closely to follow the discharge stage encountered in real hoppers, if drawdown is not compensated for by the material resuplying from the above. A different scenario, when the discharged particles are recycled back to the top of the hopper flow, was used in [242]. This technique allows for achieving the continuous flow conditions needed for the steady-state measurements.

The illustration of the computationally simulated discharge flow under the gravity is provided in Figure 2.23, while the porosity fields and wall pressures are plotted in Figure 2.23 and Figure 2.25, respectively.

Let us consider behaviour of particle contact forces (cf. Figure 2.23), porosity fields (cf. Figure 2.23) and wall pressures (cf. Figure 2.25) observed during discharge. The distribution character of particle contact forces within the granular material shows that the particles located near the orifice, where they were compressed by contact forces before the orifice was opened, are practically unloaded at the orifice opening. The unloading of the particles is caused by the dilation of material induced by orifice opening. The dilation wave spread over the whole material is effectively captured at time 0.2 s, with the drop in particles contact forces, particularly at the central axis of the hopper, indicated in Figure 2.23a, c. At time instant t=0.4 s, the material densification prevails, with increasing of particle contact force values from 5.0 N up to 30.0 N, (cf. Figure 2.23b, d). Material dilation, which is observed on particle contact forces, is also confirmed by the material porosity patterns as well as by wall pressures.

In particular, during the period of flow initiation, the dilation zone spreads over the entire hopper inducing the mass flow of granular material, (cf. Figure 2.24a, d, g).

At 0.2 s of discharge, a loosely packed granular structure, with n=0.38÷0.43 occupies the hopper up to 0.9 m above the outlet, while the layer of the densest material, with n=0.34÷0.38, is formed at the elevation, ranging from 0.9 m to 1.1 m. The material dilation leads to initial unloading of granular material within the hopper and the significant reduction of the magnitudes of particle contact forces, as demonstrated in Figure 2.24a, c. This, in turn, results in the reduction of the wall pressure as compared to the state of filling, (cf. Figure 2.25).

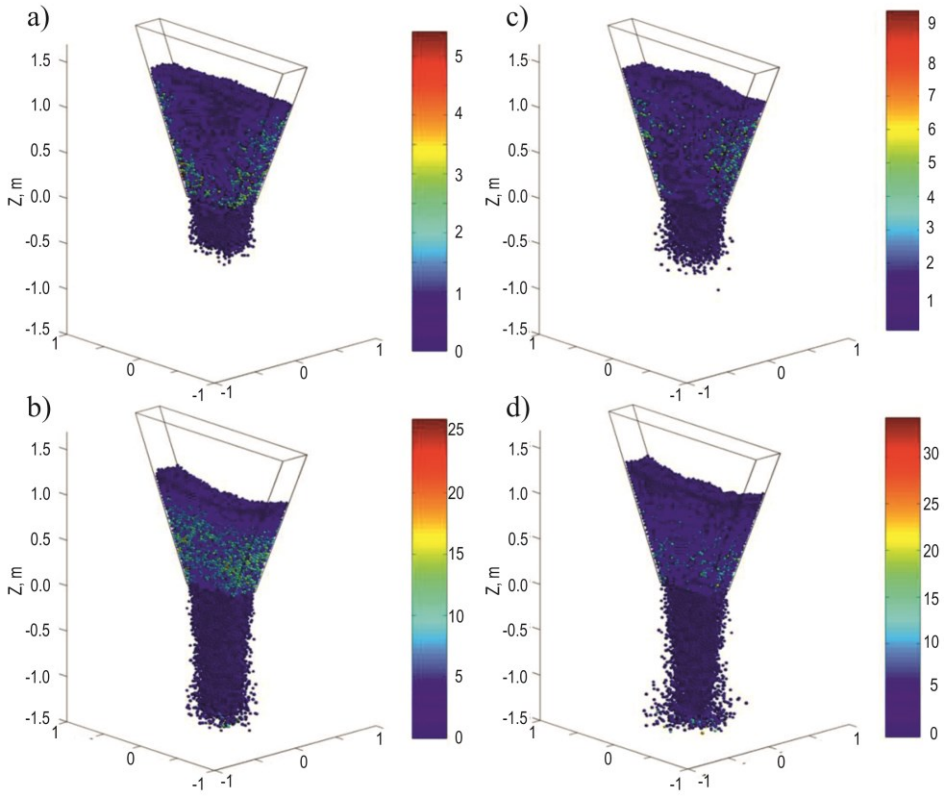

Figure 2.23. Illustration of the discharge process with inter-particle forces (expressed in N) for frictional materials: at time instant t = 0.2 s, for μ = 0.3 (a), for μ = 0.6 (c); at time t = 0.4 s μ = 0.3 (b), for μ = 0.6 (d), [238].

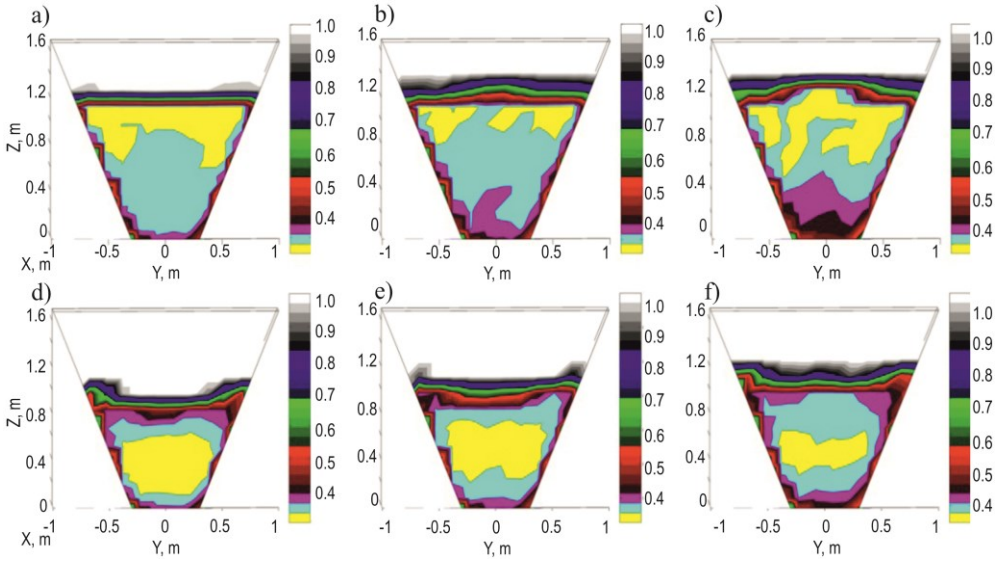

Figure 2.24. Hopper midsection porosity fields during discharge for various friction coefficients: at time instant t = 0.2 s for μ=0 (a), μ=0.3 (c), μ=0.6 (e); at time instant t = 0.4 s for μ=0 (b), μ = 0.3 (d), μ=0.6 (f), [238].

Furthermore, in all cases of particle friction, the loosely packed granular structure occures in the vicinity of the outlet, whereas the densely packed material is located in the upper zone, enveloping the material whose porosity is intermediate between loose and dense states. It can see that the porosity of these structures increases with the increasing particle friction. For instance, in the case of μ=0.6, the porosity of the dense structure varies over the range of n=0.34÷0.37 and n=0.39÷0.42 at time t=0.4 s and t=0.6 s, respectively, while, in the case of μ=0, the porosity decreases (i.e, n=0.30÷0.33, n=0.35÷0.38, for t=0.4 s and t=0.6 s, respectively). The variation of porosity with time for frictionless particles is attributed to the formation of structures of local heterogeneity producing a certain effect of friction and, in turn, some portion of material dilation can also be observed. When the number of particles tends to infinity, the frictionless granular material should behave similarly to fluid. The porosity equal to n=0.4 corresponds to the so-called random loose packing of granular material, [293].

Time-dependent evolution of the wall stresses during the discharge is shown in Figure 2.25.

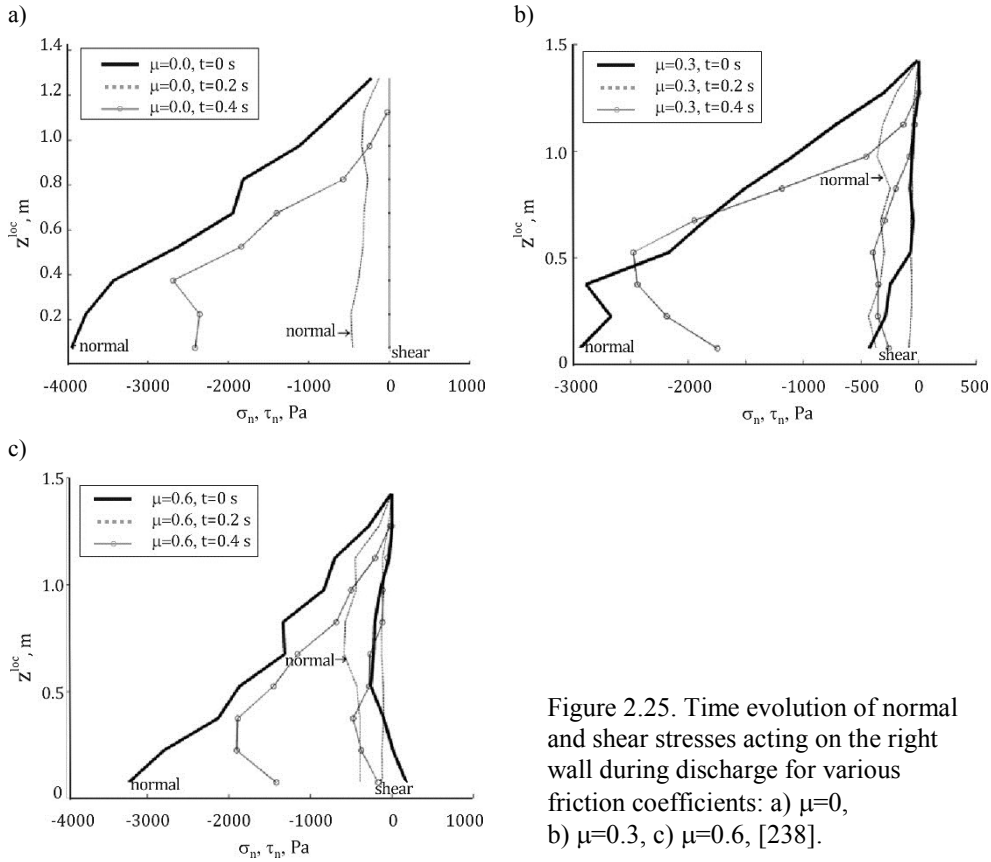

Figure 2.25. Time evolution of normal and shear stresses acting on the right wall during discharge for various friction coefficients: a) μ=0, b) μ=0.3, c) μ=0.6, [238].

As shown in Figure 2.25, normal and shear wall stresses captured at 0.2 s from the beginning of the discharge process are significantly lower than those established at the end of the filling process. Transition from the active stress state to passive develops with time, in most cases, shortly after commencement of the orifice opening. Thus, to capture the pick of over-pressure during discharge the plots vs. time is feasible. As in the case of qualitative predictions for the flat-bottomed hopper, in the wedge-shaped hopper analysis only demonstrated the pressure distribution vs. material elevation simply selecting the time instant 0.2, 0.4 s (the time instant, when the overpressure actually takes place, is not considered) in accord with the material composition within the hopper shown in Figure 2.23 and Figure 2.24. The decrease in discharge pressure (cf. Figure 2.25a, c) at the demonstrated time instants is related with reduction of material mass within the hopper due to large orifice. Decrease in pressure due to mass reduction can be seen in Figure 2.25a

plotted for the frictionless granular material. However, in Figure 2.25b, at material height 0.5 m the discharge pressure is higher than that after filling clearly indicating the propagation of the passive stress state toward the upper material surface. Above elevation of 0.5 m the active stress state is still left. Thus, the drop in wall stresses is rather high because the orifice of a significantly large size is used in present analysis.

Within 0.5 m elevation, a zone of the enlarged particle contact forces is formed in the granular material and adjacent to the wall, giving rise to the formation of unstable arches which occur and vanish during the discharge process (cf. Figure 2.25b). For the particles with μ=0.6 this situation is more localized and less illustrative, and overpressure is not captured at this time instant.

Let us consider the distribution of stresses within granular material during hopper discharge. Stress distribution within granular material was computed by using Eq. (2.32). An illustration of typical stress behaviour is presented in Figure 2.26.

Time evolution of stress components depicted in Figure 2.26a, b clearly illustrates gradual dilation of granular material during discharge. In particular, Figure 2.26a illustrates a transient state, indicating that the dilatancy wave occupies almost the whole material leading to the stress reduction at time $t = 0.2$ s, while, later, the material becomes denser resulting in the increased stresses at time $t = 0.4$ s, (cf. Figure 2.26d). For instance, the vertical stresses at the central axis of the hopper at $t = 0.2$ s is by about 5 times lower than that arising at time instant $t = 0.4$ s. During the process of filling the material exhibits compaction inducing maximal stress at the bottom, while during discharge the peak of stress travels towards the upper surface, whereas the stress falls to zero at the orifice. The increase of vertical stresses from the centre towards the walls also indicates the horizontal transfer of the stresses to the walls due to friction. It is typical that the transformation of stress fields from the convex (after filling) to the concave shape (during discharge) can be observed.

The character of shear stress distribution can be discussed briefly, (cf. Figure 2.26d). From the classical continuum model it follows that the shear stress τ_{yz} must vanish along the vertical symmetry line and change, when passing from the right to the left side of the hopper.

Figure 2.26d shows good agreement with the assumptions of the continuum model. In particular, negative shear stresses at the left-hand side wall and positive shear stress at the right-hand wall is found. In addition, the shear stresses vanish at the centre of the hopper (with a small shift of stress values to the left side) and grows up

away from the centre due to wall friction. Microscopically, these results could be explained as follows: in the centre of the hopper most of the particles flow in the absence of the rotational motion and, hence, the shear stresses, accompanying the flow in this region, vanish. At the wall, the particles slide and rotate due to the action of wall friction forces, and this results in the increased shear stresses to occur in the material. Moreover, the symmetry between shear stresses τ_{yz} and τ_{zy} was also observed.

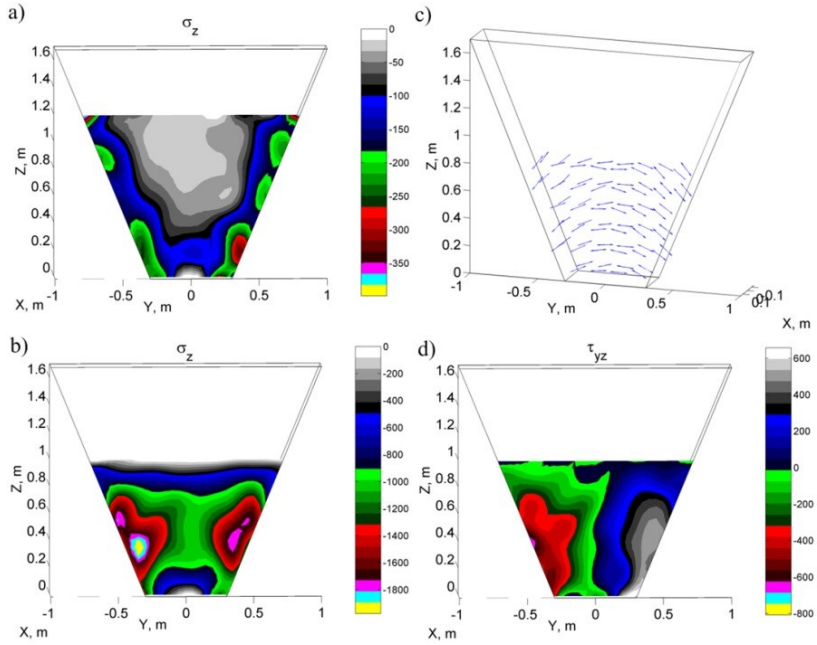

Figure 2.26. Illustration of stresses (measured in Pa) during discharge, for μ=0.3: a) σ_z at t = 0.2 s, b) σ_z at t = 0.4 s; c) trajectories of major stresses σ_1 at t = 0.4 s, d) τ_{yz} at t = 0.4 s, [238].

The trajectories of the principal stresses occurring in discharge are plotted in Figure 2.26c. It was established that the transition from the state of active to passive stresses was accompanied by the change of the direction of principal stresses σ_1 from vertical direction (cf. Figure 2.21d) observed at the end of filling to horizontal direction during discharge, (cf. Figure 2.26c). This is consistent with continuum--based indication given in [2].

Finally, the discharge process relying on the material outflow control by receiving equipment was analyzed. The outflow control was modeled by imposing the kinematical boundary condition on the bottom of the hopper, i.e. the bottom was subjected to vertical motion by imposing the initial velocity v_{bz}. Thus, the emptying process was controlled by imposing different initial velocities, while the small displacement increment was equal to one-half of maximal particle radius.

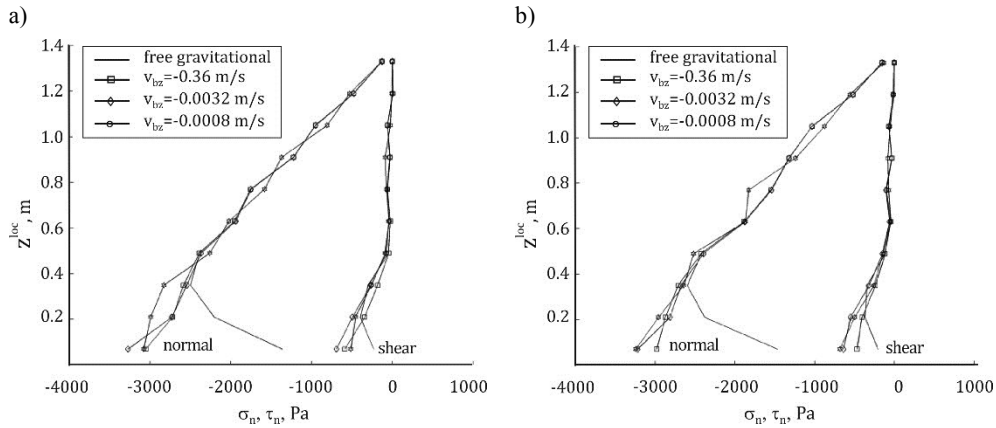

Figure 2.27. The influence of initial velocity of the bottom on the wall pressures (μ=0.3): a) left, b) right, [238].

The graph depicted in Figure 2.27 a demonstrates the influence of the initial velocity induced by the motion of the bottom on wall stresses. It can see that the increase of the bottom velocity from v_{bz} = -0.0008 m/s, representing quasi static flow, up to v_{bz} = -0.36 m/s (almost free gravitational flow) results in the diminishing of the wall normal and shear stresses. This fact is in accord with macroscopic prediction given by [2, 158], where the stresses due to inertial flow are lower than that obtained in quasi static discharge because the inertial forces oppose the gravitational forces. For comparison, normal and shear stresses of the wall induced by free gravitational fall (at $t = 0.03$ s) in the vicinity of the orifice are significantly lower than those observed in the case of the controlled discharge.

2.2.3.4. Concluding remarks

The three-dimensional simulation of the friction effect on the granular material flow was performed by applying the discrete-particle model for filling and unsteady/ /steady discharge in a wedge-shaped hopper with rough walls. The model was based

on particle contact mechanics involving Hooke's law of elastic inter-action, static and dynamic friction as well as non-conservative viscous damping forces. The results obtained can summarize as follows:

- For frictionless as well as for frictional material, the computationally obtained wall stresses are in good agreement with the wall pressure determined by using the differential slice approach. However, the differences between these stresses near the bottom have been found for the case of μ=0.6. Too small values of the inter-particle contact tangential stiffness occurring with the increasing particle friction coefficient could cause this behaviour.
- The obtained time evolution of the bulk porosity during discharge is clearly related with time variation of particle contact forces within the granular material as well as the transmission of these forces to the hopper walls causing their pressure. In particular, it is demonstrated that the increased porosity wave propagates towards the material top surface, causing the initial decrease of particle contact forces and, therefore, the decrease of wall stresses. The material dilation observed for frictionless particles can be attributed to the local heterogeneity of the particles.
- Convergence of the system's total kinetic energy to zero indicates the end of the filling process and characterizes a quasi-static state of material. It is demonstrated, however, that frictional properties result in the occurrence of particle velocity fields of different nature at the quasi-static state. For frictional materials, the vertex-like patterns prevail. On the contrary, the frictionless granular material is characterized by the radial nature of particle velocity patterns. In discharge, the mass flow patterns and the radial nature of particle velocity vectors can be observed.

DEM simulations and comparison with continuum-based analysis allows us a better understanding of granular flow and friction effects in three-dimensional wedge--shaped hoppers.

"Main content of this chapter has been published in Powder Technology, 187, 159-174, 2008".

2.2.4. A comparative analysis on granular material flow through a *space-wedged*, *plane-wedged* and *flat-bottomed* hopper

2.2.4.1. Mathematical model. Basic assumptions

Three differently shaped hoppers are investigated, while the geometry of them is defined in the same manner (cf. Figure 2.28). In particular, a different shape is described by inclination angles of the generetrix to the horizontal plane, θ_x and θ_y, respectively. The *space-wedged* hopper is specified by acute angles having values $\theta_x = 68°$ and $\theta_y = 62°$, while values $\theta_x = 68°$ and $\theta_y = 90°$ correspond to the *plane--wedged* hopper. The *flat-bottomed* hopper is stated by assuming the right angles to be $\theta_x = 90°$ and $\theta_y = 90°$. Variable dimension of the bottom L_b depends on the hopper shape, however, dimensions of the outlet D and B are held constant, for all hoppers, for the sake of comparability. The hopper walls (including the bottom) are assumed to be rigid and are considered as the fixed boundaries with friction.

The specified composition of granular material is the same, as defined in Section 2.2, and is represented by an assembly of $N = 1980$ particles. Total mass M of the material is fixed and is equal to $M = 143.7$ kg. The data of the visco-elastic particle were given in Table 2.2. Inter-particle and particle-wall friction coefficients correspond to the case of fully rough walls, and values of $\mu = 0 \div 0.6$ are simply assumed for modelling purposes. The data of the visco-elastic particle were given in Table 2.2. Inter-particle and particle-wall friction coefficient corresponds to the case of fully rough walls, and values of $\mu = 0 \div 0.6$ are simply assumed for modelling purposes. The walls are modelled by the finite planes. In the case of sliding regime, the contact tangential force is modelled by Coulomb friction role using the coefficient of friction between wall and particle.The rolling friction coefficient is also introduced to be $\mu_R = 0.002$ and 0.01. A linear spring model based on Hooke's law is used for the normal contact. The mathematical model was described in Section 2.1.

The characteristic dimension of the outlet D is assumed to be related to the maximal diameter d of the particle as $D = 8.6d$. The thickness of the hopper at the bottom is assumed to be $B = 4.3d$. The dimension of the top hopper edge is $L = 3.3D$, while the overall height of the hopper is $H = 2.88D$. Assuming that $d = 0.06$ m, the main geometrical parameters of the hoppers are defined as: $B = 0.3$ m, $L = 1.6 \div 2$ m and $H = 1.7$ m.

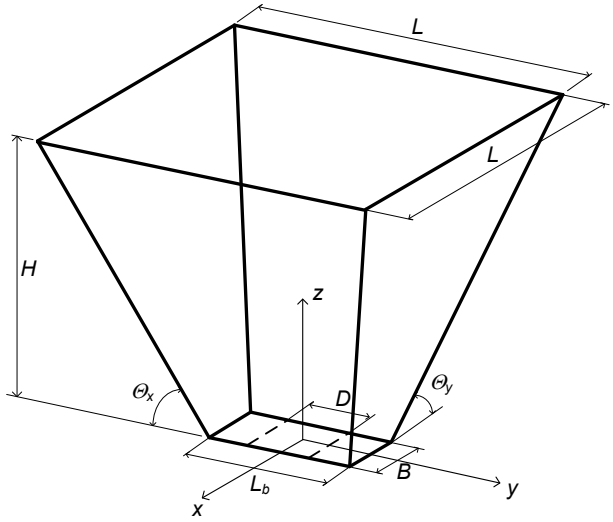

Figure 2.28. The basic geometry for description of the hopper of different shapes, [289].

The filling process is simulated by compacting the particles *en masse*, while discharge is modelled by instantly opening the orifice and allowing for free falling of the particles. Series of independent DEM simulations of the filling and discharge in three differently shaped hoppers were performed with different values of the friction coefficient but with the same above described composition of the granular material. Snapshots on the filling and discharge processes for differently shaped hoppers are summarized in Figure 2.29. The colour-bar depicted in these figures shows the contact forces acting on the particles within the granular material.

Even a visual examination of flow patterns allows identifying the important features of the discharge flow. Generally, for the case of fully rough wall, which immobilizes particle slipping downwards adjacent to the wall, the top surface of the material during the discharge transforms from a convex to a concave shape. This is quite illustratively exhibited in the case of the *flat-bottomed* hopper, (cf. Figure 2.29c, f). In particular, the depression zone above the orifice occurs at the beginning of the emptying process. Later, this depression deepens with progressing of the emptying. Its sides become more and more steeper, and when the slope of these sides reaches the angle of repose some of the particles cascade down to the central part of the material which moves faster. The nature of granular flow in the flat-bottomed hopper contains characteristic features of funnel flow.

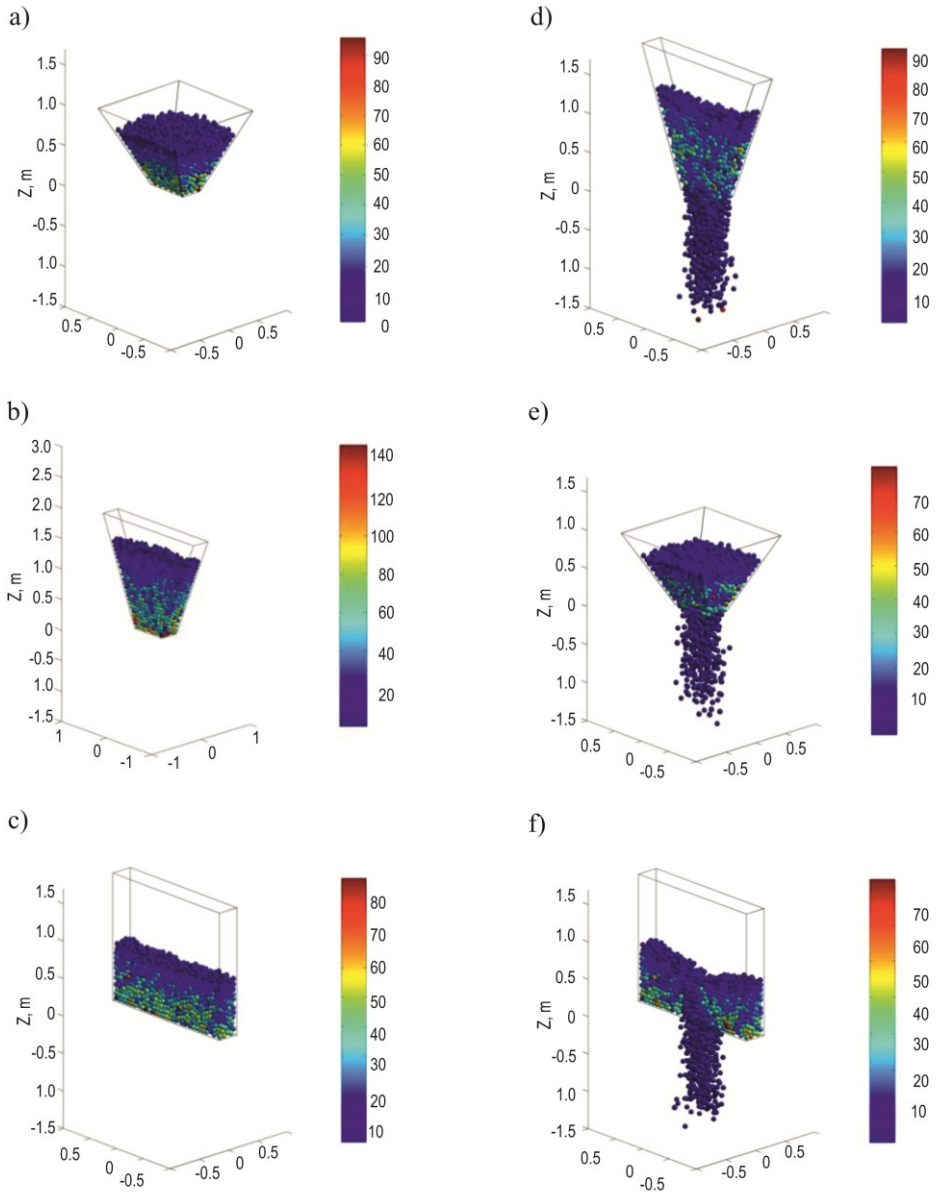

Figure 2.29. Illustration of the discharge flow at various time instants (μ=0.3, μ_R=0.3): a, d) plane-wedged hopper; b, e) space-wedged hopper; c, f) flat-bottomed hopper; a-c) the end of filling; d-f) discharge process at t = 0.4 s. Colour-bar indicates the particle contact forces measured in newtons, [289].

The character of the discharge flow in converging, i.e. in the *plane-wedged* and the *space-wedged* hoppers is different. The formation of the depression zone at the top surface starts only when the granular material overpasses some height of the hopper. This zone quite evidently expresses the final stage of the discharge.

Decompression of granular material in the middle section of the hopper indicates significant reduction of the magnitudes of particle contact forces in the discharge time period, (cf. Figure 2.29d-f). This feature clearly illustrates presence of the material dilation phenomena. It takes the place due to inter-particle friction which allows for material shearing with increasing in the porosity and, in turn, reducing in the particles contact forces.

2.2.4.2. Computational results

A comparative investigation on the main macroscopic parameters to understand how they affect the granular flow in terms of different shapes of the hopper is an important issue in development of the prediction approaches. In a framework of current investigation, computational analysis comprises particle velocity patterns, discharge flow parameters, statistical processing of particle accelerations.

Let us consider the discharge flow patterns in terms of the discharged mass. A dimensionless variable, $0 \leq w_f \leq 1$, representing the discharged mass fraction is computed as the ratio of the discharged mass, M_d to the total mass, M. A discharged mass fraction rate, i.e., mass fraction flux, is obtained as a time derivative of the discharged mass fraction, $\mathrm{d}w_f(t)/\mathrm{d}t$.

Variations of the above defined dynamic discharge flow characteristics for hoppers of different shape and different inter-particle friction coefficients, but zero rolling friction, are presented in Figure 2.30. The graphs depicted clearly indicate influence of the hopper shape and inter-particle friction. It can also state (cf. Figure 2.30d-f) that the highest discharged mass fraction rate occurs in the plane-wedged hopper, while in the space-wedged and the flat-bottomed hoppers discharge process runs in time relatively slowly.

The plane-wedged hopper discharges faster than the space-wedged one, since, in the space-wedged hopper, the bulk flow exhibits *spatial retardation* due to an ability to generate more contacts with each other and dissipate the kinetic energy. For the plane-wedged hopper, a *plane flow* occurs only.

To discuss this in detail, let us analyze the polar plot of the particle horizontal velocities v_x and v_y developed at $t = 1$ s, in the plane-wedged and space-wedged hoppers during discharge. To this end, the horizontal velocities of the particles were plotted on a circular grid as the arrows emanated from the origin, (cf. Figure 2.31).

As can be quantified by the polar plot (cf. Figure 2.31), the horizontal velocities v_x and v_y have almost isotropic distribution during discharge, for the space-wedged hopper. They maximal magnitude varies over 0.5÷0.6 m/s. In the case of the plane--wedged hopper, an anisotropic velocity distribution with domination of the component v_y is clearly observed. This component induces the particles movement toward the centre of the hopper with a twice higher velocity in comparison with the space-wedged hopper. Hence, for the space-wedged hopper an isotropic distribution of velocities leads to the ability of particles to get more contacts resulting in the space-retarded motion which reduces a vertical velocity produced by the gravity acceleration. Due to a space-retarded particles motion the space-wedged hopper discharges more slowly.

Generally, the discharge flow in the both space-wedged and flat bottomed hoppers during the time interval up to 1 s behaves, in fact, quite similarly (cf. Figure 2.30). At the beginning of discharge the nonlinear variation between the discharged mass fraction with time is detected. This is due to formation of dilation wave which forms near the bottom and quickly spread over the whole material. Speed of propagation of this wave is dependent the inter-particle contact network and material damping and friction.

It can note, that the flat-bottomed hopper cannot be completely discharged, (cf. Figure 2.30b-c). Obviously, sequentially examining the flow rates we can see that increasing of the particle friction compared to the frictionless material induces diminishing of the discharged mass fraction rate. Generally, the influence of inter-particle friction coefficient, ranging from μ=0.3 to 0.6, is a quite mild and is invariant of the hopper shape, complying with a correction factor C used in theoretical prediction for the discharged mass rate. As pointed out in [128], values of C as large as 0.64 have been reported for exceptionally smooth particles, while for frictional ones usually takes a value close to 0.58. It should note that sometimes an artificially established correction factor C serves as a remedy to fit the experimental values of the discharged mass rate with an experiment instead of new theoretical developments.

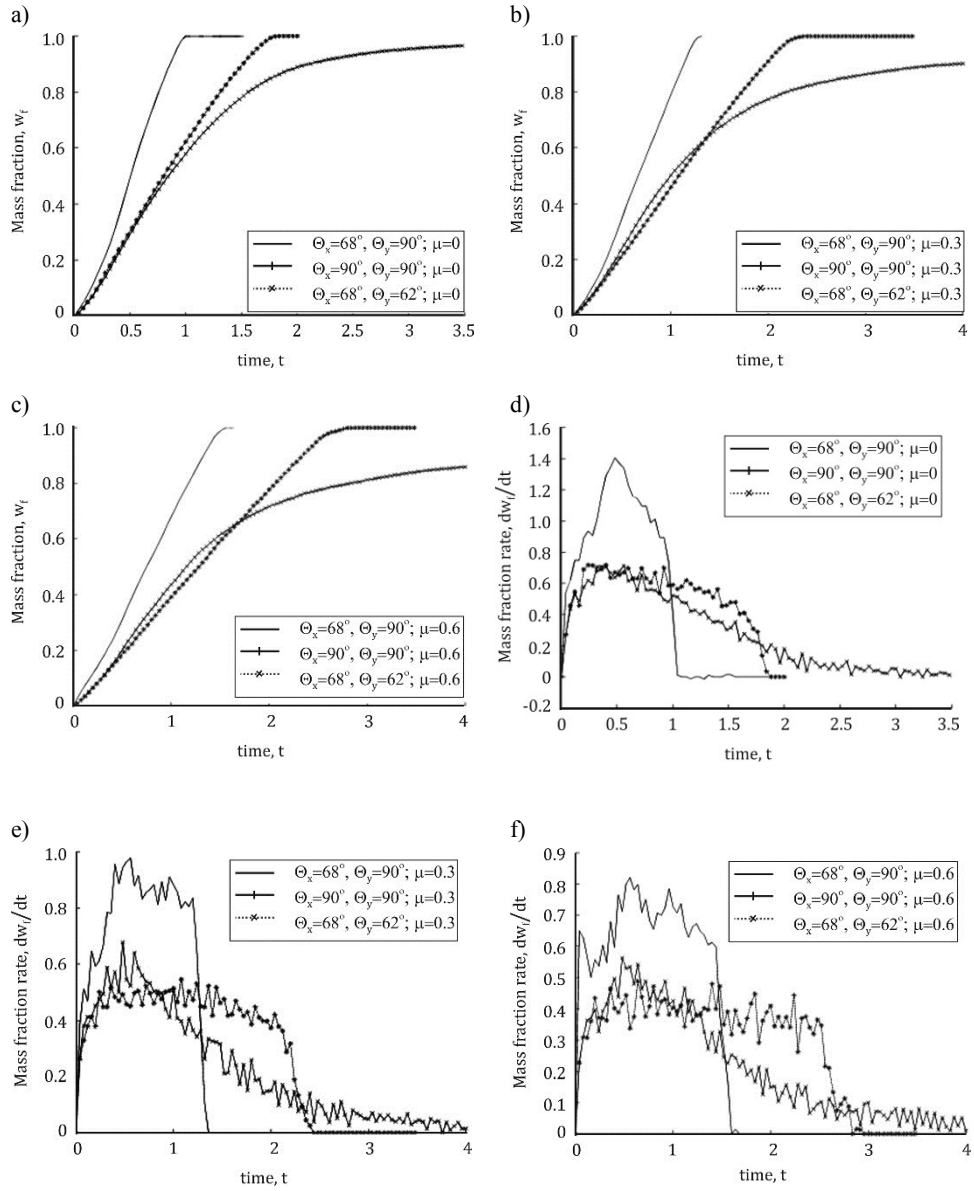

Figure 2.30. Illustration of the discharge flow parameters in different hoppers for various inter-particle frictions: a-c) time variations of the discharged mass fraction, d-f) time variations of the discharged mass fraction rate, g-i) variations of the discharged mass fraction rate against the material height. Parameters on axes dw_f/dt and H are measured in s^{-1} and m, respectively, [289] [*Continued figure on next page*].

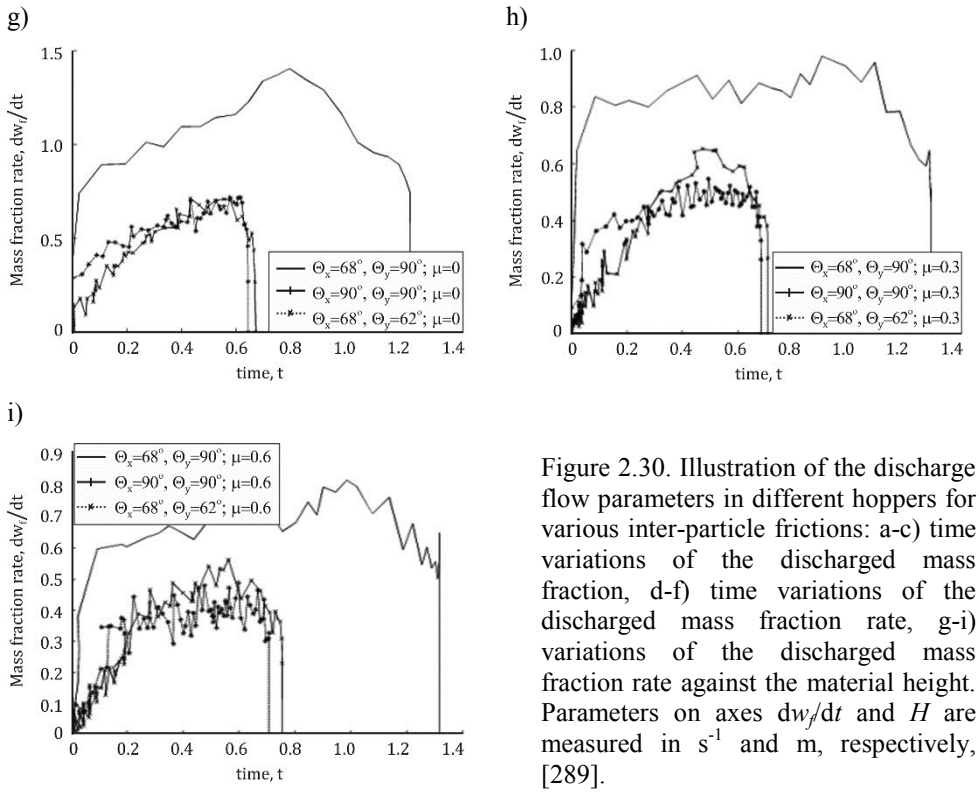

Figure 2.30. Illustration of the discharge flow parameters in different hoppers for various inter-particle frictions: a-c) time variations of the discharged mass fraction, d-f) time variations of the discharged mass fraction rate, g-i) variations of the discharged mass fraction rate against the material height. Parameters on axes dw_f/dt and H are measured in s^{-1} and m, respectively, [289].

Important issue in continuum mechanics is the detection of steady state conditions. By generalization numerous empirical observations on the frictional granular material the main geometrical conditions defining the constant discharged mass rate have been established by [128]: a) the rate is independent of material height H, provided $H > 2D$; b) the rate is independent of the orifice diameter, provided $L > 2.5D$, where L is shown in Figure 2.28, as the width of the upper edge of the hopper.

Hence, the above statements provide that the particles theoretically accelerate freely and the main parameters affecting the flow rate are the bulk density, the orifice diameter and the inter-particle frictions (irrespective to time-dependent analysis). For consideration of the frictionless materials, the inviscid fluid model defining the discharged mass rate of the fluid being proportional to $\sqrt{H}$ may be used for the sake of comparison.

By considering a variable material height in the space-wedged and flat bottomed hoppers (cf. Figure 2.29), it is easy to persuade, the material height does not match the above geometric condition (a). Let us discuss the tendencies of the discharged mass fraction rate variation against the material height, (cf. Figure 2.30 g-i).

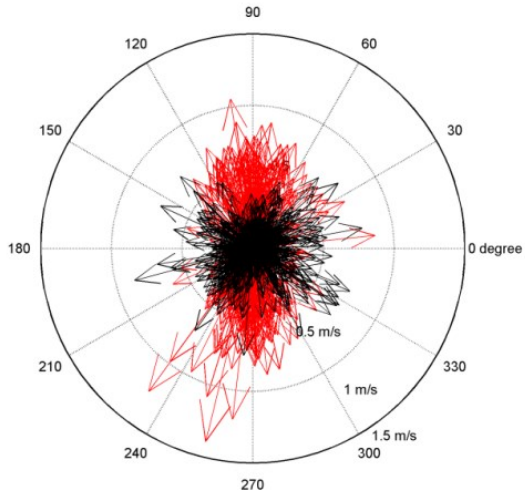

Figure 2.31. Polar plot of particle velocities v_x and v_y on a circular grid, for the plane-wedged (red colour) and space-wedged (black colour) hoppers (μ=0.6, μ_R=0), [289].

Thus, as expected, the discharged mass fraction rate of the frictionless particles (cf. Figure 2.30g) is similar to the above mentioned behaviour of fluids and seems to be proportional on $\sqrt{H}$, for geometrical configurations of the hoppers considered. For frictional particles, the discharged fraction rate should be theoretically independent on the quantity of material, typified by height, H. This indication is fulfilled for the plane wedged hopper very well within almost entire period of emptying. It means that, the discharged mass fraction rate could be effectively approximated by the straight line, for 0.2 m < H < 1.1 m. However, for the case of the space and the plane wedged hopper discharged mass fraction rate grows up from the beginning of the discharge until 0.2÷0.4 s and just at this time instant the rate remains constant. Indeed, in the case of flat bottomed hopper, the indication of the invariant rate with respect to the quantity of material is generally not valid due to the sufficiently low initial material height.

The above investigation discoveres that the most irregular random flow character occurs for the highest inter-particle friction, μ=0.6. In theoretical approaches, which are mainly devoted to flat-bottomed hoppers, the main assumption on the free acceleration of the particles near the orifice is employed. This assumption is sufficiently unclear for hoppers having the converging shape.

In order to verify the assumption concerning the state when the particles near bottom can accelerate due to gravity, the statistical analysis is employed (especially for converging shape of the hopper). The discharged material is divided into separate layers, while the three lowest layers defined by vertical coordinate intervals $z = \{0, 0.2\}$, $z = \{0.2, 0.4\}$ and $z = \{0.4, 0.6\}$ are considered. Each of the layers is characterized by relative frequency of the vertical acceleration a_z obtained by processing the values at various time instants. In this case, the relative frequency represents an estimate of the probability, indicating the proportion of cases that fall into each of several intervals of vertical accelerations a_z within the total number of attempts.

The characteristic simulation results are illustrated in Figure 2.32, where variations of the relative frequancies for the acceleration a_z occurencies obtained for the plane--wedge hopper at time instants $t = 0.4$ s is presented.

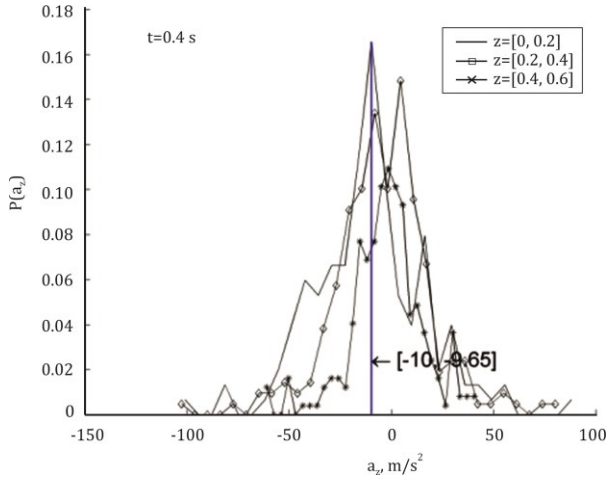

Figure 2.32. The relative frequencies for a vertical acceleration component of different layers in plane-wedged hopper, [289].

As it can be seen in Figure 2.32, for $z=\{0, 0.2\}$, the peak of relative frequencies of vertical acceleration is obtained as close as the assumed range of acceleration due to

gravity ({-10, -9.65} m/s^2). This indicates that most of the particles near the bottom accelerate freely due to gravity. Meanwhile, a significantly lower pick is obtained in the zones z={0.2, 0.4} and z={0.4, 0.6} where particles motion is sufficiently retarded due their acceleration/deceleration in the inter-particle contact collisions. Acceleration/deceleration of the particles may be attributed to the formation of series of linked stress arches (in our case at z={0.2, 0.4} and z={0.4, 0.6} zones) where above these arches the particles are packed together by retarding the flow and allowing to dominate gravitational fall at the vicinity of the bottom. For the flat bottomed hopper, the linked arches developed above the orifice were simply detected visually by plotting inter-particle contact forces web, (cf. Figure 2.11). The experimental demonstrations of such arching and forces networking is presented in [294].

Time variations of vertical component of the average outflow velocity v_z in hoppers for different values of friction coefficient μ=0.3 and μ=0.6 are depicted in Figure 2.33. The average outflow velocity was simply determined as the mean velocity of the particles located at D distance below the orifice. As it can be seen in Figure 2.33, the fastest flow generates in the plane-wedged hopper. The space-wedged hopper, in comparison to the plane-wedged one, is characterized by lower velocities and the longer discharge time. Increase of friction indicates a mild reduction in the outflow velocity magnitudes. Different durations of the discharge, i.e. residence time, are also clearly observed, because the higher particle velocity values result into shorter discharge durations.

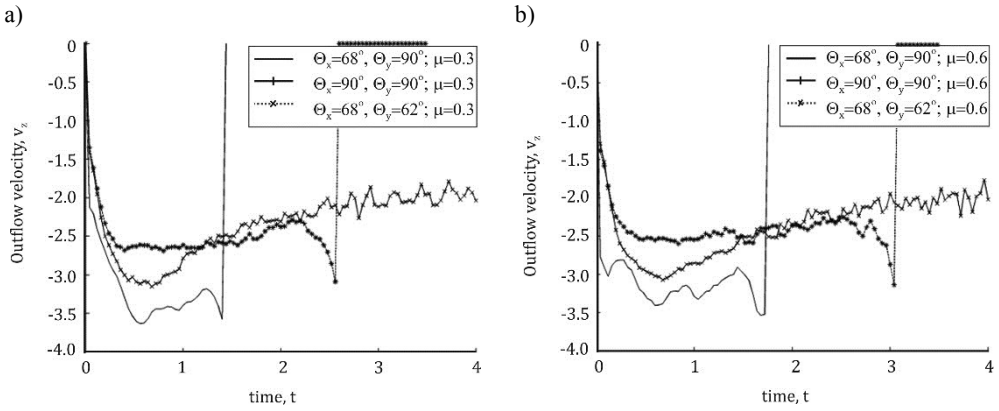

Figure 2.33 The time variations of the vertical component of the average outflow velocity (measured in m/s) in different hoppers for different friction coefficients: a) μ=0.3; b) μ=0.6, [289].

This parameter may additionally relate with a steady/unsteady state condition. Steady or unsteady flow character may specify considering time variations of this velocity for different discharge flows. The graph (cf. Figure 2.33a) not only proves presence of fluctuations but also exhibits different flow character between differently shaped hoppers. Fluctuations in the outflow velocity may be partially caused by the arch formation at the location of by about $2D$ above the orifice, (cf. Figure 2.11). A steady flow clearly prevails in the space-wedged hopper almost within the entire period of the emptying, where the velocities remain constant versus time. The unsteady inertial flow takes place during the entire period of the emptying in the flat bottomed hopper. The similar nature of the flow is also detected in the plane-wedged hopper containing, however, fluctuations.

The effect of rolling friction on behaviour of the granular material flow during the discharge process can be demonstrated by considering the total energy of the system. In the experimental tests conducted for the spherical balls, [295], values of the rolling friction coefficient have been found ranging mostly from 0.002 up to by about 0.013, depending on the material used. In the current investigation, three limiting values of $\mu_R = 0$, 0.002 and 0.01 were roughly selected to evaluate the effect of rolling friction on bulk flow. Meanwhile, the total kinetic energy, presented as a sum of the translational and rotational kinetic energies of individual particles, is considered as a main indicator. The evolution of total kinetic energy during the discharge process for the particles inside the hopper is presented in Figure 2.33, for the plane and for the space-wedged hoppers.

In Figure 2.34, the depicted graphs indicate the increase in the total kinetic energy for the case of $\mu_R = 0$, for both hoppers. This increase is essentially produced by the rotational energy, since the particles without rolling friction have a higher capability to rotate during discharge. This effect dominates at the first 0.5 s of the discharge process, when an increasing quantity of material within the hopper is able to induce the bulk flow. Later, when amount of the particles inside the hopper decreases (roughly up to 50%, cf. Figure 2.29b), the motion of individual grains can contribute even to a slight increase in the total kinetic energy for model possessing the rolling friction. Notably, the differences between the total kinetic energy evolution are sufficiently small, for the models with $\mu_R = 0.002$ and $\mu_R = 0.01$.

Thus, the selected interval of $\mu_R \in \{0.002, 0.01\}$ is not expected to take a large affect on bulk flow characteristics, and rather, the other material parameters, such as the sliding friction, have a more significant effect during the discharge process. This

also indirectly confirms the default value of $\mu_R = 0.01$ used by the commercial DEM software (EDEM™, DEM Solutions, Edinburgh, Scotland). However, the presence of rolling friction is expected to be a required and reasonable attribute to reproduce the experimental discharge behaviour of granular material for the elongated irregularly shaped particles, [250].

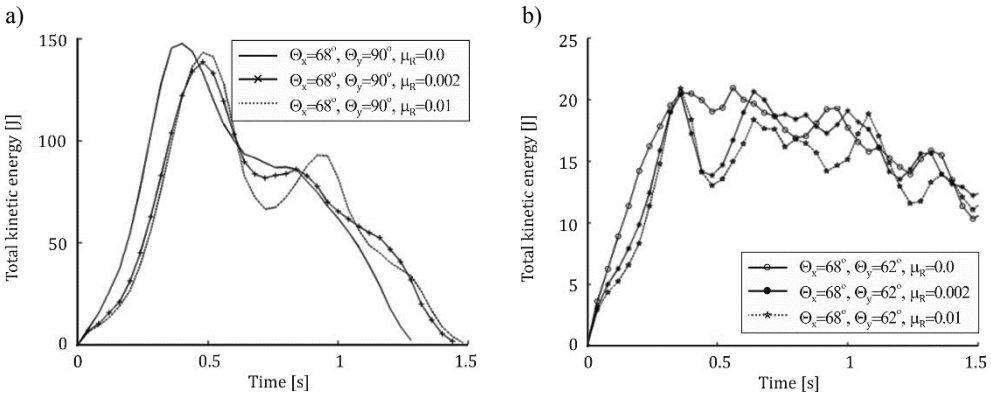

Figure 2.34. Time histories of the system kinetic energy during discharge from the plane (a) and space-wedged (b) hoppers for various rolling friction coefficients μ_R = 0, 0.002, 0.01 (μ = 0.3), [289].

2.2.4.3. Concluding remarks

The performed mathematical of filling and discharge processes in the plane-wedged, space-wedged and flat bottomed hoppers illustrated the potential of the DEM to understand and reproduce the complex flow of granular material. The obtained observations could be usefull in revising and developing the continuum models, esspecially for the case of the space-wedged hopper.

In particular, the space-wedged hopper, in comparison to the plane-wedged one, is characterized by the lower outflow velocities and the longer discharge time. The plane-wedged hopper discharges faster than the space-wedged one due to the plane flow, while, the space-wedged geometry produces a space-retarded flow, where the particles have more abilities to dissipate kinetic energy by the contacts. In particular, an isotropic distribution of velocities for the space-wedged hopper leads to the ability of particles to get more contacts resulting in the reduced vertical velocity due to the gravity acceleration. For the plane-wedged hopper, an anisotropic velocity

distribution with domination of the vertical velocity component was clearly observed. This component induces particle movements toward the centre of the hopper with almost twice higher velocity maginitude in comparison with the space--wedged hopper.

Despite a small number of particles used the obtained results are quite representative and observations comparable with the continuum-based indications. The introduced rolling friction suppresses a local spin of the particles decreasing their rotational abilities and rotational kinetic energy; however, the other parameters, such as, sliding friction, hopper shape have a more significant effect on the material bulk flow patterns in the case of values of the rolling friction coefficient considered ($\mu_R \in \{0.002, 0.01\}$).

"Main content of this chapter has been published in Advanced Powder Technology, 22, 226-235, 2011".

2.3. Quantitative predictions of granular material flow in a bin: a comparison of the computational results to the experimental data

2.3.1. Introduction

The above performed DEM simulations were devoted to qualitatively capture the main micro-macro phenomena occurring during the filling and discharge processes in different hopper shape. This Chapter shows the application of the above presented mathematical model in prediction an experimentally measured wall stress distribution and the outflow rate throughout the orifice in a 3D flat-bottomed bin. A granular aggregate of nearly round particles represented by 20,400 pea grains of 7.2÷7.8 mm in diameter is considered. In general, this investigation aims to quantitatively predict the flow parameters related to the careful identification of the material parameters. The results presented here are based on investigation published in [261].

2.3.2. Experimental investigation

2.3.2.1. Setup and measurements

The experimental setup comprised the flat bottom, a rectangular test bin made of Plexiglas and an upper, rectangular bin with a pyramid-shaped hopper fabricated from cardboard that was used for filling the test bin. The bin had the following inward dimensions: height of 800 mm, width of 252 mm, and thickness of 108 mm. These dimensions for the pyramid-shaped hopper were as follows: height of 385 mm, width of 390 mm, and thickness of 150 mm. The widths of the outlet were 42 mm for the bin and 48 mm for the container. The dimensions of the outlets were selected to reduce the discharge time and, thus, to allow the time of the computer simulation to be reduced, because the DEM analysis is highly time-consuming. All dimensions of the experimental model are presented in Figure 2.35.

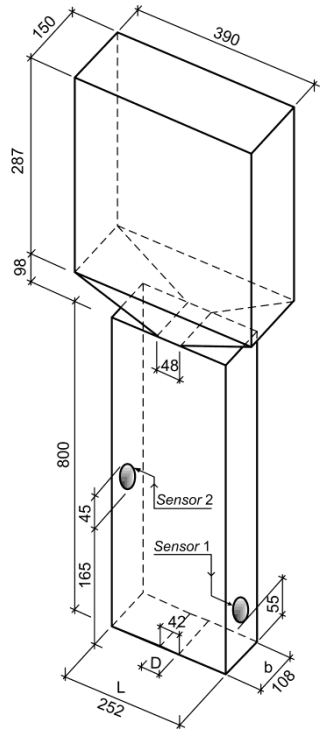

Figure 2.35. Experimental setup (dimensions are in mm).

Wall pressures were measured at two locations, one at 55 mm above the bottom on the left wall and the other at the height of 165 mm on the right wall. There were two 45-mm diameter tensometric sensors (of the type CL17) made of soft aluminium alloy and representing uniaxial strain gauge measurements. The strain gauges were connected to a data-measuring system consisting of the AD converter card ADLINK 9112. This system was linked to a computer. Measurements were controlled by a data acquisition program, which recorded and analysed the data in real time. The registration speed was 1000 readings per second. To calibrate the strain readings (mV), a weight standard was put on the sensors. Recently, the main pressure cell calibration methods have been comprehensibly investigated in [296]. The equipment (a weighing-machine sensor), controlling the outflow mass of the material, was also installed.

Granular material consisting of the pea grains was tested. These grains were simply poured into the pyramidal hopper. The measurements of the wall pressure were taken when the outlet of the upper container was opened and continued prior to opening the outlet of the test bin, i.e., under the quasi-static conditions, as well as during discharge, when the material flowed throughout the bin outlet. Wall pressures were computed via the voltage-mass conversion.

The measurements were repeated to find the average values of the data. The variation in the measured wall pressures for Sensors 1 and 2 is plotted in Figure 2.36.

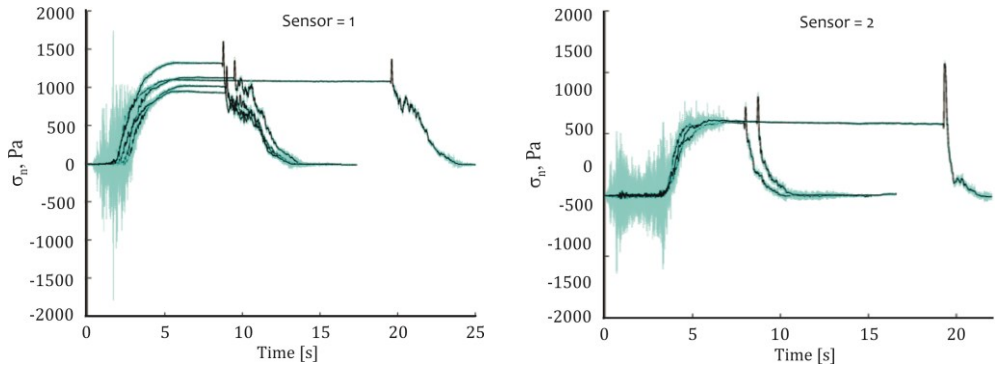

Figure 2.36. Measured and smoothed data of wall pressures from Sensors 1 and 2 vs. time.

As we can see in Figure 2.36 the measured data of wall pressures are usually of a noisy character. The noise (blue curves) is prevalent at the initial time instants during the filling of the material. This is due to the dynamic effect caused by the impact of individual particles against the sensor. However, after a certain period of filling, the continuum effect takes place, and the response of the sensor to the actions of the discrete particles is averaged due to the contribution of other particles. Therefore, the noise is greatly reduced. An important increase in the wall pressure is observed for both sensors after an instantaneous period, when the outlet was opened. This state is well known and marked by the fact that as soon as the material starts to flow, it can no longer support by the bottom of the bin; the material weight is transmitted towards the walls via the friction forces.

To reduce the noise of experiment and to avoid missing information on the original functions, the smoothing process should be performed. To this end, [297] smoothing method was implemented as a generalised moving average polynomial filter. This approach effectively preserved the narrow peak heights and widths, particularly, for the discharge pressure. The smoothed curves are plotted in Figure 2.36. The smoothed experimental curves will further be used for the comparative analysis.

The measured data on the outflow mass of the material by keeping the previous style is plotted in Figure 2.37. As it is seen in these graphs, a noisy character of the data dominated at the initial time instants during the material discharge process. This was due to the dynamical effect caused by the impact of individual particles on the weighing-machine sensor. As in the wall pressure measurements, this effect vanishes with time for the increasing outflow mass of the material.

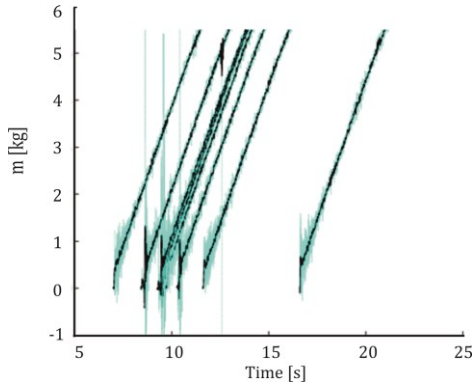

Figure 2.37. The measured and smoothed data of the outflow mass vs time.

2.3.2.2. Material properties

To apply the presented mathematical model, a number of physical properties of the granular material should be established. Physical characteristics of the pea grains, such as particle diameter, particle density and moisture content, were measured in the laboratory. Thus, the pea grains of a total mass of 5.87 kg had diameters of 7.2–7.8 mm and an average particle density of 1290 kg/m^3 (moisture content of 9%). The particle density was similar to that reported in [298].

Micro- and macro-mechanical properties of the pea grains were determined experimenttally in the laboratory of the Institute of Agrophysics of the Polish Academy of Sciences in Lublin and at the Bialystok Technical University. The experimental technique has been described in [299]. These characteristics are summarised in Table 2.3, while the elastic modulus and Poisson's coefficient of the wall made of Plexiglas were equal to 2630 MPa and 0.35, respectively.

The prediction of the silo wall pressures by the classical continuum approach is generally based on Mohr-Coulomb's yield criterion, which requires the data on granular material shearing. A triaxial test is the most accurate way to provide the shear strength of granular material in terms of the cohesion c and the internal friction angle φ. To this end, four specimens consisting of pea grains were tested in the triaxial apparatus. The triaxial test setup is depicted in Figure 2.38a.

a) b)

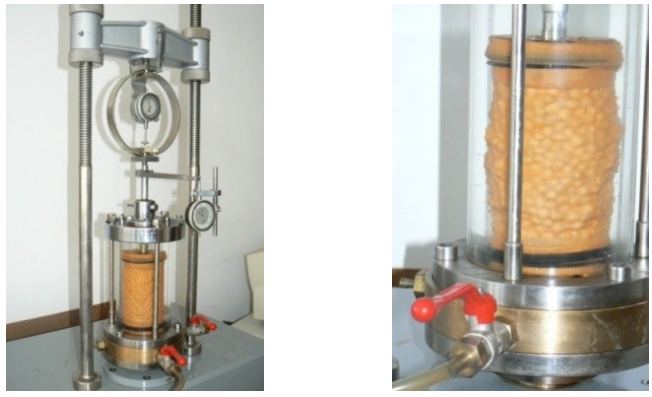

Figure 2.38. Photographs of the triaxial test equipment and the specimen in the assembled conditions (a), and at the end of the test with a bulge-type failure condition of the specimen (b).

Table 2.3. Experimental data on the particle material

Parameters	Quantity (mean ± st.dev.)	Explications and references
Microscopic scale		
Particle elasticity modulus, MPa	236.09 ± 40.89	Measured by compressing the grain between two plates according to [300] test.
Restitution coefficient (particle-wall)	0.56 ± 0.12	Determined by the drop/rebound of the grain on the plexi plate.
Rolling friction coefficient (grain-wall)	0.0167 ± 0,0011	Measured experimentally by rolling the grain from the inclined Plexiglass substrate according to [295].
Friction coefficient (particle-particle)	0.29 ± 0.09	Determined experimentally in [301].
Macroscopic scale		
Bulk elasticity modulus, MPa Poisson's ratio	4.06 ± 0.16 0.20 ± 0.01	Measured via uniaxial compression test (maximal normal pressure – 100 kPa, tester diameter 210 mm) on the basis of the descending branch of a linear dependency of vertical stress and strain occurring at the commencing of the unloading process, [302].
Internal friction angle, deg	17.02 ± 1.87	Triaxial test.
Friction coefficient (particle-wall)	0.199 ± 0.04	Determined experimentally.
Bulk density, $kg \cdot m^{-3}$	810 ± 3	Determined experimentally in [303] in accordance with Polish standard PN-73/R-74007.

In the triaxial test, a cylindrical pea grains sample placed in a plastic cell, with the sample being enclosed in a rubber membrane. The membrane connected to circular plates at the top and the bottom of the sample, with O-ring ensuring a water tight connection. The cell was filled with water, and the water pressure was controlled by a pressure unit. Since the sample was completely surrounded by water, at its cylindrical surface and at the top, a pressure equal to the cell pressure is generated in the sample. In addition to the lateral (and vertical) loading by the cell pressure, the sample also loaded by a vertical force, by means of a steel rod that passes through the top cap of the cell, (cf. Figure 2.38a). In the second stage of the test, the rod pushed down, at a constant rate, meaning that the vertical deformation rate is held constant, and that the force on the sample increases gradually. The vertical

movement of the top of the sample was measured by a mechanical measuring device, while the force gauged using a compression ring (cf. Figure 2.38a). The axial force has been gradually increased up to the failure of the specimen, and Figure 2.38b shows a bulge-type failure condition of the specimen that is usually prevalent for a loosely packed granular material. A further test procedure details is discussed in codes [304] or [305], while an excellent presenting for the determination of the shear strength from the triaxial test may be found in [306].

Particularly, the specimens with an initial height of 11.84 ± 0.12 cm, a diameter of 6.23 ± 0.043 cm, and a mass of 310.9 ± 3 g were tested. The initial porosity of the prepared specimens varied from 0.32 to 0.36, similar to the porosity developed within the silo model. The minor principal stresses equal to $\sigma_3 = 20$ kPa and $\sigma_3 = 40$ kPa were induced on the specimen by the water pressure, while axial compression was applied at a uniform rate of 11.8 mm/h. Because the load was measured by using the compression ring, the obtained displacement values were converted into the axial load.

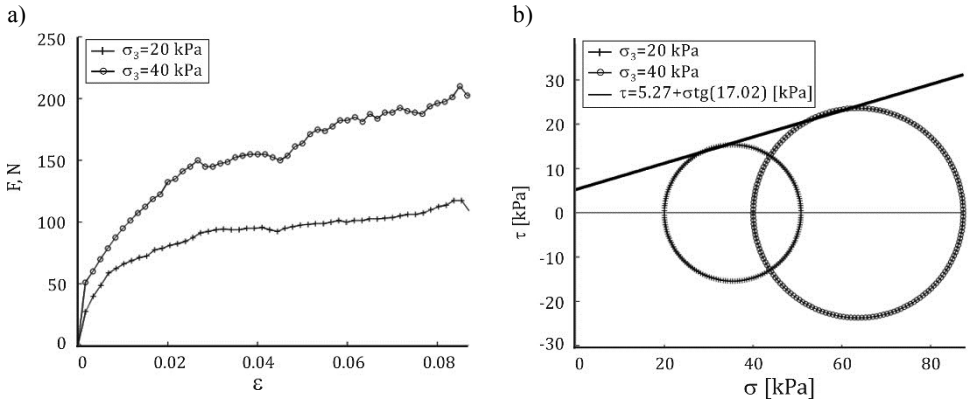

Figure 2.39. Force-strain paths from triaxial test (a) and Mohr-Coulomb's failure envelope (b).

In Figure 2.39a, the graphs of the axial strain ε vs. force F, generated during the tests, are shown. A failure force, shearing the specimen, was detected to rely on these paths, while this force per unit area A_c was used to find the deviatoric pressures $(\sigma_1 - \sigma_3)$.

A force-strain path, which is typical for loosely packed material, can be observed in Figure 2.39a for $\sigma_3 = 20$ kPa. As we can see, the sample consolidated for the whole loading range, while the peak of the shear force (strength) cannot be clearly

observed. Hence, the failure of the specimen should be based on the maximum value of the force equal to 102 N. In contrast, for $\sigma_3 = 40$ kPa, the failure mechanism consists of *an incipient* slip resulting in the disturbed consolidation path at the axial strain, varying from 0.025 to 0.05, where the incipient failure evidently occurs at a constant force equal to $F = 155$ N. In the sequel, the deformation and secondary slip of the material develops.

The pea grains have been supposed to be dry, so that there are no pore pressures, and the major principal stresses σ_1 are equal to the cell pressures plus the load F divided by the area $A_c, \sigma_1 = \sigma_3 + F/A_c$ (where $A_c = A_0/(1-\varepsilon)$ is the corrected area of the specimen, [304, 305], while A_0 is the initial area). The major stresses σ_1 at the specimen failure loads $F = 102$ N and $F = 155$ N were equal to 50.80 kPa and 87.33 kPa, respectively. By taking into account the above-defined failure loads, the failure envelope (a straight line) was resolved at the tangent to Mohr's circles and the cohesion (τ axis intercept), (cf. Figure 2.39b). The Mohr-Coulomb failure envelope in terms of the internal friction angle φ and the cohesion c was estimated analytically, deriving the following formulae for the A and B Mohr circles:

$$\varphi = \operatorname{arctg}\left(\frac{R_B - R_A}{\sqrt{(C_B - C_A)^2 - (R_B - R_A)^2}}\right), \tag{2.33}$$

$$c = \frac{R_A C_B - R_B C_A}{\sqrt{(C_B - C_A)^2 - (R_B - R_A)^2}}, \tag{2.34}$$

where $R_A = (\sigma_{1A} - \sigma_{3A})/2$, $R_B = (\sigma_{1B} - \sigma_{3B})/2$ and $C_A = (\sigma_{1A} + \sigma_{3A})/2$, $C_B = (\sigma_{1B} + \sigma_{3B})/2$ are radii and the centre locations, respectively, for A and B circles, while σ_{1A}, σ_{1B} and σ_{3A}, σ_{3B} are the major and minor principal stress, respectively, for A and B specimens.

In summary, relying on the triaxial test data presented in Figure 2.39a and using (2.33) and (2.34), the shear strength parameters for the pea grains are $\varphi = 17.02 \pm 1.87°$ and $c = 5.27 \pm 0.63$ kPa, (cf. Figure 2.39b). A direct shear test (tester diameter of 210 mm, vertical stress of 20 kPa, test procedure according to EN 1991-4, [166]) was additionally performed in the laboratory of Institute of Agrophysics of the Polish Academy of Sciences in Lublin yielded $\varphi = 16.70 \pm 2.23°$ and $c = 2.38 \pm 1.09$ kPa.

Thus, the values of the internal friction angle measured by the triaxial compression apparatus and those obtained by the direct shear test were in close proximity to each

other. To be sure that the obtained internal friction angle was appropriate for the conditions of a low vertical stress level developed in a bin model, a repose angle of the pea grain pile poured onto a horizontal plexi surface was measured. In particular, the pea grains were accurately poured as a narrow jet in the ring. The ring diameter was selected to keep the same weight of the poured material in a heap as that used in the bin test. The repose angle of the pile was very close to the internal friction angle measured in the triaxial compression apparatus.

The obtained cohesion should be mainly attributed to the difficulties in identifying the actual sample properties due to non-uniform distribution of stress and strain per sample volume caused by the non-homogeneous composition of the sample and some shear stresses produced by insufficiently smooth loading plates. Recently, an attempt to eliminate these effects, aimed at protecting against a wrong increase in the measured shear strength, has been given in [307].

2.3.3. Computational investigations

2.3.3.1. The input data and assumptions

It is difficult to measure experimentally the required micro-mechanical properties of the grains. Hence, the following assumptions and the input data for the DEM simulation were adopted. These are as follows:

1. The radii of the particles were generated by using an uniform distribution, since the grains have mild polydispersity.
2. Viscous damping properties were assumed to be identical for both particle-particle and particle-wall contacts. This assumption is mainly introduced due to the experimental difficulties to measure the grain-grain restitution coefficient. In [238, 308, 309] a variation of viscous damping parameters had a mild effect on the material outflow parameters and the values of the wall pressure developed after filling.
3. A viscous damping coefficient in the normal direction was found computationally resolving the task for the single particle rebounding from the wall. The selected value of damping coefficient equal to $\gamma_n = 8650\ s^{-1}$ computationally reproduces the experimentally measured restitution coefficient listed in Table 2.3. As a pheno-menological constant for all grains, this coefficient is applied in the simulation. Moreover, the ratio between the viscous damping coefficients in the normal and tangential directions, $\gamma_n/\gamma_t = 10$ was

additionally introduced on the present basis of knowledge. A more extensive discussion on this matter was given in [310].

4. Due to not ideal sphericity of the pea grains, as well as the variability in roughness of their surface and possible irreversible deformation during the real grain contact, a maximal value of the particle friction coefficient, equal to μ=0.4 (see, Table 2.3), was decided to select in the present simulation.
5. The friction coefficient between the grain and the wall (microscopic scale) was chosen to be the same as that for the bulk material and the wall (macroscopic scale). A small difference in these values was demonstrated in [236, 277, 311].
6. Poisson's ratio measured experimentally for the bulk material was also assumed to be the same as that for the grains. This assumption was made because of great experimental difficulties encountered in measuring Poisson's ratio for a single particle.
7. The coefficient of rolling friction for the pea grains was selected to be same as for grain-wall contact and a value of 0.017 is adopted in the current simulation (Table 2.3). It should be noticed that a systematic understanding of rolling friction on a whole granular medium is still lacking in literature. Certain attempt to investigate this phenomenon experimentally was demonstrated in [312].
8. On the pea grain level the adhesive forces were not considered; although the presence of cohesion on the bulk level was observed during the traixial test.

Finally, the mean values of all the material parameters, listed in Table 2.3, are considered to be the input data for the computational simulation, matching the experimental conditions described above. An additional analysis accounting for the variation of these parameters was not conducted due to an extensive time required for computer simulation. DEM simulations were carried out with the time step equal to 10^{-6} s.

2.3.3.2. Presentation of computational analysis

According to the described experimental setup, a simulation was carried out in several stages. In particular, the filling consisted of the settling of the material in the bin from the upper container, while the discharge flow meant the flow of the material out of the bin, starting at the instant of the opening of the outlet.

The stage of filling the upper container was conducted *en masse*, while the particles settled on the bottom of the container, the orifice was kept closed until a quasi-static state occurred. The evolution of the filling stage and the detection of the quasi-static state were performed by controlling the total kinetic energy of the system. The 'zero' of the total kinetic energy was held as an indicator terminating the stage of the container filling and starting to fill the bin. The bin-filling process and, later, its discharge are performed in a similar way. The hopper filling process and later its discharge are performed analogously. Snapshots on filling of the bin are shown in Figure 2.40.

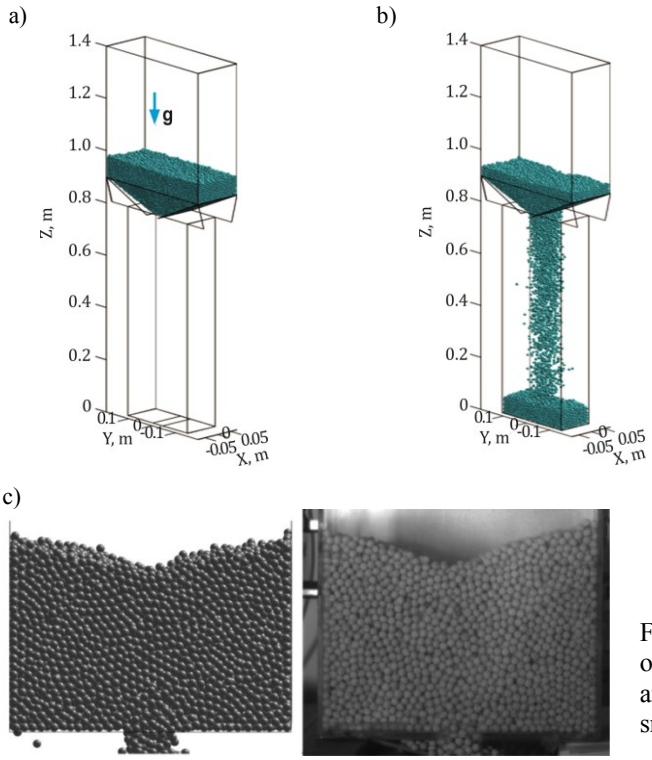

Figure 2.40. Simulation of filling of the upper container (a), bin (b) and simulation and experimental snapshots (c), [289].

As can be seen from Figure 2.40c, the computationally obtained composition of the flowing material is very similar to that generated in the experiment. A sufficiently good match was observed during the steady flow conditions. At early phase and at the end of the discharge process some difference in material compositions was discerned. During these phases the flow is greatly affected by the dynamics of individual grains, and this effect vanishes when flow becomes steady.

The particle contact forces as well as the distribution of the porosity fields obtained at the end of filling and during the discharge are depicted in Figure 2.41.

In general, the granular material is a discrete system composed of the particles, whose physical properties are not continuous with respect to position and time. Thus, an averaging procedure is required to obtain continuum-representative values. The averaging process was performed by dividing the bin into the representative spheres of sizes equal to 7–8 times the largest diameter of the particle. Fulfilling the condition of continuity was simply held by determining a sufficient amount of the particles for averaging by selecting the size of a representative volume. Finally, the computed volumetric data of the porosity were displayed on the spatial grid by implementing the cubic interpolation/extrapolation procedure. The implementation of this technique allowed us to estimate the unknown values of the porosity that lay between the probe's point in the representative spheres and to provide the smoothness of the results obtained.

A more sophisticated averaging approach based on a weighted time-space averaging method has been demonstrated in [313]. For the properly selected weighting function, it was ensured that the average properties also varied smoothly, while the contribution of different particles located near a probe point or the contribution of the time close to the time considered increased. It particularly meant that the size of the volume, in which the particle properties were averaged to obtain the continuum-representative equivalent, was not necessarily increased. In this way, the macroscopic properties, such as mass density, velocity, stresses, and couple stresses, were derived from the microscopic data of the discrete system, [253, 254]. However, a theoretically based selection of the parameters in the weighting function is lacking and still open for investigation.

The plots in Figure 2.41 mainly indicate two different ways the particle force transmission developed within the granular material at the end of filling and during discharge and demonstrate the degree of the material compaction governed by these forces. In particular, the particles located near the orifice, where they were compressed by material weight before the outlet was opened, were practically unloaded at the outlet opening. The unloading of the particles was caused by the dilation of material inducing an increase in the bulk porosity near the orifice due to the shearing effect governed by the outlet opening. It can also be observed that some particles were subjected to much higher forces as compared to other grains. This

effect may have been partially related to the connection of the particles into the local stressed arches developed within the granular material.

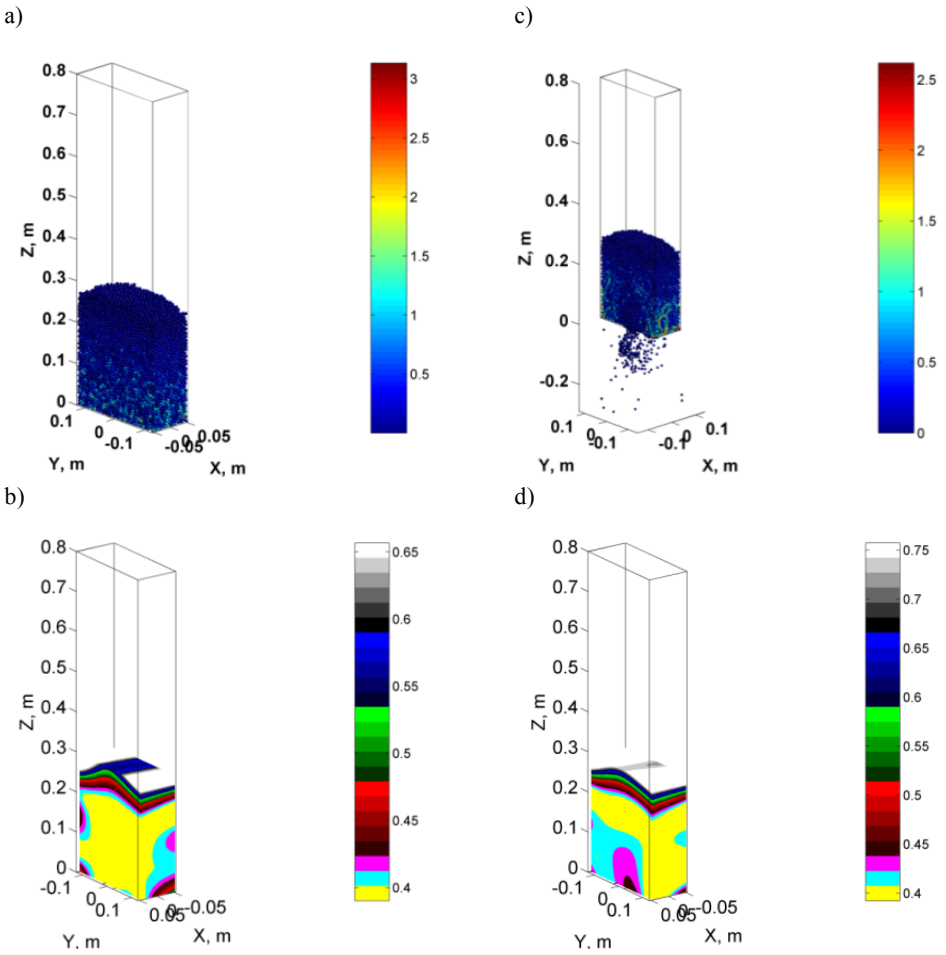

Figure 2.41. Illustration of the state of the material with inter-particle contact forces (expressed in N) and the porosity distribution within the granular material ($\mu = 0$): a-b) at the end of filling, c-d) at $t = 0.2$ s during discharge.

A porosity value of $n \approx 0.39–0.41$ (cf. Figure 2.41a) prevalent in the filling process corresponds to the so-called random loose packing of granular material. Due to the material dilation, the porosity in the zone located above the orifice occupied about two widths of the outlet and increased during discharge to about 0.44. The

alterations of the porosity near the orifice are important for defining the bulk material density for the theoretical outflow rate prediction.

In Figure 2.42 the effect of rolling friction on the contact force distribution within the granular material is demonstrated.

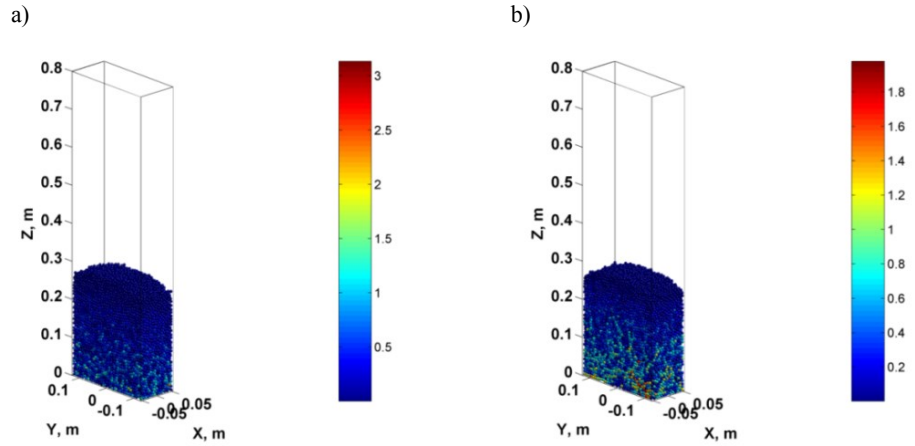

Figure 2.42. Distribution of particles contact forces within granular material:
a) $\mu = 0$, b) $\mu_R = 0.017$.

Here we observe from snapshots in Figure 2.42, account for the rolling friction results in a different forces transmission within the ensiled granular material, in particular, at the lower part of the bin is occurred (cf. Figure 2.42a and Figure 2.42b). The rolling friction produces an increase in the local heterogeneity of the particle contact forces and some particles are subjected by much higher forces in comparison with the case $\mu_R = 0$. This fact may partially relate to more abilities to develop the local stressed arches within material at the end of filling.

2.3.3.3. Results of the stress analysis

The stress patterns originated from the individual particle contact forces developed within the granular material have a major influence on the magnitude of the bin wall pressure. The prediction of the stress distribution is usually associated with the application of the method of characteristics or FEM. In general, the first approach requires only the additional application of a yield criterion resolving the force equilibrium, linking the unknown stresses, while the second method is more powerful, particularly if the analysis relies on the constitutive models that provide the stress-strain response and characterise the nature of the material flow. However,

capturing the discrete nature of granular material by the continuum-based constitutive laws has not always been successful, while the solution of the problems is always associated with the difficulties arising in the non-linear FEM analysis. In contrast, the analytical models are restricted, predicting the wall pressure, provided that the stress distribution within the granular material is assumed a priori.

In using these approaches, the DEM method is more effective because it naturally allows us to model the discrete nature of granular material and to take into account the granular dynamics, while the effect of the material dilation does not need to be legitimated mathematically by the constitutive models. Here, Newton's Eqs. (2.1-2) replace the force and momentum equilibrium, as those are used in the continuum mechanics, while the constitutive model is replaced by the model describing particle contacts (2.3-7). Meanwhile, relying on the contact forces and their contact locations within an assembly of particles, the macroscopic mean stress tensor may compute by formula (2.32).

The implementation of Eq. (2.32) for the stress analysis involves the evaluation of the collisional contribution for the interaction forces between the particles and the interactions between the particles and the walls. In general, there is also the third term involving the kinetic contribution related to the transport of particles, [313]. However, for bin flows, the stress is mainly contributed by the collisions between the particles and between the particles and the walls, [254]. Thus, Eq. (2.32) was used for the theoretical description of the stress developed within the granular material for filling and discharge states.

The experimental determination of σ_{ij} within the granular material is very complex, requiring non-invasive and precise contact force measurements. Actually, the existing experimental techniques cannot provide much information concerning the stress acting within the granular material during the bin flow. Rather, let us consider stress distribution within the granular material computed. As in the case of determining the porosity fields, the whole material was also divided into representative spheres, and the particle microscopic quantities within these spheres were homogenised. Computational implementation of formula (2.32) into DEM analysis and the verification of the obtained results were provided in [314].

The obtained distributions of the normal stresses within the granular material are depicted in Figure 2.43. Here, the illustration is restricted to the vertical, σ_{33}, and horizontal, σ_{22}, components of normal stresses.

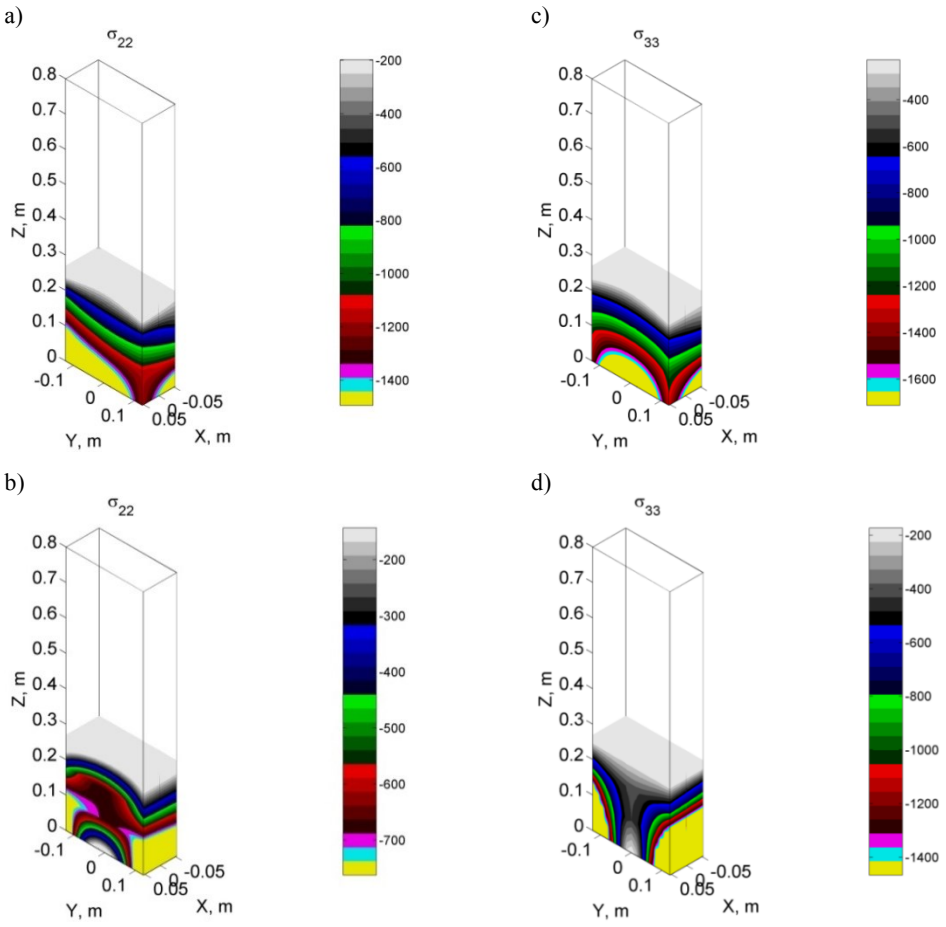

Figure 2.43. Normal stress distribution in granular material: a, c) at the end of filling; b, d) at t= 0.2s during discharge. Here, horizontal, σ_{22} and vertical, σ_{33} stresses are given in Pa.

As follows from Figure 2.43a, c, the distribution of horizontal and vertical normal stress components had mainly a convex shape along the coordinate y, and their values were lower at the walls, compared to the central part of the bin. This is due to the fact that stresses at the central axis of the bin were principal, because there is zero shear stresses here, σ_{32} (due to the symmetry), and it started growing up away from the centre due to the wall friction, reducing the stresses σ_{33}. The magnitudes of the horizontal stresses were lower than the vertical stresses because the material partially transmitted its own weight towards the wall and the bottom due to friction.

During discharge (cf. Figure 2.43b and d), the normal stresses fell to almost zero at the orifice due to the material dilation (cf. Figure 2.41d), increasing from the centre towards the walls, thereby indicating a typical transformation of the stress fields from the convex (after filling) to the concave shape (during discharge). Theoretically, the active stress state with convex stress distribution within the material is generated after the filling, while the passive stress state with the concave stress shape should develop during the discharge. A transient stress state can distinguish at 0.2 s, if the upper part of the bin is still in the active state with the passive regime propagating towards the upper boundary. As we can see in Figure 2.43c, in the upper zone of the bin, there was still a convex stress distribution, while in the lower part of the bin, the passive stress regime started to develop. This significantly affected the wall pressures, while the pressures obtained at the end of the filling process were lower than the pressures generated immediately after the outlet opening. This could also demonstrate experimentally, (cf. Figure 2.36).

When the material is in a plastic limiting state, the Mohr stress circle touches the incipient yield locus, and the yield criterion can be written in the following way:

$$F(\sigma_1, \sigma_3) = \frac{\sigma_1 - \sigma_3}{\sigma_1 + \sigma_3} - \sin\varphi \leq 0, \text{for } \sigma_1 > \sigma_2 > \sigma_3. \tag{2.35}$$

By denoting $\sin\varphi^* = \frac{\sigma_1 - \sigma_3}{\sigma_1 + \sigma_3}$, we can write the yield criterion as

$$\sin\varphi^* - \sin\varphi \leq 0. \tag{2.36}$$

Now, the internal friction angle φ^* can specify in terms of the principal stresses developed within the bin and may express as follows

$$\varphi^* = \arcsin\left(\frac{\sigma_1 - \sigma_3}{\sigma_1 + \sigma_3}\right). \tag{2.37}$$

The internal friction angle φ^* can be computed from the stresses developed within the bin and compared with the internal friction angle φ, governed by the material shear strength. In particular, following the yield criteria (2.35) and (2.36), when the obtained φ^* is equal (or very close, due to the errors) to the internal friction angle φ, determined via the triaxial test, then the material filled should be in the plastic state. Otherwise, $\varphi^* < \varphi$, and the stress state does not induce yielding.

For this purpose, the principal stresses σ_1 and σ_3 were computed as the eigen values of the stress tensor $\boldsymbol{\sigma}$ accounting for the normal and shear stresses developed within the granular material after filling. The distribution of normal stresses was shown in Figure 2.43a and 6c. The distribution of the computed internal friction angle φ^* is plotted in Figure 2.44.

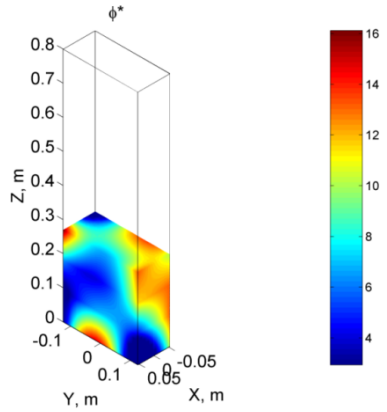

Figure 2.44. The variation of the internal friction angle (in degrees) determined from the principal stresses developed after filling.

As shown in Figure 2.44 the computed distribution of the internal friction angle, determined from the principal stress components generated within the bin, varied over the range of 2.95° and 16.11°. It was determined from the triaxial compression test that the internal friction angle $\varphi = 17.02 \pm 1.87°$, (Table 2.23). Thus, we can see that there were portions of the material (near the bottom centre, adjacent to the upper part of the wall and at the corners of the top surface of the material), where the computed φ^* was near the mean value of the experimental internal friction angle φ or slightly exceeded its lower limit. Therefore, it may be stated that the stresses developed at the end of filling were close to the Mohr-Coulomb plastic state of stress in some parts of the material, but an elastic stress state also occurred. The yielding material zones located near the top surface of the stored bulk solid in a conical hopper have also been found in a FEM analysis conducted in [315].

Furthermore, the values of the internal friction angle determined from the principal stress developed at the bin wall (cf. Figure 2.44) are close to those determined experimentally, (Table 2.46). This supports the adopted assumption of mobilisation of the wall friction.

2.3.3.4. Results of the wall pressure analysis

We next compare the predicted values of the wall pressures with those measured experimentally. The experimental values of wall pressures, presented in the previous graphs in Figure 2.36, were analysed statistically, specifying their averaged values and 95% confidence intervals. A statistical analysis was performed, establishing the level of adequacy between the experimental and computational results, i.e., verifying if the predicted values fit within the upper and lower limits of the confidence intervals. The computational wall pressures were simulated by summing up the particle-wall contact forces and averaging their resultant force over the sensor surface area. The graphs of these values and those measured experimentally, with statistical evaluation, are plotted in Figure 2.45.

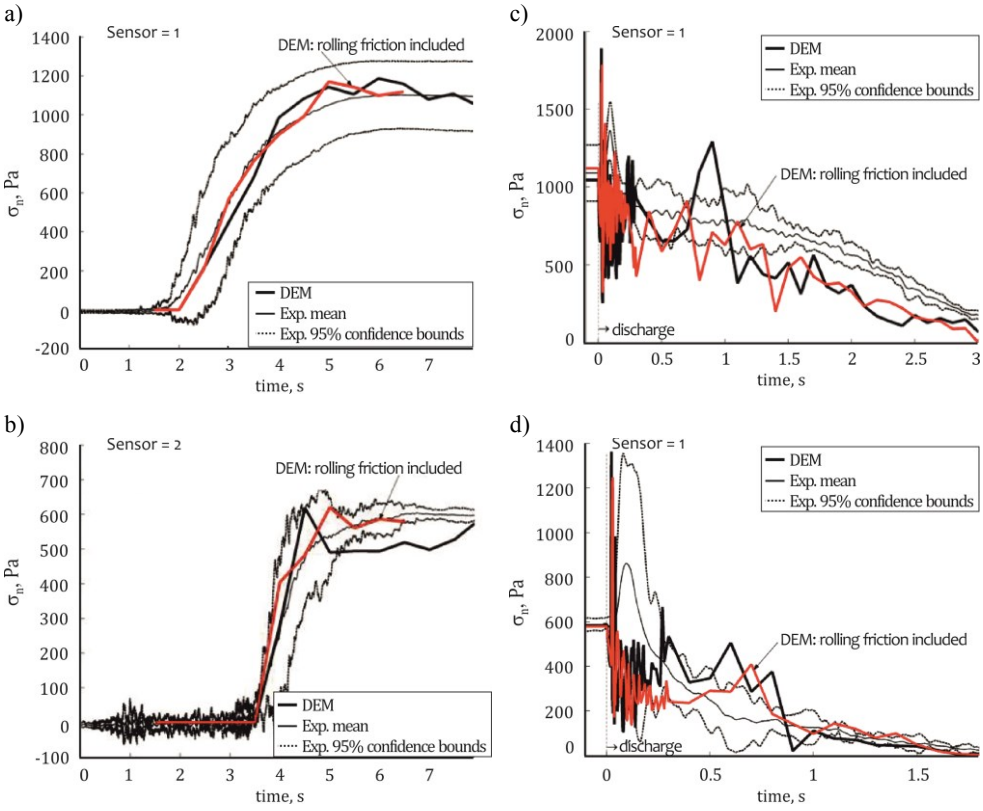

Figure 2.45. Computational and experimental results of wall pressures vs time: a, b) filling, c, d) discharge.

As we can see in Figure 2.45, the predicted wall pressures (for the case of $\mu_R = 0.017$ and for $\mu_R = 0$) mainly lay within the 95% confidence interval, where the experimental mean pressures actually take a value. This tendency applies to pressures for both sensors. The main important peaks of the discharge overpressures, recorded soon after the discharge process started, were also captured by the DEM model. However, the peaks captured by DEM were slightly shifted in time. This can result from the above adopted assumptions. It should also be noted that the values of the wall pressures determined in the area of the sensor and those derived by the stress homogenisation (cf. Figure 2.43) are in good agreement, indicating that the pressure values registered by the sensors may treat as the representative values for the wall pressures.

The effect of rolling friction ($\mu_R = 0.017$) is minimal on the wall pressures distribution at the end of filling. The current value of rolling friction coefficient slightly reduces wall pressures during discharge and increases time to develop the discharge overpressures.

Janssen's analytical solution accounting for the filling pressures, developed in the sections with vertical walls, is implemented in the most standards on bin design. It was found from the simplified force equilibrium of a horizontal slice of the ensiled material that the vertical stresses adjacent to the wall can express as a function of the depth z by the following relationship:

$$\sigma_{33} = \frac{\gamma D_h}{4\mu_w K_{pl}}\left(1 - e^{\frac{-4\mu_w K_{pl} z}{D_h}}\right), \tag{2.38}$$

where γ is the bulk material weight, $D_h = \frac{2bL}{b+L}$ is the hydraulic mean diameter for a rectangular cross-section, [128], μ_w is the friction coefficient between the bulk material and the wall, and K_{pl} is a constant defining the ratio between the horizontal and vertical stresses.

Taking into account that the friction stress, acting on the wall, satisfies Coulomb's friction rule at the interface of the bulk material and the wall for a fully mobilised friction (i.e. $\mu_w = \text{const}$), the shear and normal wall pressures may define as follows:

$$\sigma_n = K_{pl}\sigma_{33}, \tag{2.39}$$

$$\tau_n = \sigma_n \mu_w. \tag{2.40}$$

There is no universal expression for determining the constant K_{pl}. Let us assume that the granular material deforms elastically. For an isotropic material, the strain tensor is defined as

$$\varepsilon_{ij} = K\sigma\delta_{ij} + \frac{1}{2G}s_{ij}, i, j = 1, 2, 3, \tag{2.41}$$

where $3\sigma = \sigma_{kk}, s_{ij} = \sigma_{ij} - \sigma\delta_{ij}$ is the deviatoric stress tensor, δ_{ij} is the Kronecker delta, $K = (1 - 2\nu)/E$ is the bulk compliance modulus and $G = E/\big(2(1 + \nu)\big)$ and E are the shear and elastic moduli of the granular material, respectively, while ν is Poisson's ratio.

We also assume vertical strain of the material, $\varepsilon_{33} = \frac{\mathrm{d}u_z}{dz}$, without any lateral strain (i.e., no deformation of the walls), and accounting for the boundary conditions in displacements, $u_x = 0, u_y = 0$ and $\varepsilon_{11} = \frac{\mathrm{d}u_x}{\mathrm{d}x} = 0, \varepsilon_{22} = \frac{\mathrm{d}u_y}{\mathrm{d}y} = 0$, and using only the two equations of (2.41), we get

$$\sigma_{11} = \sigma_{22} = \frac{\nu}{1 - \nu}\sigma_{33}. \tag{2.42}$$

The comparison of formula (2.42) and (2.39) yields the ratio of horizontal and vertical stresses at the wall, $K_{el} = \frac{\nu}{1-\nu}$. Here, σ_{33} expresses as a function of the depth z according to Eq. (2.38).

In Janssen's solution (2.38), the prediction of K_{pl} is usually restricted by a drastic assumption about the material yielding and its location. However, the location of yielding is not known and should be always assumed in advanced. The cases describing the yielding at the wall, the yielding at the central axis of the bin, and the yielding at the centre and at the wall are considered in [2]. These relationships do not produce significantly different results for the wall pressures (up to 10–15%) in the active state of stresses but correct the shortcomings mainly associated with Janssen's analysis to some extent.

Following the plot in Figure 2.44, it would be reasonable to assume a yielding at the wall, i.e., the material is tending to slide down at the wall. In this case, the ratio of horizontal and vertical stresses may be calculated by Walker's formula, (see also [2] and [128])

$$K_{pl} = \frac{1 + \kappa \sin\varphi \cos(\omega + \kappa\varphi_w)}{1 - \kappa \sin\varphi \cos(\omega + \kappa\varphi_w)}, \tag{2.43}$$

where $\omega = \mathrm{asin}(\sin\varphi_w/\sin\varphi), \varphi_w = \mathrm{atan}(\mu_w)$ while $\kappa = -1$, for the active stress state, which is essentially prevalent in a flat bottomed bin after filling.

Following [217], when $K_{pl} > K_{el}$, an active plastic zone develops in the bottom domain, while, in the middle part, the elastic bahavior prevails, (cf. Figure 2.44). By determining which of the coefficients is larger the elastic or plastic coefficient, we can see that, $K_{pl} = 0.6 > K_{el} = 0.25$. Thus, the plastic state theoretically takes place, and the wall pressures should be determined by Mohr-Coulomb's yielding condition. This also indicates that the "plastic" pressures will be greater than the pressures calculated assuming the elastic bahavior. In [195], the authors also concluded that the non-linear analysis, taking into account the Drucker-Prager elasto-plastic yield criterion, predicts a higher wall pressure than the elastic one.

Eurocode 1 (EN 1991-4, [166]) suggests the following expression for the ratio of horizontal and vertical stresses

$$K_{pl} = 1.1(1 - \sin\varphi). \tag{2.44}$$

Recently, the main expressions for K_{pl} ratio, considering the effect of slope of the walls and appropriate shearing resistance adjacent to the walls, have been investigated for an active stress regime, [316].

The experimental pressures with that determined by the DEM and the Janssen's solution (accounting for K_{pl} and using (2.42) and (2.43)) are compared in Figure 2.44. As the input data, the material parameters and their variations, listed in Table 2.23, were applied to make the theoretical prediction.

As we can further see in Figure 2.46, the Janssen's analytical model using (2.38) underestimates the wall pressures. Recently, the similar Janssen's model deviation from the experimental results has also been found in [296].

The better fit of Janssen's solution to the experimental observation is found, when Eurocode 1 relation (2.42) for constant K_{pl} is adopted. In [317], the authors measured directly values of K_{pl} ratio for 41 bulk solids at uniaxial compression and compared these values with formula $K_{pl} = 1.2(1 - \sin\varphi)$ and also obtained the smallest deviations to the measured values.

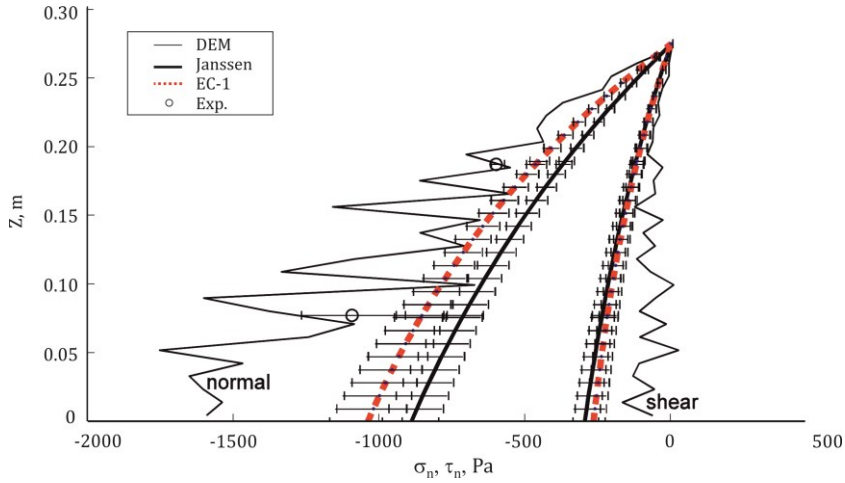

Figure 2.46. Wall pressures and their variation bounds vs. material depth.

The scattering in DEM pressure may minimise by plotting the averaged curve through the saw-toothed function or by increasing the height of the wall segment. However, the wall pressures determined on the segment height of 1.5 times of the mean diameter and that computed directly on the sensor area have approximately the same values.

Finally, the transient state and switch from the active to passive stress state during discharge is associated with the upward propagating passive state zone. This state is characterised by the sudden growth of the wall pressure at the moving interface. The analytical description of the transient state was presented in [217] for the case of a granular flow in converging hoppers. Here, the wall pressure peak that developed immediately after the orifice opening is observed both in the experiment and in DEM calculation.

2.3.3.5. Particle velocity distributions within the bin

The development of stresses within the granular material is mainly subjected to the kinetics of particles within the bin. The experimental investigations on the particle velocity profiles developed within the bin were not conducted due to technical problems, and measurements were restricted to the outflow mass establishment. Hence, a brief kinematic insight into the mean velocity profiles developed within the

bin during the material discharge may perform on the theoretical and DEM-based results.

Thus, to avoid the local effects produced by the individual grains, DEM simulations are focused on the mean parameters. Therefore, the simulated positions of the particles were averaged within the selected volume of the assembly. The difference in the averaged positions between two consecutive stages of the flow was divided by the time step of these stages.

For this propose, similar to the stress analysis, the whole domain of the material was divided into the representative spheres. The particles within these spheres were identified at a certain initial time, and the locations of the identified particles were then determined for the subsequent time instant to establish the average velocity. An averaged velocity for the representative sphere k was obtained as follows

$$\langle \mathbf{v}_k(t+\Delta t)\rangle = \frac{\langle \mathbf{x}_k(t+\Delta t)\rangle - \langle \mathbf{x}_k(t)\rangle}{\Delta t}, \tag{2.45}$$

where

$$\langle \mathrm{x}_k\rangle = \frac{1}{n}\sum_{i=1}^{n} x_i, \langle y_k\rangle = \frac{1}{n}\sum_{i=1}^{n} y_i, \quad \langle z_k\rangle = \frac{1}{n}\sum_{i=1}^{n} z_i, \ (k = 1,2,\dots m), \tag{2.46}$$

are the averaged positions of the particles in the sphere k at a certain time, x_i, y_i, z_i are the components of vector $\mathbf{x}_i$ for particle i within the sphere k.

A distribution of the mean vertical velocity developed during discharge is plotted in Figure 2.47. The averaging process was performed by specifying the representative spheres having the size equal to 7–8 times of the largest diameter of the particle.

The contour plot drawn in Figure 2.47 indicates a maximum of the vertical velocity v_3 right at the outlet and appeared to take off upward, in qualitative agreement with the well-known kinematic models and the experimental investigations reported previously in [34, 35]. The regions of the material located on the left and right corners made by the walls and the bottom, remain stagnant, while the boundary of the mobile regions is parabolic in shape.

In [87] continuum kinematical model provides a sufficiently accurate prediction of the velocity profiles using only one unknown constant, for the convergent flow region under steady state conditions. They assumed that the horizontal velocity

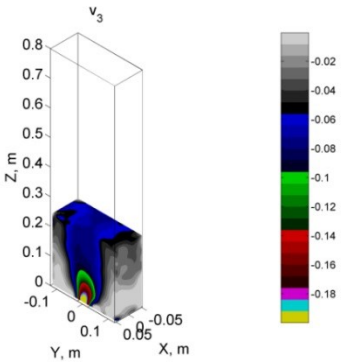

Figure 2.47. Fields of the mean vertical velocity (m/s) at 0.9 s of the discharge process: a volumetric distribution $\mu_R = 0$.

is proportional to the gradient of downward velocity v_3 (i.e., a shear rate). Application of this assumption for an incompressible material yields:

$$\frac{\partial v_3}{\partial z} = -B\frac{\partial^2 v_3}{\partial y^2} \tag{2.47}$$

where y is the horizontal distance from the vertical axis of the silo, z is a distance above the outlet, B is the proportionality factor or diffusion length referred in [141] (also discussed in detail in Chapter 1).

A Gaussian function fulfils the solution of (2.47), for v_3 and v_2

$$v_3(y,z) = \frac{Q}{\sqrt{4\pi Bz}} e^{\left(\frac{-y^2}{4Bz}\right)} \tag{2.48}$$

$$v_2(y,z) = -B\frac{\partial v_3}{\partial y} = \frac{Q}{\sqrt{4\pi Bz}}\frac{y}{2z} e^{\left(\frac{-y^2}{4Bz}\right)} \tag{2.49}$$

where Q denotes a volumetric flow rate per unit thickness of the silo, $v_3 \equiv v_z$, $v_2 \equiv v_y$.

In general, there is no theoretical way to predict B a priori and the model cannot directly be applied as a predictive approach. However, to produce the observed velocity patterns (cf. Figure 2.47) we adopt a regression analysis for a suitable choice of B. Thus, denoting the first term of (2.49), as the downward velocity at the hopper centre line, $v_3(0,z) = \frac{Q}{\sqrt{4\pi Bz}}$, we implement a non-linear least square fit to find $v_3(0,z)$ and B for the DEM-based velocity patterns, (cf. Figure 2.47). This simply allows for omitting the derivation of Q from the mass flow rate with respect to porosity evolution.

In the regions of the material located on the left and right corners of the walls, remain stagnant almost to end of discharge, while the boundary of the mobile regions is theoretically similar to Gaussian function. Distribution of the horizontal velocity v_2 over y has an inverse distribution in comparison with v_3. Horizontal velocities dominate at the wall, since the particle vertical velocities are greater at the bin centre and the particles, located at the walls, start to move toward the outlet, where the voids are formed during flow. At the centre of the bin, $v_2 = 0$ due to symmetry, thereby a vertical flow prevails here. Mathematically, there appears to be a function between the horizontal and vertical velocities, such that $v_2 = -B\frac{\partial v_3}{\partial y}$.

The obtained velocity profiles for the rolling friction coefficients of $\mu_R = 0$ and $\mu_R = 0.017$ are plotted in Figure 2.48. Here, graphs shown in Figure 2.48a, c demonstrate the evolution of velocity patterns developed within the bin at $t = 0.6$ s, while the plots in Figure 2.48b, d were obtained for $t = 1.4$ s.

As we can see in Figure 2.48c, d, accounting for the rolling friction reduces the horizontal velocity. This effect can be explained as follows: during the flow, the upper parts of the material descend more rapidly than the outer portions, and this process forms a central depression zone, (cf. Figure 2.40). As the discharge time increases, the zone becomes more steeply inclined. Then, when the slope of the stagnant zone reaches the internal friction angle, the particles cascade downward through the stagnant zone surface as they move toward the outlet. Due to frictional contact with the stagnant material, the particles moving from the walls toward the outlet start to rotate, while the rolling friction acts suppressing the horizontal motion of the particles, (cf. Figure 2.48c, d). In particular, the reduced horizontal motion of the contacting particles is generally governed by the decreased rotational velocities about the x-axis, which occurs as the result of the rolling friction, (cf. Figure 2.49). As can be observed in the plot, the rotational velocity is approximately zero at the bin corners within $z = 0.05$–0.10 m, (cf. Figure 2.49a) and increases toward the centre of the bin. Meanwhile in the upper parts of the bin, the wall friction forces induce rotational velocities. On the contrary, a considerable increase in ω_x near the wall at $t = 1.4$ s (cf. $z = 0.2$ m, in Figure 2.49b) could be attributed to the formation of rupture surfaces, where a sudden cascade down of the particles located near the wall into the central depression zone of the material takes place specifically for the case of $\mu_R = 0.017$. At the centre of the bin, the rotational (cf. Figure 2.49a, b) and horizontal motions (cf. Figure 2.48c, d) of the grains tend to zero (due to symmetry) and the effect of the rolling friction becomes minimally significant. Hence, at the

centre of the bin, the vertical velocities of particles are almost invariant due to the effects of the sliding and rolling frictions.

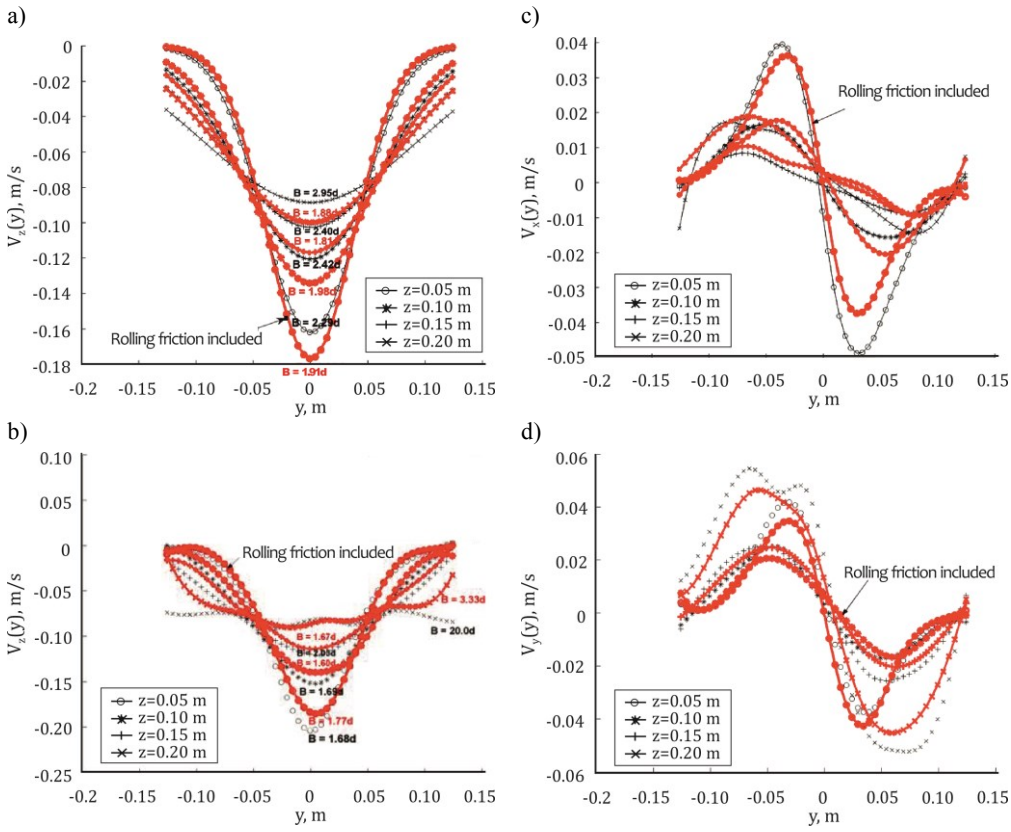

Figure 2.48. Profiles of the mean velocity for: a, b) the vertical component v_z; c, d) the horizontal component v_x, [261].

Graphs illustrating the profiles of the mean rotational velocity about the x-axis are also shown in Figure 2.49. The numerical data obtained were also focused to get the mean parameters. In this way, the rotation angles and the positions of the particles were also averaged within the selected representative volumes (size of ~10 Ø of the particle), and the difference in the averaged angle between two consecutive stages of flow was divided by the time step of these stages. This approach was used to obtain the continuum-based rotational velocities. A cubic interpolation/extrapolation was also applied to find the unknown values of the velocity components that lie between

the probe's point of the representative spheres; this approach was implemented to provide the smoothness of the results obtained.

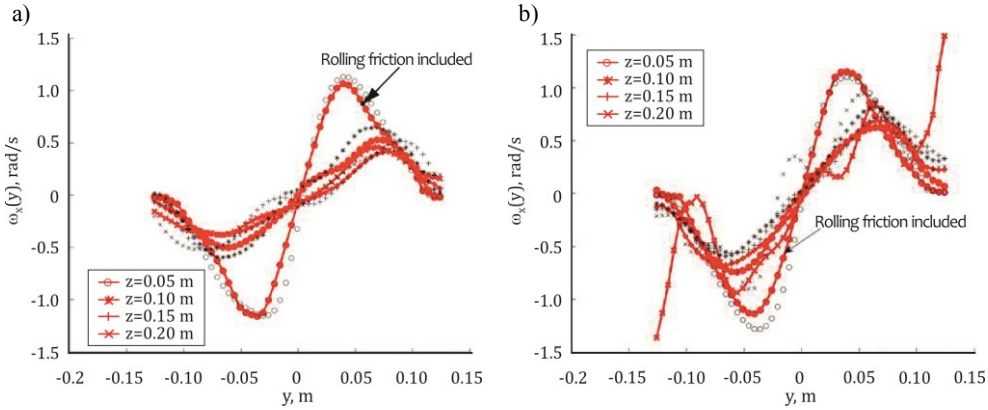

Figure 2.49. Profiles of the rotational velocity for: a) t=0.6 s, b) t=1.4 s, [261].

Because the horizontal motion of the particles is suppressed by the rolling friction, more voids can generate at the centre of the bin. This results in a less dissipation of the kinetic energy by the jostling of particles against each other, and the material located at the centre of the bin is allowed to move even faster (cf. v_z, for the case of $\mu_R = 0$ and $\mu_R = 0.017$, in Figure 2.48a). In the later stages of discharge, when the top surface of the material is formed into a great depression and the material at the centre of the bin is mainly supplied from the breakage of stagnant zones, the effect of the rolling friction becomes dominating and the vertical velocity reduces (cf. v_z, for the case of $\mu_R = 0$ and $\mu_R = 0.017$, in Figure 2.48b). As the horizontal motion is affected by the rolling friction, it can be said that the rolling friction increases the steepness of the velocity vector within the central zone of the bin.

Now, let us consider the effect of the rolling friction of the material constant B as given in [87]. Actually, there is no predictive approach for determining this constant *a priori*; therefore, we adopted a regression analysis approach via a nonlinear least squares formulation for determining the suitable choice of B and $v_z(0,z)$ to fit the Nedderman-Tüzün's nonlinear equations to the numerical velocity patterns plotted in Figure 2.49a, b. An indicator of the fit quality is demonstrated in Figure 2.50, for t = 1.4 s. These graphs show good agreement between the simulation and the fitted curves to the Nedderman-Tüzün's model, [87].

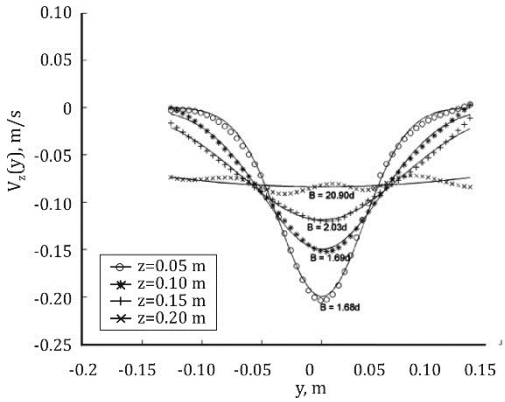

Figure 2.50. Illustration of the quality of the fit to the Nedderman-Tüzün's nonlinear model, [87].

Thus, the obtained values of B, specified in Figure 2.48a, b above each curve, clearly indicate that the material constant B reduces due to the effect of rolling friction in order to obtain a tall shape of Gaussian distribution for a continuum-based velocities prediction. This conclusion could be an additional explanation of the different values for the parameter B referred in literature. In particular, in [138] experimentally found that $B \cong (2.3–3.0)d$, for various particle sizes d. In [86], the author determined that $B \cong 2d$, for iron ore particles, while in [25, 26] it was stated that B varies even from $B \cong 1.5d$ up to $4d$.

2.3.3.6. Results of the outflow analysis

Finally, let us consider the material outflow parameters. The rate is effectively independent of the quantity of the material in the bin, when the material height H is established: $H > 2D$; and $L > 2.5D$. As it can see from the experimental setup dimensions and the settled material height after filling, these conditions are fulfilled, highlighting the fact of the sufficient material quantity within the bin and expecting a constant outflow rate with time. Thus, the material rate depends only on the bulk density ρ_b, the outlet size D x b, gravity acceleration g and the material friction. For a rectangular shape of the outlet, the outflow rate is predicted by well-known expression originally proposed by [318]:

$$\frac{\mathrm{d}m}{\mathrm{d}t} = \frac{8C}{\pi\sqrt{2}}\rho_b\sqrt{g}\frac{\left((D-kd)(b-kd)\right)^{3/2}}{(D+b-2kd)^{1/2}}, \tag{2.50}$$

where kd is the width of the so-called "empty annulus", C is the material constant, which, following [128], may assume to be 0.64 for exceptionally smooth spherical particles and 0.58 for the rough ones.

The smoothed experimental values of the material outflow mass vs. the computational prediction are plotted in Figure 2.51a. In Figure 2.51b, the outflow rates, derived from the dependencies of the outflow mass vs time (cf. Figure 2.51a), are also shown. For the theoretical predictions by Eq. (2.50), ρ_b is calculated from the filling end (cf. Figure 2.41b); while the material constant is equal C = 0.58, [128]; and k = 1.5, as originally applied by [318].

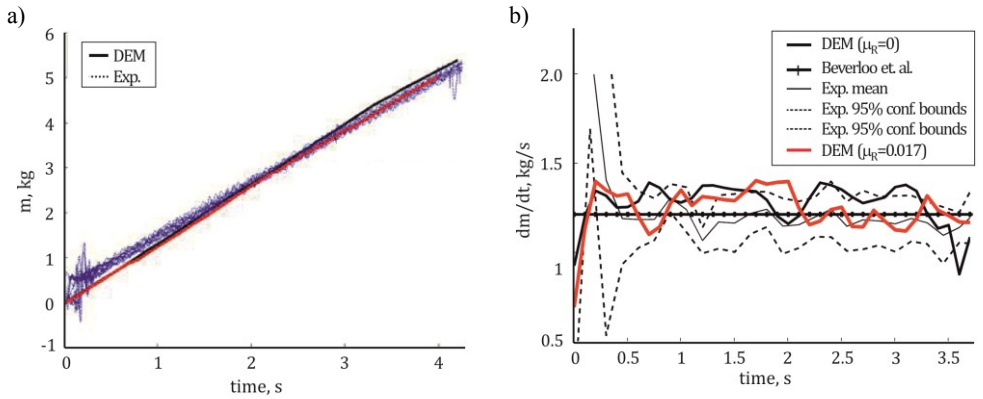

Figure 2.51. The material outflow mass (a) and rate (b) vs. time.

As it can see in Figure 2.51a, a DEM-based analysis reliably fits the experimental values of the material outflow mass. A slight deviation observed at the initial stage is mainly attributed to the dynamic effect of measuring the particles mass dropping on the scales as explained above. The effect of rolling friction is discerned at the last stages of discharge. As pointed above, this effect is related with the reduced horizontal velocity of the material and the great conical depression formed during the last stages of discharge. Also Figure 2.51a shows that the computational model with the rolling friction included, a more reliably fits the experimental values of the measured outflow mass at the last stages of discharge.

As we can further observe in Figure 2.51b, the predicted values of the outflow rate mainly lie within the 95% confidence interval. The fluctuations in the computational values, are caused by the numerical derivation with respect to time, where small inadequacies in a function increment cause significant changes in its derivative. The

predicted values by Beverloo's equation additionally confirm the measurements and data derivation. A period of discharge through approximately 1 s to 3 s may assume to be the steady flow stage.

2.3.3.7. Concluding remarks

The stress and the outflow analyses for the flat-bottomed bin model during the filling and discharge processes of the pea grains were presented. Effect of the particle rolling torque was also analysed. The computational results have been obtained with the newly elaborated elastic-frictional rolling model, where a rolling friction effect was preliminary considered by selecting two rolling friction coefficients: $\mu_R = 0$ and $\mu_R = 0.017$ (measured). The conclusions can summarise as follows:

- The validation of the stress analysis results was presented throughout a comparison of the wall pressures, measured experimentally in the bin model, with those computed. Sufficiently good agreement between the wall pressures measured and those computed by the mathematical model was found. In particular, the model values mainly do not exceed 95% confidence bounds, implying that the mathematical model rather accurately predicts the values of the wall stresses. The main peaks of the discharge overpressures, recorded soon after the commencement of the discharge process, were also captured by the mathematical model. The pea grain rolling friction coefficient ($\mu_R = 0.017$) had a minimal effect on the wall pressures, especially for the filling stage.
- Presenting the computationally determined distribution of the internal friction angle within the granular material shows that the stresses developed at the end of filling are very close to the Mohr-Coulomb plastic state of stresses within particular material portions, but an elastic stress state also takes place. Close fit of Janssen's solution to the experimental observation was found, when Eurocode 1, [166] relation for constant K_{pl} was adopted.
- A validation of the material outflow analysis was presented by comparing the computational, theoretical and experimental values for the outflow mass and its rate. The DEM model and Beverloo's approach show a good agreement with experimental data. In particular, all predicted values lie mainly within the 95% confidence interval, in which the experimental mean actually lies. It was also found that encountering the rolling friction contributes the outflow mass values at the last stages of discharge. The above statement is based on a better agreement of mathematical DEM model with the experimental data.

- The obtained velocity profiles were adequate to those determined by using the Nedderman and Tüzün kinematic model, [87]. The diffusion length values of their theoretical model were in good agreement with those reported in the literature.
  It was shown that presence of rolling leads to changes of velocity profile. The obtained material velocity profiles developed within the bin during discharge were shown that rolling friction can reduce the horizontal velocity. The material located at the centre of the bin can move vertically faster or slower (for the rolling-free case) depending on the quantity of material within the bin. The parameter b reduces due to the effect of rolling friction. This tendency may be attributed to explanation for the different values b found in literature.
- The final conclusion is that the DEM analysis provides an accurate prediction of flow parameters in the case of careful identification of the material parameters.

The investigation performed was based on the fixed mean values for the particles data. In spite of sufficiently adequate agreement between the mathematical model and the experimental values, it is clear that further research is still needed to evaluate the effects caused by the variation of the material parameters.

2.3.4. Discussion on the scale effects

It is important to recognise that DEM at its present stage of development still has its limitations. These are related to the calibration of the relevant particle parameters to correctly apply to the model and the manner in which the particle parameters may change throughout the bulk mass. Due to the presence of the diverse scale lengths combined with geometrical complexity of the hoppers, the typical minimum problem sizes for 3D applications generally range from 1,000 to 50,000 particles. Thus, there is also the limitation in the current levels of computing power to adequately deal with the extremely large numbers, usually billions, of particles of varying shape, size and composition presenting the real industrial flows in silos.

The present simulation operating with 20,400 pea grain is clearly far to applications to simulate the granular material bahavior on the real scale silos. It is well known the main DEM limitation extending the small models to real scale containers is related with an extensive usage of CPU time, when the number of grains increases (cf. [286]). For instance, in the current simulation, the 0.1 s of real discharge time (using $\Delta t = 10^{-6}$ s time step) at the commencement stage of the discharge process

requires approximately 20 hours of the computational time on a single Intel Pentium P4 3.4 GHz processor with 2.0 GB RAM memory. The simulation of this interval, carried out on the Intel Core 2 Duo Processor T7200, 2.0 GHz, 2.0 GB of RAM, uses by about 15 hours of CPU time. Finally, 0.1 s simulated on the Intel Core i5--2500 Processor, 3.3 GHz, 8.0 GB of RAM runs over 6.5 hours. The simple comparison between the CPU times illustrates the ongoing computational performance of PC desktops. Namely, speed-up between a single Pentium 4 and Core i5 processors (45 years between developments in these hard-wares) equals to factor 3. Another speedup case in computations can be achiewed by paralalising the programming code. This technique in application of the industrial silo flow problems containing up to 100,000 particles has been demonstrated in [242, 258]. Their parallel implementation has been shown that the time required to perform the necessary computational work decreases *linearly* with the number of processors employed leading to an approximately linear speedup. Our parallel investigations using MPI library and a novel algorithm of the simulation domain decomposition for each processor work via the moving particles data that can exchange processors has been reported by [257] conducting the triaxial compaction tests. The speed-up equal to 8.81 has been obtained on 10 processors of the distributed memory PC cluster. It has been demonstrated that a drastic increase of computational expenses of simulation for the poly-dispersed material in terms of CPU time is generally associated with the increase of its heterogeneity. In a silo discharge processes modelling, the gain in the computational speed-up is strongly related with the domain decomposition which is dependent on the silo geometry and the number of particles.

Thus, these results allow us to schedule that with a passage of time and ongoing research developments within the computer performance the transition from small models to large scale equivalent will be progressively solved to acceptable levels of satisfaction.

Presently, it is hardly expected that the DEM may be completely substituted for the continuum methods in the real hopper, silo design. The authors think that the advantages of both techniques should be employed for the proper solution of a particular problem. In spite the fact that the continuum modelling cannot represent the filling process at all (taking as an a priori assumptions for the filling height, initial density and angle of repose of material surface) when a properly applied, allow the highly complex cohesive bulk materials, handled by industry over widely varying environmental conditions, to be appropriately analysed. The experimental

validation of the DEM models, relying on the material data established on the micro and bulk levels, is strongly required for the ongoing DEM developments. Thus, there is a merit in recognising the important interactive role that continuum modelling can play with the ongoing research in DEM, particularly with respect to particle characterisation. To this end, the experiments in silo models have been involved in Chapter I.

Lucking from a distance on the possibilities to adequately simulate the extremely large numbers of particles dealing with the parallised computations, the use of upscale techniques can be mentioned. Indeed, the available upscaling approches adopted to simulate the granular material bahavior via DEM are very scant (cf. [319]). The coarse grained spherical and non-spherical powder models have been developed by [320]. Basically, a coarse grained powder is constituted as an effective medium that should exhibit the same dynamic and static properties as the experimental granular material. The feasibility and the limitations of the coarse graining were elucidated by them and the fundamental scaling rules for the intergranular forces were also derived. However, the upscale approach for the modelling of granular material bahavior in hoppers or silos has not been found in literature.

Consider the case, when the manipulation of particles size and their total number could provide the speedup in simulation. It is well known, that the simulation time rapidly decreases by limiting number of particles, however; the insufficient amount of particles used in the model can cause the strained physical effects.

Let us study the effect of particle size and its amount contribution to the particular bulk material parameters, such as outflow characteristics and wall pressures. To this end, the limitation in the particles amount is accounted for increasing/decreasing the particle radii to hold constant the total mass of granular material. Accordingly, three samples of granular material having approximately equal mass, but composed by the particles of different size, were considered. Thus, the samples are characterized by the amount of 20,400, 10,000 and 1,980 particles. Assume that the material is a poly-dispersed defined by the spherical particles which radii are distributed uniformly; thus, $R \in [k_1\langle R\rangle, k_2\langle R\rangle]$ (where $\langle R\rangle$ is the mean radius of the sample). The ratios of the maximal $R_{\max}$ and minimal $R_{\min}$ radii of particles to their mean radius are held the constant for all three models. Thus:

$$k_1 = \frac{R_{max}}{\langle R\rangle};\ k_2 = \frac{R_{min}}{\langle R\rangle}. \tag{2.51}$$

It was assumed that the total mass of particles is $m_{tot} = 143.57$ kg, while the corresponding total volume of the particles is $V_{tot} = 0.287$ m^3, for the given particle density, friction coefficient μ=0.3 and other parameters listed in Table 2.2.

The mean radius of particles is found in terms of the initially assumed total volume of particles by the following relationship

$$\langle R \rangle = \sqrt[3]{\frac{3V_{tot}}{4\pi N}}. \tag{2.52}$$

Finally, the minimal and maximal radii of particles, needed for generation of the particles using the uniform distribution, are found by multiplying the average radius of particle by k_1 and k_2. The following values of these ratios were assumed a priori: $k_1 = 1.134$, $k_2 = 0.851$. Thereby, the mean radii of particles $\langle R \rangle$, different for all models and equal to 0.0324 m, 0.0189 m and 0.0149 m, for N=20,400, N=10,000 and N=1,980 were found, respectively.

Now, let us discuss the results obtained for three models. A model containing 20,400 particles was assumed to be a main indicator in terms of its representation of continuum-based flow parameters due to relatively large number of the particles used. Other models were selected to investigate influence of the particle size and its amount on the material flow parameters.

The configuration of granules and contact forces after filling obtained for three aforementioned models are depicted in Figure 2.52.

As it can see in Figure 2.52, the material height after the filling process is almost the same for the all models, showing the correctness of the above relations in generation of the poly-dispersed material by the uniform distribution keeping the mass and volume constant. It should be noted that the generated total mass of particles had a difference from the expected value by about 0.5%.

A variation of particle contact forces indicates that the force transmission within the granular material varies for the models considered; in particular, at the lower part of the hopper. It can also be observed, that the amount of particle induces an increase of the local heterogeneity of particle contact force transmission. It can be clearly observed that, in the model with low amount of spheres (N=1,980), the particles are subjected to higher forces than those in the model with N=10,000 particles and much higher contact forces than in the model having N=20,400 spheres. This observation

indicates that the scaling rules for the contact forces could be implemented for the coarse grain model to exhibit the same static response. The rescaled contact forces for coarse models have been recently proposed in [320].

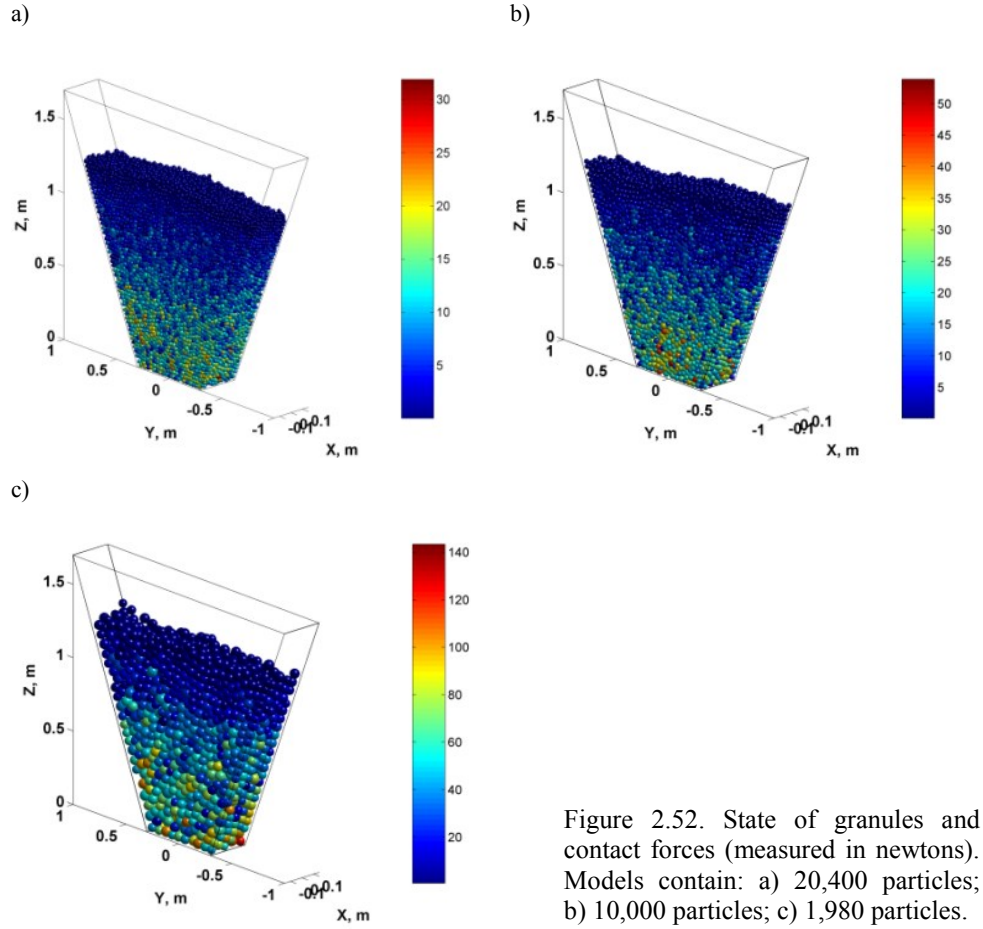

Figure 2.52. State of granules and contact forces (measured in newtons). Models contain: a) 20,400 particles; b) 10,000 particles; c) 1,980 particles.

The mean coordination number obtained after the end of filling increases, when the amaunt of particles increases (cf. Figure 2.51). This plot suggests to detect a similarity with *the effect of friction*: increase of friction coefficient results in the decreasing the mean coordination number, (cf. Figure 2.7).

Analyse the mass fraction discharged for the considered material models (cf. Figure 2.53a). The mass fraction discharged is computed numerically as the ratio of

granular material mass discharged to the total mass. In particular, the model containing 1,980 particles requires the longest time for the material discharge from the hopper, while the models with 10,000 and 20,400 particles show the shorter discharge times, respectively. The same tendency may be easily proven considering discharge fraction rates. The empirical and simulation (cf. Figure 2.16, Figure 2.30a--c) show that increasing in the particle friction coefficient reduces the fraction and its rate of discharge as the model with small number of particles. Thus, it can be treated that the decrease in the mass fraction discharged may be related by additional friction induced by the material heterogeneity. This effect relieves with the increasing of the amount of particles in the model.

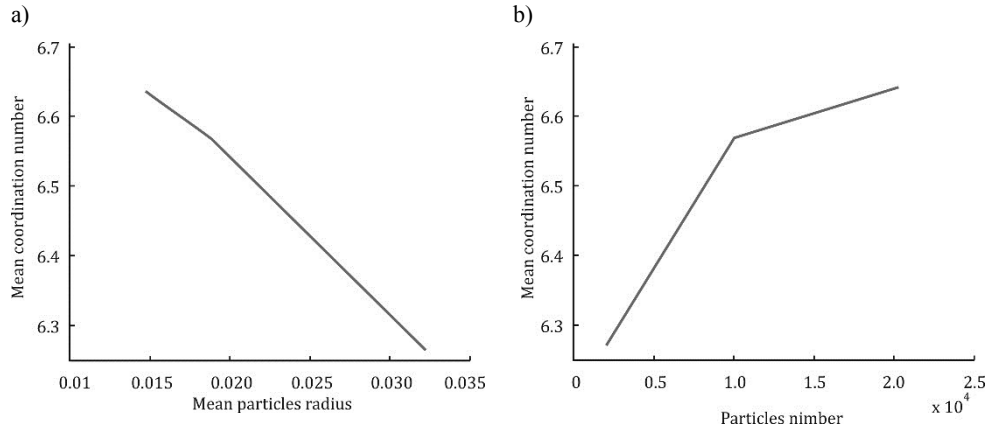

Figure 2.53. Mean coordination number after end of filling vs. the mean particle radius (a) and vs. particles number (b).

The effect of the particles amount on wall pressures is also depicted in Figure 2.54b. Theoretically, granular material possessing the friction is able to transmit friction forces, originated from the particle contacts, to the hopper walls. As a result, wall shear pressures grow with the material depth resulting in the non-linear increase in wall normal pressure instead of its linear dependency. In other words, the friction forces developed within the material relieve the normal component of wall pressure, but increase in its shear component. This tendency can be observed in the graphs plotted in Figure 2.54b, where the model with 1,980 particles produces lowest normal and highest shear pressure values in comparison with other models. Values of these components for models containing 10,000 and 20,400 particles are quite close with each other, particularly for shear pressures.

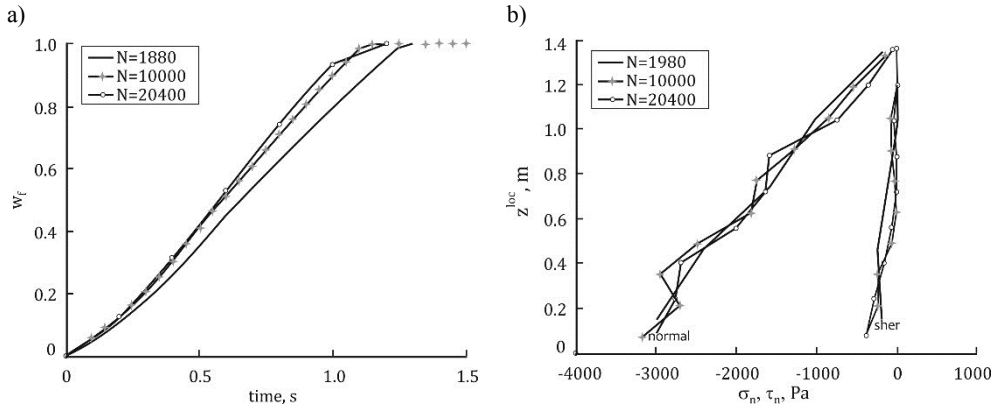

Figure 2.54. Mass fraction discharged vs. time (a); normal and shear pressures of the left wall vs. material depth (b).

Thus, the obtained decrease of wall normal pressures and increase in its shear component is attributed to the above observed additional friction effect due to material heterogeneity occurred in model with minimal number of the particles. It should be noted that this decrease is quite mild for the current hopper model, but it may be sufficiently larger in a tall hopper.

Finally, the decrease in particles number with increasing the particle radii can be treated as production of an *artificial* friction due to material. Due to this, the model with minimal number of particles produces (in comparison with the large models): a) the decreased mass fraction and its rate during discharge; b) the longest time for the full material discharge; c) the decreased normal and increased shear pressures of walls. To support this interpretation, it is also noticeable, that the non-zero shear stresses for frictionless material was obtained, [314] for a relatively small number of the particles causing certain heterogeneity of material.

These results should be treated as the preliminary investigation indicating that the modification of particle friction coefficient in terms of particle minimal and maximal radii could be developed to obtain the similarity of the models with different amount of particles (probably without rescaling in the contact forces). The decrease in amount of particles (with increase in their size to hold the given material mass) and exhibiting the same values for the continuum-based indicators such as, the outflow mass, coordination number and wall pressures can be used in analysis of large silo systems saving the CPU time. For instance, the speedup of model with N=1,980 in comparison to that operating with 20,400 particles was equal to 40 times.

Bibliography

1. A. W. Jenike. *Gravity Flow of Bulk Solids*. University of Utah Engineering Experiment Station, Bulletin 108, USA, 1961.
2. A. Drescher. *Analytical Methods in Bin-load Analysis.* Elsevier, Amsterdam, 1991.
3. A. W. Jenike, J. R. Johanson. Bin Loads. *Journal of the Structural Division*, ASCE, 94(4), 1968.
4. A. W. Jenike, J. R. Johanson. On the theory of bin loads, *Transactions ASME*. 91, Ser. B, 2, 339-344, 1969.
5. J. W. Carson, *Silo failures: Case histories and lessons learned.* Third Israeli Conference for Conveying and Handling of Particulate Solids, Dead Sea Israel, May, 2000.
6. J. F. Chen, J. M. Rotter, J. Y. Ooi, Z. Zhong. Flow patterns measurement in a full scale silo containing iron ore*, Chemical Engineering Science*, 60, 3029-3041, 2005.
7. J. Nielsen, V. Askegaard. Scale errors in model tests in granular media with special reference to silo models. *Powder Technology,* 16, 1, 123-130, 1977.
8. H. E. Wright, G. F. Cudahy , J. T. Van Kuren. Degradation of laser beam by a two-dimensional turbulent jet. *AIAA Journal*, 17, 10, 1091-1097, 1979.
9. J. Nielsen, N. O. Kristiansen. *Related measurements of pressure condition in full scale barley silo and in silo model.* Proc. of the International Conference on Design of Silos for Strength and Flow, University of Lancaster, Powder Advisory Centre, September, 1980.
10. J. Munch-Andersen, J. Nielsen. Size effects in large grain silos. *Bulk Solids Handling*, 6, 885-889, 1986.
11. J. Nielsen. *Pressures from flowing granular solids in silos*. Philosophical Transactions of the Royal Society of London. Series A, Mathematical Physical, and Engineering Sciences 356 (1747), 2667-2684, 1998.
12. A. Borcz, M. Maj. *Experimental Research on Loose Material Pressure and Temperature Distribution in Full Scale Silos*. Proceedings of International Symposium – Reliable Flow of Particulate Solids II, Oslo, Norway, 23-25 August, 763-768, 1993 .
13. A. Łapko. Efekty oddziaływania materiału sypkiego na żelbetowe ściany komór w eksploatowanych silosach na zboże. *Nauki Techniczne,* 71, Białystok Technical University, 224, 1989.

14. J. Tejchman. *Silo Quake-Measurement, A Numerical Polar Approach and a Way for its Suppression*. Proc. International Conference on Advances in Steel Structures, Hong Kong, 11-14 December, 795-800, 1996.
15. M. Kamiński. Untersuchungen des Zuckerdrucks in Silos: Tl 1. Symmetrische Entleerung und Einfluss der Fullart. *Zuckerindustrie*, Jg. 111, 7, 649-655, 1986.
16. M. Kamiński. Badania naporu bezkohezyjnych materiałów sypkich w silosach. *Prace Naukowe Instytutu Budownictwa Politechniki Wrocławskiej*. Wrocław, 253, 1986.
17. M. Kamiński. Determining the pressure of sugar stored in silos, *Bulk Solids Handling,* 9, 1, 33-41, 1989.
18. M. Kamiński, H. Hamadeh. Experimental investigation on funnel flow and wall pressure variation in silos. *Powder Handling and Processing*, 6, 4, 1-5, 1994.
19. M. Kamiński, H. Hamadeh. Measurement of pressure distribution inside the Silo Model. *Powder Handling & Processing*, 8, 2, 153-154, 1996.
20. M. Kamiński, R. Antonowicz. Pressure of bulk solids and reducing increase in pressure during silo discharge**.** *Powder Handling and Processing*, 12, 3, 271-276, 2000.
21. K. Diamountene, M. Kamiński. Studies of pressures in full-scale silos. *Bulk Solids Handling*, 23, 6, 1-5, 2003.
22. M. Kamiński, M. Maj. *A method of measure bulk solids pressure against silo wall in models and full scale silos.* The 4th International Conference for Conveying and Handling of Particulate Solids. Proceedings. ORTRA, Budapest, May 27-30, Vol. 1, Eds. H. Kalman, J. Gyenis. p 6-107 – 6-112, 2003.
23. J. F. Chen, J. M. Rotter, J. Y. Ooi. A Review of Numerical Prediction Methods for Silo Wall Pressures. *Advances in Structural Engineering*, 2, 2, 119-135, 1999.
24. J. M. Rotter, J. Y. Ooi, C. Lauder, I. Coker, J. F. Chen, B. G. Dale. *A study on a flow patterns in an industrial silo.* Proc. of the International Symposium on Reliable Flow Particulate Solids, II EFChE Publ., S 96, Oslo, 517-524, 1993.
25. A. Medina, J. Andrade, J. A. Cordova, C. Treviño. Gravity induced in granular flow measurements in a 2D silo with a lateral bottom exit. *Physics Letters A,* 273, 109-116, 1998.
26. A. Medina, J. A. Córdova, e. Luna, c. Treviño. Velocity field measurements in granular gravity flow in a near 2D silo. *Physics Letters A*, 250, 111-116, 1998.
27. R. M. Lueptow, A. Akonur, T. Shinbrot. PIV for granular flow. *Experiments in Fluids*, 28, 2, 183-186, 2000.
28. A. J. Waters, A. Drescher. Modelling plug flow in bins/hoppers. *Powder Technology*, 113, 168-175, 2000.
29. M. Ostendorf, J. Schwedes. *Application of optical measurement techniques on the investigation of bulk solids flow behaviour in silos*. International Congress for Particle Technology, Partec 2004, Nüremberg, Germany, 16-18 March, 2004.

30. M. Ostendorf, J. Schwedes. Application of Particle Image Velocimetry for velocity measurements during silo discharge, *Powder Technology*, 158, 69-75, 2005.
31. I. Sielamowicz, T. A. Kowalewski. *DPIV technique in modelling granular material flow in a model of silo made of Plexiglas*. International Congress for Particle Technology, PARTEC2004, Nüremberg, Germany, 16-18 March, 2004.
32. J. U. Böhrnsen, H. Antes, M. Ostendorf, J. Schwedes. Silo discharge: Measurement and Simulation of Dynamic Behaviour in Bulk Solids. *Chemical Engineering Technology*, 27, 71-76, 2004.
33. M. Niedostatkiewicz, J. Tejchman. Application of a particle image velocimetry technique for deformation measurements of bulk solids during silo flow. *Powder Handling and Processing*, 17, 4, 216-220, 2005.
34. I. Sielamowicz. Experimental analysis of granular material flows using the technique of digital particle image velocimetry. *Engineering Transactions*, 53, 2, 195-227, 2005.
35. I. Sielamowicz, S. Błoński, T. A. Kowalewski. Optical Technique DPIV in Measurements of Granular Material Flow, Part 1 of 3. *Chemical Engineering Science*, 60, 2, 589-598, 2005.
36. I. Sielamowicz, S. Błoński, T. A. Kowalewski. Optical Technique DPIV in Measurements of Granular Material Flow, Part 2 of 3 – Converging Hoppers. *Chemical Engineering Science*, 61, 5307-5317, 2006.
37. C. Słonimski, M. Niedostatkiewicz, J. Tejchman. Application of particle image velocimetry (PIV) for deformation measurement during granular silo flow. *Powder Technology*, 173, 1-18, 2007.
38. D. A. Steingart, J. W. Evans. Measurements of granular flow in two-dimensional hoppers by particle image velocimetry. Part I: experimental method and results. *Chemical Engineering Science*, 60, 1043-1051, 2005.
39. G. W. Baxter, R. P. Behringer, T. Faggert, G. A. Johnson. *Phys. Rev. Lett*. 62, 2825, 1989.
40. P. Evesque, J. Rajchenbach. *Statistics of glass sphere avalanches in a partly filled rotating cylinder. Powder and Grains*. ed. J. Biarez, R. Gourves, Balkema, Rotterdam, 214-224, 1989.
41. E. Clement, J. Duran, J. Rajchenbach. Experimental study of heaping in a two--dimensional ‘‘sand pile’’. *Phys. Rev. Lett*. 69, 1189–1192, 1992.
42. J. Duran, T. Mazozi, E. Clément, J. Rajchenbach. Size segregation in a two--dimensional sandpile: Convection and arching effects, *Phys. Rev*. E 50, 5138, 1994.
43. H. K. Pak, R. P. Behringer. „Bubbling in vertically vibrated granular materials”. *Nature 371*, 231-233, 1994.
44. R. J. Adrian. Particle imaging technique for experimental fluid mechanics. *Annual Review of Fluid Mechanics*, 23, 261-304, 1991.

45. R. Kvapil. *Theorie der Schuttgutbewegung*. VEB Verlag Technik, Berlin, 1959.
46. P. M. Blair-Fish, P. L. Bransby. Flow patterns and wall stresses in a mass-flow bunker. *Journal of Engineering for Industry*, 95, 17-26, 1973.
47. A. Drescher, T. W. Cousens, P. L. Bransby. Kinematics of the mass flow of granular material through a plane hopper. *Geotechnique*, 28, 1, 27-42, 1978.
48. J. Y. Ooi, J. F. Chen, J. M. Rotter. Measurement of solids flow patterns in a gypsum silo. *Powder Technology*, 99, 3, 272-284, 1998.
49. M. Nakagawa, S. A. Altobelli, A. Caprihan, E. Fukushima, E.-K. Jeong. Non--invasive measurements of granular flows by Magnetic Resonance Imaging. *Exp Fluids*, 16: 54-60, 1993.
50. E. E. Ehrichs, H. M. Jaeger, G. S. Karczmar, J. B. Knight, V. Yu. Kuperman, S. R. Nagel. *Science 267*, 1632, 1995.
51. C. F. Harwood. Powder segregation due to vibration. *Powder Technology*, 16, 51-57, 1997.
52. M. Chinaud, T. Delaunay, Ph. Tordjeman. An experimental study of particle sedimenta-tion using ultrasonic speckle velocimetry. *Measurement Science and Technology*, 21, 2010.
53. L. Hesselink. Digital image processing in flow visualization. *Annual Review of Fluids Mechanics*, 20, 421-485, 1988.
54. J. Westerweel. *Digital particle image velocimetry – theory and application*. Delft University Press, 1993.
55. C. E. Willert, M. Gharib. Digital particle image velocimetry. *Experiments in Fluids,* 10, 181-193, 1991.
56. L. Lourenco, A. Krothapalii. On the accuracy of velocity and vorticity measurements with PIV. *Experiments in Fluids*, 18, 421-428, 1995.
57. J. H. Sun, D. A. Yates, D. E. Winterbone. Measurements of the flow field in a diesel engine combusection chamber after combusection by cross-correlation of high-speed photographs. *Experiments in Fluids*, 20, 335-345, 1996.
58. H. T. Huang, H. E. Fiedler, J. J. Wang. Limitation and improvement of PIV. Part I: Limitation of conventional techniques due to deformation of particle image patterns. *Experiments in Fluids*, 15, 168-174, 1993.
59. P. T. Tokumaru, P. E. Dimotakis. Image correlation velocimetry. *Experiments in Fluids*, 19, 1-15, 1995.
60. L. G. Gui, W. Merzkirch. A method of tracking ensembles of particle images. *Experiments in Fluids*, 21, 465-468, 1996.
61. G. M. Quenot, J. Pakleza, T. A. Kowalewski. Particle image velocimetry with optical flow. *Experiments in Fluids*, 25, 177-189, 1998.

62. M. Raffel, Ch. E. Willert, J. T. Kompenhans. *Particle image velocimetry: a practical guide,* Berlin, 1998.

63. S. W. Smith. *The Scientist and Engineer's Guide to Digital Signal Processing*. California Technical Publishing, 1997.

64. M. A. Sutton, S. R. McNeill, J. D. Helm, J. Y. Chao. *Advances in Two-Dimensional and Three-Dimensional Computer Vision.* Topics in Applied Physics, Springer Berlin / Heidelberg, 77, 323, 2000.

65. K. Nübel. *Experimental and numerical investigation of shear localization in granular materials.* Publication Series of the Institute of Soil and Rock Mechanics, 62, University Karlsruhe, 2002.

66. D. J. White, W. A. Take,M. D. Bolton. Soil deformation measurements using particle image velocimetry (PIV) and photogrammetry. *Geotechnique,* 53, 7, 619-631. 2003.

67. K. Hutter, N. Kuerchner. *PIV for granular avalanches, Dynamical Response of Granular and Powder Materials in Large and Catastrophic Deformations*. Springer, 2003.

68. A. L. Rechenmacher. 2006 Grain-scale processes governing shear band initia-tion and evolution in sands. *Journal of the Mechanics and Physics of Solids*, 54, 1, 22-45, 2006.

69. W. C. Kohse. *Experimentell Untersuchung von Scherfugenmustern in Granulaten, Diplomarbeit*, Institute for Soil and Rock Mechanics, University of Karlsruhe, 1-42, 2002.

70. G. R. Watson, J. M. Rotter. A finite element kinematic analysis of planar granular solids flow. *Chemical Engineering Science*, 51, 3967-3978, 1996.

71. R. M. Nedderman. The use of the kinematic model to predict the development of the stagnant zone boundary in the batch discharge of a bunker. *Chemical Engineering Science*, 50, 6, 959-965, 1995.

72. J. A. S. Cleaver, R. M. Nedderman. The measurement of velocity profiles in conical hoppers. *Chemical Engineering Science,* 48, 21, 3703-3712, 1993.

73. J. S. Giunta. Flow patterns of granular materials in flat-bottom bins. *Journal of Engineering for Industry, Transactions of the ASME*, 91, 406-413, 1969.

74. H. Takahashi, H. Yanai. Flow profile and void fraction of granular solids in a moving bed. *Powder Technology,* 7, 205-214, 1973.

75. T. V. Nguyen, C. Brennen, R. H. Sabersky. Gravity flow of granular materials in conical hoppers. *Journal of Applied Mechanics, Transactions of the ASME,* 46, 529--535, 1979.

76. J. Tejchman. Behaviour of a Granular Medium in a Silo – Model Tests in a Plane Silo with Parallel Walls. Part I. *Archives of Civil Engineering*, XXXVII, 4, 1993.

77. U. Tüzün, R. M. Nedderman. Investigation of the flow boundary during steady-state discharge from a funnel-flow bunker. *Powder Technology,* 31, 1, 27-43, 1982.
78. D. P. Graham, A. R. Tait, R. S. Wadmore. Measurement and prediction of flow patterns of granular solids in cylindrical vessels, *Powder Technology,* 50, 1, 66--76, 1987.
79. K. F. Zhang, J. Y. Ooi. A kinematic model for solids flow in flat-bottomed silos. *Geotechnique*, 48, 4, 545-553, 1988.
80. R. Hill. *The Mathematical Theory of Plasticity*. Clarendon Press, Oxford, 1950.
81. W. Prager, P. G. Hodge. *Theory of Perfectly Plastic Solids*. Dover Publ., New York, 1968.
82. J. Salençon. *Applications of the theory of plasticity in soil mechanics*, Wiley New York, 1977.
83. J. Litwiniszyn J. Statistical methods in the mechanics of granular bodies. *Rheologica Acta*, 1, 2-3, 146-150, 1958.
84. J. Litwiniszyn. The model of a random walk of particles adopted to researches on problem of mechanics of loose media. *Bulletin l'Academie Polonaise Sciences,* 11, 61--70, 1963.
85. W. W. Mullins. *Stochastic theory of particle flow under gravity,* Journal of Applied Physics, 43, 665-677, 1972.
86. W. M. Mullins. Critique and comparison of two stochastic theories of gravity-induced particle flow. *Powder Technology*, 23, 115-119, 1979.
87. R. M. Nedderman, U. Tüzün. A kinematic model for the flow of granular materials. *Powder Technology*, 22, 243-253, 1979.
88. U. Tüzün, G. T. Houlsby, R. M. Nedderman, S. B. Savage. The flow of granular materials-II Velocity distribution in slow flow. *Chemical Engineering Science*, 37, 1691-1709, 1982.
89. A. Drescher, M. Ferjani. Revised model for plug/funnel flow in bins. *Powder Technology,* 141, 44-54, 2004.
90. W. Szczepiński. On the movement of granular materials in bins and hoppers, Part I – Two-dimensional problems. *Engineering Transactions*, 51, 4, 419-431, 2003.
91. W. Szczepiński W. On the movement of granular materials in bins, Part II – Three-dimensional problems. *Engineering Transactions*, 51, 4, 433-444, 2003.
92. Z. Kotulski, W. Szczepiński. *Rachunek błędów dla inżynierów*, PWN, (Error Analysis with Applications in Engineering), 2004.
93. G. J. Weir. A mathematical model for dilating, non-cohessive granular flow in steep--walled hoppers. *Chemical Engineering Science*, 59**,** 149-161, 2004.

94. J. Tejchman, M. Klisiński. 2001 FE-studies on rapid flow of bulk solids in silos. *Granular Matter*, 3, 4, 215-231, 2001.

95. A. W. Jenike. *Storage and Flow of Solids,*. University of Utah Engineering Experiment Station, Bulletin 123, USA, 1964 .

96. S. B. M. Moreea, R. M. Nedderman. Exact Stress and Velocity Distributions in a Cohesionless Material Discharging from a Conical Hopper. *Chemical Engineering Science*, 51, 16, 3931-3942, 1996.

97. J. Kozicki, J. Tejchman. Simulations of flow patterns in silos with a cellular automaton – part 1. *Task Quarterly*, 9, 1, 81-103, 2005.

98. G. R. Watson. *Flow patterns in flat bottomed silos*. PhD thesis, University of Edinburgh, 1993.

99. M. G. Perry, E. Rothwell, W. T. Woodfin. Model studies of mass flow bunkers: II velocity distributions in the discharge of solids from mass flow bunkers. *Powder Technology*, 14, 81-92, 1976.

100. C. Ruckenbrod, J. Eibl. *Numerical Results to Discharge Process in Silos*. Proceedings International Symposium – Reliable Flow of Particulate Solids II, Oslo, Norway, 23-25 August, 1993.

101. J. M. Rotter. *Critical Design Features of Steel Industrial Storage Structures*, in Development in Structural Engineering (ed. B.H.V. Topping), Spon, London, 909-928, 1990.

102. J. M. Rotter. *Guide for the Economic Design of Circular Metal Silos*. Spon, London, 2000.

103. H. A. Janssen. Versuche über Getreidedruck in Silozellen. *Zeitschrift des Vereines Deutscher Ingenieure*, 39 (35), 1045-1049, 1895.

104. M. Könen. *Berechnung des Seiten und Bodendrucks in Silos*, Zentralblatt, Bauverwaltung, 16, 446-449, 1985.

105. K. Pieper, F. Wenzel. Comments on DIN1055: Design Loads for Buildings Loads in Silos Bins. *Beton und Stahlbetonbau*, 6-11, 1963.

106. D. M. Walker. An Approximate Theory for Pressure and Arching in Hoppers. *Chemical Engineering Science*, 21, 975-997, 1966.

107. A. G. Homes. Lateral Pressures in Granular Material in Silos. *ASME Paper*, 72-MH--30 for Meeting, Sept, 17-20, 1972.

108. J. K. Walters. A Theoretical Analysis of Stresses in Silos with Vertical Walls. *Chemical Engineering Science*, 28, 13-21, 1973.

109. A. W. Jenike, J. R. Johnson, J. W. Carson. Bin Loads – Part 3. Mass Flow Bins. *Transaction ASME,* 95 (Ser. B, No 1), 6-12, 1973.

110. M. Reimbert, A. Reimbert. *Silos: Theory and Practice*, Trans. Technical Publications, 1976.

111. M. Reimbert, A. Reimbert. Discussion of Design Friction Loads for Concrete Silos. *ACI Structural Journal*, 84 (2), 178-179, 1987.

112. G. Abdel-Sayed, F. Monasa, W. Siddall. Cold-Formed Steel Farm Structures, Part 1: Grain Bins. *Journal of Structural Engineering, ASCE*, 111(ST10), Oct., 2065-2089, 1985.

113. P. C. Arnold, A. G. McLean, A. W. Roberts. *Bulk Solids: Storage, Flow and Handling*, Tunra Ltd. Bulk Solids Handling Research Associates, University of Newcastle, Australia, 1980.

114. E. H. Gaylord, C. N. Gaylord. *Design of Steel Bins for Storage of Bulk Solids*. Prentice Hall, 1984.

115. A. G. Bishara. *Interaction of Bin and Stored Bulk Solids, Design of Steel Bins for the Storage of Bulk Solids*, (ed. J. M. Rotter), The University of Sydney, 27-33, 1985.

116. A. G. Bishara, S. S. El-Azazy, T. D. Huang. Practical Analysis of Cylindrical Farm Silos Based on Finite Element Analysis. *ACI Journal*, November – December, 456--462, 1981.

117. J. Y. Ooi, J. M. Rotter. Wall Pressures in Squat Steel Silos from Finite Element Analysis. *Computers and Structures*, 37(4), 361-374, 1990.

118. R. A. Lohnes, J. M. Rotter, J. Y. Ooi. *Application of the Finite Element Method for Calculating Stresses in Silos*. NATO Scientific Collaboration Project, Final Report, 1994.

119. N. Nanninga. Does the usual method of calculation for establishing pressures on walls sand bottom of silos give safe results. *De Ingenieur*, 44, 190-194, 1956.

120. D. M. Walker. *A Theory of Gravity Flow of Cohesive Powders*, Central Electricity Generating Board, UK SW Region, R&D Dept Report, no. 22, 1964.

121. J. Y. Ooi, J. M. Rotter, L. Pham. Systematic and Random Features of Measured Pressures on Full-Scale Silo Walls. *Engineering Structures*, 12(2), 74-87, 1990.

122. P. C. Arnold, A. G. McLean. 1976 An analytical solution for the stress function at the wall of a converging channel. *Powder Technology*, 13, 255-260, 1976.

123. A. G. McLean, P. C. Arnold. Improved analytical flow factors for mass-flow hoppers. *Powder Technology*, 15, 279-281, 1976.

124. A. Khelil, J. C. Roth. Gravitational flow behaviour of granular materials. *European Journal of Mechanics B/Fluids*, 13, 1, 57-72, 1994.

125. H. Sakaguchi, E. Ozaki. Analysis of the formation of arches pluging the flow of granular materials. *In Powders and Grains,* 93, Balkema, Rotterdam, 1993.

126. H. Sakaguchi, E. Ozaki, T. Igarashi. Plugging of the Flow of Granular Materials during the Discharge from a Silo. *International Journal of Modern Physics B (IJMPB)*, 7, 9/10, 1949-1963, 1993.

127. R. C. Brown, J. C. Richards. *Principles of Powder Mechanics*. New York: Pergamon, 1970.

128. R. M. Nedderman. *Statics and kinematics of granular materials*. Cambridge University Press, New York, 1992.

129. D. C. Hong, J. A. McLennan. Molecular dynamics simulations of hard sphere granular particles. *Physica A 187*, 1-2, 159-171, 1992.

130. D. Hirshfeld, Y. Radzyner, D. C. Rapaport. Molecular dynamics studies of granular flow through an aperture. *Physics Review E 56*, 4404-4415, Issue 4, 1997.

131. K. D. Kafui, C. Thornton. Some observations on granular flow in hoppers and silo. *Powders & Grains '97* (Behringer & Jenkins, eds.) Balkema, 511-514, 1997.

132. F. Wang, C. Gardner, D. G. Schaeffer. Steady-state computation of granular or in an axisymmetric hopper. *SIAM Journal of Applied Mathematics*, 52, 1076, 1992.

133. U. Haüssler, UJ. Eibl. Numerical investigations on discharging silos. *Journal of Engineering Mechanics Division*, ASCE 110 (EM6), 957-971, 1984.

134. M. L. Srinivasa,P. R. Nott, R. K. Kesava. Fully developed flow of coarse granular materials through a vertical channel. *Chemical Engineering Science*, 52, 6, 913-933, 1997.

135. W. Volk. *Applied Statistics for Engineers*, second edition, by Mc Graw-Hill, 1969.

136. L. Likiesh, J. Liaga. *Osnownyje tablicy matiematiczeskoj statistiki*, Moskwa, 1985.

137. H. Caram, D. C. Hong. Random-walk approach to granular flows. *Physical Review Letters*, 67, 7, 828-831, 1991.

138. U. Tüzün, R. M. Nedderman. Experimental evidence supporting kinematic modelling of the flow of granular media in the absence of air drug. *Powder Technology*, 24, 257--266, 1979b.

139. W. W. Mullins. Experimental Evidence for the Stochastic Theory of Particle Flow Under Gravity. *Powder Technology*, 9, 29-37, 1974.

140. J. Choi, A. Kudrolli, R.R. Rosales, M. Z. Bazant. Diffusion and Mixing in Gravity--Driven Dense Granular Flows. *Physical Review Letters*, 92, 17, 174-301, 2004.

141. J. Choi, A. Kudrolli, M. Z. Bazant. Velocity profile of granular flow inside silos and hoppers *Journal of Physics: Condensed Matter*, 17, S2533-S2548, 2005.

142. A. Samadani, A. Pradhan, A. Kudrolli. Size segregation of granular matter in silo discharge. *Phys. Rev.* E 60, 7203-7209, 1999.

143. I. Sielamowicz, M. Czech, T. A. Kowalewski. Empirical description of granular flow inside a model silo with vertical walls. *Biosystems Engineering*, 108, 334-344, 2011.

144. C. S. Chou, J. Y. Hsu, Y. D. Lau. Flow patterns and stresses on the wall in a two--dimensional flat-bottomed bin. *Journal of Chinese Institute of Engineers, Transactions of the Chinese Institute of Engineers*, Series A, 26, 4, 397-408, 2003.

145. W. G. Pariseau. Discontinuous velocity fields in gravity flows of granular materials through slots. *Powder Technology*, 3, 218-226, 1969.

146. J. Lee, S. C. Cowin, J. S. Templeton. An experimental study of the kinematics of flow through hoppers. *Trans. Society Rheology*, 18, 247-269, 1974.

147. P. A. Langston, U. Tüzün, D. M. Heyes. Distinct element simulation of interstitial air effects in axially symmetric granular flow in hoppers. *Chemical Engineering Science*, 51, 873-891, 1996.

148. P. A. Langston, M. S. Nikitidis, U. Tüzün, D. M. Heyes, N. M. Spyrou. Microstructural simulation and imaging of granular flow in two- and three dimensional hoppers. *Powder Technology,* 94, 59-72, 1997.

149. E. B. Pitman. Stress and Velocity Fields in Two- and Three Dimensional Hoppers. *Powder Technology*, 47, 219-231, 1986.

150. R. Dosekun. *The flow of granular materials*, Ph.D. thesis, University of Cambridge, 1980.

151. R. M. Nedderman. The measurement of the velocity profile in a granular material discharging from a conical hopper. *Chemical Engineering Science*, 43, 1507-1516, 1988.

152. J. R. Johanson, A. W. Jenike. Stress and velocity fields in gravity flow of bulk solids. *University of Utah Engineering Experiment Station, Bulletin 116*, USA, 1962.

153. R. M. Horne, R. M. Nedderman. Analysis of switch stresses in two-dimensional bunkers. *Powder Technology*, 19, 2, 235-241, 1978.

154. R. M. Horne, R. M. Nedderman. Stress distributions in hoppers. *Powder Technology*, 19, 243-254, 1978.

155. J. A. S. Cleaver, R. M. Nedderman. Theoretical predictions of stress and velocity profiles in conical hoppers. *Chemical Engineering Science,* 48, 21, 3696-3702, 1993.

156. H. G. Polderman, J. Boom, E. de Hilster, A. M. Scott. Solids flow velocity profiles in mass flow hoppers. *Chemical Engineering Science*, 42, 4, 737-744, 1987.

157. H. G. Polderman, A. M. Scott, J. Boom. Solids stresses in bunkers with inserts. *Int. Chem. Engng. Symp*. Ser., No. 91.227-240, 1985.

158. Z. Mróz, Cz. Szymański. Gravity flow of a granular material in a converging channel. *Arch. Mech.*, 23, 897-917, 1971.

159. J. Tejchman. Behaviour of granular medium in a silo – a numerical Cosserat approach. Part 3. *Archives of Civil Engineering,* 1, 7-28, 1993.

160. J. Tejchman. Behaviour of a Granular Medium in a Silo - Model Tests in a Plane Silo with Convergent Walls. Part II. *Archives of Civil Engineering*, XXXVII, 4, 1993.

161. J. Tejchman. Dynamical Phenomena in Silos During Discharge. *Archives of Civil Engineering*, XL 1, 1994.

162. R. L. Michałowski. Flow of granular material through a plane hopper. *Powder Technology*, 39, 29-40, 1984.

163. R. L. Michałowski. Flow of granular media through a plane parallel/converg-ing bunker, *Chemical Engineering Science*, 42, 11, 2587-2596, 1987.

164. P. L. Bransby, P. M. Blair-Fish. Initial deformations during mass flow from a bunker: observations and idealizations. *Powder Technology*, 11, 273-288, 1975.

165. I. Sielamowicz, M. Czech. Analysis of the radial flow assumption in a converging model silo. *Biosystems Engineering*, 106, 412-422, 2010.

166. EN 1991-4 Eurocode 1: Actions on structures: Part 4: Actions in silos and tanks. 2004.

167. PN-89/B-03262, Polish Standard: Silosy żelbetowe na materiały sypkie. Obliczenia statyczne, (in Polish), 1989.

168. ACI 313, *Alternate Design Procedure,* Discussion Document before ACI Committee 313 on Concrete Bins, Silos and Bunkers for Storing Granular Materials, ACI, Detroit, 1989.

169. AS 3774, *Loads on Bulk Solids Containers*, Australian Standards Association of Australia, Sydney, 1996.

170. J. M. Rotter. *Guide for the Economic Design of Metal Silos*, E&FN Spon, London, 1989.

171. A. W. Jenike. Denting of Circular Bins with Eccentric Draw Points, *Journal of the Structural Division ASCE 93* (ST1) 27-35, 1967.

172. J. G. M. Wood. *The Analysis of Silo Structures Subject to Eccentric Discharge*, Proc., 2nd Int. Conf. on Design of Silos for Strength and Flow, Stratford-upon-Avon, 132-144, 1983.

173. J. M. Rotter. *The analysis of steel bins subject to eccentric discharge. Proc*., 2nd Inter. Conference on Bulk Materials Storage Handling and Transportation, Ins. of Eng., Wollongong, Australia, July, 264-271, 1986.

174. ENV 1991 - Part 4. Eurocode 1, *Actions on silos and tanks*, Brussels, Belgium, 2003.

175. F. Ayuga, M. Guaita, P. J. Aguado, A. Couto. Discharge and the eccentricity of the hopper influence on the silo wall pressures. *Journal of Engineering Mechanics*, 127, 10, 1067-1074, 2001.

176. Anon. *Reliable Flow of Particulate Solids*, EFCE Publication Series (European Federation of Chemical Engineers), 49, 1985.

177. S. A. Thompson, J. L. Usry, J. A. Legg. Loads in a Model Grain Bin as Affected by Various Unloading Techniques. *Transactions of the ASAE,* 29, 2, 1986.

178. D. K. Pokrant, M. G. Britton. Investigation into the Effects of Eccentric Drawoff and Flowrate in Model Grain Bin Studies. *Paper-American Society of Agricultural Engineers*, 86-4076, 1986.

179. M. Kamiński. Der Betrieb von Silos mit exzentrischen Auslauf. *Bautechnik*. Jg. 56, H. 6, 203-204, 1979.

180. M. Kamiński. Untersuchung des Zuckerdruckes in Silos: Tl 2. *Exzentrische Entleerung. Zuckerindustrie*, Jg. 111, 10, 916-921, 1986.

181. E. Hampe, M. Kamiński. Der Einfluss exzentrischer Entleerung auf die Druck-verhealtnisse in Silos. *Bautechnik*, Jg. 61, 1 H, 73-82, 2 H, 136-142, 1984.

182. A. Łapko, W. Stachurski. Experimental investigations on interaction between the reinforced concrete silo walls and the granular medium, (in Polish: Eksperymentalne badania niektórych efektów współpracy żelbetowych po-włok silosów z ośrodkiem sypkim w komorach elewatorów zbożowych). *Archiwum Inżynierii Lądowej*, XXXII, 4, PWN, 427-443, 1987.

183. H. M. Haydl. Eccentric Discharge in Circular Silos. *Proceedings of the Insti-tution of Civil Engineers*, 83, 2, 1987.

184. S. S. Safarian, E. C. Harris. Post-tensioned Circular Silos for Modern Industry. *Bulk Solids Handling*, 7, 2, 1987.

185. J. M. Rotter, P. T. Jumikis, S. P. Fleming, S. J. Porter. *Experiments on the buckling of thin-walled model silo structures*, Research Report-University of Sydney, R570, 1988.

186. H. de Clercq. Investigation into Stability of a Silo with Concentric and Eccentric Discharge. *Civil Engineers in South Africa*, 32, 3, 103-7, 1990.

187. G. E. Blight. Eccentric Discharge of a Large Coal Bin with Six Outlets. *Bulk Solids Handling*, 11, 2, 451-457, 1991.

188. A. Borcz A., Abd el Rahim Hamdy. Wall Pressure Measurements in Eccentrically Discharged Cement Silos. *Bulk Solids Handling*, 11, 2, 469-476, 1991.

189. F. Shalouf, S. Kobielak. Reduction of the dynamic flow pressure in grain silo by using discharge tubes. *Powder Handling Processing*, 13, 1, 2001.

190. M. Molenda, J. Horabik, S. A. Thompson, I. J. Ross. Bin Loads Induced by Eccentric Filling and Discharge of Grain. *Transactions of the ASAE,* 45, 3, 781-785, 2002.

191. C. S. Chou, Y. C. Chuang, J. Smid, S. S. Hsiau, J. T. Kuo. Flow patterns and stresses on the wall in a moving granular bed with eccentric discharge. *Advanced Powder Technology*, 13, 1, 1-13, 2002.

192. C. S. Chou, J. Y. Hsu, Y. D. Lau. The granular flow in two-dimensional flat-bottomed hopper with eccentric discharge. *Physica A Statystical Mechanics and its Applications*, 308, 1-4, 46-58, 2002.

193. M. Wójcik, G. G. Enstad, M. Jecmenica. Numerical Calculations of Wall Pressures and Stresses in Steel Cylindrical Silos with Concentric and Eccentric Hoppers. *Journal of Particulate Science and Technology*, 21(3), 247-258, 2003.

194. C. S. Chou, J. Y. Hsu. Kinematic model for granular flow in a two-dimensional flat--bottomed hopper. *Advanced Powder Technology*, 14, 3, 313-331, 2003.

195. J. S. Guaita, A. Couto, F. Ayuga. Numerical Simulation of Wall Pressure during Discharge of Granular Material from Cylindrical Silos with Eccentric Hoppers. *Biosystem Engineering*, 85, 1, 101-109, 2003.

196. C. Y. Song, J. G. Teng. Buckling of Circular steel silos subject to code-specified eccentric discharge pressures. *Engineering Structures*, 25, 1397-1417, 2003.

197. K. Nübel, W. Huang. A study of localized deformation pattern in granular media. *Computer Methods in Applied Mechanics and Engineering*, 193, 2719-2743, 2004.

198. J. Tejchman. Modelling of shear localisation and autogenous dynamic effects in granular bodies. *Habilitation Monograph*, 140, 1-353, Veroffentlichungen des Institutes für Bodenmechanik und Felsmechanik der Universität Fridericiana in Karlsruhe, 1997.

199. J. Tejchman. Shear Zones and Dynamic Effects During Silo Emptying – Part 1. *Archives of Civil Engineering*, XLII, 4, 1997.

200. J. Tejchman. Shear Zones and Dynamic Effect During Silo Emptying – Part 2. *Archives of Civil Engineering*, XLII, 4, 1997.

201. I. Sielamowicz, M. Czech, T. A. Kowalewski. Empirical description of flow parameters in eccentric flow inside a model silo. *Powder Technology*, 198, 381-394, 2010.

202. I. Sielamowicz, M. Czech, T. A. Kowalewski. Empirical analysis of eccentric flow registered by the DPIV technique inside a silo model. *Powder Technology*, 212, 38-56, 2011.

203. J. Tejchman, G. Gudehus. *Verspannung, Scherfugenbildung und Selbster-regung bei der Siloentleerung*, in: J. Eibl, G. Gudehus (Eds.), Silobauwerke und ihre spezifischen Beanspruchungen, Deutsche Forschungsgemeinschaft, Wiley-VCH, 245-284, 2000.

204. J. Tejchman. *Scherzonenbildung und Verspannungseffekte in Granulaten unter Berücksichtigung von Korndrehungen*. Publication Series of the Institute of Soil and Rock Mechanics, University of Karlsruhe, 117, 1-236, 1989.

205. M. Niedostatkiewicz, J. Tejchman. Measurements of changes of the bulk solid density during granular flow in silos. *Powder Handling and Processing*, 17, 2, 76-83, 2005.

206. J. Tejchman, G. Gudehus. Shearing of a narrow granular layer with polar quantities. *International Journal for Numerical and Analytical Methods in Geomechanics*, 25, 1, 1–28, 2001.

207. I. Vardoulakis. *Scherfugenbildung in Sandkörpern als Verzweigungsproblem*, PhD thesis, Institute for Soil and Rock Mechanics, University of Karlsruhe, 70, 1997.

208. J. Desrues. *La localization de la deformation dans les materiaux granulaires*. PhD thesis, USMG and INPG, Grenoble, 1984.

209. F. Löffelmann. *Theoretische und experimentelle Untersuchungen zur Schütt-gut-Wand-Wechselwirkung und zum Mischen und Entmischen von Granulaten*, PhD thesis, University of Karlsruhe, 1989.

210. T. Yoshida, F. Tatsuoka, M. Siddique. *Shear banding in sands observed in plane strain compression,* [in:] R. Chambon, J. Desrues, I. Vardoulakis (Eds.), Localisation and Bifurcation Theory for Soils and Rocks, Balkema, Rotterdam, 165-181, 1994.

211. Z. Więckowski, M. Klisiński. Finite deformation analysis of motion of granular materials in a silo. *Archives of Mechanics*, 47, 617-633, 1995.

212. P. G. De Gennes. 1998 Reflections on the mechanics of granular matter. *Physic A 261*, 267-293, 1998.

213. P. G. De Gennes. Granular matter: a tentative view. *Rev. Mod. Phys.*, 71(2), S374-S382, 1999.

214. Z. Mróz, K. Kwaszczyńska. Certain boundary problems for granular materials with density hardening. *Engineering Transactions*, 19(1), 15-42, 1971.

215. J. Schwedes, H. Feise. Modelling of pressures and flow in silos. *Chemical Engineering Technology*, 18, 96-109, 1995.

216. A. Drescher. *Some aspects of flow of granular material in hoppers.* Phil. Trans. R. Soc. London A 356, 2649-2666, 1998.

217. Z. Mróz, I. Sielamowicz. Deformation zones in granular materials in converging hoppers during filling and discharge processes. *Engineering Transactions*, 51(4), 461-491, 2003.

218. R. M. Horne, R. M.Nedderman. Analysis of the Stress Distribution in Two--Dimensional Bins by the Method of Characteristics. *Powder Technology*, 14, 93-102, 1976.

219. Y.-H. Wu, R. Collinson. Determination of velocity and stress discontinuities in quasi-static granular flows. *Anziam Journal*, 42(E), C1558-C1579, 2000.

220. J. Tejchman, G. Gudehus. Silo-music and silo-quake experiments and a numerical Cosserat approach. *Powder Technology*, 76(2), 201-212, 1993.

221. J. Eibl, G. Rombach. *Numerical investigations on discharging silos*. Proc. 6th International Conference on Numerical Methods in Geomechanics, V1, Balkema, Rotterdam, 317–320, 1988.

222. S. A. Elaskar, L. A. Godoy, D. D. Gray, J. M. Stiles. A viscoplastic approach to model the flow of granular solids. *International Journal of Solids and Structures*, 37, 2185--2214, 2000.

223. J. Tejchman, T. Ummenhofer. Bedding effects in bulk solids in silos: experiments and a polar hypoplastic approach. *Thin-Walled Structures 37*, 333-361, 2000.

224. B. Sukumaran, A. K. Ashmaway. Influence of inherent particle characteristics on hopper flow rate. *Powder Technology*, 138, 46-50, 2003.

225. P. A. Cundall. A computer model for rock-mass behaviour using interactive graphics for the input and output of geometric data. Rep. AD/A-001 602, *U.S. National Technical Information Service*, 1974.

226. P. A. Cundall, O. D. L. Strack. A discrete numerical model for granular assemblies. *Geotechnique*, 29, 47-65, 1979.

227. C. S. Campbell, C. E. Brennen. *Computer simulation of shear flows of granular material. Mechanics of granular materials: New models and constitutive relations*. Elsevier, Amsterdam, 1983.

228. O. R. Walton. *Particle – dynamic calculations of shear flow. Mechanics of granular materials, New models and constitutive relations.* J. T. Jenkins and M. Satake, eds. Elsevier, Amsterdam, 327-338, 1983.

229. C. Thornton. *Application of DEM to process engineering problems in DEM*. In: 1st US Conference, Colorado School of Mines Press, 87-100, 1989.

230. P. A. Langston, U. Tüzün, D. M. Heyes. Continuous potential discrete particle simulations of stress and velocity fields in hoppers, Transition from fluid to granular flow. *Chemical Engineering Science*, 49(8), 1259-1275, 1994.

231. P. A. Langston, U. Tüzün, D. M. Heyes. Discrete element simulation of granular flow in 2D and 3D hoppers: dependence of discharge rate and wall stress on particle interactions. *Chemical Engineering Science*, 50(6), 967-987, 1995.

232. P. A. Langston, U. Tüzün, D. M. Heyes. Discrete element simulation of internal stress and flow fields in funnel flow hoppers. *Powder Technology*, 85, 153-169, 1995.

233. J. S. Leszczyński. *A discrete model of the dynamics of particle collisions in granular flows*. Monograph 106, Częstochowa University of Technolog, 2003.

234. J. S. Leszczyński. A discrete model of a two-particle contact applied to cohesive granular materials. *Granular Matter*, 5, 2, 91-98, 2005.

235. J. S. Leszczyński, T. Błaszczyk. Modeling the transition between stable and unstable operation while emptying a silo. *Granular Matter*, 13, 4, 429–438, 2011.

236. S. Masson, J. Martinez. Effect of particle mechanical properties on silo flow and stresses from distinct element simulations. *Powder Technology*, 109, 164-178, 2000.

237. J. Sykut, M. Molenda, J. Horabik. DEM simulation of the packing structure and wall load in a 2-dimensional silo. *Granular Matter*, 10, 273-278, 2008.

238. R. Balevičius, R. Kačianauskas, M. Mróz, I. Sielamowicz. Discrete particle investigation of friction effect in filling and unsteady/steady discharge in three dimensional wedge-shaped hopper. *Powder Technology*, 187, 159-174, 2008.

239. J. F. Ferellec, J. Martinez, S. Masson, K. Iwashita. *Influence of particle rolling resistance on silo flow in DEM simulations.* In: Kishino (ed), Powders and Grains, Swets & Zetlinger, Lisse, 409-412, 2001.

240. K. Iwashita, M. Oda. Micro-deformation mechanism of shear banding process based on modified distinct element. *Powder Technology*, 109, 192-205, 2000.

241. D. Hirshfeld, D. C. Rapaport. Granular flow from a silo: discrete-particle simulations in three dimensions. *Eur. Phys. J. E 4*, 193-199, 2001.

242. P. W. Clearly, M. L. Sawley. DEM modelling of industrial granular flows: 3D case studies and the effect of particle shape on hopper discharge. *Applied Mathematical Modelling*, 26, 89-111, 2002.

243. S. Takeuchi, X. Wang, M. J. Rhodes. Discrete element study of particle circulation in a 3-D spouted bed. *Chemical Engineering Science* 60, 1267-1276, 2005.

244. A. Džiugys, B. J. Peters. An Approach to Simulate the Motion of Spherical and Non-Spherical Fuel Particles in Combustion Chambers. *Granular Material*, 3(4), 231-266, 2001.

245. P. A. Langston, M. A. Al-Awamleh, F. Y. Fraige, B. N. Asmar. Distinct element modelling of non-spherical frictionless particle flow. *Chemical Engineering Science*, 59, 425-435, 2004.

246. J. Li, P. A. Langston, C. Webb, T. Dyakowski. Flow of sphero-disc particles in rectangular hoppers – a DEM and experimental comparison in 3D. *Chemical Engineering Science*, 59, 5917-5929, 2004.

247. A. A. Mirghasemi, L. Rothenburg, E. L. Matyas. Influence of particle shape on engineering properties of assemblies of two-dimensional polygon-shaped particles, *Geotechnique,* 52(3), 209-217, 2000.

248. C. Nouguier-Lehon, E. Vincens, B. Cambou. Structural changes in granular materials: The case of irregular polygonal particles. *International Journal of Solids and Structures*, 42(24-25), 63, 56-6375, 2005.

249. D. Markauskas, R. Kačianauskas. Investigation of the rolling resistance in DEM simulations of piling. *Journal of Vibroengineering*, 11, 3, 482-490, 2009.

250. D. Markauskas, R. Kačianauskas. Investigation of rice grain flow by multi-sphere particle model with rolling resistance. *Granular Matter*, 13, 143-148, 2011.

251. D. Markauskas, R. Kačianauskas, A. Džiugys, R. Navakas. Investigation of adequacy of multi-sphere approximation of elliptical particles for DEM simulations. *Granular Matter*, 12, 1, 107-123, 2010.

252. H. P. Zhu, A. B. Yu. Steady-state granular flow in a three-dimensional cylindrical hopper with flat bottom: microscopic analysis. *Journal of Physics D, Applied Physics*, 37, 1497-1508, 2004.

253. H. P. Zhu, A. B. Yu. Steady-state granular flow in 3D cylindrical hopper with flat bottom: macroscopic analysis. *Granular Matter*, 7, 97-107, 2005.

254. H. P. Zhu, A. B. Yu. Micromechanic modelling and analysis of unsteady-state granular flow in cylindrical hopper. *Journal of Eng. Math*., 52, 307-320, 2005.

255. R. Balevičius, R. Kačianauskas, A. Džiugys, A. Maknickas, K. Vislavičius. DEMMAT code for numerical simulation of multi-particle dynamics. *Information Technology and Control*, 34(1), 71-78, 2005.

256. A. Maknickas, A. Kačeniauskas, R. Kačenauskas, R. Balevičius, A. Džiugys. Parallel DEM software for simulation of granular material. *Informatica*, 17, 2, 207-224, 2006.

257. R. Kačianauskas, R. Maknickas, A. Kačeniauskas, D. Markauskas, R. Balevičius. Parallel discrete element simulation of poly-dispersed granular material. *Advances in engineering software*, 41, 1, 52-63, 2010.

258. P. W. Clearly. Industrial particle flow modelling using discrete element method. *Engineering Computations*, 26, 6, 698-743, 2009.

259. A. Datta, B. K. Mishra, S. P. Das, A. Sahu. A DEM analysis of flow characteristics of noncohesive particles in hopper. *Materials and Manufactu-ring Processes*, 23, 2, 195--202, 2008.

260. S. C. Negi, Z. Lu, J. C. Jofriet. A Numerical Model for flow o granular material in Silos. Part 2: Model Validation. *Journal of Agricultural Engineering Research*, 68, 231-236, 1997.

261. R. Balevičius, R. Kačianauskas, Z. Mróz, I. Sielamowicz. Investigation of wall stress and outflow rate in a flat-bottomed bin: A comparison of the DEM model results with the experimental measurements. *Powder Technology*, 214, 322-336, 2011.

262. C. González-Montellano, A. Ramírez, A. Gallego, F. Ayuga. Validation and experimen-tal calibration of 3D discrete element models for the simulation of the discharge flow in silos. *Chemical Engineering Science*, doi: 10.1016/j.ces.2011.07. 009, 2011.

263. R. Balevičius, A. Džiugys, R. Kačianauskas. Discrete element method and its application to the analysis of penetration into granular media. *Journal of Civil Engineering and Management*, 10(1): 3-14, 2004.

264. G. A. Kőhring. Computer simulations of granular materials: the effects of mesoscopic forces. *Journal de Physique I France,* 4, 12, 1779-1782, 1994.

265. G. A. Kőhring. *Dynamical simulations of granular flows on multi-processor computers*. Computational methods in applied sciences *'96*, John Wiley & Sons Ltd., 190-196, 1996.

266. R. D. Mindlin, H. Deresiewicz. Elastic spheres in contact under varying oblique forces. *Journal of Applied Mechanics Transactions of ASME*, 20, 327-344, 1953.

267. A. E. Skinner. A note on the influence of interparticle friction on the shearing strength of a random assembly of spherical particles. *Geotechnique*, 19, 150-157, 1969.

268. O. R. Walton. *Effects of interparticle friction and particle shape on dynamic angles of repose via particle-dynamics simulation*. In: Mechanics and Statistical Physics of Particulate Materials, June 8-10, La Jolla, California, 1994.

269. A. Mohamed, M. Gutierrez. Comprehensive study of the effects of rolling resistance on the stress–strain and strain localization behavior of granular materials. *Granular Matter*, 12, 527-541, 2010.

270. K. L. Johnson. *Contact mechanics*. New York: Cambridge University Press, 1985.

271. D. Tabor. The mechanism of rolling friction. I. The plastic range. *Proceedings of the Royal Society of London. Series A. Mathematical and Physical Sciences*, 229, 1177, 181-198, 1955.

272. D. Tabor. The mechanism of rolling friction. II. The elastic range. *Proceedings of the Royal Society of London. Series A. Mathematical and Physical Sciences*, 229,1177, 198-220, 1955.

273. J. P. Bardet, Q. Huang. *Rotational stiffness of cylindrical particle contacts.* In: Powders and Grains '93, Proc. 2nd International Conference on Micromechanics of Granular Media, Birmingham, 39-43, 1993.

274. J. Rojek, F. Zarate, C. Agelet de Saracibar, C. Gilbourne, P. Verdot. Discrete element modelling and simulation of sand mould manufacture for the lost foam process. *International Journal for Numerical Methods in Engineering*, 62, 1421-1441, 2005.

275. C. Zhou, J. Y. Ooi. Numerical investigation of progressive development of granular pile with spherical and non-spherical particles. *Journal of Mechanics of Materials*, 41, 6, 707-714, 2009.

276. J. Ai, J. F. Chen, J. M. Rotter, J. Y. Ooi. Assessment of Rolling Resistance Models in Discrete Element Simulations. *Powder Technology*, 206, 269-282, 2011.

277. A. P. Grima, P. W. Wypych. Investigation into calibration of discrete element model parameters for scale-up and validation of particle–structure interactions under impact conditions, Powder Technology, 212, 1, 198-209, 2011.

278. A. P. Grima, P. W. Wypych. Discrete element simulations of granular pile formation. Method for calibrating discrete element models. *Engineering Computations: International Journal for Computer-Aided Engineering and Software*, 28, 3, 314-339, 2011.

279. Y. C. Zhou, B. D. Wright, R. Y. Yang, B. H. Xu, A. B. Yu. Rolling friction in the dynamic simulation of sand pile formation. *Physica A,* 269, 536-553, 1999.

280. H. P. Zhu, A. B. Yu. A theoretical analysis of the force models in discrete element method. *Powder Technology*, 161, 122-129, 2006.

281. C. M. Wensrich, A. Katterfeld. Rolling friction as a technique for modelling particle shape in DEM. *Powder Technology*, 217, 409-417, 2012.

282. M. P. Allen, D. J. Tildesley. *Computer simulation of liquids*. Clarendon Press, Oxford, 1991.

283. R. Balevičius, R. Kačianauskas. *DEM analysis of granular flow in pyramidal hoppers. In: II European conference on computational mechanics*. Solids, structures and coupled problems in engineering. Lisbon, Portugal 5-8 June: proceedings, 2006.

284. P. A. Thompson, G. S. Grest. Granular flow: friction and the dilatancy transition. *Physical Review Letters*, 67, 1751-1754, 1991.

285. B. N. Asmar, P. A. Langston, A. J. Matchett, J. K. Walters. Validation tests on a distinct element model of vibrating cohesive particle systems. *Computers and Chemical Engineering*, (26), 785-802, 2002.

286. R. Balevičius, R. Kačianauskas, A. Džiugys, A. Maknickas, K. Vislavičius. Investigation of performance of programming approaches and languages used for numerical simulation of granular material by the discrete element method. *Computer Physics Communications*, 175(6), 404-415, 2006.

287. R. Balevičius, R. Kačianauskas, Z. Mróz, I. Sielamowicz. Discrete Element Method applied to multiobjective optimization of discharge flow parameters in hoppers. *Structural and Multidisciplinary Optimization*, 31(3):163-175, 2006b.

288. R. Balevičius, R. Kačianauskas, Z. Mróz, I. Sielamowicz. Microscopic and macroscopic analysis of granular material behaviour in 3D flat-bottomed hopper by the discrete element method. *Archives of Mechanics*, 59, 3, 231-257, 2007.

289. R. Balevičius, R. Kačianauskas, Z. Mróz, I. Sielamowicz. Analysis and DEM simulation of granular material flow patterns in hopper models of different shapes. *Advanced Powder Technology*, 22, 226-235, 2011.

290. P. Meakin, R. Jullien. Periodic disc packings generated by random deposition in narrow channels. *Europhys. Letters*, 15, 851, 1991.

291. A. T. Procopio, A. Zavaliangos. Simulation of multi-axial compaction of granular media from loose to high relative densities. *Journal of the Mechanics and Physics of Solids*, 53, 1523-1551, 2005.

292. J. Christoffersen, M. Mehrabadi, S. Nemat-Nasser. A micro-mechanical description of granular material behavior. *Journal of Applied Mechanics*, 48, 2, 339-344, 1981.

293. R. M. German. *Particle Packing Characteristics*. Pinceton, N.J.: Metal Powder Industrial Federation, 1989.

294. O. Pouliquen, R. Gutfraind. Stress Fluctuations and Shear Zones in Quasi--Static Granular Chute Flows. *Phys. Review*, E 53, 557-561, 1996.

295. W. R. Ketterhagen, R. Bharadwaj, B. C. Hancock. The coefficient of rolling resistance (CoRR) of some pharmaceutical tablets. *International Journal of Pharma-ceutics*, 392, 107-110, 2010.

296. A. Ramirez, J. Nielsen, F. Ayuga. On the use of plate-type normal pressure cells in silos Part 1: Calibration and evaluation. *Computers and Electronics in Acriculture*, 71, 71-76, 2010.

297. A. Savitzky, M. J. E. Golay. Smoothing and Differentiation of Data by Simplified Least Squares Procedures. *Analytical Chemistry*, 36(8), 1627-1639, 1964.

298. I. Yalçin, C. Özarslan, T. Akbaş. Physical properties of pea (Pisum sativum) seed. *Journal of Food Engineering*, 79, 731-735, 2007.

299. M. Molenda, J. Horabik. *Własności fizyczne sypkich surowców spożywczych. Zarys katalogu.* Lublin, 2002.

300. N. N. Mohsenin. *Physical Properties of Plant and Animal Materials*. Gordon and Breach Publ. Inc., New York, 1978.

301. J. Łukaszuk, M. Molenda, J. Horabik, J. Wiącek. Method of measurement of coefficient of friction between pairs of metallic and organic objects. *Acta Agrophysica*, 13(2), 407-418 (in Polish), 2009.

302. A. Sawicki, w. Świdziński. Cyclic compaction of soils, grains and powders. *Powder Technology*, 85, 97-104, 1995.

303. J. Horabik, M. Molenda. Physical properties of granular food materials. *Acta Agrophysica*, 74, 1-89, 2002.

304. GOST 12248-96 (1996) Soils. Laboratory methods for determining the strength and strain characteristics (in Russian).

305. BS 1377 (1990) Part 7: Shear strength tests (total stress).

306. R. W. Day. *Foundation engineering handbook: design and construction with the 2006 international building code*. The McGraw-Hill Companies, Inc., New York, 2006.

307. J. Amšiejus, N. Dirgėlienė, A. Norkus, D. Žilionienė. Evaluation of soil shear strength parameters via triaxial testing by height versus diameter ratio of sample. *The Baltic Journal of Road and Bridge Engineering*, 4(2), 54-60, 2009.

308 G. H. Ristow. Simulating granular flow with molecular dynamics. *Journal de Physique I France*, 2(5), 649-662, 1992.

309. G. H. Ristow, H. J. Herrmann. Forces on the walls and stagnant zones in a hopper filled with granular material. *Physica A*, 213, 474-481, 1994.

310. H. Kruggel-Emden, E. Simsek, S. Rickelt, S. Wirtz, V. Scherer. Review and extension of normal force models for the Discrete Element Method. *Powder Technology*, 171, 157-173, 2007.

311. W. R. Ketterhagen, J. S. Curtis, C. R. Wassgren, B. C. Hancock. Predicting the flow mode from hoppers using the discrete element method. *Powder Technology*, 195(1), 1-10, 2009.

312. F. Vittorio De Blasio, M.-B. Saeter. Rolling friction on a granular medium. *Physical Review E 79*, 022301-1-4, 2009.

313. H. P. Zhu, A. B. Yu. Averaging method of granular material. *Physical Review*, E, 66, 021302-1-10, 2002.

314. R. Balevičius, D. Markauskas. Numerical stress analysis of granular material. *Mechanika*, 66(4) 12-17, 2007.

315. J. Y. Ooi, J. M. Rotter. Elastic predictions of pressures in conical silo hoppers. *Engineering Structures*, 13(1), 2-12, 1991.

316. S. K. Shukla, J. G. Loughran, N. Sivakugan. Stress within a cohesionless granular fill in a storage vessel with sloping walls during initial static loading. *Powder Technology*, 192(3), 389-393, 2009.

317. A. Kwade, D. Schulze, J. Schwedes. *Determination of the Stress Ratio in Uniaxial Compression Tests Part 1 and 2*. Powder Handling & Processing 6(2) and 6(2) 61-65, 199-203, 1994.

318. W. A. Beverloo, H. A. Leniger, J. Van de Welde. The flow of granular solids through orifices. *Chemical Engineering Science*, 15, 260-268, 1961.

319. Ch. Zhao, B. E. Hobbs, A. Ord, P. Hornby, Sh. Peng, L. Liu. Particle simulation of spontaneous crack generation problems in large-scale quasi-static systems. *International Journal for Numerical Methods in Engineering*, 69(11), 397-421, 2007.

320. C. Bierwisch, T. Kraft, H. Riedel, M. Moseler. Three-dimensional discrete element models for the granular statics and dynamics of powders in cavity filling. *Journal of the Mechanics and Physics of Solids*, 57, 10–31, 2009.

Cited web pages in the text:

http://www.bulk-solidshandling.com/webcasts

http://www.inzynierbudownictwa.pl/biznes,bhp,artykul,przyczyny_techniczne_wystepowania_zagrozen _awarii_i_katastrof_budowlanych

Appendix 1

Section 1.6.1. Analysis of the experimental results

Table 1. Readings at level H=5 cm

Readings taken from the left and the right part of the velocity profile at level H=5 cm (red profile), V_y [mm/s]. Number of readings 30					
Time [s]	Distance from the symmetry axis x [cm]				
	0	1	2	3	4
3.75	36.5	30.0 32.0	20.0 25.0 [1)]	5.0 7.0	0 0.5
15	37.0	22.0 23.0	16.0 17.0	7.0 7.0	1.0 2.0
30	40.0	31.0 32.0	17.0 15.0	7.0 3.0	1.0 1.0
40	34.0	23.0 30.0	17.0 15.0	7.0 5.0	1.0 0
52.5	37.0	28.0 27.0	15.0 13.0	8.0 4.0	1.0 0
60	37.0	32.0 28.0	18.0 15.0	6.0 4.0	1.0 0

Table 2. Readings at level H=10 cm

Readings taken from the left and the right part of the velocity profile at level H=10 cm (black profile), V_y [mm/s]. Number of readings 36						
Time [s]	Distance from the symmetry axis x [cm]					
	0	1	2	3	4	5
3.75	28.0	27.0 30.0	26.0 25.0	17.0 18.0	1.0 [1)] 5.0	0 0
15	26.0	23.0 24.0	20.0 20.0	17.0 17.0	10.0 10.0	3.0 2.0
30	24.0	23.0 24.0	20.0 20.0	16.0 15.0	10.0 8.0	3.0 2.0
40	24.0	24.0 23.0	20.0 20.0	17.0 15.0	9.0 8.0	3.0 2.0
52.5	25.0	24.0 24.0	22.0 22.0	15.0 15.0	7.0 7.0	2.0 2.0
60	27.5	27.0 27.0	22.0 23.0	14.0 13.0	7.0 7.0	2.0 2.0

Table 3. Readings at level H=20 cm

Readings taken from the left and the right part of the velocity profile at level H=20 cm (green profile), V_y [mm/s]. Number of readings 40								
Time [s]	Distance from the symmetry axis x [cm]							
	0	1	2	3	4	5	6	7
3.75	23.0	22.0 23.0	21.0 22.0	19.0 20.0	10.0 12.0	0 1.0	0 0	0 0
15	17.0	18.0 18.0	18.0 18.0	17.0 17.0	15.0 16.0	10.0 10.0	2.0 3.0	0 0
30	17.0	17.0 17.0	17.0 17.0	17.0 17.0	15.0 15.0	13.0 10.0	5.0 5.0	1.0 1.0
40	17.0	17.0 17.0	17.0 17.0	17.0 17.0	13.0 13.0	10.0 9.0	6.0 5.0	2.0 1.0
52.5	20.0	19.0 20.0	17.0 17.0	15.0 15.0	12.0 12.0	10.0 10.0	6.0 7.0	3.0 3.0

Table 4. Readings at level H=30 cm

Readings taken from the left and the right part of the velocity profile at level H=30 cm (dark blue profile), V_y [mm/s]. Number of readings 32								
Time [s]	Distance from the symmetry axis x [cm]							
	0	1	2	3	4	5	6	7
3.75	20.0	19.0 20.0	19.0 19.0	19.0 18.0	13.0 15.0	3.0 7.0	1.0 1.0	0 0
15	17.5	17.0 17.0	17.0 17.0	17.0 17.0	15.0 15.0	9.0 10.0	2.0 4.0	0 0
30	17.0	17.0 17.0	17.0 17.0	17.0 16.0	15.0 13.0	12.0 12.0	7.0 7.0	2.0 2.0
40	18.0	17.0 17.0	16.0 15.0	15.0 13.0	14.0 12.0	12.0 9.0	9.0 8.0	5.0 3.0

Table 5. Readings at level H=40 cm

Readings taken from the left and the right part of the profile at level H=40 cm (blue profile), V_y [mm/s]. Number of readings 24								
Time [s]	Distance from the symmetry axis x [cm]							
	0	1	2	3	4	5	6	7
3.75	19.0	18.0 18.0	18.0 18.0	17.0 18.0	12.0 16.0	3.0 8.0	0 0.5	0 0
15	17.0	17.0 17.0	17.0 16.0	16.0 16.0	13.0 15.0	8.0 10.0	2.0 5.0	0 0
30	17.0	16.0 16.0	15.5 15.0	14.0 13.0	13.0 12.0	11.0 11.0	9.0 10.0	3.0 5.0

Table 6. Readings at level H=50 cm

Readings taken from the left and the right part of the profile at level H=50 cm (purple profile), V_y [mm/s]. Number of readings 16								
Time [s]	Distance from the symmetry axis x [cm]							
	0	1	2	3	4	5	6	7
3.75	18.0	18.0 17.0	17.5 18.0	15.0 17.5	10.0 17.0	5.0 12.0	1.0 2.0	0
15	16.5	16.5 17.0	16.0 16.0	14.0 15.0	13.0 13.0	8.0 10.0	5.0 8.0	1.0 3.0

Statistical analysis of experimental results

Table 7. Statistical values for calculation of the confidence interval for level *H*=5 cm

Distance from the symmetry axis [cm] / Statistical values	*x*=0	*x*=1	*x*=2		*x*=3	*x*=4
			before rejecting	after rejecting		
$\bar{V}_y$	36.92	28.17	16.92	16.27	5.83	0.71
S	1.742	3.555	2.985	1.763	1.518	0.59
α	0.05	0.05	0.05	0.05	0.05	0.05
n	6	12	12	11	12	12
$t_{n-1,1-\frac{\alpha}{2}}$	2.571	2.201	2.201	2.228	2.201	2.201
$t_{n-1,1-\frac{\alpha}{2}}\frac{S}{\sqrt{n-1}}$	2.00	2.36	1.98	1.24	1.01	0.39
$\bar{V}_y - t_{n-1,1-\frac{\alpha}{2}}\frac{S}{\sqrt{n-1}}$	34.92	25.81	14.94	15.03	4.82	0.32
$\bar{V}_y + t_{n-1,1-\frac{\alpha}{2}}\frac{S}{\sqrt{n-1}}$	38.92	30.53	18.90	17.51	6.84	1.10

Table 8. Statistical values for calculation of the confidence interval for level H=10 cm

Distance from the symmetry axis [cm] / Statistical values	x=0	x=1	x=2	x=3	x=4		x=5
					before rejecting	after rejecting	
$\overline{V_y}$	25.75	25.00	21.66	15.75	7.42	8.0	1.92
S	1.574	2.121	2.014	1.422	2.431	1.537	0.954
α	0.05	0.05	0.05	0.05	0.05	0.05	0.05
n	6	12	12	12	12	11	12
$t_{n-1,1-\frac{\alpha}{2}}$	2.571	2.201	2.201	2.201	2.201	2.228	2.201
$t_{n-1,1-\frac{\alpha}{2}}\frac{S}{\sqrt{n-1}}$	1.81	1.41	1.34	0.94	1.61	1.08	0.63
$\bar{V}_y - t_{n-1,1-\frac{\alpha}{2}}\frac{S}{\sqrt{n-1}}$	23.94	23.59	20.32	14.81	5.81	6.92	1.29
$\bar{V}_y + t_{n-1,1-\frac{\alpha}{2}}\frac{S}{\sqrt{n-1}}$	27.56	26.41	23.00	16.69	9.03	9.08	2.55

Table 9. Statistical values for calculation of the confidence interval for the level H=20 cm

Distance from the symmetry axis x [cm] / Statistical values	0		1		2		3	4	5	6	7
	before rejecting	after rejecting	before rejecting	after rejecting	before rejecting	after rejecting					
$\overline{V_y}$	18.14	17.77	17.84	17.65	17.32	17.15	16.38	13.54	8.68	4.27	1.30
S	1.736	1.137	1.631	1.318	1.531	1.261	1.704	1.721	3.306	3.066	1.559
α	0.05	0.05	0.05	0.05	0.05	0.05	0.05	0.05	0.05	0.05	0.05
n	14	13	28	27	28	27	28	28	28	28	28
$t_{n-1,1-\frac{\alpha}{2}}$	2.448	2.178	2.051	2.055	2.051	2.055	2.0518	2.0518	2.0518	2.0518	2.0555
$t_{n-1,1-\frac{\alpha}{2}}\frac{S}{\sqrt{n-1}}$	1.03	0.72	0.64	0.53	0.60	0.51	0.67	0.68	1.31	1.21	0.63
$\overline{V_y}-t_{n-1,1-\frac{\alpha}{2}}\frac{S}{\sqrt{n-1}}$	17.11	17.05	17.20	17.12	16.72	16.64	15.71	12.86	7.37	3.06	0.67
$\overline{V_y}+t_{n-1,1-\frac{\alpha}{2}}\frac{S}{\sqrt{n-1}}$	19.17	18.49	18.48	18.18	17.92	17.66	17.05	14.22	9.99	5.48	1.93

Appendix 2

Section 25.1. Experimental readings taken from velocity profiles

Table 1. Readings at level H=9.5 cm

Time [s]	Readings taken from the left and the right part of the velocity profile. Distance from the symmetry axis x [cm]			
	0	5	10	15
7	3.8	3.3 3.0	1.8 1.6	0.6 0.3
23	4.5	4.0 3.5	2.5 1.4	1.0 0.1
53	4.2	3.5 3.0	1.8 1.2	0.4 0.1

Table 2. Readings at level H=19 cm

Time [s]	Readings taken from the left and the right part of the velocity profile. Distance from the symmetry axis x [cm]			
	0	5	10	15
7	3.7	3.3 3.1	1.9 2.2	0.9 1.0
23	4.2	3.4 3.8	2.2 2.5	0.8 0.8
53	3.8	3.4 3.3	2.1 2.0	1.0 0.8

Table 3. Readings at level *H*=28.5 cm

Time [s]	Readings taken from the left and the right part of the velocity profile. Distance from the symmetry axis *x* [cm]				
	0	5	10	15	20
7	3.8	3.6 3.15	2.5 2.0	1.5[1)] 0.5	0.8[1)] 0.3
23	3.8	3.5 3.2	2.3 2.0	0.8 0.6	0.2 0.1
53	3.5	3.3 2.9	2.3 1.7	0.85 0.5	0.1 0

The values marked with [1)] will be removed from data set in the further analysis.

Table 4. Readings at level *H*=38 cm

Time [s]	Readings taken from the left and the right part of the velocity profile. Distance from the symmetry axis *x* [cm]					
	0	5	10	15	20	25
7	3.8	3.7 3.5	2.7 2.7	1.5 1.7	0.8 0.9	0.7 0.6
23	3.8	3.5 3.5	2.2 2.3	0.8 0.8	0.2 0.1	0 0
53	3.5	3.3 3.1	2.4 2.3	1.3 1.2	0.3 0.4	0.05 0.15

Statistical analysis of the experimental results

Table 5. Statistical values for calculation of the confidence interval for level *H*=9.5 cm

Distance from the symmetry axis *x* [cm] / Statistical values	0	5	10	15
r [cm]	22.5	23.05	24.62	27.04
$\bar{V}_y$	4.17	3.38	1.72	0.42
S	0.2867	0.3436	0.4099	0.3131
α	0.05	0.05	0.05	0.05
n	3	6	6	6
$t_{n-1,1-\frac{\alpha}{2}}$	4.303	2.571	2.571	2.571
$t_{n-1,1-\frac{\alpha}{2}}\frac{S}{\sqrt{n-1}}$	0.87	0.40	0.47	0.36
$\bar{V}_y - t_{n-1,1-\frac{\alpha}{2}}\frac{S}{\sqrt{n-1}}$	3.30	2.98	1.25	0.06
$\bar{V}_y + t_{n-1,1-\frac{\alpha}{2}}\frac{S}{\sqrt{n-1}}$	5.04	3.78	2.19	0.78

Table 6. Statistical values for calculation of the confidence interval for level *H*=19 cm

Distance from the symmetry axis *x* [cm] / Statistical values	0	5	10	15
r [cm]	32.0	32.39	33.53	35.34
$\bar{V}_y$	3.9	3.38	2.15	0.88
S	0.216	0.245	0.1893	0.0898
α	0.05	0.05	0.05	0.05
n	3	6	6	6
$t_{n-1,1-\frac{\alpha}{2}}$	4.303	2.571	2.571	2.571
$t_{n-1,1-\frac{\alpha}{2}}\frac{S}{\sqrt{n-1}}$	0.66	0.24	0.22	0.10
$\bar{V}_y - t_{n-1,1-\frac{\alpha}{2}}\frac{S}{\sqrt{n-1}}$	3.24	3.14	1.99	0.78
$\bar{V}_y + t_{n-1,1-\frac{\alpha}{2}}\frac{S}{\sqrt{n-1}}$	4.56	3.62	2.37	0.98

Table 7. Statistical values for calculation of the confidence interval for level *H*=28.5 cm

Distance from the symmetry axis [cm] / Statistical values	*x*=0 [*r*=41.50]	*x*=5 [*r*= 41.80]	*x*=10 [*r*= 42.69]	*x*=15 [*r* =44.13]		*x*=20 [*r* =46.07]	
	no rejecting	no rejecting	no rejecting	before rejecting	after rejecting	before rejecting	after rejecting
r [cm]	32.0	32.39	33.53	35.34	35.34		
$\bar{V}_y$	3.7	3.28	2.13	0.79	0.65	0.25	0.14
S	0.1414	0.2305	0.2625	0.3445	0.1483	0.2630	0.1020
α	0.05	0.05	0.05	0.05	0.05	0.05	0.05
n	3	6	6	6	5	6	5
$t_{n-1,1-\frac{\alpha}{2}}$	4.303	2.571	2.571	2.571	2.776	2.571	2.776
$t_{n-1,1-\frac{\alpha}{2}}\frac{S}{\sqrt{n-1}}$	0.43	0.27	0.30	0.40	0.21	0.30	0.14
$\bar{V}_y - t_{n-1,1-\frac{\alpha}{2}}\frac{S}{\sqrt{n-1}}$	3.27	3.01	1.83	0.33	0.44	- 0.16	0.0
$\bar{V}_y + t_{n-1,1-\frac{\alpha}{2}}\frac{S}{\sqrt{n-1}}$	4.13	3.55	2.43	1.15	0.109	0.55	0.28

Table 8. Statistical values for calculation of the confidence interval for level *H*=38 cm

Distance from the symmetry axis *x* [cm] / Statistical values	0	5	10	15	20	25
r [cm]	51.0	51.24	51.97	53.16	54.78	56.80
$\bar{V}_y$	3.7	3.4	2.43	1.22	0.45	0.25
S	0.1414	0.1528	0.1972	0.3337	0.2986	0.2887
α	0.05	0.05	0.05	0.05	0.05	0.05
n	3	6	6	6	6	6
$t_{n-1,1-\frac{\alpha}{2}}$	4.303	2.571	2.571	2.571	2.571	2.571
$t_{n-1,1-\frac{\alpha}{2}}\frac{S}{\sqrt{n-1}}$	0.43	0.18	0.23	0.38	0.34	0.33
$\bar{V}_y - t_{n-1,1-\frac{\alpha}{2}}\frac{S}{\sqrt{n-1}}$	3.27	3.22	2.20	0.84	0.11	- 0.08
$\bar{V}_y + t_{n-1,1-\frac{\alpha}{2}}\frac{S}{\sqrt{n-1}}$	4.13	3.58	2.66	1.60	0.79	0.58

In Tables 5–8, *r* [cm] is the radius measured from the measurement point to the outlet.

The results with were were rejected using statistics *K* criteria, [136]:

$$K = \frac{\left|V_{y_i} - \bar{V}_y \max\right|}{S}, \tag{1}$$

where V_{y_i}– is the *i-th* reading taken from the experiments for all time instants, $\bar{V}_y$– the average value of experimental readings.

If the value of statistics *K* exceeds the critical value then V_{y_i} should be rejected. The values of statistics *K* calculated from formula (1) and Tables 1–4 are listed in Table 9 where the critical values are also given according to [136].

Table 9. Values of statistics *K* and critical values

Level *H*=28.5 cm	Distance from the symmetry axix *x* [cm]			
	15		20	
	K	critical value	*K*	critical value
	2.061	1.996	2.091	1.996

The hypothesis H_o was stated:

$$H_o : \mu_1=\mu_2=\cdots\mu_j\cdots\mu_k \tag{2}$$

where: H_o is the zero hypothesis equal to average velocities for *j-th* object (*j-th* height), in our case $j=1\ldots k$ and $k=4$, (four various heights analyzed in the model). The sums of squares S_i and S_{ij} for the inter- and intra-objective variations, respectively were calculated to confirm this hypothesis, according to the formulae:

$$S_i = \sum_{i=1}^{k} n_i(\bar{x}_i - \bar{x})^2, \tag{3}$$

$$S_{ij} = \sum_{i=1}^{k}\sum_{j=1}^{k} n_i(\bar{x}_i - \bar{x})^2, \tag{4}$$

where: x_{ij} is the value of velocity V_y for *i-th* object and *j-th* repetition, $\bar{x}_i$ is the average value for *i-th* object, $\bar{x}$ – is the average value of velocity for all readings, in our case $i=1, 2, 3, 4$ and $k=4$, $j=1, 2, 3$ and $n_i=n=3$.

Applying formulae (3) and (4), statistics *F* was calculated:

$$F = \frac{S_i}{k-1} \Big/ \frac{S_{ij}}{k(n-1)}, \tag{5}$$

and we compare it to the quantile of *F Snedocor* distribution $\boldsymbol{F_{k-1,\,k(n-1),\alpha}}$.

The results calculated from formulae (3)–(5) and Tables 1–4 are listed in Table 10.

Table 10. Statistical values for the analysis of variance

	Statistical values							
Distance from the symmetry axis x [cm]	Sums of squares for inter-objective variation S_i	Sums of squares for intra-objective variation S_{ij}	Degrees of freedom for S_i, $k-1$	Degrees of freedom for S_i, $k(n-1)$	Average squares for S_i	Average squares for S_{ij}	Statistics F	$F_{k-1,k(n-1),\alpha}$
0	0.4367	0.5100	3	8	0.1456	0.0638	2.282	4.07
5	0.02759	0.3600	3	8	0.009197	0.045	0.2044	4.07
10	0.6625	0.4367	3	8	0.2208	0.05459	4.0447	4.07
15	0.9756	0.4900	3	8	0.3265	0.06125	5.3306	4.07

Analyzing the values listed in the last two columns in Table 10 (Appendix) it is seen that for the significance level α=0.05 the velocity does not depend on the height for measurement points located at x=0, 5, 10 cm. But at the points located at x=15 cm the velocity depends on the height. The values depicted in Figure 1.45 confirm this conclusion. Another analysis was performed to confirm the above. Using the values presented in Figure 1.45 the velocity for the points located at x=0, 5, 10, 15 cm was described in the following form:

$$\hat{y} - a + bx, \tag{6}$$

where x is the height of the analyzed level, y – velocity V_y . On the basis of the readings listed in Tables 1–4, coefficients a and b were determinated by the least squares method and listed in Table 11 given in Appendix

Table 11. Statistical values for the confirmation of significance of the coefficients *a* and *b*

Distance from the symmetry axis *x* [cm]	Statistical values							
	Coefficient *a*	Coefficient *b*	S_e	S_a	S_b	t_a	t_b	$t_{n-2,1-\alpha/2}$ $t_{n-1,1-\alpha/2}$
0	4.27	- 0.01695	0.0977	0.1197	0.0046	35.67	3.68	4.303
5	3.37	$-4.21\ 10^{-4}$	0.0686	0.0840	0.00323	40.11	0.1303	4.303
10	1.58	0.0222	0.1302	0.1595	0.00613	9.91	0.3623	4.303
15	0.25	0.0228	0.2398	0.2937	0.0113	0.951	2.021 3.71	3.182

The variance of standard deviation S_e was calculated according to the formula:

$$S_e = \sqrt{\frac{\sum_{i=1}^{n}(y_i - \hat{y}_i)^2}{n-2}} \quad (7)$$

The standard errors S_a and S_b were determinated from formulae:

$$S_a = S_e \sqrt{\frac{\sum_{i=1}^{n} x_i^2}{n\sum_{i=1}^{n}(x_i - x)^2}} \quad (8)$$

$$S_b = \frac{S_e}{\sqrt{\sum_{i=1}^{n}(x_i - \bar{x})^2}} \quad (9)$$

The hypothesis of the significance of coefficients *a* and *b* was verified by calculating the statistics:

$$t_a = \frac{|a|}{S_a}, t_b = \frac{|b|}{S_b}. \quad (10)$$

We state two hypothesis H_0: $\begin{matrix} a = 0 \\ b = 0 \end{matrix}$

and the opposite hypothesis: H: $\begin{matrix} a \neq 0 \\ b \neq 0 \end{matrix}$.

The values of statistics calculated from formula (10) were compared to the quantile of *tStudent* distribution: $t_{n-2,1-\alpha/2}$ or $t_{n-1,1-\alpha/2}$.

Appendix 3

Section 3.4.5. Empirical analysis of the flow of the flax seeds in the model with smooth walls. Discharge from the right

Table 1. Readings at level H=5 cm

Time [s]	Velocities V_y [mm/s] at the distance from the symmetry axis x [cm]						
	1	2	3	4	5	6	1
1	36.0	37.0	30.0	15.0	5.0	1.0	0
25	23.0	25.0	22.0	20.0	16.0	5.0	0
50	34.0	35.0	33.0	17.0	8.0	6.0	2.0
75	38.0	39.0	32.0	17.0	5.0	3.0	1.0
100	27.0	28.0	25.0	15.0	9.0	2.0	0

Table 2. Readings at level H=10 cm

Time [s]	Velocities V_y [mm/s] at the distance from the symmetry axis x [cm]								
	0	1	2	3	4	5	6	7	8
1	24.0	25.0	22.0	17.0	11.5	4.0	3.0	1.0	0
25	21.0	20.0	19.0	20.0	20.0	17.0	6.0	0	0
50	20.0	21.0	23.0	19.0	17.0	15.0	8.0	6.0	0
75	28.0	29.0	29.0	25.0	13.0	6.0	4.0	4.0	2.0
100	9.0	11.0	17.0	17.0	16.0	13.0	10.0	7.0	3.0

Table 3. Readings at level H=20 cm

Time [s]	Velocities V_y [mm/s] at the distance from the symmetry axis x [cm]										
	0	1	2	3	4	5	6	7	8	9	10
1	17.0	18.0	17.0	15.0	13.0	11.0	9.0	6.0	4.0	2.0	1.0
25	17.0	18.0	18.0	18.0	18.0	17.0	13.0	8.0	1.0	0	0
50	16.0	17.0	17.0	17.5	17.0	18.0	16.5	15.0	8.0	0	0
75	16.0	17.0	19.0	18.0	17.0	15.0	14.0	11.0	7.0	2.5	0

Table 4. Readings at level H=30 cm

Time [s]	Velocities V_y [mm/s] at the distance form the symmetry axis x [cm]															
	0	1	2	3	4	5	6	7	8	9	10	11	12	13	14	15
1	15.0	16.0	15.0	14.0	14.0	11.0	9.0	7.0	6.0	5.0	4.0	3.0	2.0	1.0	1.0	0
25	14.0	15.0	15.0	15.0	15.0	15.0	14.0	13.0	10.0	2.0	0	0	0	0	0	0
50	16.0	17.0	17.0	17.0	17.0	16.0	15.0	14.0	11.0	5.0	0	3.0	0	0	0	0

Table 5. Readings at level H=40 cm

Time [s]	Velocities V_y [mm/s] at the distance form the symmetry axis x [cm]																
	0	1	2	3	4	5	6	7	8	9	10	11	12	13	14	15	16
1	14.0	15.0	15.0	15.0	15.0	14.0	12.5	11.0	9.0	7.0	6.0	5.0	4.0	3.0	2.0	1.0	1.0
25	13.0	14.0	15.0	14.0	14.0	13.5	12.0	11.0	10.0	9.0	2.0	0	0	0	0	0	0
50	7.0	8.0	10.0	14.5	14.0	16.0	14.0	13.0	12.5	12.5	11.0	7.0	2.0	0	0	0	0

Table 6. Readings at level H=50 cm

Time [s]	Velocities V_y [mm/s] at the distance form the symmetry axis x [cm]																					
	0	1	2	3	4	5	6	7	8	9	10	11	12	13	14	15	16	17	18	19	20	21
1	15.0	16.0	16.0	17.0	16.0	15.0	14.0	13.0	11.0	10.0	9.0	7.0	5.0	4.0	3.0	2.5	2.5	2.0	1.5	1.5	1.5	1
25	6.0	8.0	10.0	11.0	12.0	12.0	12.0	12.0	12.0	11.0	10.0	5.0	0	0	0	0	0	0	0	0	0	0

Table 7. Readings at level H=60 cm

Time [s]	Velocities V_y [mm/s] at the distance form the symmetry axis x [cm]																							
	0	1	2	3	4	5	6	7	8	9	10	11	12	13	14	15	16	17	18	19	20	21	22	23	24
1	15.0	15.5	16.0	16.0	15.5	16.0	14.0	14.0	12.0	11.0	10.0	8.0	8.5	7.0	5.0	4.5	4.5	3.5	3.0	2.5	2.0	2.0	1.5	1	1

STATISTICAL ANALYSIS OF THE EXPERIMENTAL RESULTS

Table 8. Statistical values for calculation of the confidence interval for level H=5 cm

Distance from the symmetry axis x [cm] / Statistical values	0	1	2	3	4	5	6
$\bar{V}_y$	31.6	32.8	28.4	16.8	8.6	3.4	1.5
S	5.678	5.381	4.224	1.833	4.030	1.855	0.5
n	5	5	5	5	5	5	2
$t_{n-1,1-\frac{\alpha}{2}}$	2.7764	2.7764	2.7764	2.7764	2.7764	2.7764	12.706
$t_{n-1,1-\frac{\alpha}{2}}\frac{S}{\sqrt{n-1}}$	7.88	7.47	5.86	2.54	5.59	2.58	6.35
$\bar{V}_y - t_{n-1,1-\frac{\alpha}{2}}\frac{S}{\sqrt{n-1}}$	23.72	25.33	22.54	14.26	3.01	0.82	0
$\bar{V}_y + t_{n-1,1-\frac{\alpha}{2}}\frac{S}{\sqrt{n-1}}$	39.48	40.27	34.26	19.34	14.19	5.98	7.85

Table 9. Statistical values for calculation of the confidence interval for level H=10 cm

Distance from the symmetry axis x [cm] / Statistical values	0	1	2	3	4	5	6	7	8
$\overline{V_y}$	20.4	21.2	22.0	19.6	15.5	11.0	6.2	4.5	2.5
S	6.344	6.013	4.099	2.939	3.0	5.099	2.561	2.291	0.5
n	5	5	5	5	5	5	5	4	2
$t_{n-1,1-\frac{\alpha}{2}}$	2.7764	2.7764	2.7764	2.7764	2.7764	2.7764	2.7764	3.1824	12.706
$t_{n-1,1-\frac{\alpha}{2}} \frac{S}{\sqrt{n-1}}$	8.81	8.35	5.69	4.08	4.16	7.08	3.56	4.21	6.35
$\overline{V_y} - t_{n-1,1-\frac{\alpha}{2}} \frac{S}{\sqrt{n-1}}$	11.59	12.85	16.31	15.52	11.34	3.92	2.64	0.29	0
$\overline{V_y} + t_{n-1,1-\frac{\alpha}{2}} \frac{S}{\sqrt{n-1}}$	29.21	29.55	27.69	23.68	19.66	18.08	9.76	8.71	8.85

Table 10. Statistical values for calculation of the confidence interval for level H=20 cm

Distance from the symmetry axis x [cm] / Statistical values	0	1	2	3	4	5	6	7	8	9	10	11
$\overline{V_y}$	16.5	17.5	17.75	17.125	16.25	15.25	13.125	10.0	5.0	2.25	1	1
S	0.5	0.5	0.829	1.244	1.920	2.681	2.701	3.391	2.739	0.25	1	-
n	4	4	4	4	4	4	4	4	4	2	1	-
$t_{n-1,1-\frac{\alpha}{2}}$	3.1824	3.1824	3.1824	3.1824	3.1824	3.1824	3.1824	3.1824	3.1824	12.706		
$t_{n-1,1-\frac{\alpha}{2}}\frac{S}{\sqrt{n-1}}$	0.92	0.92	1.52	2.29	3.53	4.93	4.96	6.23	5.03	3.18		
$\overline{V_y}-t_{n-1,1-\frac{\alpha}{2}}\frac{S}{\sqrt{n-1}}$	15.58	16.58	16.23	14.84	12.72	10.32	8.17	3.77	0	0		
$\overline{V_y}+t_{n-1,1-\frac{\alpha}{2}}\frac{S}{\sqrt{n-1}}$	17.42	18.42	19.27	19.42	19.78	20.18	18.09	16.23	10.03	5.43		

Table 11. Statistical values for calculation of the confidence interval for level H=30 cm

Distance from the symmetry axis x [cm] / Statistical values	0	1	2	3	4	5	6	7	8	9	10	11	12	13	14
$\overline{V_y}$	15.0	16.0	15.67	15.33	15.33	14.0	12.67	11.33	9.0	4.0	4.0	3.0	2.0	1.0	1.0
S	0.816	0.816	0.943	1.247	1.247	2.16	2.625	3.091	2.16	1.414					
n	3	3	3	3	3	3	3	3	3	3	1	1	1	1	1
$t_{n-1,1-\frac{\alpha}{2}}$	4.3027	4.3027	4.3027	4.3027	4.3027	4.3027	4.3027	4.3027	4.3027	4.3027					
$t_{n-1,1-\frac{\alpha}{2}}\frac{S}{\sqrt{n-1}}$	2.48	2.48	2.87	3.79	3.79	6.57	7.99	9.40	6.57	4.30					
$\overline{V_y}-t_{n-1,1-\frac{\alpha}{2}}\frac{S}{\sqrt{n-1}}$	12.52	13.52	12.80	11.54	11.54	7.43	4.68	1.93	2.43	0					
$\overline{V_y}+t_{n-1,1-\frac{\alpha}{2}}\frac{S}{\sqrt{n-1}}$	17.48	18.48	18.54	19.12	19.12	20.57	20.66	20.73	15.57						

Table 12. Statistical values for calculation of the confidence interval for level H=40 cm

Distance from the symmetry axis x [cm] / Statistical values	0	1	2	3	4	5	6	7	8
$\overline{V_y}$	11.33	12.33	13.33	14.5	14.33	14.50	12.83	11.67	10. 5
S	3.091	3.091	2.357	0.408	0.471	1.080	0.850	0.943	1.472
n	3	3	3	3	3	3	3	3	3
$t_{n-1,1-\frac{\alpha}{2}}$	4.3027	4.3027	4.3027	4.3027	4.3027	4.3027	4.3027	4.3027	4.3027
$t_{n-1,1-\frac{\alpha}{2}}\frac{S}{\sqrt{n-1}}$	9.40	9.40	7.17	1.24	1.43	3.29	2.59	2.87	4.48
$\overline{V_y}-t_{n-1,1-\frac{\alpha}{2}}\frac{S}{\sqrt{n-1}}$	1.93	2.93	6.17	13.26	12.90	11.21	10.24	8.80	6.02
$\overline{V_y}+t_{n-1,1-\frac{\alpha}{2}}\frac{S}{\sqrt{n-1}}$	20.73	21.73	20.50	15.74	15.76	17.79	15.42	14.37	14.98

Cont. Table 12.

Distance from the symmetry axis x [cm] / Statistical values	9	10	11	12	13	14	15	16
$\overline{V_y}$	9.5	6.33	6.0	3.0	3.0	2.0	1.0	1.0
S	2.273	3.682	1.0	1.0				
n	3	3	2	2	1	1	1	1
$t_{n-1,1-\frac{\alpha}{2}}$	4.3027	4.3027	12.706	12.706				
$t_{n-1,1-\frac{\alpha}{2}} \frac{S}{\sqrt{n-1}}$	6.92	11.20	12.71	12.71				
$\overline{V_y} - t_{n-1,1-\frac{\alpha}{2}} \frac{S}{\sqrt{n-1}}$	2.58	0	0	0				
$\overline{V_y} + t_{n-1,1-\frac{\alpha}{2}} \frac{S}{\sqrt{n-1}}$	16.42	17.57	18.71	15.71				

Table 13. Statistical values for calculation of the confidence interval for level H=50 cm

Distance from the symmetry axis x [cm]	Statistical values						
	$\overline{V_y}$	S	n	$t_{n-1,1-\frac{\alpha}{2}}$	$t_{n-1,1-\frac{\alpha}{2}}\frac{S}{\sqrt{n-1}}$	$\overline{V_y}-t_{n-1,1-\frac{\alpha}{2}}\frac{S}{\sqrt{n-1}}$	$\overline{V_y}+t_{n-1,1-\frac{\alpha}{2}}\frac{S}{\sqrt{n-1}}$
0	10.5	4.5	2	12.706	57.18	0	67.68
1	12.0	4.0	2	12.706	50.82	0	62.82
2	13.0	3.0	2	12.706	38.12	0	31.45
3	14.0	3.0	2	12.706	38.12	0	52.12
4	14.0	2.0	2	12.706	25.41	0	39.41
5	13.5	1.5	2	12.706	19.06	0	32.56
6	13.0	1.0	2	12.706	12.71	0.29	25.71
7	12.5	0.5	2	12.706	6.35	6.15	18.85
8	11.5	0.5	2	12.706	6.35	5.15	17.85
9	10.5	0.5	2	12.706	6.35	4.15	16.85
10	9.5	0.5	2	12.706	6.35	3.15	15.85
11	6.0	1.0	2	12.706	12.706	0	18.71
12	5.5		1				
13	4.0		1				
14	3.0		1				
15	2.5		1				
16	2.5		1				
17	2.0		1				
18	1.5		1				
19	1.5		1				
20	1.5		1				
21	1.0		1				

Appendix 4

Section 3.4.6. Empirical description of asymmetric flow in the model. Discharge from the left

Table 1. Readings at level H=5 cm

Time [s]	Velocities V_y [mm/s] at the distance from the symmetry axis x [cm]						
	0	1	2	3	4	5	6
1	34.0	33.5	25.0	15.0	4.0	1.0	0
25	12.0	20.0	24.0	23.0	15.0	6.0	1.0
50	29.5	32.0	31.5	20.0	7.0	5.0	1.0
75	25.0	32.5	27.0	15.0	7.0	5.0	3.0
100	23.5	27.5	29.0	25.0	13.0	3.0	1.0

Table 2. Readings at level H=10 cm

Time [s]	Velocities V_y [mm/s] at the distance from the symmetry axis x [cm]								
	0	1	2	3	4	5	6	7	8
1	16.0	16.7	16.0	16.0	12.0	7.0	4.0	1.0	0
25	16.5	19.0	20.0	18.5	19.0	15.0	7.0	0	0
50	15.0	18.0	19.0	17.0	17.0	16.0	11.0	6.0	0
75	13.5	18.0	18.5	18.0	14.0	10.0	8.0	8.0	5.0
100	14.0	20.5	21.5	20.0	17.0	12.0	8.0	3.0	1.5

Table 3. Readings at level H=20 cm

Time [s]	Velocities V_y [mm/s] at the distance from the symmetry axis x [cm]										
	0	1	2	3	4	5	6	7	8	9	10
1	17.0	18.0	17.0	15.0	13.0	11.0	9.0	6.0	4.0	2.0	1.0
25	17.0	18.0	18.0	18.0	18.0	17.0	13.0	8.0	1.0	0	0
50	16.0	17.0	17.0	17.5	17.0	18.0	16.5	15.0	8.0	0	0
75	16.0	17.0	19.0	18.0	17.0	15.0	14.0	11.0	7.0	2.5	0

Table 4. Readings at level H=30 cm

Time [s]	Velocities V_y [mm/s] at the distance form the symmetry axis x [cm]															
	0	1	2	3	4	5	6	7	8	9	10	11	12	13	14	15
1	10.0	10.0	10.0	11.0	12.0	11.0	11.0	10.0	9.0	8.0	5.0	4.0	2.5	2.5	2.0	1.5
25	12.0	12.0	12.0	12.5	12.0	12.0	11.5	12.0	10.0	5.0	0	0	0	0	0	0
50	12.5	13.0	13.0	13.0	12.5	12.5	13.3	12.0	10.0	7.0	3.0	3.0	0	0	0	0

Table 5. Readings at level H=40 cm

Time [s]	Velocities V_y [mm/s] at the distance form the symmetry axis x [cm]																
	0	1	2	3	4	5	6	7	8	9	10	11	12	13	14	15	16
1	9.5	10.0	10.5	11.0	11.5	11.0	11.0	10.5	10.5	10.0	8.0	7.0	5.0	4.0	2.5	2.0	1.5
25	11.8	11.8	11.8	11.0	11.5	10.5	12.0	11.5	10.0	7.5	4.0	0	0	0	0	0	0
50	11.0	11.5	12.0	12.0	12.0	12.0	11.5	10.5	10.0	9.0	7.0	2.0	0	0	0	0	0

Table 6. Readings at level H=50 cm

Time [s]	Velocities V_y [mm/s] at the distance form the symmetry axis x [cm]																		
	0	1	2	3	4	5	6	7	8	9	10	11	12	13	14	15	16	17	18
1	10.0	10.0	10.0	11.0	11.5	10.5	12.5	12.0	12.0	10.0	9.0	8.5	7.5	6.0	5.0	4.0	3.0	2.5	1.5
25	10.	11.0	11.0	10.5	10.5	11.0	11.5	10.0	9.0	8.0	6.5	4.5	1.0	0	0	0	0	0	0

Table 7. Readings at level H=60 cm

Time [s]	Velocities V_y [mm/s] at the distance form the symmetry axis x [cm]																					
	0	1	2	3	4	5	6	7	8	9	10	11	12	13	14	15	16	17	18	19	20	21
1	10.0	8.0	11.0	11.5	11.5	12.0	11.5	11.0	12.5	11.5	10.5	10.0	9.0	8.0	6.0	5.5	5.0	5.0	3.0	3.0	2.0	1.5

Table 8. Statistical values to calculate the confidence interval for level *H*=5 cm

Distance from the symmetry axis *x* [cm] / Statistical values	0	1	2	3	4	5	6
$\bar{V}_y$	24.8	29.1	27.3	19.6	9.2	4.0	1.5
S	7.38	4.994	2.713	4.079	4.118	1.789	0.866
n	5	5	5	5	5	5	4
$t_{n-1,1-\frac{\alpha}{2}}$	2.7764	2.7764	2.7764	2.7764	2.7764	2.7764	3.1824
$t_{n-1,1-\frac{\alpha}{2}}\frac{S}{\sqrt{n-1}}$	10.24	6.93	3.77	5.66	5.72	2.48	1.59
$\bar{V}_y - t_{n-1,1-\frac{\alpha}{2}}\frac{S}{\sqrt{n-1}}$	14.56	22.17	23.53	13.94	3.48	1.52	0
$\bar{V}_y + t_{n-1,1-\frac{\alpha}{2}}\frac{S}{\sqrt{n-1}}$	35.04	36.03	31.07	25.26	14.92	6.48	3.09

Table 9. Statistical values to calculate the confidence interval for level H=10 cm

Distance from the symmetry axis x [cm] / Statistical values	0	1	2	3	4	5	6	7	8
$\overline{V_y}$	15.0	18.44	19.0	17.9	15.8	12.0	7.2	4.5	3.25
S	1.14	1.263	1.819	1.356	2.482	3.286	2.315	2.693	1.75
n	5	5	5	5	5	5	5	4	2
$t_{n-1,1-\frac{\alpha}{2}}$	2.7764	2.7764	2.7764	2.7764	2.7764	2.7764	2.7764	3.184	12.706
$t_{n-1,1-\frac{\alpha}{2}} \frac{S}{\sqrt{n-1}}$	1.58	1.75	2.52	1.88	3.45	4.56	3.21	4.94	22.23
$\overline{V_y} - t_{n-1,1-\frac{\alpha}{2}} \frac{S}{\sqrt{n-1}}$	13.42	16.69	16.48	16.02	12.35	7.44	3.99	0	0
$\overline{V_y} + t_{n-1,1-\frac{\alpha}{2}} \frac{S}{\sqrt{n-1}}$	16.58	20.19	21.52	19.71	19.25	16.56	10.41	9.45	25.49

Table 10. Statistical values to calculate the confidence interval for level H=20 cm

Distance from the symmetry axis x [cm] / Statistical values	0	1	2	3	4	5	6	7	8	9	10	11
$\overline{V_y}$	11.94	13.0	13.56	13.44	13.38	13.0	12.0	10.25	6.88	4.0	2.5	2.0
S	1.327	1.768	1.504	1.204	0.893	1.275	1.225	1.479	3.090	0.816		
n	4	4	4	4	4	4	4	4	4	3	1	1
$t_{n-1,1-\frac{\alpha}{2}}$	3.1824	3.1824	3.1824	3.1824	3.1824	3.1824	3.1824	3.1824	3.1824	4.3027		
$t_{n-1,1-\frac{\alpha}{2}} \frac{S}{\sqrt{n-1}}$	2.44	3.25	2.76	2.21	1.64	2.34	2.25	2.72	5.68	2.48		
$\overline{V_y} - t_{n-1,1-\frac{\alpha}{2}} \frac{S}{\sqrt{n-1}}$	9.5	9.75	10.8	11.23	11.74	10.66	9.75	7.53	1.2	1.52		
$\overline{V_y} + t_{n-1,1-\frac{\alpha}{2}} \frac{S}{\sqrt{n-1}}$	14.38	16.25	16.32	15.65	15.02	15.34	14.25	12.97	12.56	6.48		

Table 11. Statistical values to calculate the confidence interval for level H=30 cm

Distance from the symmetry axis x [cm] / Statistical values	0	1	2	3	4	5	6	7	8	9	10	11	12	13	14	15
$\overline{V_y}$	11.5	11.67	11.67	12.17	12.17	11.83	11.93	11.39	9.67	6.67	4.0	4.0	2.5	2.5	2.0	1.0
S	1.08	1.247	1.247	0.849	0.055	0.624	0.688	0.943	0.471	1.247	1.0					
n	3	3	3	3	3	3	3	3	3	3	2	1	1	1	1	1
$t_{n-1,1-\frac{\alpha}{2}}$	4.3027	4.3027	4.3027	4.3027	4.3027	4.3027	4.3027	4.3027	4.3027	4.3027	12.706					
$t_{n-1,1-\frac{\alpha}{2}}\frac{S}{\sqrt{n-1}}$	3.29	3.79	3.79	2.58	0.17	1.90	2.09	2.87	1.43	3.79	12.71					
$\overline{V_y}-t_{n-1,1-\frac{\alpha}{2}}\frac{S}{\sqrt{n-1}}$	8.21	7.88	7.88	9.59	12.0	9.93	9.84	8.46	8.24	2.88	0					
$\overline{V_y}+t_{n-1,1-\frac{\alpha}{2}}\frac{S}{\sqrt{n-1}}$	14.75	15.46	15.46	14.75	12.34	13.73	14.02	14.2	11.1	10.46	16.71					

Table 12. Statistical values to calculate the confidence interval for level H=40 cm

Distance from the symmetry axis x [cm] / Statistical values	0	1	2	3	4	5	6	7	8
$\overline{V_y}$	10.77	10.83	11.43	11.33	11.67	11.17	11.5	10.83	10.17
S	0.953	0.624	0.665	0.471	0.236	0.624	0.408	0.471	0.236
n	3	3	3	3	3	3	3	3	3
$t_{n-1,1-\frac{\alpha}{2}}$	4.3027	4.3027	4.3027	4.3027	4.3027	4.3027	4.3027	4.3027	4.3027
$t_{n-1,1-\frac{\alpha}{2}} \frac{S}{\sqrt{n-1}}$	2.90	1.90	2.02	1.43	0.72	1.90	1.24	1.43	0.72
$\overline{V_y} - t_{n-1,1-\frac{\alpha}{2}} \frac{S}{\sqrt{n-1}}$	7.87	8.93	9.41	9.90	10.95	9.27	10.26	9.40	9.45
$\overline{V_y} + t_{n-1,1-\frac{\alpha}{2}} \frac{S}{\sqrt{n-1}}$	11.67	12.73	13.45	12.76	12.39	13.07	12.74	12.26	10.89

Cont. Table 12.

Distance from the symmetry axis [cm] / Statistical values	x=9	x=10	x=11	x=12	x=13	x=14	x=15	x=16
$\bar{V}_y$	8.83	6.33	4.5	5.0	4.0	2.5	2.0	1.5
S	1.027	1.700	2.500					
n	3	3	2	1	1	1	1	1
$t_{n-1,1-\frac{\alpha}{2}}$	4.3027	4.3027	12.706					
$t_{n-1,1-\frac{\alpha}{2}}\frac{S}{\sqrt{n-1}}$	3.12	5.17	31.77					
$\bar{V}_y - t_{n-1,1-\frac{\alpha}{2}}\frac{S}{\sqrt{n-1}}$	5.71	1.16	0					
$\bar{V}_y + t_{n-1,1-\frac{\alpha}{2}}\frac{S}{\sqrt{n-1}}$	11.95	11.50	36.27					

Table 13. Statistical values to calculate the confidence interval for level H=50 cm

Distance from the symmetry axis x [cm]	Statistical values						
	$\overline{V_y}$	S	n	$t_{n-1,1-\frac{\alpha}{2}}$	$t_{n-1,1-\frac{\alpha}{2}}\frac{S}{\sqrt{n-1}}$	$\overline{V_y}-t_{n-1,1-\frac{\alpha}{2}}\frac{S}{\sqrt{n-1}}$	$\overline{V_y}+t_{n-1,1-\frac{\alpha}{2}}\frac{S}{\sqrt{n-1}}$
0	10.25	0.25	2	12.206	3.18	7.07	13.43
1	10.5	0.5	2	12.206	6.35	4.15	16.85
2	10.5	0.5	2	12.206	6.35	4.15	16.85
3	10.75	0.25	2	12.206	3.18	7.57	13.93
4	11.0	0.5	2	12.206	6.35	4.65	17.35
5	10.75	0.25	2	12.206	3.18	7.57	13.93
6	12.0	0.5	2	12.206	6.35	5.65	18.35
7	11.0	1.0	2	12.206	12.71	0	23.71
8	10.5	1.5	2	12.206	19.06	0	29.56
9	9	1.0	2	12.206	12.71	0	21.71
10	7.75	1.25	2	12.206	15.88	0	23.63
11	6.5	2.0	2	12.206	25.41	0	31.91
12	7.5		1				
13	6.0		1				
14	5.0		1				
15	4.0		1				
16	3.0		1				
17	2.5		1				
18	1.5		1				
19	0.5		1				

Notations:

$\bar{V}_y$ – average vertical velocity,

S – standard deviation [92, 135],

α – significance level,

n – number of readings,

$t_{n-1,1-\frac{\alpha}{2}}$ – quantile of *tStudent* distribution,

$t_{n-1,1-\frac{\alpha}{2}}\frac{S}{\sqrt{n-1}}$ – half of the confidence interval,

$\bar{V}_y - t_{n-1,1-\frac{\alpha}{2}}\frac{S}{\sqrt{n-1}}$ – lower limit of the confidence interval,

$\bar{V}_y + t_{n-1,1-\frac{\alpha}{2}}\frac{S}{\sqrt{n-1}}$ – upper limit of the confidence interval.